UNIVERSITE LILLE 1

Sciences et Technologies

Ecole Doctorale N°104: Sciences de la Matière, du Rayonnement et de l'Environnement

THESE

pour obtenir le grade de :

Docteur de l'Université de Lille 1

Spécialité : Optique & Lasers, P-C, Atmosphère

Présentée et soutenue publiquement le 23 Juin 2011
par

Shan ZENG

Comparaison et analyse statistique des propriétés nuageuses dérivées des instruments POLDER et MODIS dans le cadre de l'expérience spatiale A-Train

(Comparison and statistical analysis of cloud properties derived from POLDER and MODIS instruments into the framework of the A-Train spatial experiment)

JURY

Mme	:	Claudia	STUBENRAUCH	Président
Mr	:	Jean-Louis	DUFRESNE	Rapporteurs
		William B.	ROSSOW	
MM	:	Anne	LIFERMANN	Examinateurs
		Jacques	PELON	
		Jérôme	RIEDI	
Mr	:	Timothy	GARRETT	Invité
MM	:	Frédéric	PAROL	Directeur de thèse
		Céline	CORNET	Co-encadrant de thèse

Laboratoire d'Optique Atmosphérique
U.F.R de Physique Fondamentale
Université Lille 1 Sciences et Technologies
59655 Villeneuve d'Ascq
France

RESUMÉ

Les observations des différents A-Train satellites fournissent une occasion sans précédent d'étudier les composants atmosphériques y compris les nuages. Dans cette étude, nous avons développé une analyse statistique afin de comparer le taux de couverture nuageuse, la phase thermodynamique et l'épaisseur optique des nuages restituées par deux capteurs passifs de l'A-Train: POLDER (Polarization and Directionality of the Earth Reflectance) et MODIS (MODerate Resolution Imaging Spectroradiometer).

Tout d'abord les variations régionales et saisonnières du taux de couverture nuageuse des deux captures et les biais entre eux sont étudiés. Ces biais sont retrouvés principalement liée avec la résolution spatiale, les aérosols, les cirrus et des types de surface.

Ensuite la phase thermodynamique des nuages sont analysées. Ces produits dérivés par deux capteurs passifs sont comparées et étudiées en s'appuyant sur les structures verticales et les propriétés optiques des nuages restituées simultanément par un autre A-Train membre, CALIOP (Cloud-Aerosol Lidar with Orthogonal Polarization). Cela permet d'identifier et de qualifier les biais présents dans l'ensemble des 3 données considérées. Parmi ces biais, l'impact des géométries d'observation, des cirrus fins, des aérosols, des surfaces enneigées, des nuages multicouches et fractionnés sont discutées. Les valeurs de haute confiance sont selectionées par la suite pour étudier à l'échelle mondiale ou régionale la transition verticale de l'eau liquide à la glace et les variations de cette transition avec les régimes de formation et de développement des nuages, tout particulièrement la dynamique à grande échelle et la microphysique des nuages.

Enfin l'épaisseur optique des nuages sont étudiées. Les effets de la résolution spatiale, de la microphysique et de l'hétérogénéité des nuages sont principalement étudiés pour mieux comprendre des écarts importants entre deux capteurs passifs.

ABSTRACT

The A-Train observations provide an unprecedented opportunity for synchronous monitoring of the entire atmosphere including clouds at the global scale. In this study we illustrate a statistical analysis and comparison of cloud cover, thermodynamic phase and cloud optical thickness mainly derived from the coincident POLDER (Polarization and Directionality of the Earth Reflectance), and MODIS (MODerate Resolution Imaging Spectroradiometer) sensors in the A-Train constellation.

We presented first the results of extensive study of the regional and seasonal variations of cloud cover from POLDER and MODIS and discuss the possible factors linked to the potential biases between them, among which the spatial resolution, aerosols, cirrus and particular surfaces are particularly concerned.

Cloud top phase products were then compared between the two passive sensors and discussed in view of cloud vertical structure and optical properties derived simultaneously from collocated CALIOP (Cloud-Aerosol Lidar with Orthogonal Polarization, another A-Train member) observations, which allow to identify and qualify potential biases present in the 3 considered dataset. Among those, we discussed the impact of observed geometries, thin cirrus, aerosols, snow/ice surfaces, multilayer and fractional cloud cover on global statistics of cloud phase derived from POLDER and MODIS passive measurements. Based on these analyses we selected cloud retrievals of high confidence to study the global and regional vertical ice-water transition and the variations of this transition with cloud formation and development regimes, particularly the impact of large-scale dynamics and cloud microphysics.

Cloud optical thicknesses were finally studied. The impacts of spatial resolution, cloud microphysics and heterogeneity are mainly discussed for the understanding of the significant biases on optical thickness from the two sensors.

ACKNOWLEDGEMENTS

Table of contents

List of Tables

List of Figures

List of Acronyms

ADEOS   Advanced Earth Observing Satellite
AIRS   Atmospheric Infrared Sounder
AIST   Along Track Scanning Radiometer
BT   Brightness Temperature
BTD   Brightness Temperature Difference
CALIOP   Cloud-Aerosol Lidar with Orthogonal Polarization
CALIPSO   Cloud-Aerosol Lidar and Infrared Pathfinder Satellite Observations
CCD   Charged Coupled Device
CCN   Cloud Condensation Nucleation
CERES   Cloud and the Earth's Radiant Energy System
CF   Cloud Fraction
CFC   Cloud Fraction Combined
CFD   Cloud Fraction Day
CNES   Centre National D'étude Space
COT   Cloud Optical Thickness
CTT   Cloud Top Temperature
ECMWF   European Center for Medium-Rang Weather Forecast
EOS   Earth Observing System
FOV   Fill Of View
ERB   Earth Radiation Budget
FDTD   Finite Difference Time Domain
GEWEX   Global Energy and Water Cycle Experiment
GCM   Global Climate Model
IIR   Imaging Infrared Radiometer
IR   Infrared
IWA   Ice Water Algorithm
IPA   Independent Pixel Approximation
IPCC   Intergovernmental Panel on Climate Change
ISCCP   International Satellite Cloud Climatology Projet
ITCZ   InterTropical Convergence Zone
JAXA   Japan Aerospace Exploration Agency
LOA   Laboratoire d'Optique Atmosphérique
LUT   Looking Up Table
MISR   Multi-angle Imaging SpectroRadiometer
MODIS   Moderate Resolution Imaging Spectroradiometer
NASA   National Aeronautics and Space Administration
NH/SH   North (South) Hemisphere
NIR   Near Infrared
OCO   Overseas Contingency Operation
OMI   Ozone Monitoring Instrument
OT   Optical Thickness
PARASOL   Polarization and Anisotropy of Reflectances for Atmospheric Sciences
            coupled with Observations from a Lidar
PDF   Probability Density Function
PM   POLDER MODIS
POLDER   Polarization and Directionality of the Earth's Reflection
PPH   Plan Parallel Hypothesis

RMS	Root Mean Square
SEVIRI	Spinning Enhance Visible and Infrared Imager
SST	See Surface Temperature
ST	Strom Track
SW	Short Wave
SZA	Solar Zenith Angle
TOA	Top of Atmosphere
VZA	Viewing Zenith Angle
WV	Water Vapor

Chapter 1 Introduction

1.1 Context

Climate changes have become a major concern since the end of last century. The broad agreement has been reached among climate scientists that the global air and surfaces temperatures are in course of increasing and would maintain this increasing trend for a long period. According to the last IPCC (Intergovernmental Panel on Climate Change) report (2007), it is more than 90% probable that human activities are largely responsible for the modern-day climate changes. To struggle the global warming and protect our common earth, the united efforts from the whole society are needed. After years of continuous researches and vigorous propaganda on climate changes, more and more persons have recently recognized the importance to alleviate global warming. At the end of 2009, the Copenhagen climate summit was hold for the purpose of creating global collaboration between countries to reduce the carbon emission. No matter how many accords have been made during the summit, seeking for the globally environmental protection and the sustainable development is indeed a long way and we are just on this way.

For the current earth, as reported in IPCC report in 2007, the global surface temperature has increased by $0.74 \pm 0.18\ ^\circ C$ between the start and the end of the 20th century and especially during the last 50 years when the increasing speed was about twice rapid as being observed for the whole 100 years. It also reported that a probably continuous rise for a further 1.1 to $6.4\ ^\circ C$ could happen during the twenty-first century. Associated to the global warming of the climate system, besides the evident increasing of global average air and ocean temperatures, a widespread melting of snow and sea ice, and the subsequent rising of the global average sea level are also evidently observed. At continental, regional and ocean basin scales, numerous long-

term changes in climate have also been found. This contains the changes in arctic temperatures, ice coverage, precipitation amounts, ocean salinity, wind patterns and aspects of extreme weather.

From radiative forcing assessment, IPCC reported that anthropogenic warming lead to a global radiative forcing of [+0.6 to +2.4] Wm^{-2}. This anthropogenic warming mixes many different effects, among which the greenhouse gases with a radiative forcing of [+2.07 to +2.53] Wm^{-2}, and the aerosols with a radiative forcing of [-0.9 to -0.1] Wm^{-2} are two important and well-known sources. In fact, the global warming does not mean a simple increasing atmospheric temperature caused by the effect of the greenhouse gases, various feedbacks are involved and connected. Among all effects, only parts of them are qualified and understood. The feedback with the largest potential impact involves the clouds, which permanently cover almost 50% -70% of the earth surface (Stephens, 2004; Bony et al., 2006; Dessler, 2010). As one of the most important components in the atmosphere, clouds affect the flow of energy within Earth's atmosphere and to its surface. Clouds reflect a large quantity of sunlight out to the space while at the same time these make an important contribution to Earth's greenhouse effect. Research shows that, as a result of both warming and cooling effects, clouds overall cool our earth. The net radiative forcing of global clouds at top of atmosphere is about -20 W.m² comparing to the annual average of 340 $W.m^2$ received by the Earth-atmosphere system (Ramanathan, 1989). A small change in cloudiness and cloud properties would play an extremely important and direct role on radiative balance of the Earth-Atmosphere system and would amplify or offset climatic temperature perturbations. Recent studies also show that the large differences of climate sensitivity estimations among models are found associated primarily to the inter-model differences in cloud feedbacks (Stephens, 2004; Dufresne and Bony, 2008). The impact of clouds on climate changes is complex. In current time, understanding the role of clouds in regulating both weather and climate is still at an early stage. It remains as one of the largest uncertainties in future projections of climate change by global climate models, owing to the large variations of clouds cover, the physical complexity of cloud processes and the small scale of individual clouds relative to the size of the model computational grid. With different cloud microphysical, physic-chemical, dynamics and radiative formation processes, different types of clouds have different effects on the energy balance (Hartmann et al., 1992). This is still under investigation for particular clouds.

Beside the feedback from the complex clouds themselves, clouds are in fact linked with many feedback processes in the climate system, such as, cloud and water vapor feedback, cloud, lapse rate and precipitation feedback, cloud and sea ice albedo feedback, cloud and soil moisture feedback, cloud, chemistry and marine biosphere feedback (Council, 2003). The well known "aerosols indirect effect" can affect the formation and properties of clouds (Twomey, 1974; Albrecht, 1989; Pincus and Baker, 1994; Ramanathan *et al.*, 2001). By enhancing the anthropogenic aerosol concentration, cloud albedo and lifetime could increase and therefore impact the climate. The radiative forcing from the indirect cloud albedo effect is estimated as -0.7 Wm^{-2} IPCC, 2007. In addition, the increasing greenhouse gases may impact the cloud cover but currently this effect still represents large uncertainty in models (IPCC, 2007). Furthermore, clouds as a vital link in the global water cycle system can carry and transfer in horizontal (from tropics to poles and from ocean to land) and vertical directions (from surface to top of atmosphere) the water and the latent heat by evaporation or condensation, which accompany their formation, dispersion and movement. It is associated to the precipitation, which is also one of the greatest changes of climate.

Cloud impacts on the energy balance and on the water cycle system are thus of a great importance. Its role to climate changes has not been well qualified. A lot of work waits to be done.

Recently, great efforts have been devoted to the cloud studies with many different observations (surface observations, radiosonde, radar/lidar, airborne measurements…) especially from the modern satellites, which provide a continuous monitoring of the atmosphere state over the whole globe, day after night. After several decades of progress, many kinds of meteorological satellites (both geostationary satellites and sun-synchronous orbit satellites) with various advanced instruments onboard have been developed. The rapid progress of science and technology allows the onboard sensors to have now a high spatial resolution so as to identify the smaller elements in the field of view. They also own more advanced performances that have already been well controlled (active, passive, polarized, multi-directional, multi-spectral…). Different from the looking-up observations at the ground, the satellites observe the uppermost level of clouds and get their properties by collecting and analyzing the captured radiances at the top of atmosphere, which are the result of scattering, absorption and emission of the atmospheric components (e.g.

clouds, aerosols, and gases). As the cloud properties are not direct measurements, inversions need to be performed. Differences in the retrieved cloud properties can thus appear according the type of instruments and the used inversion techniques. Typically, recent ground and satellite observations show a consistent reduction trend of high cloud cover during the period of 1980-1990 (IPCC, 2007). However, the regional and multi-decadal trend of total cloud cover and low-level clouds has no clear consensus.

A better understanding on clouds and their climatic effects requires a careful establishment of the global and long-term cloud records. Many international organizations and projects like ISCCP (International Satellite Cloud Climatology Project), PATMOS-X and GEWEX (Global Energy and Water Cycle Experiment) are therefore founded to do these jobs. The GEWEX cloud assessment actually combines multi-satellites products (e.g. ISCCP, MODIS, CALIPSO, POLDER, CERES, MISR, PATMOSX, AIRS, ATSR…) to study the cloud climatologies at the global scale. This accumulation of cloud records and the combined analysis of them need to first produce a unified dataset from different satellites with their own distinct characteristics and retrieval techniques. Indeed this unifying process is indispensable and important as it permits not only to establish the confident and continuous temporal and regional observations but also to discover the strengths and weaknesses of each technique. Different techniques may have more or less difficulties to detect some of the atmospheric components and to determine their properties. One step of great importance is therefore to compare and validate the cloud observations between different satellites. This inter-comparison between satellites can supply the traditional validation for satellite measurements from the ground-based/airborne measurements.

Since May 4, 2002, the launch of AQUA, a group of five (would be more) sun-synchronous orbit satellites called A-Train is focused on a combination study of the atmosphere (clouds, aerosol, gases, precipitation…) through their independent but complementary missions. This is an unprecedented opportunity to better understand distinctive detection techniques and would lead to the improvements of retrieval techniques. As a consequence, we could get more correct information about atmospheric structures and components and then to better describe and understand the complex interactions among these atmospheric components on climate changes that are needed to support the cloud and climate models.

My Ph.D. work concerns statistic studies of level 2 and 3 cloud properties

retrieved from POLDER/PARASOL and MODIS/AQUA, which are two members of this A-Train constellation. The active instrument CALOP/CALIPSO, also in this constellation, is used to assist the work if necessary. As a support to the GEWEX cloud assessment and cloud studies on climate changes, this work performing global scale studies of cloud products gives scientific concepts on cloud properties to all users of these two satellites so as to better understand what clouds are observed from these satellites and how confident they can represent the real cloud properties in the real atmosphere. The main cloud properties studied here are cloud cover, cloud phase and cloud optical thickness, which are among the most basic and crucial cloud properties, but still present some uncertainties with the limited techniques and knowledge of nowadays.

Concerning cloud detections, for example, the automatic distinction between the clear sky and cloudy scene is not trivial and depends on the characteristics and retrieval techniques of different sensors and also on the cloud structures and its environmental conditions. For instance, passive remote sensing using radiation contrast tests have bad skills to detect optically thin clouds such as cirrus (Wylie and Menzel, 1989), to separate clouds and heavy aerosols (Remer *et al.*, 2005) and to discriminate clouds over brilliant or snow-sea ice surface (Rossow *et al.*, 1989; Roy *et al.*, 2002). Cloud phase and optical thickness are two parameters related to cloud microphysical processes such as collection of water molecules, diffusion and collection of smaller drops, break-up of large drops, evaporation, ice nucleation and so on. Facing such complex microphysical processes, satellite observations and retrievals would have many limitations. For cloud phase, identification of mixed and supercooled water clouds and description of cloud phase in broken scenes and multi-layer systems still remains weak (Key and Intrieri, 2000; Kokhanovsky *et al.*, 2006; Riedi *et al.*, 2010; Wolters *et al.*, 2010). For cloud optical thickness, various size distributions and concentrations of cloud particles, complex ice crystal shapes and vertical and horizontal heterogeneities would also lead to retrieval uncertainties (Nakajima and King, 1990; Mishchenko *et al.*, 1996; Zhang *et al.*, 2009; Iwabuchi and Hayasaka, 2002). As the radiative forcing from clouds strongly depends on these cloud properties, to further discuss the changes of cloud properties amplifying or diminishing the surface warming, one of the most important steps is to get more correct cloud information from the satellite observations.

In the following chapter, we continue to give a brief presentation about clouds.

1.2 Clouds and their roles in the climate system

1.2.1 Cloud formation and structure

A cloud is a visible aggregation of small particles of condensed water, frozen crystals or a mixture of both, suspended in the atmosphere above the Earth surface and resulting of a series of microphysical processes (Robert A. Houze, 1994). Clouds are formed when air containing water vapor is cooled below a critical temperature (called dew point) and result of the condensation or sublimation of moisture into droplets or ice crystals on the nearest microscopic particles called condensation nuclei. Once a water droplet or ice crystal has been formed, it continues to grow either by condensation and sublimation onto the particle surface accompanying the release of latent heat or by the coalescence process. The second process makes the cloud development more rapid. The latent heat energy released during cloud formation process is important and can increase the vertical motion in clouds especially in convective clouds.

In fact, clouds can develop in any air mass containing aerosol particles (used as condensation nuclei) that becomes slightly supersaturated (relative humidity becomes more than 100%). Supersaturation occurs in cooling air by different atmospheric lifting mechanisms such as convergence lifting (e.g. in the interior of continents and near the equator), frontal lifting (e.g. in mid-latitudes along the polar front), orographic uplift (e.g. along the west coast of Canada) and radiative cooling. These mechanisms enhance cloud development and thus cloud cover. On the contrary, when the air mass descends in the adiabatic atmosphere (means no temperature inversion) (e.g. subtropical subsidence-area over desert), accompanying the warming process, the clouds disappear and the droplets transfer back to vapor.

During the cloud developing process, the water state in clouds can be changed between ice, liquid water and vapor by sublimation, condensation, and evaporation. In condition of strong vertical convection, when up-drifting liquid droplets pass the freezing level, they can turn to crystals. However, freezing is a complex process and in nature, freezing temperature can be much lower than 0°C. Water droplets colder than 0° C are called supercooled. Supercooled water drops occur often in abundance

in clouds with top temperatures between 0° C and -15° C, with decreasing amounts at colder temperatures (Smith, 1990). At temperatures colder than -15° C, sublimation is prevalent. However, the strong vertical currents could carry more supercooled water to great heights where temperatures are much colder than -15° C. Supercooled water has been observed at temperatures as cold as -40° C over continent (Del Genio *et al.*, 1996; Feigelson, 1978) and -30° over ocean (Curry *et al.*, 1990).

The cloud formation and development are not uniform processes. This determines the intrinsic heterogeneous structures of clouds. In horizontal direction, clouds vary on all spatial scales from planetary down to about 30m and the cloud fields are characterized by different number densities and different size distributions of particles (Albers *et al.*, 1999). In vertical direction, clouds are also non-uniform in appearance, which can be thinner or thicker and in microphysics, which can contain ice or water particles with different shapes and sizes. Taken low-level water clouds like warm stratocumulus as an example, the droplet radii distribution width decreases with height which means more appearance of large particles in cloud top (Miles *et al.*, 2000), where for high ice clouds like cirrus, very small crystals appear at the cloud top and its sizes decrease with height (Heymsfield and Iaquinta, 2000).

1.2.2 Cloud classification

- Clouds are mostly located between the sea level and the tropopause. As presented above, the underlying mechanism of cloud processes varies with region and season and contributes to the variations of cloud microphysical and macrophysical properties. It is thus impossible to simulate all the clouds in a single model. To simplify the studies of clouds and their effects on climate changes, clouds are grouped by cloud macrophysical and microphysical properties. The traditional and typical classification used by the international meteorology community is only based on their visual appearance and altitude (Robert A. Houze, 1994). According to this classification, there are 10 types of clouds (Figure 1.2-1 a):
- The cumulonimbus (Cb), cirrus (Ci), cirrostratus (Cs), cirrocumulus (CC), which are high clouds with a cloud top altitude between 20,000 and 40,000 ft (6,100–12,200 m).

- The altocumulus (Ac), altostratus (As), nimbostratus (Ns), which are intermediate clouds at the high of 6,500 to 20,000 ft (1,980–6,100 m).
- The stratus (St), stratocumulus (Sc), and cumulus (Cu), which are low clouds at 6,500 to 20,000 ft (1,980–6,100 m).

However, cloud studies use often computer technology and thus need simple and numerical cloud classification instead of visual separation so that it could be easy to assess the properties of different types of clouds and also to be used in meteorological cloud models and global climate models (GCM, Yao and Del Genio, 2002). The ISCCP criterion (Rossow and Schiffer, 1999) to classify the clouds is shown in Figure 1.2-1 (b). According to this classification, there are 9 types of clouds depending on the cloud top pressure and optical thickness. The separating boundaries of high, middle and low clouds are made at levels of 440hPa and 680hPa and those of thin and thick clouds are at levels of optical thickness of 3.6 and 23. High clouds include cirrus (Ci), which is one of the problematical types of clouds in remote sensing characterized by thin, wisplike strands, cirrostratus (Cs) and deep convection clouds (Cb). Low clouds include cumulus (Cu), stratocumulus, and stratus (St). Thin clouds include Ci, altocumulus (Ac), and Cu. Thick clouds include Cb, nimbostratus and St.
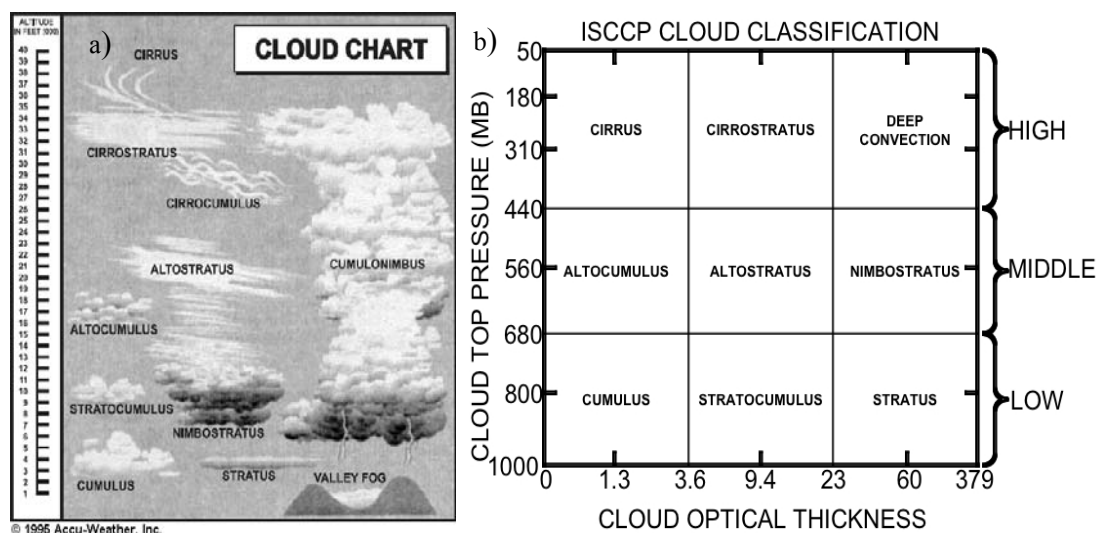
Figure 1.2-1 – *Schematic representation of the types of clouds (a) and classification from ISCCP (b).*

With clouds grouped in this way, it is easier to devote efforts in separate studies on each class of clouds, their microphysical, dynamical and radiative properties and their associated cloud feedbacks. With more correct information about these clouds, the knowledge of their effects on climate would be more accurate.

1.2.3 Clouds and the radiative budget of the Earth

1.2.3.1   Radiative balance of the Earth-Atmosphere system

The Earth-Atmosphere climate system adjusts the energy in a way that tends toward maintaining a balance between that reaches the Earth from the sun and that goes from Earth back out to space. Scientists refer it as Earth's "radiation budget". Over long-term, at the top of atmosphere (TOA), the incoming solar radiation is balanced by the Earth-Atmosphere system releasing longwave radiation and reflected shortwave radiation (see Figure 1.2-2). The solar radiation reaching the TOA is about 340 $W.m^{-2}$. About 30% of this radiation is reflected by the Earth-Atmosphere and 70% is emitted to space in longwave radiation. 2/3 of the shortwave reflected radiation is due to the clouds and aerosols and 1/3 due to the surface. Clouds and aerosols are thus key components of Earth-Atmosphere radiative system. Generally speaking, three processes will impact the radiation budget:
- Changes of solar radiation reached on Earth
- Changes of albedo, namely the reflection of solar shortwave radiation back to space (e.g. changes in cloud cover, distribution of vegetation, aerosols…)
- Changes of emitted longwave radiation from Earth (e.g. changes of greenhouse gas concentration)

Included in these three ways, various radiative forcings are used to estimate the changes of radiation and climate. In fact, in a very thin layer of atmosphere at a certain altitude, upward and downward radiation also tend toward constant balance. This basis conception of radiative balance induces the radiation transfer from one layer to another.
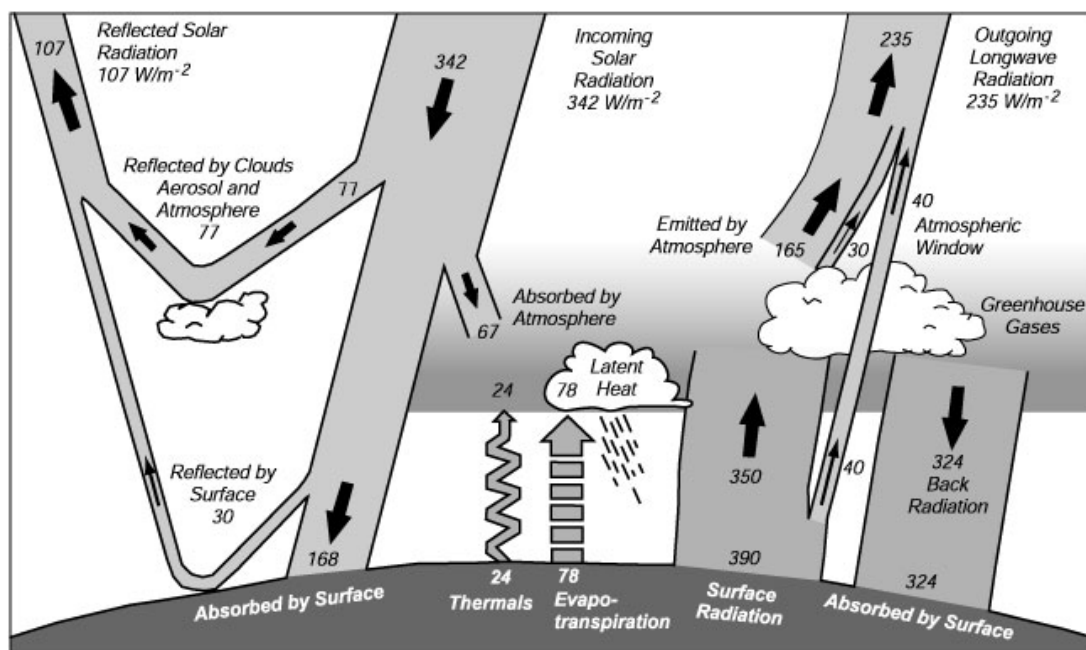
Figure 1.2-2 – *Estimate of the Earth's annual and global mean energy balance (Kiehl and Trenberth, 1997).*

1.2.3.2   Cloud radiative feedback

The 3.7 W.m^{-2} imbalance (around 3°C) of "Direct Greenhouse Forcing" measured at the TOA caused by an instantaneous CO2 doubling has been already reported (IPCC, 2001). However, the main feedbacks associated with this increase of CO2 and global warming involve clouds. Warming is expected to change the distribution and types of clouds such as that surface warming causes an increase of high level clouds (Hansen *et al.*, 1984), which in return rebuilt the global cloud feedback.

Depending on their altitude and optical thickness, clouds can have opposite effects. Figure 1.2-3 describes two cloudy conditions for radiative forcing. The left figure presents the typically high (cold) thin clouds like cirrus radiative effect. They are transparent to the shortwave radiation and have a small cloud albedo effect. At the same time, they trap outgoing longwave radiation due to their cold cloud top and thus the energy emitted to the outer space is much lower than that with no presence of clouds which suggests large cloud greenhouse forcing. As a result of the two mutual effects: a large portion of longwave radiation trapped in the atmosphere and a small portion of shortwave radiation sent back to space, these clouds enhance the

atmospheric greenhouse warming. The right figure presents the typically low thick clouds radiative effect. Thicker clouds, opposite to transparent clouds, reflect more shortwave radiation to space, they prevent the solar energy from reaching the Earth's surface. On the other hand, as they are low and close to the warm surface, the cloud top temperature is nearly the same order as surface temperature and the contrast of longwave radiation emitted at this level with and without cloudiness is small. The net effect of these low thick clouds is to cool the surface.

High clouds (Cirrus):	Low clouds (Stratocumulus) :
Small albedo effect (or parasol)/	Strong albedo effect /
Strong greenhouse effect	Small greenhouse effect
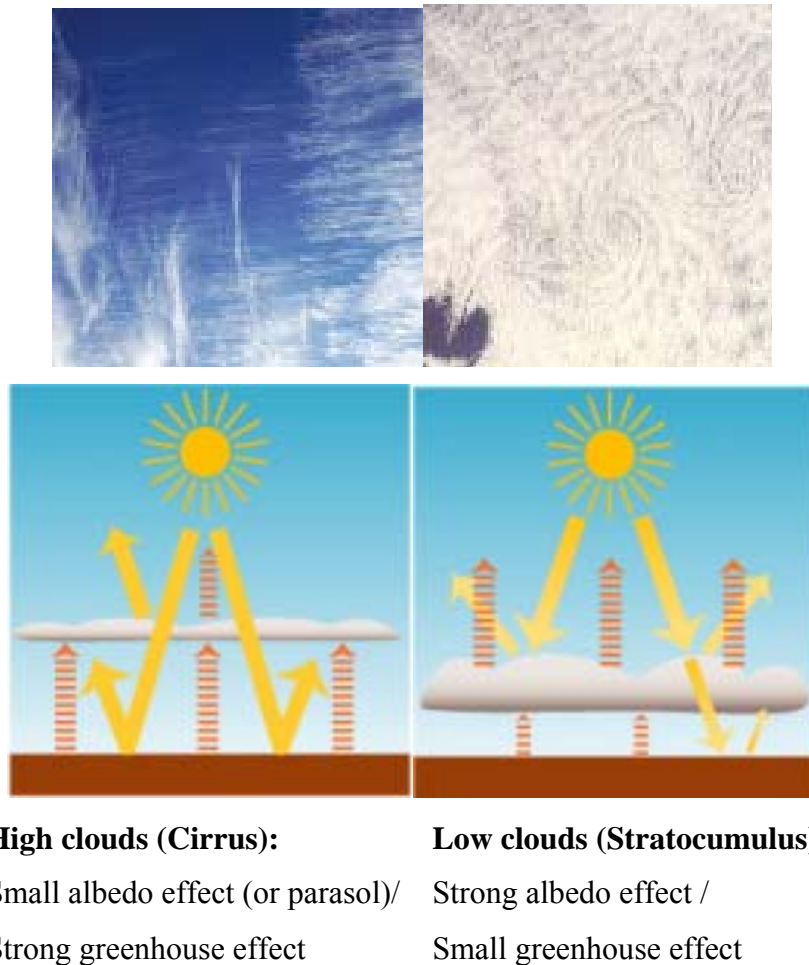
Figure 1.2-3 – *Schematic cloud radiative feedbacks for high and low clouds.*

Overall, the presence of clouds increases the amount of solar radiation reflected into space by about 50 W.m^{-2} and reduces the outgoing long-wave radiation by about 30 W.m^{-2} and after all, exerts a cooling effect (-20 W.m^{-2}) (Ramanathan *et al.*, 1989; Harrison *et al.*, 1990). Either a net warming or cooling effect depends on region and season and also the details of clouds such as cloud types and cloud microphysics. These details were poorly observed and are difficult to represent in climate models

(Dufresne and Bony, 2008) before the use of satellite data.

More studies (Poetzsch-Heffter *et al.*, 1995; Hansen *et al.*, 1997) found that in the low-level troposphere, water clouds such as stratus and midlevel nimbostratus contribute about 80% to the total cooling among all clouds. The radiative forcing from these clouds as part of outgoing longwave radiation is small (less than 20%), while their contribution as part of reflected solar radiation is large (almost 50%). On the contrary, in the high upper troposphere, negative forcing happens as the presence of cirrus.

1.3 Organization of the dissertation

In this chapter, I introduced the context of my Ph.D. work and some basic concepts on clouds and their role in the climate system. In summary, clouds and cloud-climate changes are important but have not yet been totally understood. The A-Train satellites, which are devoted to the study of clouds and aerosols, consist of coincident observations from different instruments. My work focuses on comparison and analysis of level 2 and 3 cloud products of POLDER and MODIS, which are part of the A-Train mission.

In chapter 2, I begin with a description of the three satellites used: PARASOL, AQUA and CALIPSO and the characteristics of the onboard sensors used: POLDER, MODIS and CALIOP. To make effective comparisons, two merged-datasets (PM and CALTRACK) have been first created and validated with the official data and are also presented in chapter 2. The PM data is used for the main work to get comparisons between POLDER/MODIS, while the CALTRACK data is used for further studies with a combination of the active sensor CALIOP. From this chapter, we will understand the different instrumental characteristics and why comparisons between POLDER and MODIS are necessary and interesting. In the following chapters (3, 4 and 5), we will present the results of different comparisons. This could give us useful information to better understand each retrieval method and the characteristics of cloud properties associated to these methods. Chapters 3, 4 and 5 focus on cloud cover, cloud thermodynamic phase and cloud optical thickness, respectively.

First, we worked on cloud cover in chapter 3 because this is the first cloud parameter retrieved in the algorithm. In this chapter, we give a brief description on the

operational cloud-detection algorithms and point out the potential advantages and inconveniences behind them. After that, cloud fractions obtained from POLDER and MODIS over one year are analyzed, and seasonal, latitudinal, angular and vertical variations, and also histograms and geographical distributions are compared.

In chapter 4, the cloud thermodynamic phases, which are retrieved after cloud detection but before cloud optical thickness, are studied. This work is divided into two parts. In the first part, we validated the cloud phase of passive sensors (POLDER & MODIS) with the active sensor (CALIOP). In the second part, we made studies on the vertical ice-water transition with relations to large scale dynamics and cloud microphysics.

Chapter 5 concerns the cloud optical thickness comparisons between POLDER and MODIS products and the evaluation of their differences according to cloud cover, microphysics, cloud heterogeneity and so on.

Chapter 2
Instruments and datasets

2.1 The A-Train mission

As the instruments used in this work are all onboard the A-Train satellites, we would like to first give an introduction about the A-Train constellation. The Afternoon or "A-Train" satellite constellation consists of five American and French satellites (Aura, Parasol, CALIPSO, CloudSat, Aqua) , which fly in a formation of a few minutes apart on a sun-synchronous orbit with flying height at approximate 705 km and speed of more than 24,000 km (15,000 miles) per hour. All of them pass over the equator at about 1:30 p.m. local time (see Figure 2.1-1).
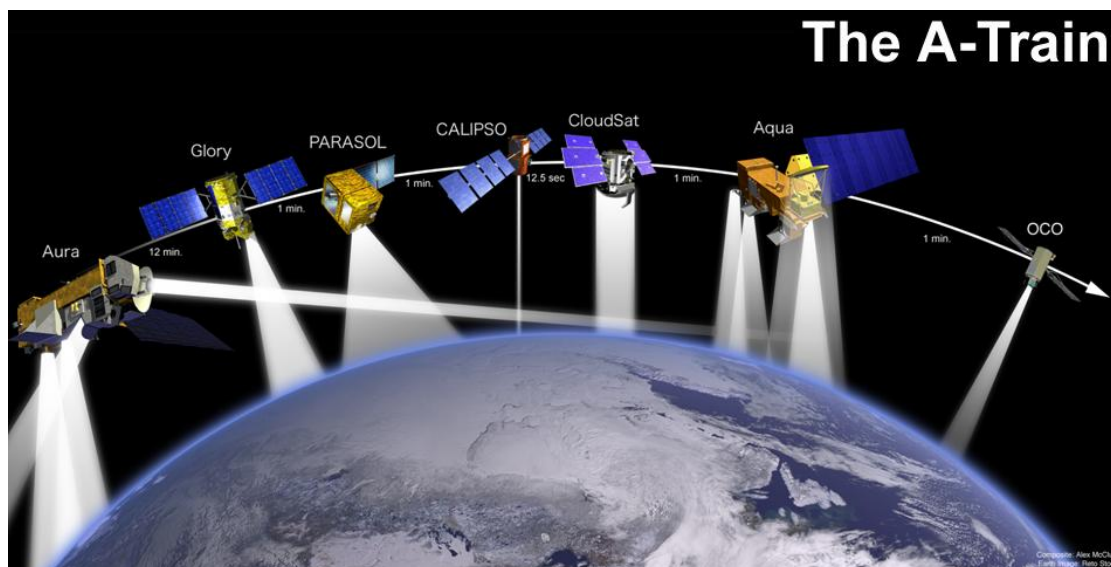
Figure 2.1-1 – *The so-called 'A-Train' constellation consisting of five satellites (Aqua, CloudSat, CALIPSO, PARASOL and Aura). In 2011, Glory, another satellite, was foreseen to joint the constellation and to take place of PARASOL (failure of launch). The OCO-2 will be launched in 2013.*

This spatial train of satellites is designed to offer simultaneous observations of the Earth-atmosphere system, i.e. the surfaces (land, ocean, snow…) and atmospheric components (aerosols, gases and clouds). These observations aim to give us a more correct definition and description of aerosols and clouds and their associated properties, better understanding of their changes in response to the environment changes, and also quantitative assessment of their impacts on climate changes. In this constellation, each satellite has its own characteristics and strengths to detect certain phenomenons. Together with five satellites, it can offer complementary information so as to avoid the problematic retrievals only from one satellite. Table 2.1-1 below gives a summary of the five satellite positions, their primary missions and the onboard instruments.

Spacecraft	Position	Summary of Mission	Instruments Carried
Aqua Launched on May 4, 2002	Lead spacecraft in formation.	Synergistic instrument package studies global climate with an emphasis on water in the Earth/atmosphere system, including its solid, liquid and gaseous forms	• AIRS (Atmospheric Infrared Sounder) • AMSU-A (Advanced Microwave Sounding Unit) • HSB (Humidity Sounder for Brazil) • AMSR-R (microwave radiometer) • CERES (Clouds and the Earth's Radiant Energy System) • MODIS (Moderate Resolution Imaging Spectroradiometer)
CloudSat on Apr. 28, 2006	Lags Aqua by between 30 seconds and 2 minutes. Must maintain extremely precise positioning relative to both Aqua and CALIPSO to permit synergistic measurements with Aqua and CALIPSO	Spaceborne Radar will allow for most detailed study of vertical structure and properties of clouds and for a better characterization of the role that clouds play in regulating the Earth's climate.	• CPR (Cloud Profiling Radar) is a 94 GHz radar
CALIPSO on Apr. 28, 2006	Lags CloudSat by no more than 15 seconds. Must maintain position relative to Aqua to permit synergistic measurements with Aqua.	Observations from spaceborne lidar, combined with passive imagery, will lead to improved understanding of the role that aerosols and clouds play in regulating the Earth's climate, in particular, how the two interact with one another.	• CALIOP (Cloud-Aerosol Lidar with Orthogonal Polarization) • IIR (Imaging Infrared Radiometer) • WFC (Wide Field Camera)
PARASOL on Dec. 18,	Lags CALIPSO by about 1 minute.	Directional total and polarized light	• POLDER(Polarization and Directionality of the

2004		measurements will allow a better characterization of clouds and aerosols in the Earth's atmosphere, in particular, distinguishing natural and anthropogenic aerosols.	Earth's reflectance)
Aura on Jul. 15, 2004	Lags Aqua by about 15 minutes but crosses equator 8 minutes behind Aqua due to different orbital track to allow for synergy with Aqua.	Synergistic payload will study atmospheric chemistry, focusing on the horizontal and vertical distribution of key atmospheric pollutants and greenhouse gases and how these distributions evolve and change with time	• HIRDLS (High Resolution Dynamics Limb Sounder) • MLS (Microwave Limb Sounder) • OMI (Ozone Monitoring Instrument) • TES (Tropospheric Emission Spectrometer)

Table **2.1-1** – *Lists of satellites in the A-Train constellation, their positions within the constellation, their mission summaries and their corresponding scientific instruments. More details are summarized on th*e NASA website: http://www-calipso.larc.nasa.gov/about/atrain.php.

Three satellites in A-Train constellation having been used for this inter-comparison exercise: AQUA, PARASOL and CALIOP. The onboard instruments considered are MODIS, POLDER and CALIOP. From the original official datasets provided for each instrument, two merged datasets are created: the PM dataset and the CALTRACK dataset, which will be described later in section 2.4. In the next sections, we will focus on a basic presentation of sensor characteristics, retrieval processes, datasets and different cloud products.

2.2 Instruments

2.2.1 POLDER/PARASOL Mission

POLDER is a wide field of view imaging radiometer designed to provide the first global systematic measurements of multi-spectral, multi-directional solar radiation and polarization[1] reflected by the Earth/atmosphere system (Deschamps *et al.*, 1994). CNES is responsible for the bus, payload command control and ground segments, while the Laboratoire d'Optique Atmosphérique (LOA, in Lille) leads the

---

[1] Nature light is unpolarized. From unpolarized light, if the orientation and distribution of oscillations in the plane perpendicular to the traveling direction has been rebuilt due to scattering, transmission, reflection or refraction, light becomes polarized. Polarization is described from a set of Stokes parameters

scientific mission. The main scientific objective of this micro-satellite is to observe the atmosphere (clouds, aerosols), even if it can also be used to observe ocean color and land surfaces.

The first instrument POLDER-1 flew on JAXA / ADEOS-I (Advanced Earth Observing Satellite) from November 1996 until June 1997, developed by the Japanese space agency. POLDER-2 flew on ADEOS-II, this continued to ADEOS-I, from April 2003 until October 2003. A modified version of instrument, PARASOL, greatly benefited the developments of payload and demeter in the program of POLDER, flew on the first micro-satellite of CNES and joined the A-Train constellation in December 2004.

POLDER consists of a digital camera including a **detection array CCD** (Charged Coupled Device) that is composed of 274×242 pixels with a low spatial resolution (ground size of 6km×7km) and permits the acquisition of observation between ± 51 ° (2100km) along track and ± 43 ° perpendicular to it, a **wide field of view telemetric optics** for both along-track and cross-track direction with a maximum field of view of 114°, and a **rotating wheel** that carries spectral filters and polarizers. In addition, the acquisition of a sequence of images every 19.6 seconds allows for observing the same ground target up to 16 times with different geometries. This instrumental concept therefore allows multidirectional observations.

The filter wheel supports 15 filters (6 filters non-polarized and 9 polarized filter) from blue (443 nm) to near infrared (1020nm). The 1020 nm channel added for PARASOL conducts observations that can be compared with observations from the CALIOP lidar. For each of the three "polarized" wavelengths, filters are identically associated to three polarizers placed at a 60° angle from one another. Table 2.2-1 summarizes the details of each wavelength measured by POLDER. The 9 channels are defined by their central wavelength, bandwidth and also their dynamics. Some channels operate in high dynamics and others in low dynamics, which are necessary to meet the scientific objectives of POLDER. Figure 2.2-1 shows the response functions in each channel.

Channel	Central wavelength (nm)	Band Width (nm)	Polarisation	Main mission
443NP	443.9	13.5	no	Aerosols, ERB
490P	491.5	16.5	yes	Aerosols, EBR, Ocean color
565NP	563.9	15.5	no	Ocean color
670P	669.9	15.0	yes	Vegetation, aerosols, ERB
763NP	762.8	11.0	no	Cloud top pressure
765NP	762.5	38.0	no	Aerosols, CTP
865P	863.4	33.5	yes	Vegetation, aerosols, ERB
910NP	906.9	21.0	no	Water vapor amount
1020NP	1019.4	17.0	no	Optimized synergy with CALIPSO

Table 2.2-1 – *Characteristics of spectral bands selected by POLDER instrument on PARASOL (Bréon and CNES Parasol Team, 2006). NP: non-polarized, P: polarized.*
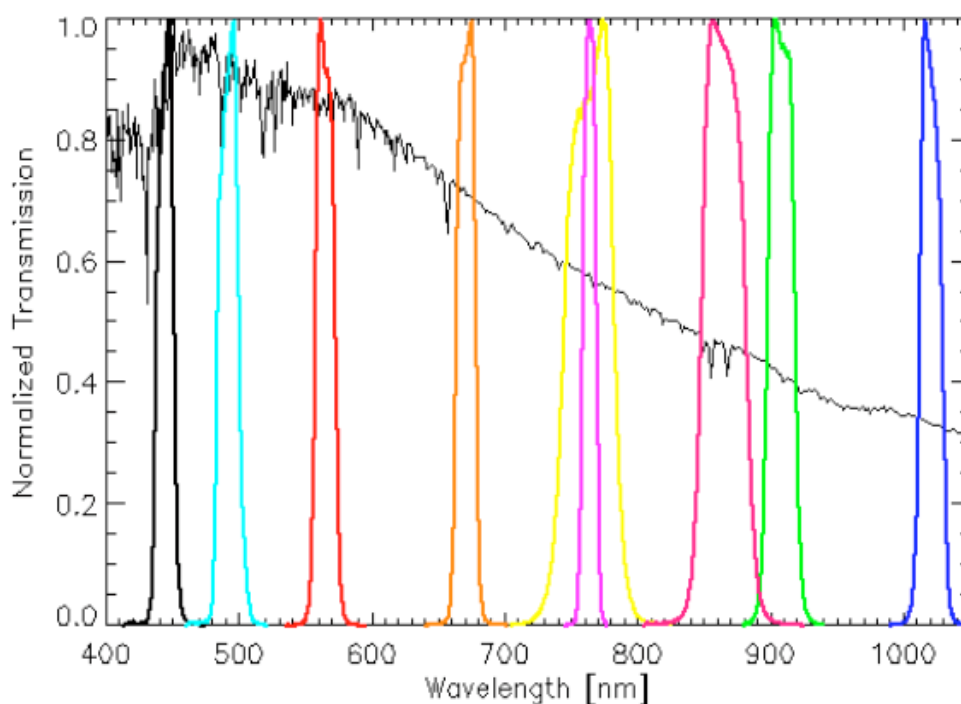
Figure 2.2-1 – *Standardized filter functions for POLDER channels according to the wavelength together with the solar irradiance spectrum. When a channel is polarized (P), the function is presented by the average of three components (Bréon and CNES Parasol Team, 2006). For the 443nm channel, polarized (P) or not (NP) have the same filter functions.*

POLDER radiation measurements and retrieved level 2 and 3 products are collected and produced by the ICARE data and services center. The Level 1 products include the calibrated radiances and solution of Stokes parameters (I, Q, U). The level 2 and 3 products are separated in two chains: "Earth Radiation Budget, Water Vapor and Clouds" and "Aerosols". The products of the chain "ERB WV & clouds" are averaged and stored in "super-pixel", which corresponds to 3×3 pixels (20×20 km^2 at the equator) in its latest data version (Buriez *et al.*, 1997; Parol *et al.* 1999). The level 2 products are the result of pixel based retrievals and daily statistics, which are stored in 14 to 15 ascendant orbits. The level 3 products are the monthly statistics derived from level 2 aggregations.

2.2.2 MODIS/AQUA Mission

The multispectral imaging radiometer MODIS (Moderate Resolution Imaging Spectroradiometer) has been developed by NASA and is on board EOS (Earth Observing System) Terra (descending orbit) and Aqua (same ascending orbit as POLDER) satellites (King et al., 1992). This instrument is designed to monitor the atmospheric properties, such as water vapor, aerosols, clouds and the interaction between land, atmosphere and ocean. It was launched aboard the Aqua satellite and joined the A-Train constellation in May 2002. MODIS scans in a plane perpendicular to velocity vector of spacecraft, with the maximum scan extending up to 55° on either side of nadir. It yields a wide swath of 2330 km centered on the satellite ground track and provides complete coverage of the entire globe every 2 days. Moreover, it offers a total 36 band observations that spread from visible to thermal-infrared (0.41-15μm) and three nadir spatial resolutions: 250m (2 channels), 500m (5 channels) and 1000m (29 channels). Bandwidth characteristics are summarized in Table 2.2-2. The response of each channel is determined by an interfering filter on a matrix detector imaging a scene of 10km along the track.

Band	Wavelength (nm)	Resolution (m)	Commentary
1	620-670	250	Land/Cloud/Aerosol Bondaries
2	841-876	250	
3	459-479	500	Land/Cloud/Aerosol Properties
4	545-565	500	
5	1230-1250	500	
6	1628-1652	500	
7	2105-2155	500	
8	405-420	1000	Ocean Color/ Phytoplankton/ Biogeochemistry
9	438-448	1000	
10	483-493	1000	
11	526-536	1000	
12	546-556	1000	
13	662-672	1000	
14	673-683	1000	
15	743-753	1000	
16	862-877	1000	
17	890-920	1000	Atmospheric Water Vapor
18	931-941	1000	
19	915-965	1000	
20	3.660-3.840	1000	Surface/Cloud Temperature
21	3.929-3.989	1000	
22	3.929-3.989	1000	
23	4.020-4.080	1000	
24	4.433-4.498	1000	Atmospheric Temperature
25	4.482-4.549	1000	
26	1.360-1.390	1000	Cirrus Clouds / Water Vapor
27	6.535-6.895	1000	
28	7.175-7.475	1000	
29	8.400-8.700	1000	Cloud Properties

30	9.580-9.880	1000	Ozone
31	10.780-11.280	1000	Surface/Cloud
32	11.770-12.270	1000	Temperature
33	13.185-13.485	1000	
34	13.485-13.785	1000	Cloud Top
35	13.785-14.085	1000	Altitude
36	14.085-14.385	1000	

Table 2.2-2 – *Characteristics of spectral bands selected for the MODIS instrument aboard AQUA (Ackerman et al., 2010).*

The MODIS level 2 cloud products (daily cloud data) are retrieved by combination of infrared and visible techniques. Among these products, cloud fraction, cloud shortwave-near infrared phase, effective radius, optical thickness and integrated water path are derived at 1-km pixel resolution using the MODIS visible, near-infrared and shortwave infrared bands; cloud top temperature, cloud top pressure, effective emissivity and infrared cloud phase are produced by using infrared bands for both day and night at 5×5 1-km-pixel resolution. The final level 2 product file covers a five-minute time interval either in 5km or in 1km resolution. The output grid for 5km resolution parameters is 270 pixels in width by 406 pixels in length for nine consecutive granules and every tenth granule has an output grid size of 270 by 408 pixels. For 1km resolution parameters, the output grid is 1354 pixels in width by 2030 pixels in length for nine consecutive granules and every tenth granule has an output grid size of 1354 by 2040 pixels.

2.2.3 CALIOP/CALIPSO Mission

The Cloud-Aerosol Lidar and Infrared Pathfinder Satellite Observations (CALIPSO) mission is a satellite mission on Earth Science observation that has been developed within the framework of collaboration between NASA Langley Research Center (LaRC) and the French space agency, Centre National D'Etudes Spatical (CNES) (Winker *et al.*, 2003). This mission provides unique measurements to improve our understanding of global radiative effects of aerosols and clouds in the

Earth's climate system. CALIPSO was launched on April 28, 2006 together with the cloud profiling radar (CPR) system on the CloudSat satellite. The CALIPSO payload combines three co-aligned, nadir-viewing instruments: an active two-wavelength (532 nm and 1064 nm) polarization-sensitive lidar instrument (Cloud-Aerosol Lidar with Orthogonal Polarization, CALIOP), a passive Infrared Imaging Radiometer (IIR), and a visible Wide Field Camera (WFC) to probe the vertical structures and properties of thin clouds and aerosols over the globe, to identify cloud ice/water phase (via the ratio of signals in two orthogonal polarization channels), and a qualitative classification of aerosol size (via the wavelength dependence of the backscatter intensity). Generally, data from these three instruments will be used together to measure the radiative and physical properties of cirrus clouds. The instrument characteristics are summarized in Table 2.2-3.

Characteristic	Value
CALIOP wavelengths	532 nm, 1064 nm
polarization	532 nm, $\parallel$ and $\perp$
pulse energy	110 mJ each wavelength
footprint	100 m
vertical resolution	30-60 m
horizontal resolution	333 m
WFC wavelength	645 nm
spectral bandwidth	50 nm
IFOV/swath	125 m/ 61 km
IIR wavelengths	8.65 μm,10.6 μm,12.0μm
spectral resolution	0.6 μm – 1.0 μm
IFOV/swath	1 km/64 km

Table 2.2-3 – *Main characteristics of the three CALIPSO instruments (Winker et al., 2003).*

The level 1 CALIOP data collects the atmospheric return of the backscatter intensity at 1064nm and at two orthogonally polarized components of 532nm backscattered signal from a telescope of an all-beryllium 1-meter diameter. The Lidar level 2 cloud and aerosol products are stored separately into two general classes: the layer products (CLay or ALay) and the profile products (CPro or APro). Layer data are generated at three horizontal resolutions for clouds (1/3km, 1km and 5km) and at

5km horizontal resolution for aerosols. Profile data is generated at 5km horizontal resolution for clouds and 40km for aerosols. Lidar layer products consist of a sequence of column descriptors, each one of which is associated with a variable number of layer descriptors. The column descriptors specify the temporal and geophysical location of column of the atmosphere through which a given lidar pulse travels. Also included in the column descriptors are indicators of surface lighting condition, information about the surface type and the number of features as either clouds or aerosols identified within the columns. For each feature within a column, a set of layer descriptor is reported. These layer descriptors provide information about the spatial and optical characteristics of a feature, such as base and top altitudes, integrated attenuated backscatter, and optical depth. More information about CALIOP /CALIPSO can be found on the official website: http://eosweb.larc.nasa.gov/PRODOCS/calipso/table_calipso.html

2.3 Processing Algorithm Outlines

2.3.1 POLDER Algorithm Schematic

The "ERB, WV and Clouds" processing line is one branch of POLDER algorithm. It consists of cloud detection and cloud properties retrieval algorithm. The general scheme of this processing is shown in Figure 2.3-1. With this process, the original radiation collected in level 1 is inversed step by step to the cloud products in level 2 and 3. The first step of the process is to perform the cloud detection, which contains a series of tests to determine the feature of the scene: clouds, or the cloud free surfaces (land/ocean). Then, cloud phase is only retrieved for the cloudy scene. After that, other cloud properties such as cloud optical properties and cloud pressures can be retrieved for the scenes whose cloud cover and cloud thermodynamic phases have been already determined. Detailed descriptions about how each parameter is derived can be found respectively in chapters 3 (for cloud cover), 4 (for cloud phase) and 5 (for cloud optical thickness).

Level 1 Product
(POLDER   radiances)

Correction for gaseous absorption

Apparent pressure

Cloud detection

Cloud phase

Cloud optical thickness

Precipitable
Water content

SW Albedo

Cloud pressure
(Oxygen and Rayleigh pressure)

pixel scale

- -

super-pixel scale

Spatial synthesis

Level 2 Product

Monthly means

Level 3 Product
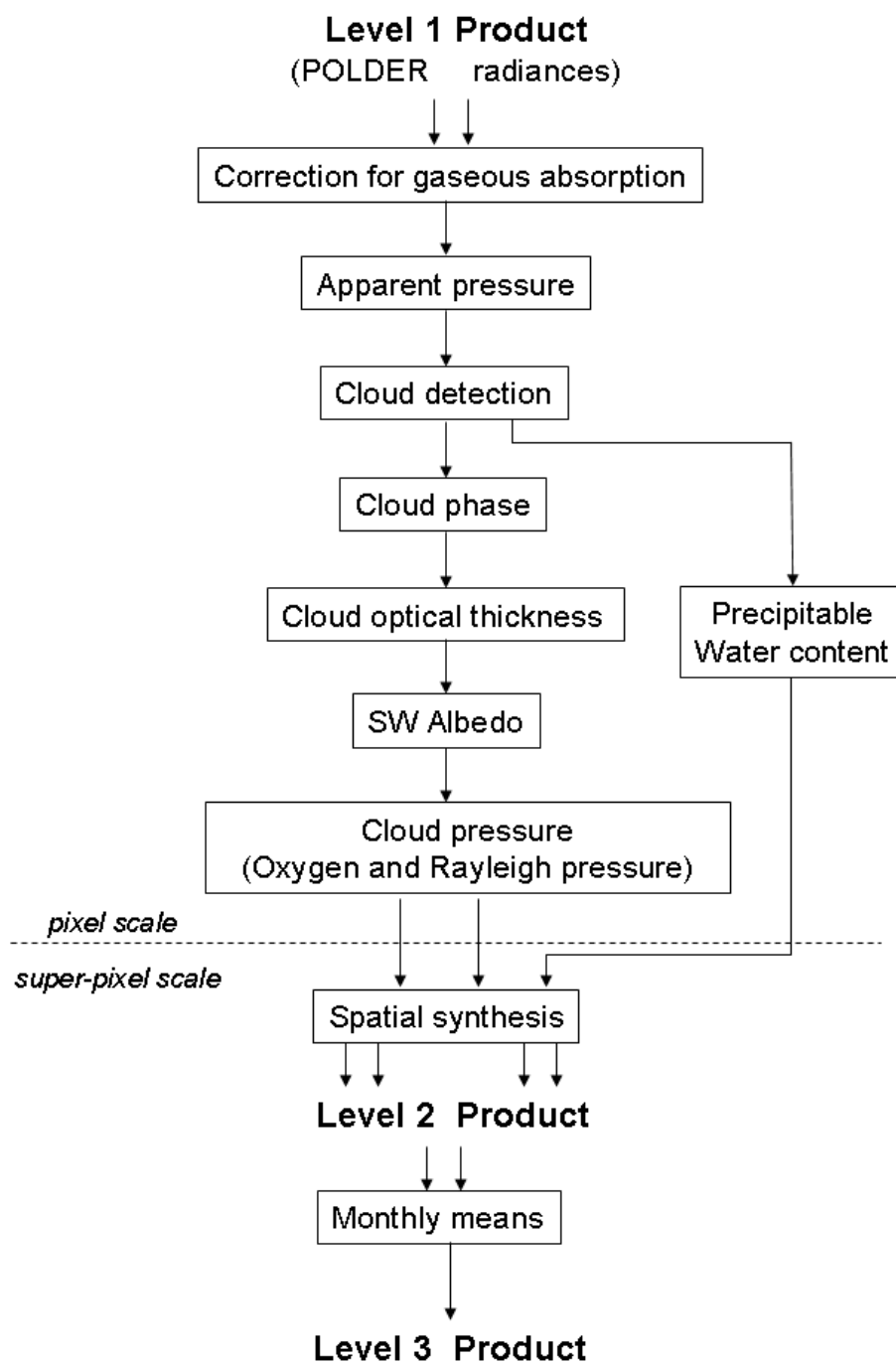
Figure 2.3-1 – *Schematic description of the "ERB, WV and Clouds" processing in POLDER Algorithm (Buriez et al., 1997).*

2.3.2 MODIS Algorithm schematic

Generally speaking, the MODIS cloud processing line is similar to the POLDER one (see Figure 2.3-2): from the collected level 1 radiation, level 2 (daily

products) and 3 (monthly products) data are derived. In level 2 processing, the cloud mask is performed first, cloud phase and pressure then, and the cloud optical properties and cloud albedo at last (schematics from ATBD-MOD05 show the atmosphere processing in MODIS algorithm that consists of both aerosol and cloud processes). Compared to POLDER, they use different methods for the detailed retrieval of cloud properties (see chapters 3, 4 and 5).
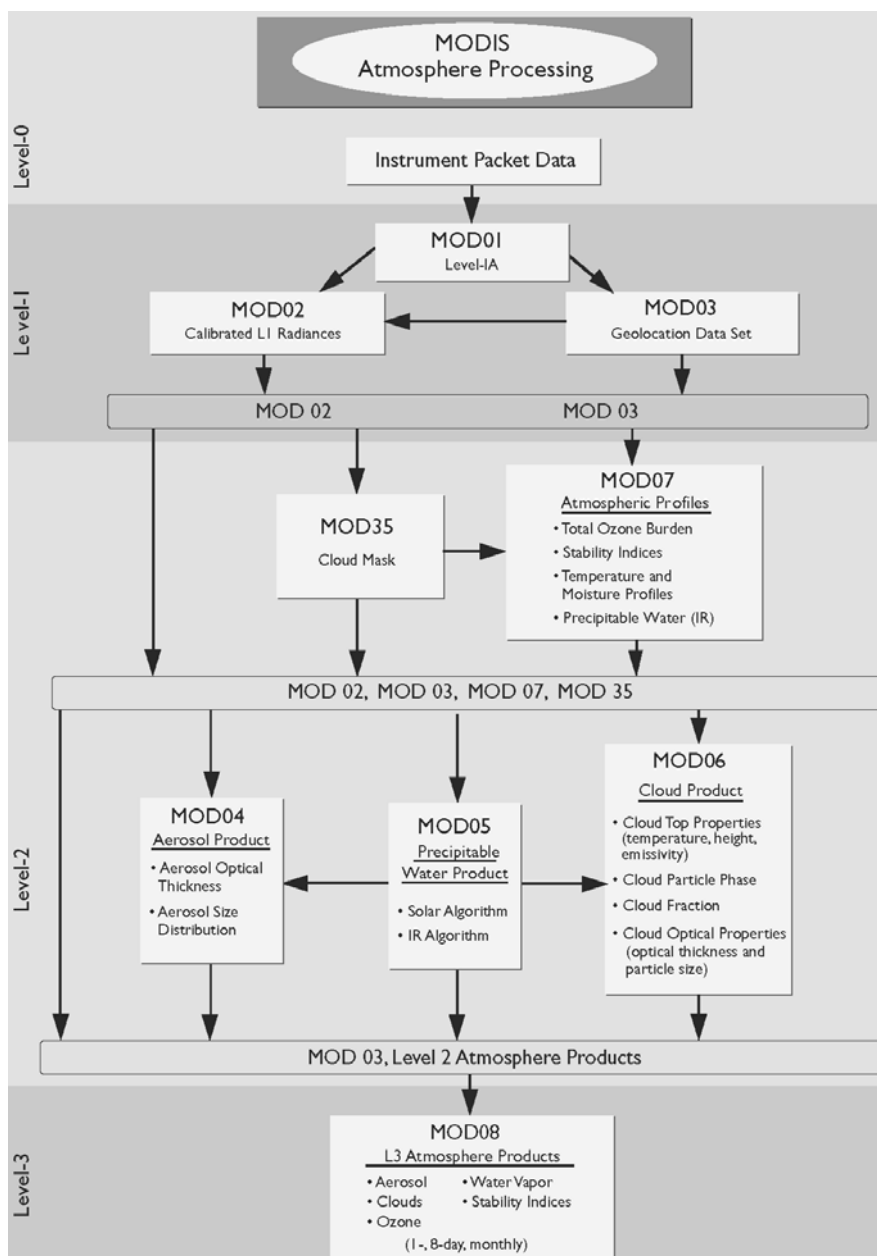
Figure 2.3-2 – *Schematic description of the atmospheric processing in MODIS Algorithm from ATBD-MOD-05.*

2.3.3 CALIOP Algorithm schematic

The CALIOP level 2 processing system is composed of three modules, which have the general function of detecting layers, classifying the layers, and performing extinction retrievals. These three modules are the Selective Iterated BoundarY Locator (SIBYL), the Scene Classifier Algorithm (SCA), and the Hybrid Extinction Retrieval Algorithms (HERA) (see Figure 2.3-3). Level 2 lidar processing begins with the SIBYL module that operates on a sequence of scenes consisting of segments of level 1 data covering 80 km in along-track distance. The module averages these profiles to horizontal resolutions of 5, 20 and 80 km respectively, and detects features at each of these resolutions. The SCA module then classifies these generic features as clouds or one of five aerosol types, based primarily on scattering strength and the spectral dependence of the lidar attenuated backscattering (Liu *et al.*, 2005). This module can further discriminate between ice/water clouds relying on the layer-averaged lidar depolarization ratio and ancillary information such as altitude and temperature (Hu *et al.*, 2002). The SCA module also uses a combination of observed parameters and a priori information to select appropriate values for the initial lidar ratios and multiple scattering factors required for retrieving extinction and optical thickness in the HERA module.
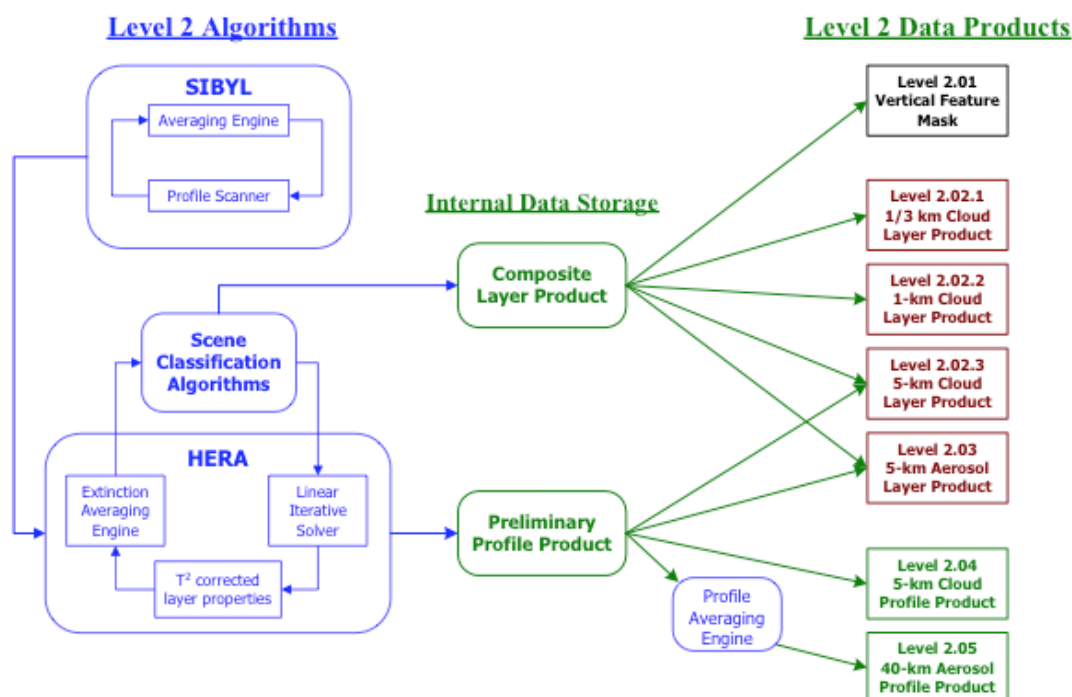
Figure 2.3-3 – *Schematic description of the CALIOP level 2 processing algorithm from CALIOP ATBD document.*

2.4 Datasets

In order to facilitate inter-comparison and analysis of POLDER, MODIS and CALIOP products, we have used different "merged" datasets achieved from the official individual products. Two datasets have been considered for our studies: The first one called PM Dataset (for **P**older-**M**odis) has been used for the comparison between POLDER and MODIS. The second one called CALTRACK Dataset has been primarily used for the interpretation and validation of passive observations using the active sensors. In this sub-section, we provide a more detailed description of these merged datasets.

2.4.1 PM Dataset

It is not convenient to compare POLDER and MODIS cloud products by directly using the official data files because they are stored in very different ways.

The MODIS official cloud products in level 3, corresponding to the monthly averages, are stored in latitude versus longitude rectangular grids, from 90°N to 90°S and 180°W to 180°E with a 1°×1° grid box resolution. The Level 2 products are stored in granule, which covers a five-minute time interval, at either 1 kilometer or 5 kilometers pixel resolution. The POLDER level 1 products are geolocated on a fixed integrated sinusoidal grid with pixel resolution of 6×6 km^2. The official level 3 (corresponding to the monthly averages) and level 2 (corresponding to instantaneous pixel based retrievals) POLDER cloud products are provided at the super-pixel resolution (3×3 pixels) that corresponds to approximately 20×20 km^2. In order to facilitate the statistical comparisons between the two passive sensors at either global or superpixel scale, and also in order to extract more benefits and information from the two sensors that own similar orbit but different sensor characterizations, the Laboratoire d'optique atmosphérique (LOA) and the ICARE data service center have created a new dataset that directly combines the two sensor products in a single dataset called PM Dataset. This joint dataset contains all AQUA/MODIS collection 5 level 2 cloud products and PARASOL/POLDER collection 2 level 2 cloud products collocated and reprojected in a common integrated sinusoidal grid. POLDER single orbit files are used as reference for the collocation of the coincident MODIS granules. For PM collocation, the sinusoidal grid is centered on POLDER ascending node longitude. The new dataset preserves completely POLDER cloud products while the MODIS products are averaged within each POLDER superpixel via a nearest pixel approximation collocation. So the final joint products can provide all coincident POLDER and MODIS cloud products at the same spatial resolution of about 20×20 km^2.

The advantages of this new dataset are obvious: as referred in the previous paragraph, it contains coincident products from the two sensors at much higher resolution than level 3 aggregated products. Second, the new dataset provides more information of cloud properties from the two sensors compared to only one of them.

Before the comparison work, some cloud products will be particularly introduced here because they cannot be directly averaged or copied to the new dataset. It is important to know and keep in mind how these are produced.

- The cloud phase from MODIS is given in digital presentations: 1 for ice, 2 for liquid, 3 for mixed. The averaged values at superpixel have no useful meaning. So the reproduction of this cloud product needs careful attention. In fact, we reproduce the phase from MODIS by counting the number of ice, liquid and mixed pixels in the POLDER super-pixel. If all of the MODIS pixels in the POLDER super-pixel have ice (liquid or mixed) phase, the final phase is straightly labeled as ice (liquid or mixed). In the "mixed" situations where both liquid and ice are present within a POLDER superpixel, if the liquid (ice) count is greater than twice the ice (liquid) count in the POLDER super-pixel, we labeled as liquid (ice) dominated phase, otherwise the pixels are classified as mixed phase.

- There are no product of ice, water and mixed cloud fractions for POLDER, and they are produced by the combination of cloud fraction and cloud phase.

- Concerning the MODIS cloud fraction, there are two different daytime (the solar zenith angle less than 81.4°) products in its level 3 parameter list. One is called "Cloud Fraction Day Mean", and the other "Cloud Fraction Combined FMean". The "day mean" cloud fraction (hereafter referred as CFD) is directly obtained from the official cloud mask (MOD35); the "combined mean" cloud fraction (hereafter referred as CFC) is recomputed and associated to the pixels for which cloud optical properties (e.g. cloud phase) have been successfully retrieved (Hubanks *et al.*, 2008). CFC product is in level 3 but not in level 2 of the official data, so we have recalculated this product in the PM Dataset. For CFC, a "clear sky restoral" algorithm is applied to the initial cloud mask before attempting optical properties retrieval. This algorithm helps to remove the pixels which are initially either falsely detected as cloudy (e.g. the heavy aerosol events, residual sun-glint contamination) or only partly cloudy (e.g. the cloud edges). So after the "clear sky restoral", most of the edges of cloud especially over ocean have been cut down and the aerosols like blowing dust and sand around Africa have been reclassified as clear sky. A direct consequence is, the CFC is always smaller than or equal to the CFD. Compared to the CFD, the CFC is theoretically smaller biased to the real cloud fraction in regions of intense aerosols transport, and it also

intrinsically underestimates cloud fraction in areas where fractional cloud cover is dominant. This CFC product is important for our analysis, but we need to always keep in mind that the "combined mean" cloud fraction does not represent the total cloud fraction but the cloud fraction for which optical properties have been derived. This part of the cloud fraction in absolute value and relative to the total cloud fraction needs to be specially understood so as to correctly interpret the statistical characteristics of cloud optical properties. In the following, it may be considered that the two cloud fractions derived from MODIS actually provide an upper (all clouds) and lower (solid clouds) limit of the global cloud fraction that should encompass POLDER cloud fraction at all times. The relative values of these three cloud fractions can also provide valuable information on cloud cover characteristics and the associated uncertainties.

Finally, let us note that we used the following definition for "differences" between POLDER and MODIS products. The differences for a cloud product between the two sensors are POLDER minus MODIS; and also the differences are computed only for those pixels lying in the common swath (e.g. pixels that have been instantaneously observed by both POLDER and MODIS). Indeed, retrieved cloud properties (especially the cloud fraction) can vary significantly with viewing geometry (Maddux *et al.*, 2010), and it is important to prevent the introduction of systematic biases by considering pixels that are never observed by one instrument (see Figure 2.4-2 and chapter 3 for more details about this issue).

The period of this comparison study is from December 2007 to November 2008, which ensures to provide sufficient sampling so that the statistical results are representative. We started from December 2007 to avoid the retrieval problems from MODIS optical properties, which have been identified and corrected after September 2007 (Platnick *et al.*, 2007) and also to avoid the lack of POLDER data in summer 2007. In the following and unless otherwise stated, all statistic results concern this period.

Before using the new dataset, we must verify its consistency with respect to the official level 3 products. Figure 2.4-1 displays the latitudinal variations of cloud fraction averaged over one year for POLDER level 3 official data, MODIS level 3 official data (both CFC and CFD) and our new dataset collected and averaged over the same period. The latitudinal variations of cloud fraction obtained from our joint

level 2 dataset show consistency with the official level 3 data. The small differences observed for CFC between the official and the joint PM Dataset have been attributed to one main difference in computing level 3 statistics: the MODIS official level 3 algorithm computes statistics by sampling every one over five level 2 pixels while we choose for the present analysis to average all level 2 MODIS pixels at POLDER super-pixel scale. In this figure, we also plotted POLDER maximal and minimal cloud fraction errors that are associated to the difference of cloud mask with or without applying reclassification tests (the spatial and temporal dispersion tests). These upper and lower cloud fractions of POLDER are comprised between CFC and CFD except at higher latitudes where fewer detection tests can be executed due to risk of snow cover. Among the three cloud fractions, MODIS CFD is closest to the ISCCP one with more clouds in ITCZ and polar zones while fewer clouds in the middle latitudes.
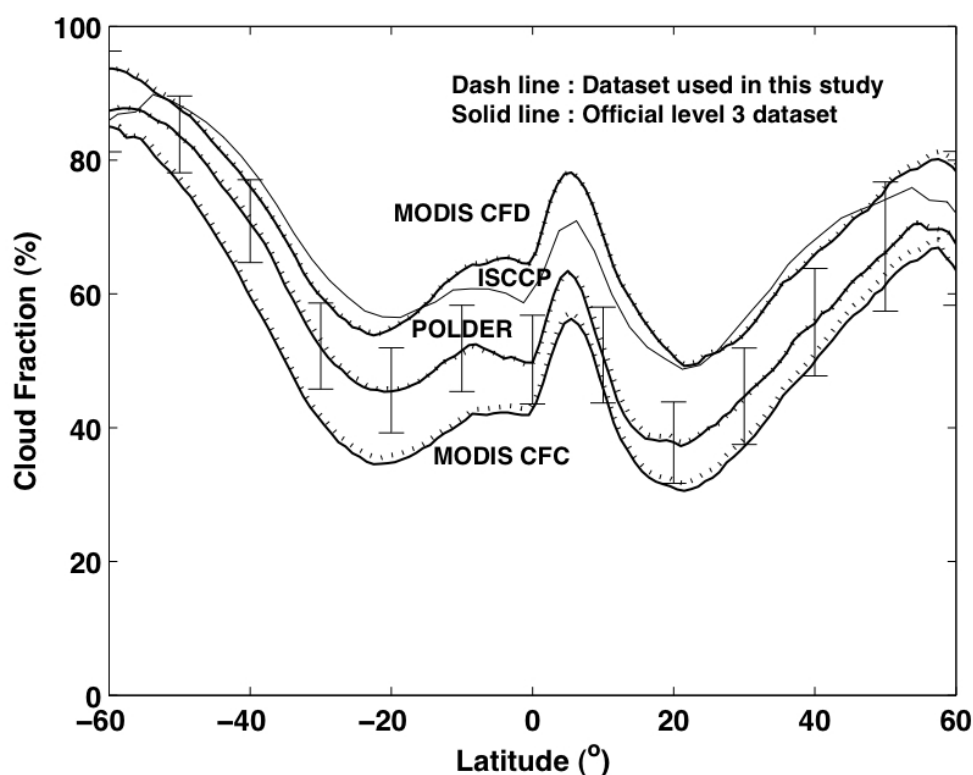
Figure 2.4-1 – *Latitudinal variations of cloud fraction of POLDER and MODIS for the official level 3 dataset and for the dataset created for this study. Error bars present for POLDER the minimal and maximal cloud covers (from level 3) obtained before the reclassification tests. The ISCCP cloud fraction is for the period of 1984 to 2007.*

As referred above, the coincident PM data for the following studies and comparisons correspond to the common POLDER/MODIS swath. As observed by MODIS, viewing geometry dependencies can make large differences between the observations from nadir and from the edge of the scan (Maddux *et al.*, 2010). The MODIS swath includes and is larger than POLDER one. This could thus produce statistically systematical biases due to the observations from the edges of MODIS swath that are outside of the POLDER one. Figure 2.4-2 shows one-year latitudinal cloud fraction (CFC) averaged respectively over the MODIS swath (large swath or original swath), POLDER swath (small swath or common swath) and the edges of swath (corresponding to MODIS minus POLDER swath). We note about 2-3% of cloud fraction differences between MODIS original and common swath. More detailed studies about the viewing geometry dependencies of the cloud products are given in section 3.3.4 for cloud cover, section 4.3 for cloud phase and section 5.6 for cloud optical thickness.
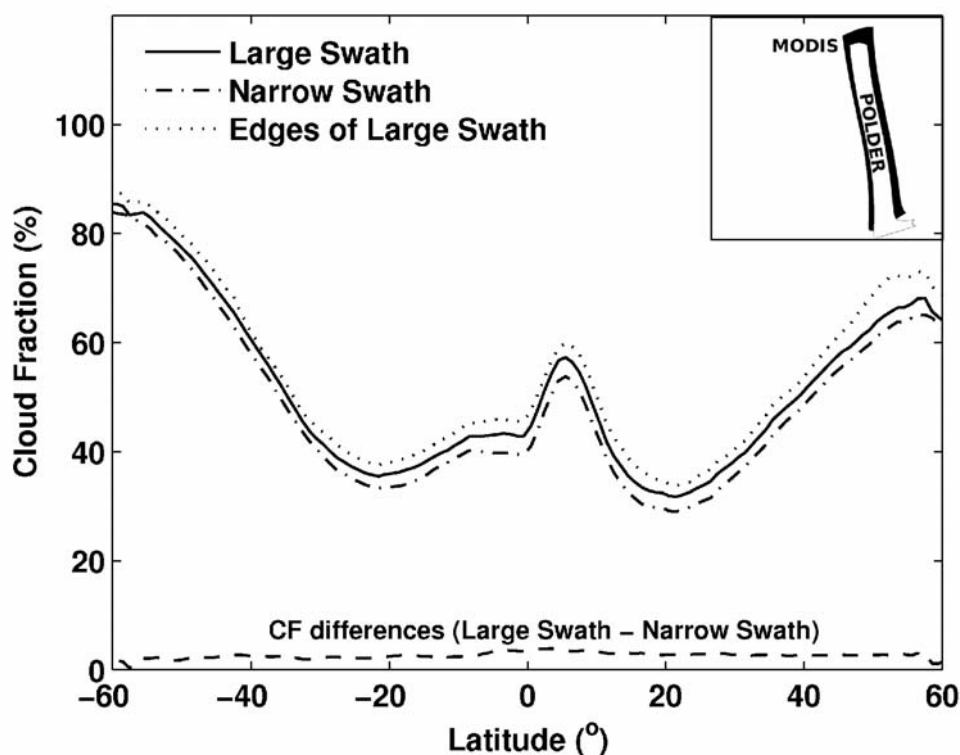
Figure 2.4-2 – *Latitudinal variations of cloud fraction (CFC) averaged in MODIS swath (large swath), POLDER swath (small swath) and the edges of swath (edge of MODIS swath outside of POLDER one).*

2.4.2 CALTRACK Dataset

CALTRACK is an application created by ICARE data and services center that extracts some variables issued of different sensors and meteorological products (CALIOP, IIR, MODIS, CERES, ECMWF, PARASOL, CLOUDSAT, OMI and may be more in the future). The products contain the coincidences issued of many sensors under the CALIOP subtract for 2 horizontal resolutions: 333m for level-1 products and 5km for level-2 products. The coincident products of different sensors are sampled and filtered from the official files also with the nearest pixels approximation to every shot of CALIOP Lidar. The input profiles from the three sensors used in our studies are listed in Table 2.4-1. A detailed description of this dataset together with its creation strategy can be found at the ICARE website: http://www.icare.univ-lille1.fr/projects/calxtract/.

Sensor	Products	Products
CALIOP (Collection 2)	L1	Level 1 : radiation
	CLay05km	Level 2 : cloud layer products at 5km
	CPro05km	Level 2 : cloud profile products at 5km
	ALay05km	Level 2 : aerosol layer products at 5km
	APro05km	Level 2 : aerosol profile products at 5km
MODIS (Collection 5)	L1B	Level 1 : radiation
	MYD04	Level 2 : aerosol products
	MYD05	Level 2 : precipitable water vapor
	MYD06	Level 2 : cloud products
POLDER (Collection 2)	L1	Level 1 : radiation
	RB2	Level 2 : cloud & radiative budget products
	OC2	Level 2 : aerosol products over ocean
	LS2	Level 2 : aerosol products over land

Table 2.4-1 – *List of the input data collection and files for CALIOP, MODIS and POLDER sensors.*

Compared to the PM dataset, this dataset contains more information from different sensors in the A-Train constellation, especially the active sensor CALIOP

and CLOUDSAT that could provide the vertical structures of clouds and aerosols. However, the narrow orbit swath of this dataset results in a much lower sampling and reduced statistical representatives.

2.4.3 Meteorological data from ECMWF

The European Centre for Medium-Range Weather Forecasts (ECMWF) model runs every 12 hours, with a temporal resolution of model output of 1 day (24 hours) and forecasts out to 10 days. Some meteorological parameters such as the vertical velocity (mb.s^{-1}) that will be used in this report are from ECMWF 6hours products. These data are chosen for the nearest coincident location of satellites pixels with less than 6 hours previous to satellites passing times. For detailed descriptions of available data, see on the official website: http://www.ecmwf.int/.

2.5 Common cloud products between POLDER and MODIS

The cloud products from the two sensors are different: POLDER has no products from infrared channels (e.g. cloud top temperature and emissivity, multilayer flag…). The particle effective radius can be produced from POLDER by using the polarization information under very specific conditions. This product is thus not provided in the official data. On the contrary, POLDER could offer the particle shape information thanks to the 16 directional observations. The common cloud products from the two sensors contain the cloud cover, thermodynamic phase, cloud optical thickness, cloud top pressure, which are main cloud properties used for our study in the following sections.

Chapter 3

Cloud Cover

3.1 Introduction

As presented in chapter 1, clouds cover about 50%-70% of the earth (Rossow and Schiffer, 1991) and are essential components of the atmosphere. They influence the earth's climate by virtue of their radiative properties both in the solar spectral (Hobbs and Deepak, 1981) and thermal-infrared spectral (Hunt, 1982) regions and because of their role in the hydrological cycle. This has been demonstrated both from satellite observations (Ramanathan, 1987; Ramanathan *et al.*, 1989) and modeling studies (Ramanathan *et al.*, 1983; Cess *et al.*, 1989). These radiative effect depends on a synthesis of fundamental properties from the clouds including the cloud amount, cloud optical thickness, cloud thermodynamic phase, cloud albedo, cloud vertical structure, cloud top pressure and so on. Better descriptions of the clouds and their properties are required to understand correctly the climate system and its natural or human induced variations. In this chapter, we concentrate our study on cloud cover.

Benefit from the modern satellites, especially the A-Train constellation, which provide a platform in the effort to monitor the earth-atmosphere system and to understand its various components among which clouds are recognized of primary importance. Cloud studies from space observations have been an increasingly growing interest in the researches on both macrophysical and microphysical properties. These observations of cloud from onboard-satellite instruments have the advantage of a global coverage with a high space-time resolution. Taking advantage of satellite observations, long records of cloud properties are established to understand the climate changes at both regional and global scales. Accuracy and limitations of

these climatology records need to be clearly established to assess potential trends in cloud cover and its associated properties. This calls for the establishment of additional and carefully characterized datasets that can serve as reference to evaluate longer records derived from a series of operational satellites. A-Train satellites queued in line provide an unprecedented opportunity to make effort on the study of global atmosphere. This group of satellites provides within minutes of each other, thorough information about our atmosphere from a set of passive and active sensors with broad performances and application ranges. As parts of the A-Train, Aqua carrying MODIS (MODerate-resolution Imaging Spectroradiometer) and PARASOL carrying POLDER (Polarization and Directionality of the Earth Reflectance), fly in ascending orbit and cross the equator within 105 seconds of one another at around 1:30 p.m. local time. Among its noticeable instrumental characteristics, MODIS provides a relatively high spatial resolution as well as a wide spectral coverage from solar, near infrared (NIR), to thermal infrared (IR) spectrum (Platnick *et al.*, 2003) while the virtues of POLDER rely on its multi-polarization, multi-directionality and multispectral capability (Parol *et al.*, 2004). These different characteristics make each sensor to identify clouds in different ways. Analyses that combine the two different sensors can not only obviously help to obtain a more accurate representation of global cloud cover and cloud properties, a better comprehension of them and their effects on the radiative budget, but also they provide in a first place a better understanding of both sensors' characteristics and abilities to retrieve cloud properties, especially their cloud detection performances. Recent joint analyses of MODIS and POLDER cloud datasets have been demonstrated of great interest. For example, a statistical comparison of the cloud properties from level 3 made by Parol et al. (2007), showed the overall consistency of cloud detection schemes. The comparison of cloud thermodynamic phase product, led to the development by Riedi et al., (2007) of a new synergistic algorithm to improve cloud phase identification. Also, the comparison of cloud droplet radii retrieved from POLDER and MODIS observations by Bréon and Doutriaux-Boucher (2005), had demonstrated systematic biases over ocean with only hypothetical explanations linked to either retrieval issues or insufficient knowledge of microphysical processes at cloud top. Finally, the comparison of ice cloud optical thickness by Zhang *et al.*, (2009), focused on the inherently difficult problem of providing a realistic representation of ice crystal microphysical properties and the impact of associated uncertainties for climate studies.

Cloud cover derived from satellite measurements is of crucial importance among cloud properties. It is in form of a cloud detection or mask, which is a raster image with pixels indicating presence or absence of cloud within the sensor's Fill of View (FOV). The identification of cloud-contaminated pixels is crucially important since it is a first compulsory step for further cloud properties retrieval and clear atmospherically profile retrieval. Any difficulty in establishing cloud detection/mask, in turn causes errors in the determination of other cloud properties. Better understanding of cloud detection and classification is therefore required, which would improve the retrieval of cloud top pressure, optical depth, effective radius, and so on. It would also benefit the parameterization schemes for GCMs.

The major distinctions between the clouds and the clear background are: (1) The brightness. Clouds are composed of droplets or ice crystals. This is the nature to discriminate the clouds from the clear surfaces (land/ocean) and the aerosols. The consisting of water droplets and crystals makes the optical properties of clouds different from the backgrounds according to the value of refractive index, which determines the scattering and absorption behaviors. In general, clouds reflect more radiation and are brighter than the background. (2) The temperature. The behind mechanics of cloud processing are the vapor condensation as a result of decreasing temperature, so clouds are formed only in colder places. The infrared emission, which depends on temperature, is therefore efficient to discriminate colder clouds from warmer surfaces. (3) The vertical location. In the troposphere, temperature decreases with altitude. Clouds locate in colder sky that means at a higher altitude. In addition, as clouds are high, the presence of clouds could cut down the loading path of vapor and the absorption and scattering path of gases and molecules (the absorption bands of different gases are listed in annex 1). (4) Other clouds characteristics such as the cloud heterogeneity. The spectral variations of cloud radiative properties and so on, are also useful indicators in cloud identification processing.

To correctly and automatically discriminate the clouds from satellites measurements, a series of complex threshold tests from visible to thermal IR are applied to convert the measured radiances to the identification of clouds, aerosols and ground surfaces. Because each threshold test has more or less sensitivity to detect certain types of cloud that are related to certain environments, the cloud detection/mask could produce some problematic cloud discriminations. In general, cloud detection/mask issues are mainly founded either with relation to cloud types,

such as thin cirrus, low stratus at night and small cumulus that the difficulty of discrimination is due to insufficient radiation contrast to the background, or with relation to broken clouds and cloud edges that the retrieval pixels are not completely filled with clouds, or with relation to particular environmental conditions such as snow and sea ice coverage, deserts, sun-glint, cloud shadow, heavy aerosols loading, and night time, in which condition charactering cloud and clear-sky are inappropriate. Instrumental characteristics such as the spatial resolution, sensor noise and spectral coverage can also impact the quality of cloud detection/mask. In addition, the choice of thresholds in each test and mathematical classification method in the algorithm can as well bring errors into cloud amount calculation. Seeing so many uncertainties of cloud separation, it is therefore necessary to assess the quality of cloud detection/mask for each instrument. Not only the cloud assessments between passive satellite sensors and active grounded instruments (e.g. radar, lidar and meteorology observations), but also inter-satellite assessments are in pressing needs.

In the following presentation, the statistical comparison and analysis of cloud cover derived from POLDER and MODIS instruments are organized. A brief overview on cloud detection/mask and the behind theories is provided individually for the two sensors in the first section. Then statistical results, detailed analyses and further discussions on potential differences of cloud detection are shown in the next sections. This main part of work concludes a full-aspect comparison on cloud cover from regional, temporal, angular and vertical distributions. An additional validation with the active sensor CALIOP is made at last for problematic cloud detections that are mainly referred to thin cirrus. Finally, a summary of main findings and outlook is provided.

3.2 Main features of cloud detection algorithms

3.2.1 POLDER

The POLDER algorithm is in fact a cloud detection algorithm, which is a little different to the cloud mask that masks out any possible clouds and gives solid classification of clear sky. On the contrary, POLDER provides solid clouds identification. As a component of the "ERB & clouds" processing line, POLDER

algorithm is based on a series of separated and independent threshold tests. They are applied to each individual pixel for every viewing (Buriez *et al.*, 1997; Parol *et al.*, 1999). Four tests aim at detecting clouds and three additional tests are applied to identify clear pixels. If a pixel fails to pass all these seven tests, and remains unclassified, angular and spatial variability tests will be used. An undetermined pixel for a certain direction has its decision first depending on the agreed results of other directions, otherwise depending on the spatial variation if in some directions it is clear while in others directions it is cloudy or all of directions are undetermined. Clouds are expected to have higher spatial variability of reflectance compared to aerosols. Afterwards, when all of elementary pixels are identified as either clear-sky or cloudy, the cloud fraction (CF) is computed at super-pixel scale (3×3 pixels), direction by direction. The final cloud fraction is averaged over all 16 directions.

The four tests used to detect cloudy pixels are:

1. **The apparent pressure test** (apparent pressure is obtained from the estimate of oxygen absorption around 763nm) (Vanbauce *et al.*, 1998) identifies a pixel as cloudy only when the apparent pressure is markedly lower than the surface pressure. This test can be applied over all types of surface (including bright surfaces such as sun-glint, snow covered and desert). It is sensitive to the middle and high thick clouds and has weaker skills to detect the very low, thin or broken clouds.

2. **The solar reflectance test** labels a pixel as cloudy when the 865nm (or 490nm) reflectance over ocean (or land) is significantly higher than the value estimated from clear-sky conditions. This test is effective to identify the bright clouds over dark surfaces but may be ineffective for very thin clouds.

3. **The double 865nm polarized reflectance test** is based on the different features between cloudy and clear-sky conditions specifically in the rainbow directions. When polarized reflectance value is significantly lower than a low threshold for no matter what scattering angle and surface, a pixel is labeled as cloudy. This test can yield false cloud detection in case of optical thick aerosol (dust) events. In addition, in the rainbow direction outside of polarizing surface (sun-glint), a pixel is labeled as cloudy if it has the typical strong polarized features of liquid clouds (Goloub *et al.*, 2000; Parol *et al.*, 2004). This part of test depends strongly on the range of accessible scattering angle.

4. **The 490nm polarized reflectance test** labels a pixel as cloudy if its value (The 490nm polarized reflectance is contributed mainly by molecules above the clouds) is noticeably lower than the clear-sky value (Goloub *et al.*, 1997).

Three additional tests are applied to confirm clear sky scenario when none of the above tests identified a cloudy situation.

1. First, **an 865nm (490nm) low reflectance test** out of sun-glint directions over ocean (land) is applied to check that reflectance does not exceed a threshold corresponding to an upper limit for clear sky.

2. Secondly, **spectral variability of reflectance** is observed between 865 and 443 nm out of sun-glint region to test if it is large enough.

3. Thirdly, **the apparent pressure** is quite close to the surface level in sun-glint direction or over bright surface.

In summary, POLDER carries forward the strengths of multi-spectral, multi-directional and polarization capability to discriminate the solid clouds (with optical properties) from clear sky. Confidence index is provided to qualify the cloud detection process. This index ranges from 0 to 1 and is computed based on the number of available useful viewing directions and overall number of tests indicating either cloudy or clear-sky conditions. Index equal to 1 corresponds to high confidence of detection while 0 indicates poor confidence. In presence of aerosols, thin, broken clouds or cloud edges, this index tends toward low value.

3.2.2 MODIS

The MODIS algorithm is a cloud mask (MOD35, Ackerman *et al.*, 1998; Platnick *et al.*, 2003), which consists of a series of threshold tests based on the contrast between cloudy scene and the background surface in a given target area of 1×1 km^2 pixel. Once a pixel is identified as one of the particular conceptual domains (land, water, coast, desert, snow/ice for both day and night), each threshold test will be performed to indicate a level of confidence. This series of tests combines the 250-m and 1-km cloud mask and is assembled into five different groups that indicate similar cloud conditions. They are arranged so that independence between groups is maximized. The minimum confidence is determined for each group from in-group tests and the final cloud mask confidence (value Q) is then determined from the

products of results for each group. After all tests, a summary is provided and a pixel is classified as one of four situations: confident clear (Q>0.99), probably clear (0.99>Q>0.95), uncertain/probably cloudy (0.95>Q>0.66) or cloudy (Q<0.66). For confidence values between 0.66 and 0.95, spatial and temporal continuity tests are further applied in order to determine whether the pixel is confidant clear or confidant cloudy. The final cloud fraction is then computed from 5×5 km^2 cloud mask pixel and stored in MODIS level 2 cloud fraction day product (FCD). As referred in Chapter 2, in the PM data we have another cloud fraction product that is the solid cloud fraction for clouds owning optical properties (CFC) and recalculated from an additional "clear sky restoral" algorithm. Thus both the CFC and POLDER cloud fraction concern about the more confident clouds.

Recent modifications to the operational algorithm (Ackerman *et al.*, 2007; Frey *et al.*, 2008) have led to significant progress in cloud detection in polar regions, at night and in sun-glint regions. Compared to POLDER, the MODIS algorithm greatly benefits from higher resolution and the absorption, emission and reflectance information provided by NIR and IR channels. Thus the MODIS algorithm has better skills for detection of thin cirrus, low clouds over snow and heavy aerosols. Table 2.1-1 lists many threshold tests grouped and used to detect different cloud types over different surfaces in MODIS algorithm.

Scene	Solar	Thermal	Comments
Low cloud over water	$R_{0.87}$, $R_{0.67}/R_{0.87}$, $BT_{11} - BT_{3.7}$	Difficult. Compare BT_{11} to daytime mean clear-sky values of BT_{11}; BT_{11} in combination with brightness temperature difference tests; Over ocean, expect a relationship between $BT_{11} - BT_{8.6}$, $BT_{11} - BT_{12}$ due to water vapor amount being correlated to SST	Spatial and temporal uniformity tests sometimes used over water scenes; Sun-glint regions over water present a problem.
High Thick cloud over water	$R_{1.38}$, $R_{0.87}$, $R_{0.67}/R_{0.87}$	BT_{11}; $BT_{13.9}$; $BT_{6.7}$; $BT_{11}-BT_{8.6}$; $BT_{11}-BT_{12}$	
High Thin cloud over water	$R_{1.38}$	$BT_{6.7}$; $BT_{13.9}$; $BT_{11}-BT_{12}$; $BT_{3.7}-BT_{12}$	For $R_{1.38}$, surface reflectance for atmospheres with low total water vapor amounts can be a problem
Low cloud over snow	$(R_{0.55}-R_{1.6})/(R_{0.55}+R_{1.6})$; $BT_{11}-BT_{3.7}$	$BT_{11}-BT_{6.7}$; $BT_{13}-BT_{11}$ Difficult, look for inversions	Ratio test is called, NDSI. $R_{2.1}$ is also dark over snow and bright for low cloud.
High thick cloud over	$R_{1.38}$; $(R_{0.55}-$	$BT_{13.6}$; $BT_{11}-BT_{6.7}$; $BT_{13}-BT_{11}$ Look for inversions, suggesting	

snow	$R_{1.6}$/($R_{0.55}$ +$R_{1.6}$);	cloud-free.	
High thin cloud over snow	$R_{1.38}$; ($R_{0.55}$-$R_{1.6}$)/($R_{0.55}$+ $R_{1.6}$);	$BT_{13.6}$; BT_{11}-$BT_{6.7}$; BT_{13}-BT_{11}	Look for inversions, suggesting cloud-free region.
High thick cloud over vegetation	$R_{1.38}$; $R_{0.87}$; $R_{0.67}$/ $R_{0.87}$; ($R_{0.87}$-$R_{0.65}$)/($R_{0.87}$ + $R_{0.65}$);	BT_{11}; $BT_{13.9}$; $BT_{6.7}$; BT_{11}-$BT_{8.6}$; ; BT_{11}-BT_{12};	
High thin cloud over vegetation	$R_{1.38}$; $R_{0.87}$; $R_{0.67}$/ $R_{0.87}$; ($R_{0.87}$-$R_{0.65}$)/($R_{0.87}$ + $R_{0.65}$);	$BT_{13.9}$; $BT_{6.7}$; BT_{11}-$BT_{8.6}$; BT_{11}-BT_{12};	Tests a function of ecosystem to account for variations in surface emittance and reflectance.
Low cloud over bare soil	$R_{0.87}$; $R_{0.67}$/ $R_{0.87}$; BT_{11}-$BT_{3.7}$; $BT_{3.7}$-$BT_{3.9}$	BT_{11} in combination with brightness temperature difference test. $BT_{3.7}$-$BT_{3.9}$; BT_{11}-$BT_{3.7}$;	Difficult due to brightness and spectral variation in surface emissivity. Surface reflectance at 3.7 and 3.9 μm is similar and therefore thermal test is useful
High Thick cloud over bare soil	$R_{1.38}$; $R_{0.87}$; $R_{0.67}$/ $R_{0.87}$;	$BT_{13.9}$; $BT_{6.7}$; BT_{11} in combination with brightness temperature difference test.	
High Thin cloud over bare soil	$R_{1.38}$; $R_{0.87}$; $R_{0.67}$/ $R_{0.87}$; BT_{11}-$BT_{3.7}$;	$BT_{13.9}$; $BT_{6.7}$; BT_{11} in combination with brightness temperature difference test. For example $BT_{3.7}$-$BT_{3.9}$;	Difficult for global applications. Surface reflectance at 1.38 μm can sometimes cause a problem for high altitude deserts. For BT difference tests, variation in surface emissivity can cause false cloud screening

Table **3.2-1** - *General approaches to cloud detection over different land types using satellite observations that relay on thresholds for reflected and emitted energy from ATBD-MOD-35*

3.2.3 CALIOP

The CALIOP scene feature classification algorithm (Liu *et al*., 2005), describes how to classify the scene into cloud and aerosol layer types, and further into cloud and aerosol layer subtypes. The former classification can be achieved by using the β'-χ'-z separating method (see Figure 3.2-1). Clouds have larger backscatter coefficients and higher color ratios than aerosols with the separating threshold depending on altitude. This final separation is determined and based on the probability density functions defined as the probability that one or more attributes (e.g. β', χ') are associated with clouds and aerosols. If the measured attributes are inferior

to the confident aerosol threshold, the scene is classified as aerosols and if they are superior to the confident cloud threshold, the scene is then classified as clouds. Otherwise, if the values are between these two thresholds, the likelihood could belong to either clouds or aerosols, and additional considerate attributes may allow an unambiguous classification.
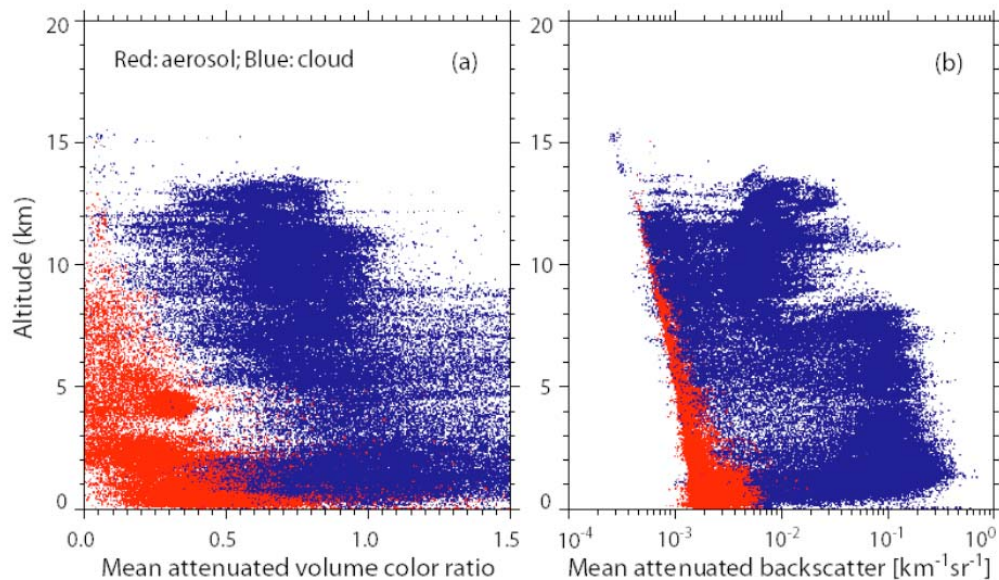
Figure 3.2-1 – *Scatter plot of mean attenuated volume color ratio (χ') and backscatter (β') of nearly 230 000 features observed by CPL during the THORPEX-PTOST mission (Liu et al., 2005).*

CALIOP sub-typing classification of clouds is based on lidar measurements and with combination of cloud top pressure and cloud opacity: the separating boundaries of high, middle and low clouds are made at levels of 680hPa and 440hPa; opaque and transparent clouds are determined from the signal of surface for which opaque clouds have no signal from the surface (for CALIOP, in presence of clouds with optical depths greater than 3-5, the signal from lower layers can be obscured by the overlaying clouds). Sub-typing classification flowchart is shown in Figure 3.2-2.

Cloud fraction is finally computed along a line over an 80km horizontal segment. This parameter is simply estimated as the ratio of the number of 1-km profiles with clouds found below 3km to the number of the total 1-km profiles in the 80km segment.

Category 0:   Low, overcast, thin (transparent St, StCu, and fog)
Category 1:   Low, overcast, thick (opaque St, StCu, and fog)
Category 2:   Transition stratocumulus
Category 3:   Low, broken (trade Cu and shallow Cu)
Category 4:   Altocumulus (transparent)
Category 5:   Altostratus (opaque, As, Ns, Ac)
Category 6:   Cirrus (tranparaent)
Category 7:   Deep convective (opaque As, Cb, Ns)
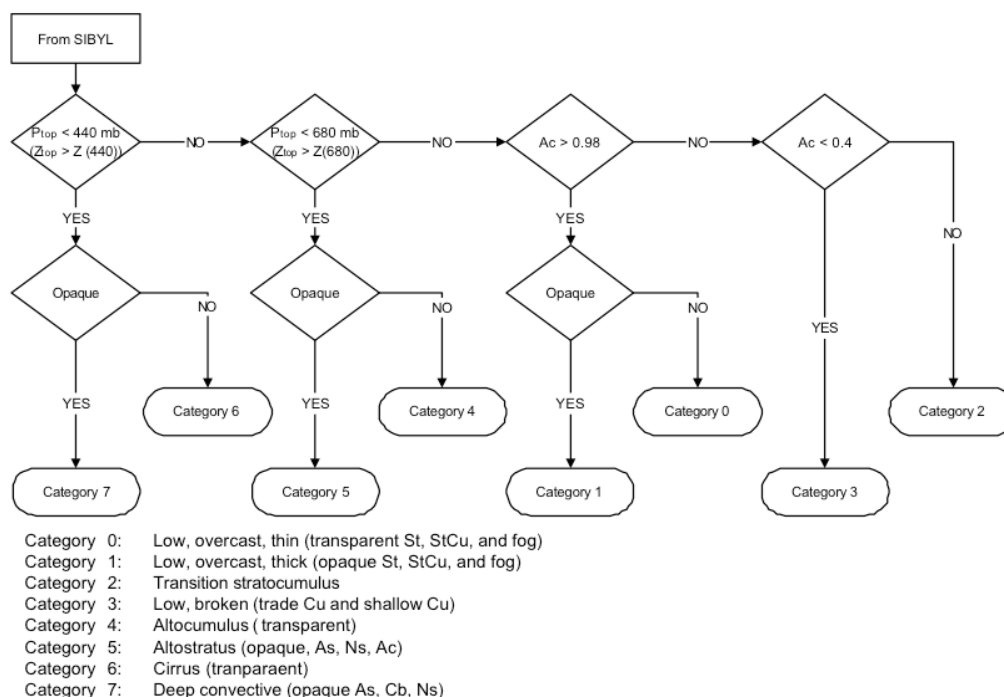
Figure **3.2-2** – *Flowchart of the sub-typing of clouds from Liu et al. (2005). Ac: cloud cover. P_{top}: cloud top pressure.*

3.3 Statistical cloud detection and cloud fraction comparison from POLDER and MODIS

Before the presentation and study of cloud fractions and their differences between the two passive sensors, we start from a rough assessment of the pixel scene classification. As seen in chapter 2, the smallest scene for the coincident POLDER and MODIS observations corresponds to a POLDER super-pixel (also the PM pixel). It is classified into either cloudy or clear sky (Cloudy: CF>0 and clear: CF=0). For cloudy scene, it can be further identified as overcast or broken (overcast: CF=1; broken: 0<CF<1). In a first step of the pixel scene classification assessment, we will mainly focus on the statistical occurrence frequency of each scene type (clear/broken/overcast) determined from one sensor and from the combination of the two sensors. This occurrence frequency is of course different to the cloud fraction that will be studied later as the occurrence frequency concerns how often one type of scene occurs, while cloud fraction concerns how many clouds are found. Anyway,

these two concepts have an important relation and the occurrence frequency of clear/broken/overcast scenes will help us to understand the statistical cloud fraction.

In Table 3.3-1, we report the annual (Dec. 2007 to Nov. 2008) and global (90°S to 90°N) occurrence frequency for different scenes according to three classes: overcast cloudy, broken and clear for three different cloud fraction products of the two sensors: POLDER, CFD MODIS and CFC MODIS (seen in chapter 2). At PM pixel scale, POLDER has 22% of clear scenes, 43% of broken cloudy scenes and 34% of overcast cloudy scenes. The occurrence frequencies of clear, broken and overcast cloudy scenes for MODIS CFC are 26%, 42% and 32% respectively and for MODIS CFD are 9%, 56% and 35% respectively. It is clear from these figures that MODIS CFC detects the most of clear scenes and the least of broken scenes while MODIS CFD detects the least of clear scenes and the most of broken scenes. Compared to clear and broken scenes, the occurrence frequencies of overcast cloudy scenes show smaller differences among the three cloud fraction products.

(%)	POLDER	MODIS (CFC)	MODIS (CFD)
Clear	22	26	9
Overcast	34	32	35
Broken	43	42	56

Table 3.3-1 – *The occurrence frequencies at PM pixel scale for clear, overcast and broken cloudy scenes determined from MODIS CFC, MODIS CFD and POLDER cloud fraction.*

In Table 3.3-2, we report the occurrence frequencies for different combined scenes over the same period as Table 3.3-1. The total pixel number in the assessment is 3.3E+08. Looking at the first line of the table for example, the occurrence frequency of clear scenes for both POLDER and MODIS CFC is about 18% and of cloudy scenes is 69%. Only 12% of the scenes show disagreements on cloud-clear sky classification. This pixel-to-pixel comparison result suggests that the cloud-clear sky separation for the two sensors in overall is satisfactory and similar with the agreement percentage up to 88%.

For the 69% of scenes in cloudy condition classified by the two sensors, 25% are overcast and 29% are broken. No more than 0.6% of the total scenes give

disagreement on the scene classification with one sensor declared clear but the other overcast. This suggests that it is rare for both sensors to misclassify the clear sky (or overcast clouds) as the overcast clouds (or clear sky) and again confirms the satisfactory cloud-clear sky separation for the two sensors. The disagreements between the two are mainly from the overcast-broken scenes and the clear-broken scenes separations. The percentage of the misclassified overcast-broken clouds (one as overcast clouds and the other as broken clouds for POLDER and MODIS) is about 14.7% (8.7%+6.0%) and of the misclassified clear-broken clouds (one as clear sky and the other as broken clouds for the two sensors) is about 12% (3.8%+8.2%). We conclude hence that, for the two sensors, the definition and identification of broken clouds are different, which are also the main difficulties in cloud detection for all satellites.

We can also look at other combined cloud products in Table 3.3-2 to understand scene classification. For example, the percentage of the MODIS CFD clear and CFC cloudy scenes is 0% which is reasonable as CFC is calculated from CFD by restoring some clear pixels from cloudy, thus it is no more than CFD; the percentage of the MODIS CFD broken and CFC clear scenes is about 16.5% and the MODIS CFD overcast and CFC clear (broken) scenes about 0.3% (4%). It is also reasonable because the restoral of clear sky is mainly from the cloud edges.

(%)	Cld-Cld	Cld-Clr	Clr-Cld	Clr-Clr	Ove-Ove	Ove-Bro	Ove-Clr	Bro-Ove	Bro-Bro-	Bro-Clr	Clr-Ove	Clr-Bro
P-M.C	69.3	8.5	4.2	18.0	25.4	8.7	0.2	6.0	29.3	8.2	0.4	3.8
P-M.D	76.9	0.9	13.4	8.7	26.3	7.9	0.0	7.8	34.9	0.9	0.6	12.9
M.D-M.C	73.4	16.8	0.0	9.6	30.2	4.0	0.3	1.5	37.7	16.5	0.0	0.0

Table 3.3-2 – *The occurrence frequencies for different combined scenes determined from different cloud fraction products noted in Table 3.3-1, P=POLDER, M.C=MODIS CFC, M.D=MODIS CFD, cld=Cloudy, Clr=Clear, Ove=Overcast, Bro=Broken. For example Column: Cld-Clr and line:P-M.C means POLDER (cloudy) and MODIS CFC (clear).*

We could continue to plot the geographical distributions and angular variations for the occurrence frequency of different scenes and different combined scenes, which may provide more information to study the cloud detection/mask of the two sensors. For example, we could expect that overcast clouds occur more often in the oblique viewing directions. However, as cloud-clear sky separation and cloud fraction have potential relations, in the following, the comparison is directly for cloud fraction.

3.3.1 Global cloud fraction and latitudinal variations

In Table 3.3-3, we show the global annual cloud fraction for POLDER and for the two MODIS products (CFD and CFC) over land and ocean, for ice and water clouds separately. MODIS detects about 65% (CFD) and 50% (CFC) of cloudiness over the whole globe compared to 57% for POLDER. Both instruments detect fewer clouds over land than over ocean, in accordance with established climatologies (Warren *et al.*, 1986; Warren *et al.*, 1988; Rossow and Schiffer, 1991; Rossow and Schiffer, 1999; Stubenrauch *et al.*, 2010). Difference between POLDER cloud fraction and MODIS CFC (CFD) is 7% (-8%) on global average. Compared to MODIS CFC, POLDER observes more water clouds and fewer ice clouds. This will be confirmed and analyzed in the following.

	Total			Land			Ocean		
	Tot	Liq	Ice	Tot	Liq	Ice	Tot	Liq	Ice
POLDER	57	35	16	48	30	14	63	39	17
CFC(MOD)	50	28	22	38	20	18	53	31	22
CFD(MOD)	65	-	-	50	-	-	70	-	-

Table 3.3-3 – *Global averaged cloud fraction from POLDER and MODIS for total, liquid and ice cloud over land and ocean. Note that the separation liquid/ice does not exist for MODIS CFD.*

In Figure 3.3-1, we present latitudinal variations of cloud fraction. They have been restricted to the zone between 60°S and 60°N to discard the complex situations in polar regions due to snow covered surfaces and day/night transition where

POLDER has little skills due to lack of thermal infrared channels. This figure shows that, following the synoptic atmospheric motion, variations of cloud fraction from both satellites follow a "W" shape, with high values in the InterTropical Convergence Zone (ITCZ) and Storm Tracks (STs) areas of each hemisphere and low values in the subtropical subsidence areas. This variation agrees with other climatology studies (Rossow and Schiffer, 1999; Minnis *et al.*, 2004; Stubenrauch *et al.*, 2010).   As explained in chapter 2, the CFC cloud fraction is much smaller than the CFD one and in agreement with Table 3.3-3, POLDER cloud fraction is between the two MODIS cloud fractions. It is about 10% higher than the MODIS CFC and 10% lower than the MODIS CFD. The difference between POLDER and MODIS CFC is larger in the south hemisphere, especially in mid-latitude areas (40°S) and tends to decrease at higher latitudes.
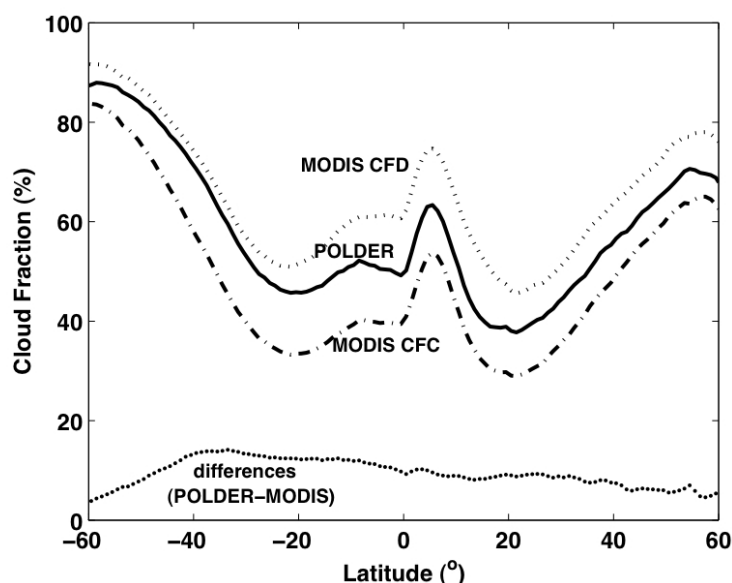
Figure 3.3-1 – *Latitudinal variations of cloud fraction from POLDER and MODIS.*

In Figure 3.3-2, we plot the latitudinal variations of the cloud fraction for water and ice clouds separately. We again obtain consistent results with Table 3.3-3, that is, POLDER detects more water clouds with a quasi-constant bias for every latitude and on the contrary MODIS detects more ice clouds. For ice clouds, differences tend to be larger in the ITCZ and STs regions and smaller in subtropical subsidence areas.
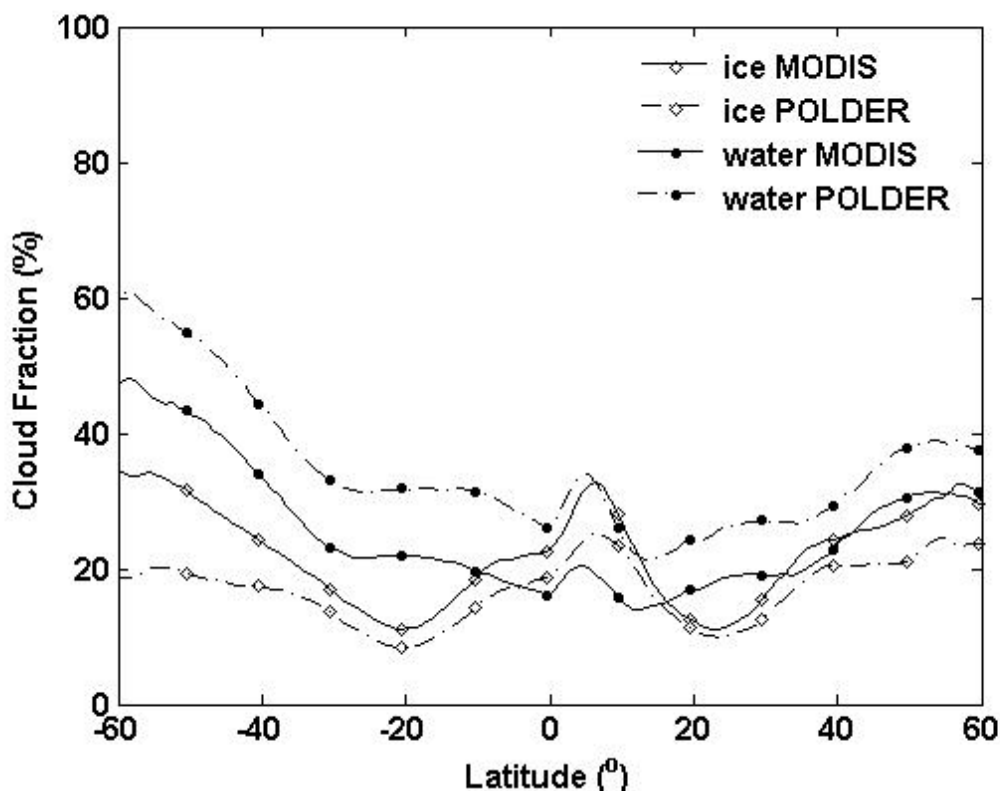
Figure 3.3-2 – *Latitudinal variations of ice and water cloud fraction from POLDER and MODIS.*

3.3.2 Seasonal variations

In Figure 3.3-3, we present the seasonal variations of MODIS (CFC) and POLDER cloud fractions. We focus on the seasonal cycle and represent here the differences between monthly averages and annual average. This representation masks out systematic bias (10%) between the two sensors (see Figure 3.3-1) and points out the main characteristics of the cloud fraction seasonal variations. Figure 3.3-3 displays this seasonal cycle over land and over ocean for four different zones: the tropics and subtropics (0°-30°) and the mid-latitude (30°-60°) regions of each hemisphere. Although a systematic and significant bias between POLDER and MODIS CFC has been observed in Figure 3.3-1, their seasonal cycles follow similar behavior in the four zones. Over land in the subtropics, cloud fraction rises to a maximum value in summer and goes down to a minimum in winter for each hemisphere. Situations are reversed in mid-latitude regions where more clouds are

found in winter. Over ocean, seasonal variations appear less pronounced. These very similar seasonal variations of cloud fraction agree with other studies (Stubenrauch *et al.*, 2006) and confirm that the differences between POLDER and MODIS do not change with season. Beyond this generally good agreement, we can still notice some minor inconsistencies existing for certain regions and seasons. For example, over ocean in the south hemisphere, POLDER detects a little bit more clouds than MODIS CFC during the summer (June-July-August) and over land in mid-latitudes of north hemisphere POLDER observes fewer clouds during winter.
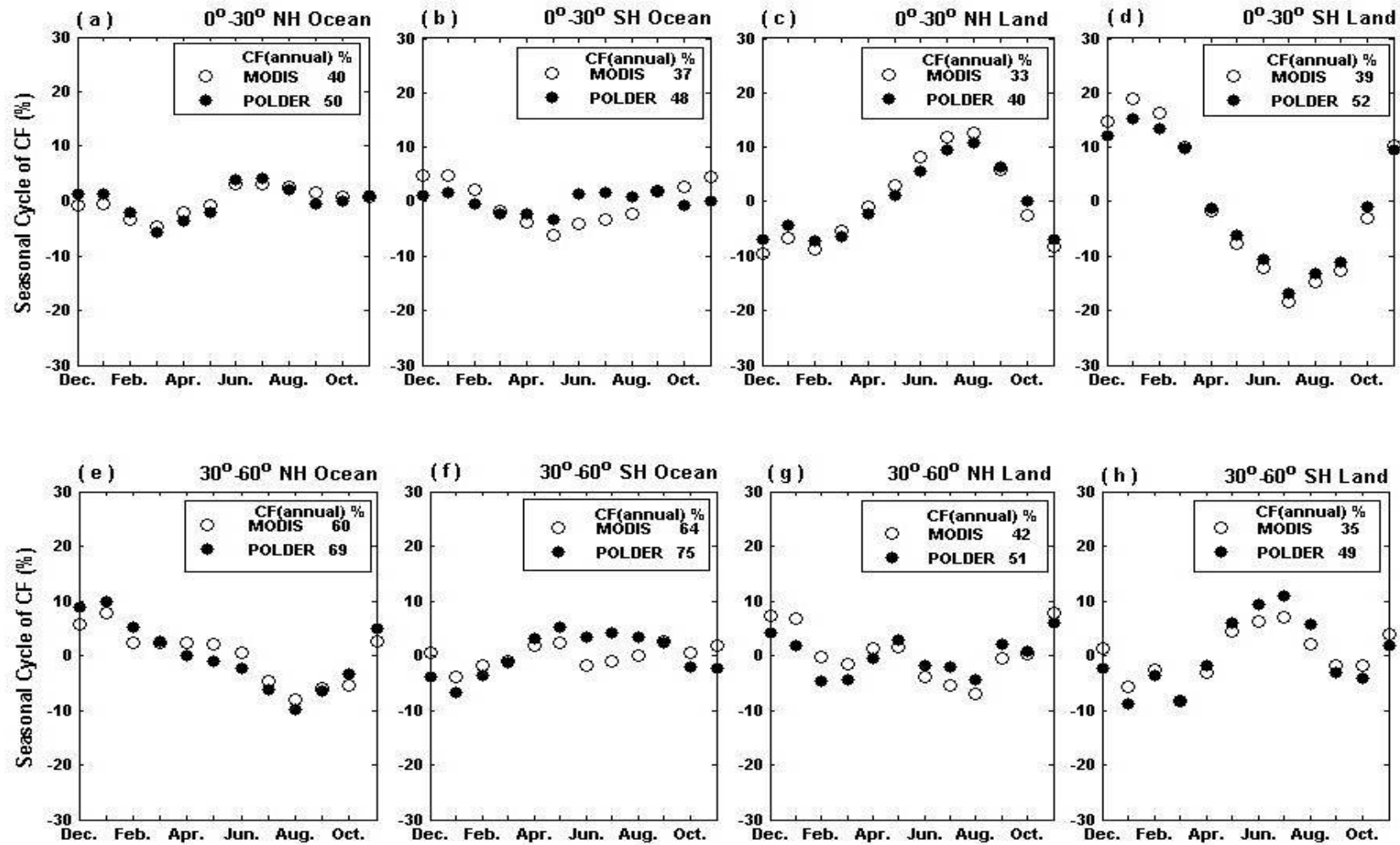
Figure 3.3-3 – *Seasonal variations of cloud cover in subtropics over ocean for the north hemisphere (a); for the south hemisphere (b), over land for the north hemisphere (c); for the south hemisphere (d); in mid-latitudes and over ocean, for the north hemisphere (e); for the south hemisphere (f); in mid-latitudes and over land for the north hemisphere (g); for the south hemisphere (h).*
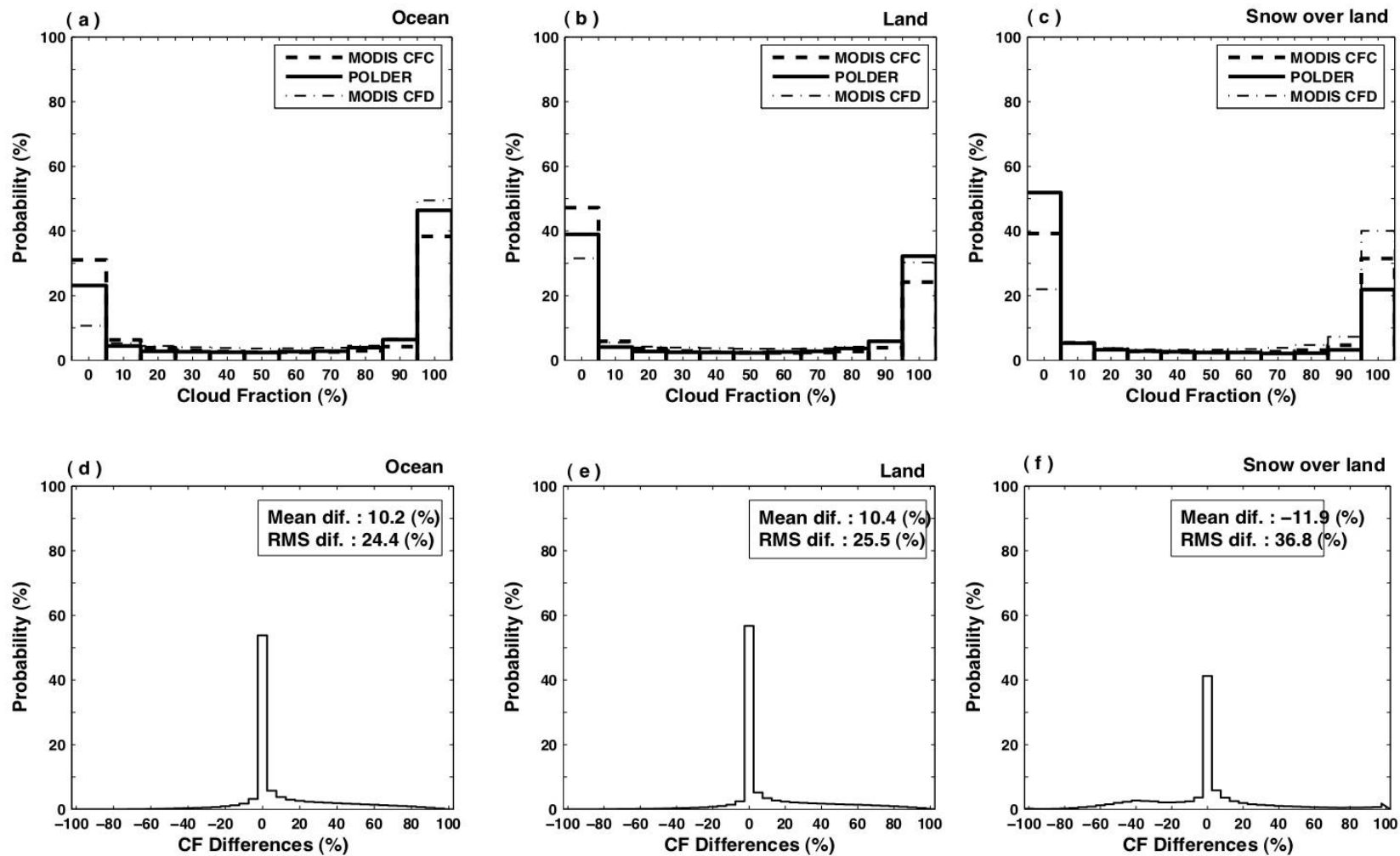
Figure 3.3-4 – *Histograms of cloud fraction over ocean (a), over land (b), and over snow-covered land (c); Histograms of cloud fraction difference over ocean (d), over land (e) and over snow-covered land (f).*

3.3.3 Differences between MODIS and POLDER cloud fractions.

To better understand the cloud fraction differences observed between the two sensors, we plotted in Figure 3.3-4 the Probability Density Functions (PDFs) of cloud fractions and their differences for the full year over three types of surface: ocean without snow/ice cover, land without snow/ice cover and land covered by snow/ice. Most of the POLDER and MODIS pixels are labeled as either clear or overcast (Figure 3.3-4 a, b, c). At the resolution of the PM Dataset (about $20 \times 20 \text{km}^2$), about 30% of the cloud cover is fractional. Over land and ocean, more (less) POLDER pixels are declared overcast compared to MODIS CFC (to MODIS CFD). This is the opposite over snow, where more POLDER pixels are labeled as clear compared to MODIS CFC. Again in these figures, we can notice the higher cloud cover over ocean than over land.

In Figure 3.3-4 d, e and f we report the mean values of the cloud fraction differences (POLDER-MODIS CFC) for the whole year. The mean values are 10.6%, 10.8% and -11.9% respectively over ocean, over land and over snow. Dispersion values represented by Root Mean Square (RMS) are respectively 24%, 26% and 36% over these three types of surfaces. Thus, we notice that the lowest mean difference and dispersion are observed over ocean and that a negative mean difference and the larger dispersion are obtained over snow/ice covered surfaces.

In order to locate the significant differences observed between POLDER and MODIS CFC cloud covers, Figure 3.3-5 presents geographical distributions of POLDER and MODIS cloud fractions for different seasons. It also reports the differences for the overall clouds among the three cloud fractions. Differences CF(Polder)-CFC are also presented for water and ice clouds separately. In general, POLDER and MODIS cloud fractions show similar geographical distributions, as already seen in the zonal variations presented in Figure 3.3-1 with an overall larger CFD than POLDER which in return is larger than CFC. Visually, MODIS CFC appears closer to POLDER cloud fractions. We note that the difference between MODIS CFD and MODIS CFC is larger in strong aerosol loading regions and in broken cloud areas.

For the three cloud fractions, high values are associated with deep convection located in the ITCZ, in STs and monsoon areas, and along the west coast of the continents (stratocumulus areas). Low values are associated to the subtropical ocean and deserts in subsidence regions. As already identified, differences between total cloud fractions are found almost everywhere positive and range from 0 to 20%. Ice cloud fraction differences are mostly negative ranging from -20% and 0. Namely, POLDER detects more clouds than MODIS CFC in overall, but MODIS detects more ice clouds than POLDER. Of course these results from a combination of absolute cloud detection sensitivity and cloud phase determination differences are difficult to sort out without going into details of the respective cloud phase products.

From the geographical distributions in Figure 3.3-5, we can point out and classify some major regional and seasonal features. Related reasons are discussed in the next section:

Large positive differences between POLDER and MODIS CFC while negative differences between MODIS CFD and POLDER are observed especially in spring and summer in the eastern and southern Africa, center of South America, Australia and in summer of North Asia (see section 3.4.1), Note these regions are mostly over land where cloud fractions are smaller suggesting that broken clouds dominate.

Large positive differences (POLDER minus MODIS CFC) higher than 30% are observed during summer in the central part of South Africa and during winter in Gulf of Guinea. We note that ice cloud fraction differences show also large positive values in the same place and time (see section 3.4.3).

Negative differences between POLDER and MODIS CFC corresponding to large positive difference between MODIS CFD and POLDER are observed during the whole year over Greenland and Antarctica and during winter above Siberia and North America. (see section 3.4.2).

Negative differences (POLDER minus MODIS CFC) are observed during spring and summer in the transition zone between desert and non-desert area (e.g. Sahara or Thar Desert in northwest of Indian, see section 3.4.2)

Strong negative differences for ice cloud fraction associated with large positive differences for water cloud are observed around the ITCZ (Indonesia, western equatorial Pacific Ocean, equatorial South America), in the mid-high latitude STs regions and in Indian during the monsoon (see section 3.4.4).

We also notice small negative differences in northern Pacific Ocean around (50°N, 180°E (W)), during spring and summer (see section 3.4.2).
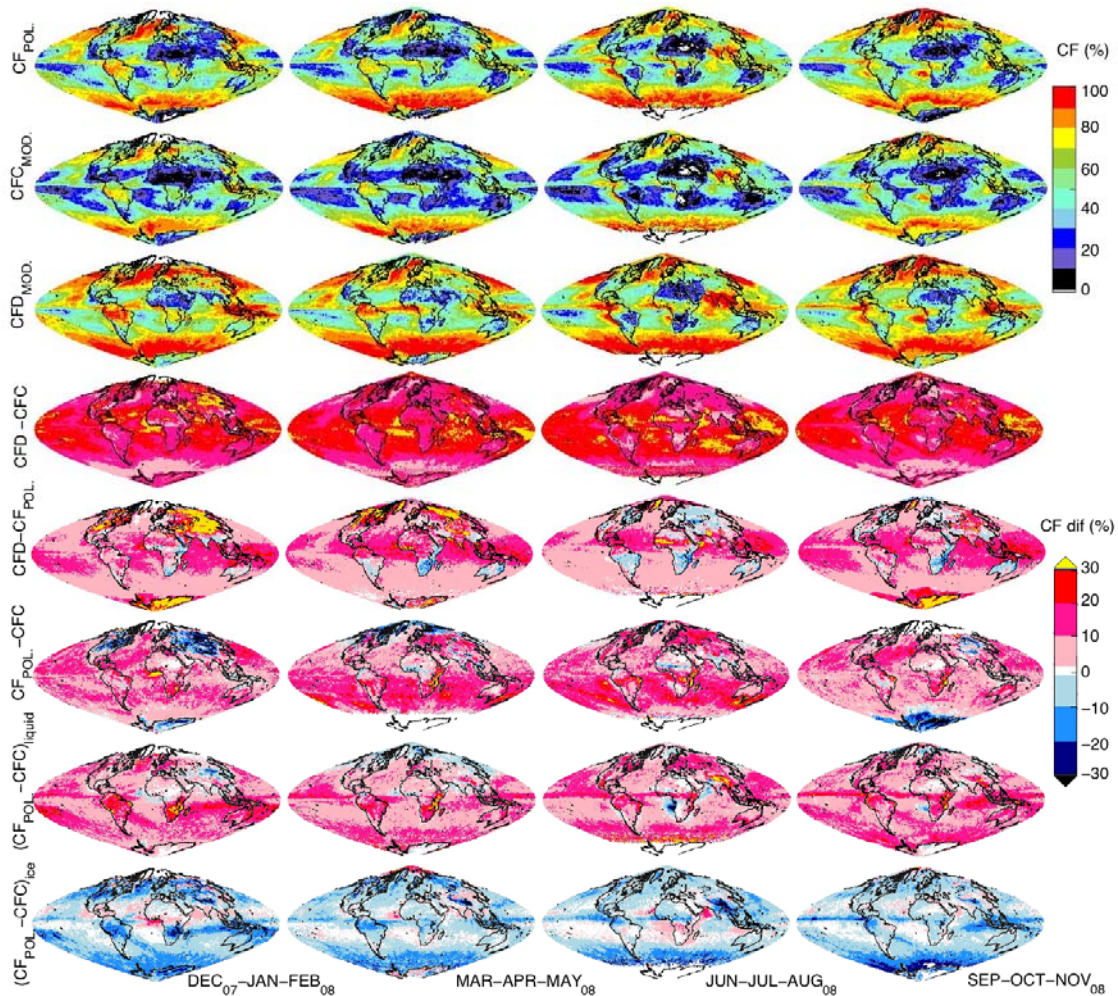
Figure 3.3-5 – *Geographical distribution of cloud fraction for POLDER (1st row), for MODIS CFC (2nd row) and for MODIS CFD (3rd row); geographical distribution of cloud fraction differences for MODIS CFD minus CFC (4th row), for MODIS CFD minus POLDER (5th row), for POLDER minus MODIS CFC (6th row) and also for water cloud fraction differences POLDER minus MODIS CFC (7th row) and ice cloud fraction differences POLDER minus MODIS CFC (8th row) during the four seasons in 2008.*

3.3.4 Angle dependence of cloud cover

Figure 3.3-6 presents different cloud fractions over ocean and land as a function of the view zenith angle (VZA) for solar angular bins of 5º. Negative view zenith angles correspond to backscattering directions with a relative azimuth angle less than 90º and positive values to forward directions with a relative azimuth angle greater than 90º. For MODIS, which obtains the observations by an east-west scanning, the VZA is directly linked to the cross-track distance from the center of orbit: the nadir direction corresponds to the center of the orbit and oblique directions to the edges with the backscattering directions in the eastern of the swath. For POLDER, which uses a CCD matrix, increasing VZAs correspond to increasing rings from the center of the wide two dimensional instantaneous field of view.

Over ocean (Figure 3.3-6 a, b and c), at first glance, it seems that cloud fraction increases steadily with the solar zenith angles (SZA) for both sensors. This is an artifact and is mainly due to statistic occurrences of SZA that are linked to specific latitudinal regions. Indeed, SZA tends to increase with latitudes as does cloud fraction for the latitudes between 20º and 60º (see Figure 3.3-1 and Figure 3.3-7).

Besides, we notice that MODIS cloud fraction has a stronger dependence (Maddux *et al.*, 2010) than POLDER on the VZA with an increase more pronounced in the forward directions. The growth of cloud amount with VZA has already been observed and explained as a consequence of an increase of observed cloud sides (Minnis, 1989). This effect can also be accentuated in case of thin clouds because they are better detected in oblique views, as the slant path through the cloud is longer. Detection of thin and fractional clouds can also explain the difference in cloud amount between forward and backscatter directions. As more radiation is scattered into forward directions, radiative threshold will lead to detect more clouds in these directions. In addition, spatial contrast used to select cloudy pixel will be enhance by shadow effects (Zhao and Di Girolamo, 2004). The increase of cloud fraction with VZA can also come from a resolution effect (Wielicki and Parker, 1992) as MODIS pixels near the swath edges cover more than 4 times larger areas than those at the center. Thanks to the POLDER optical design (combination of telecentric optics and aspherical lenses), the instrument does not present this drawback and provides an

almost constant spatial resolution throughout its wide field of view, independent of the viewing angle (Deschamps et al., 1994). This can explain, in part, why the POLDER cloud fraction does not depend as much as MODIS on the VZA value. In addition, MODIS with a higher spatial resolution can certainly better identify broken clouds in near nadir direction compared to oblique directions while POLDER with a lower spatial resolution is not able to see well the gaps between clouds even in near nadir directions.

Again we note that, as already done in section 3.3.1, the mean cloud fraction of POLDER is about 10% greater than those of MODIS (CFC).

Compared to the angular distribution of cloud fraction over land (Figure 3.3-6 e, f and g), over ocean the cloud amount dependence of solar angle is less important for high solar angles and more important for low solar angles, which may be related to the latitudinal variations. For low solar angles, they show similar angular variations for ocean: increasing cloud amount with VZA and pronounced in forward directions. However for high solar angles, increasing cloud amount with VZA is more pronounced in backward directions especially for solar angle equal to 25°-35° (low solar angle regions include many deserts). As we known, cloud mask uses the radiation contrast between clouds and the background to select clouds and over land the background radiation is variable depending on regions and seasons, and hard to obtain from satellites because of less sampling of clear sky. Cloud detection over land could therefore show more uncertainties. Without looking into the statistic angular dependence of clear sky radiation that is an important parameter in cloud processing line over land, it is hard to conclude. The impact of angular clear sky radiation on cloud detection could perhaps help in the future to make progress in cloud detection/mask over land with more correctness.

Figure 3.3-6 d and h presented here are prepared for later studies of cloud phase. The MODIS VZA represents the west-east location to the center of the orbit. From this figure, it shows no statistic differences of cloud fraction for POLDER when the pixel locates in the eastern, western or the center of the orbit (see chapter 4).
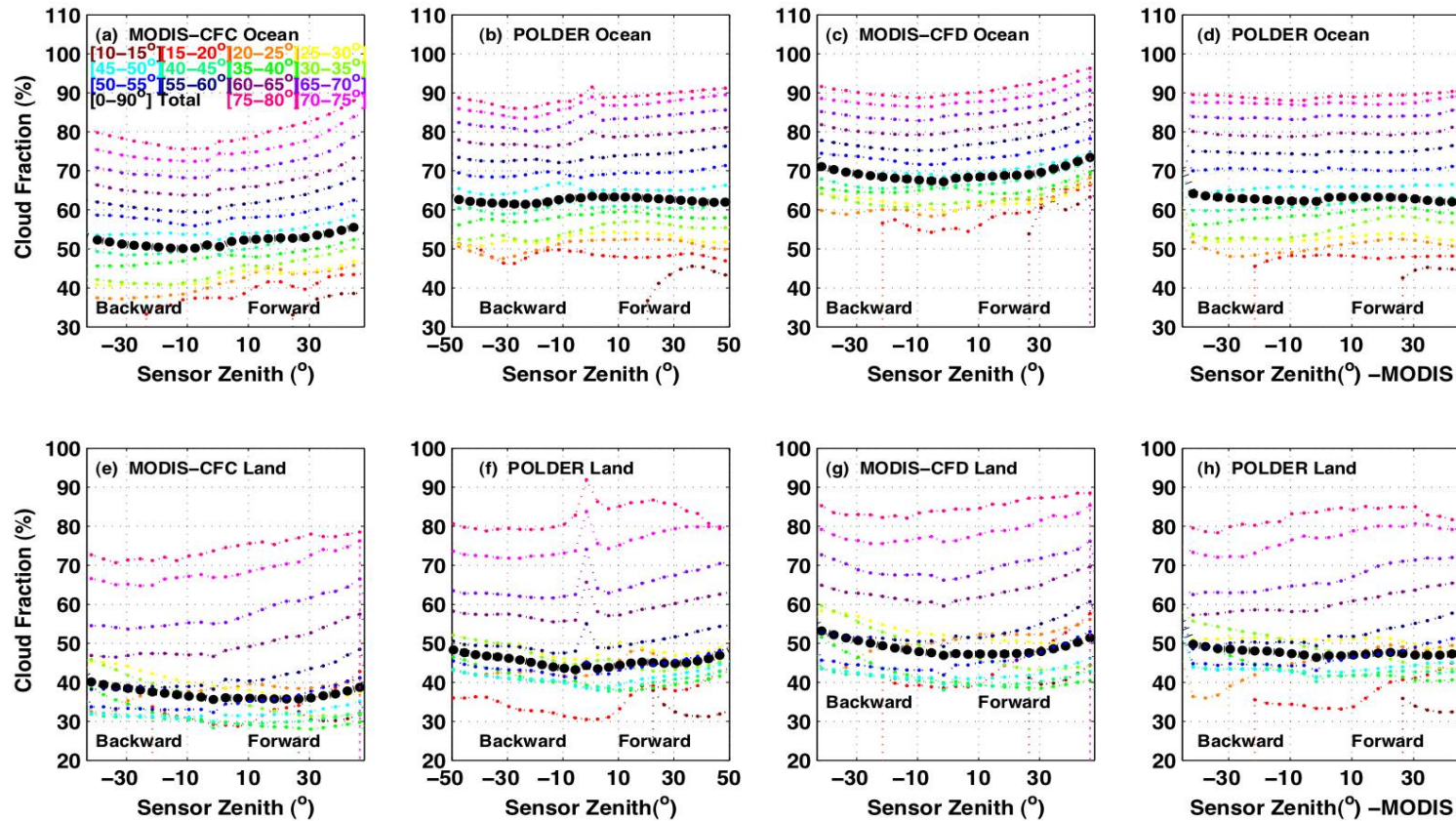
Figure 3.3-6 – *Cloud Fraction as a function of sensor zenith angle for different solar zenith bins for overcast clouds over ocean derived from MODIS CFC (a), from POLDER (b); for overcast clouds over land derived from MODIS CFC (e), from POLDER (f); for broken clouds over ocean derived from MODIS CFC (c) and from POLDER (d); for broken clouds over land derived from MODIS CFC (g) and from POLDER (h). Bold black curve is the mean value with no separation of solar zenith. Negative angles denote the absolute relative azimuth inferior to 90°, namely backward scattering directions. Subfigures d and h will be discussed in chapter 4.*
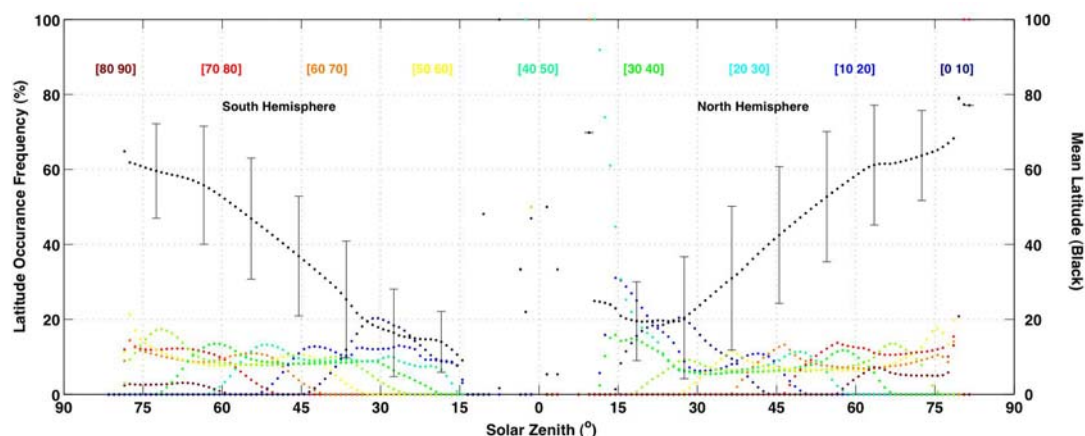
Figure 3.3-7 – *Occurrence frequency of latitudinal regions as a function of Solar Zenith angle measured by MODIS. The color represent different latitudinal zones of every 5 degrees marked in the figure for North Hemisphere and South Hemisphere. The pick of latitudinal frequency moves with solar zenith. The black dotted lines with the error bar mean the corresponding averages and dispersions of latitude.*

3.3.5 Vertical localization of the clouds

In section 3.3.3, we have studied the cloud fraction from the global distribution, namely a horizontal distribution. In this section, we will study the vertical location of the clouds, which is also important and allows to thoroughly show the cloud 3D distribution around the Earth.

As we know, many satellites provide the classification for high, middle and low clouds with the ISCCP separation criterion (seen in chapter 1), which helps to give a quick visualization and quantitative measurement of the cloud vertical distribution. In our following analysis, we do not show the cloud vertical distribution from the study of the high, middle or low cloud fraction between the two sensors but from the study of cloud cover for every vertical level. The main reason is that the differences in cloud top pressure between POLDER and MODIS have not been studied and they may bias the cloud fraction for each cloud class. In fact, different cloud top pressures have their own accuracy. For example, the oxygen pressure from POLDER has cloud photon penetration problem; the co2 slicing pressure will give a false cloud top retrieval in case of temperature inversion in the boundary layer. To avoid the uncertainties from cloud top pressure retrievals and to benefit from the coincident observations of the PM data, we plot cloud cover as function of MODIS

cloud top temperature (see Figure 3.3-8) to show the cloud vertical distribution Cloud top temperature is derived from the CO_2 pressure and the atmospheric profile excepted for low clouds where it is determined from the 11micron band, (Platnick *et al.*, 2003). In Figure 3.3-8, the cloud fractions and their differences between the two sensors as function of cloud top temperature is calculated from one year data and for four different regions over ocean and land as Figure 3.3-3. The main findings are:

- Not surprisingly, cloud fraction decreases when cloud top temperature increases. In the cold atmosphere, the cirrus, deep convective clouds and multi-layered clouds which are extended contribute to large cloud fraction while in the warm atmosphere the low broken cumulus contributes to small cloud fraction. Closer to the ground, more often appears fractional clouds.

- The cloud vertical distribution depends on region. Over ocean in the tropics and subtropics, for a temperature level around 0°C where generally appears the warm low clouds, cloud fraction shows a peak possibly because of the large occurrence of extended stratocumulus to the west coast of the continent.

- The cloud fraction differences between POLDER and MODIS-CFC (POLDER minus MODIS-CFC) do not show a quasi-constant bias of about 10% anywhere as shown in the latitudinal variations. The differences are about 10% in the warm atmosphere and tend to zero or slightly negative value in the cold atmosphere. This decrease of cloud fraction difference has been observed for all regions except at the poles. Agreed to Figure 3.3-2, it again confirms that the negative difference of ice cloud fraction is partially from cloud detection.

- In subfigure e, the cloud fraction differences (POLDER-MODIS CFC) over snow on land are found negative with important values for almost every temperature level, which means POLDER cloud fraction is much inferior to MODIS-CFC. POLDER largely misses both low and high clouds. However, over ice in ocean (see subfigure j), the differences are negative only in the warm atmosphere, namely POLDER misses only the low clouds over sea ice. This is because the penetration of the oxygen pressure makes the cloud top of the low clouds close to the ground and thus the pixel is classified as clear case.
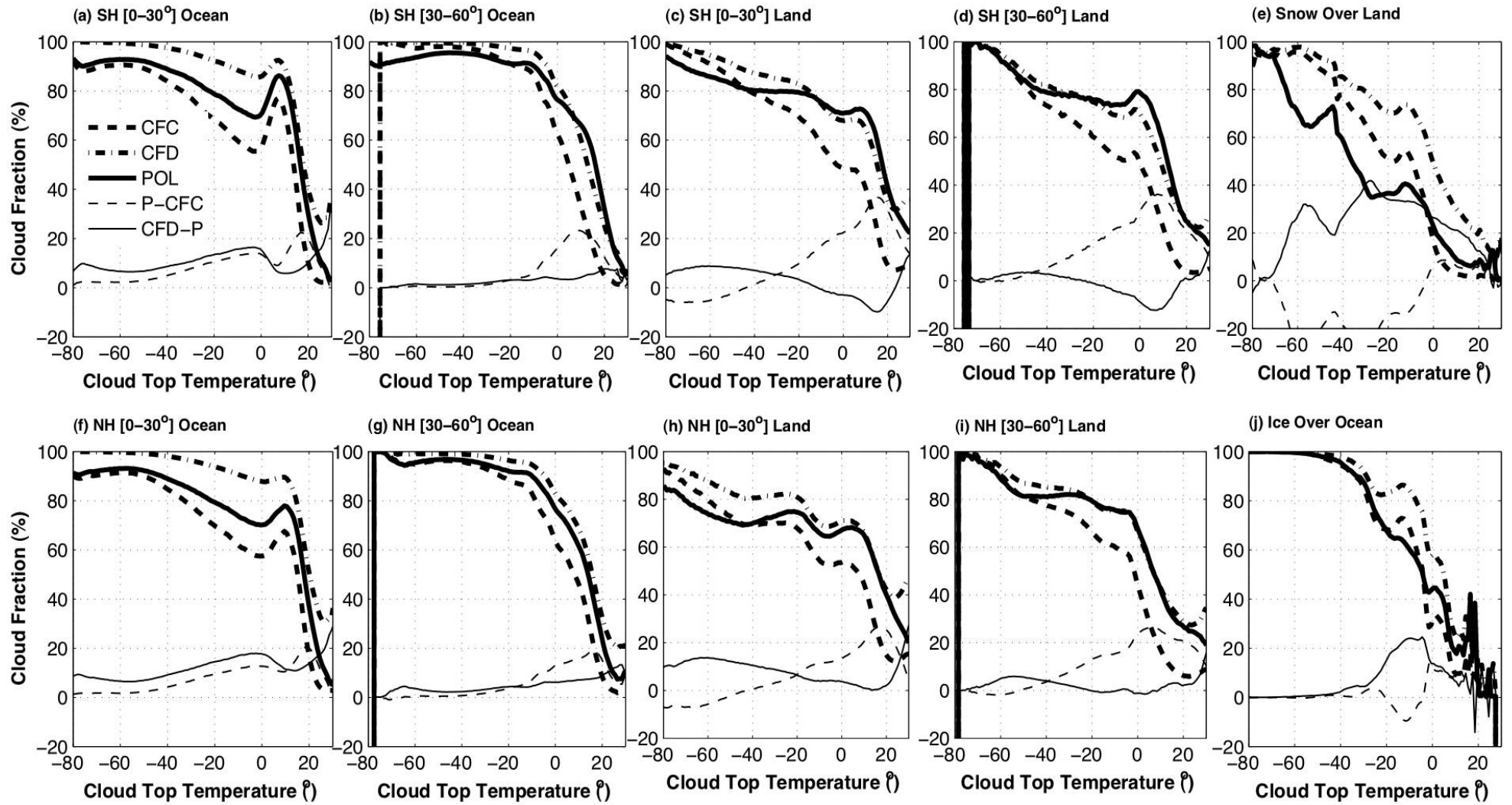
Figure 3.3-8 – *Three types of cloud Fraction as a function of cloud top temperature derived from MODIS IR band*

3.4 Discussions

From Figure 3.3-5, it is clear that both satellites are able to capture correctly the main features of global cloud cover and that observed differences are not randomly distributed. This calls for a particular attention in order to identify specific situations where cloud climatologies could present significant uncertainties related to specific cloud macrophysical/microphysical properties or environmental conditions. In section 3.3.3, we listed most noticeable differences and noted that their signs and amplitudes depend on the considered region and/or season. Reasons behind these differences are not obvious at first glance and may be due either to intrinsic instrument characteristics (resolution, spectral range) or to cloud detection algorithms. In this section, we try to explain most of the significant differences observed in order to identify and quantify uncertainties inherent to POLDER and MODIS cloud products, and from there, to point out potential biases relevant to general cloud climatologies. This exercise can also provide useful guidance to improve POLDER and MODIS cloud detection algorithms or create an optimal merged cloud fraction dataset.

3.4.1 Impact of sensor spatial resolutions

Figure 3.3-4 d, e and f, show that differences between POLDER and MODIS CFC cloud fraction are close to zero for more than 50% of the cases independently of surface type. These null differences are associated with either totally overcast or clear scenes, which appear very frequent (close to 60%) at the POLDER super-pixel scale (see Figure 3.3-4 a, b and c). In these situations, both instruments determine consistently (and presumably correctly) the cloud coverage. Not surprisingly, differences happen, mostly for partly cloudy pixels (broken clouds or cloud edges). Indeed, as presented in section 2, POLDER and MODIS have different spatial resolutions that are 1×1 km^2 for MODIS at nadir compared to 6×7 km^2 for POLDER. Differences on cloud fraction due to spatial resolution have already been observed and studied (Wielicki and Parker, 1992). Large effects are found for boundary layer clouds but differences are limited for thin cloud like cirrus. For algorithms using

threshold methods, two opposite effects control the errors. With a lower spatial resolution, on one hand, the amount of optically thin clouds will be underestimated whereas thick clouds tend to be overestimated. Indeed, the statistical threshold for a low-resolution sensor needs to be large enough to discriminate cloud-contaminated scene from clear scene accounting for the instrument noise, which leads to miss some thin clouds. On the other hand, low-resolution sensors will usually tend to classify more partly cloudy pixels into overcast situations as spatial resolution degrades, leading to an overestimation of cloud fraction. The occurrence frequency of the second situation increases as fractional clouds get thicker. According to these two opposite effects, if small clouds cover a POLDER pixel, the average reflectance may be sufficient (insufficient) for the pixel to be declared as cloudy if small clouds are (not) bright enough. In any case, the 6×7 km^2 area observed by POLDER would be declared as either overcast or clear ignoring the under-pixel cloud cover variations. On the other hand, MODIS with a smaller pixel resolution is able to distinguish clear scene among fractional clouds at scale of POLDER pixel. The statistic results show in Figure 3.3-5 that POLDER cloud fraction is generally larger than MODIS CFC over almost the whole globe. In land areas, where may exist a lot of fractional clouds over bright surfaces (e.g. Eastern and Southern Africa, Australia, South of South America), POLDER cloud fraction is about equal or even larger than CFD (negative differences) and in the mean while significant positive differences appear (>30%) between POLDER cloud fraction and MODIS CFC. This is explained by one of the two competitive effects described here-above. Fractional clouds are probably bright clouds and over bright surface that produce the larger observed differences between the high and low resolution instruments, POLDER with its lower resolution detects more clouds compared to any MODIS cloud fraction. For the fractional clouds over the subsidence tropical ocean, we see significant positive cloud cover differences between POLDER and MODIS CFC and small positive differences between MODIS CFD and POLDER. This illustrates the difference between MODIS CFC and CFD that MODIS CFD tends to classify more pixels containing even small clouds or cloud edges as cloudy while MODIS CFC cuts off a great number of them as explained in chapter 2. The statistic results also show that these systematically positive CF differences between POLDER and CFC are almost not dependent on the latitude and the season

(see Figure 3.3-1 and Figure 3.3-3). It confirms that this systematic bias (close to 10%) is not related to environmental conditions.

3.4.2 Impact of the surface types

According to the surface types, cloud detection algorithms are not all the same efficient. In this section, we analyze MODIS and POLDER cloud fraction differences in relation with the ground surface type. In Figure 3.3-4, we have noticed that histograms of cloud fraction differences are slightly different according to the type of surface: the dispersion (RMS) and mean difference are a little smaller over ocean than over land but much more important over snow covered surfaces. The cloud detection is obviously easier over ocean than over land. Indeed, over ocean, out of sun-glint regions, the dark background is an ideal surface to perform threshold tests for all satellite instruments using solar wavelengths whereas over land or in sun-glint region, the surfaces are brilliant and thus make the use of such tests much more complex. In addition, terrestrial surface reflectances are highly variable in space and time.

Over snow covered surfaces, cloud detection is even more difficult since snow surfaces are often as cold and brilliant as clouds. In Figure 3.3-4 c, we see that POLDER comparing to MODIS classifies more pixels as clear. This implies a negative mean difference with the largest dispersion values (Figure 3.3-4 f). The omission of clouds by POLDER is also observed in Figure 3.3-5 over mid-high latitude continent (northern America and northern Asia) during winter and in Greenland where negative differences appear for the whole year. Indeed, the MODIS cloud detection algorithm takes advantage of the thermal IR bands whereas POLDER, which uses mainly an apparent pressure test, detects well middle and high clouds and some thick clouds but misses many low-cloud situations. This has been again confirmed by Figure 3.3-8 e and j, large differences correspond to warmer cloud layers.

More specifically, in section 3.3.3, we pointed out the negative differences observed in the transition zones between desert and non-desert. Two reasons may explain these differences. One concerns the clear sky ground reflectance. That is, for POLDER, it is derived from a time series and analyzed by the POLDER "land surfaces" processing team (Leroy *et al.*, 1997) while the MODIS algorithm uses

statistical desert mask to mark the desert border and may falsely identify desert area that can be classified as cloudy (Roy et al., 2002). This issue has been noticed and improved in the MODIS cloud mask algorithm but during particular seasons when plants grow rapidly, it is not excluded that a statistical threshold in the desert mask may still lead MODIS to label false desert pixels. Another reason may lie on the better detection of the very thin cirrus by MODIS.

Sun-glint regions are also particular surfaces that make cloud detection a very difficult task when using solar wavelengths. Indeed, as the solar reflectance is very high in the sun-glint directions, a choice of threshold between clear and cloudy scenes is unachievable. Consequently, MODIS uses the so-called Sea-Surface Temperature (SST) test to improve the discrimination of low clouds with above-freezing cloud-top-temperatures (Ackerman et al., 1998). And moreover, a low product of the mean and standard deviation of 0.86-μm reflectances calculated over the pixel of interest and eight neighboring pixels is used to restore the clear sky from the uncertain. However, for those low clouds as warm as the sea surface, cloud detection may still be false (Frey et al., 2008). Concerning POLDER, only the apparent pressure test and the low 865nm polarized reflectance test are used in the sun-glint directions and the cloud amount is finally averaged over the direction both in and out of sun-glint that will generally minimize the possible bias due to sun glint.

To look for possible differences in cloud detection between sun-glint directions and out of sun-glint directions, we plot in Figure 3.4-1 the histograms of cloud fraction for all pixels, for pixels corresponding to MODIS sun-glint directions (0º-36º from the specular direction) and for pixels out of sun-glint. Since the two satellites are almost in line, whenever MODIS is contaminated by sun-glint, some directions of POLDER will also be. Note that to avoid geographical or seasonal biases, histograms are limited to regions between 30°N and 60°N during summer in 2008. Figure 3.4-1 b shows less overcast pixels in sun-glint directions for both sensors compared to Figure 3.4-1 c out of sun-glint directions. However again, this appears to be a geographical effect. As A-train satellites cross the equator at around 1:30 p.m. local time, sun-glint regions always correspond to smaller viewing angles compared to out of sun-glint angles. According to Figure 3.3-6, that leads to larger cloud fraction outside of sun-glint due to view angle dependence of cloud detection. Another noticeable difference between Figure 3.4-1 b and c is the smaller difference

in quasi-clear pixels detection between the two sensors compared to out of sun-glint directions. The reason for this is not obvious but cloud fraction of POLDER being averaged over all the 16 directions, even if more pixels are falsely classified as clear in sun-glint directions, in average with other directions or by reclassification, the error will be minimized and the cloud fraction will always be greater than zero. However, in sun-glint directions, MODIS uses the SST test and the spatial deviation test from 0.86-µm reflectances, which can falsely classify certain sun-glint as cloudy and then lead MODIS to find less clear pixels compared to out of sun-glint directions. This tends to reduce, in sun-glint directions, the difference between the numbers of clear pixels observed by POLDER and MODIS. Nevertheless, overall, no really significant differences are observed between the three histograms. This is confirmed by Figure 3.3-6 where no unusual angular variations of cloud fraction corresponding to sun-glint directions (observed in forward direction around the solar angle value) can be detected except maybe for small solar angles (between 15°-20°).

In addition during the present study, we identify a default in the POLDER cloud detection scheme. In some specific area, the POLDER algorithm detects fractional cloud cover where the scene is clearly overcast. This comes from a threshold problem in the glitter direction. As explained here-above, in this particular direction, cloud detection is mainly based on the comparison of the apparent pressure with the ground pressure. Consequently, in regions of low clouds with an apparent pressure too close to the surface pressure, the algorithm classifies the pixel as clear in the sun-glint directions and as cloudy in the other directions. The average over all directions results thus in a fractional cloud cover. This issue happens mostly in northern Pacific Ocean around (50°N, 180°E (W)), during spring and summer when very low clouds appear.
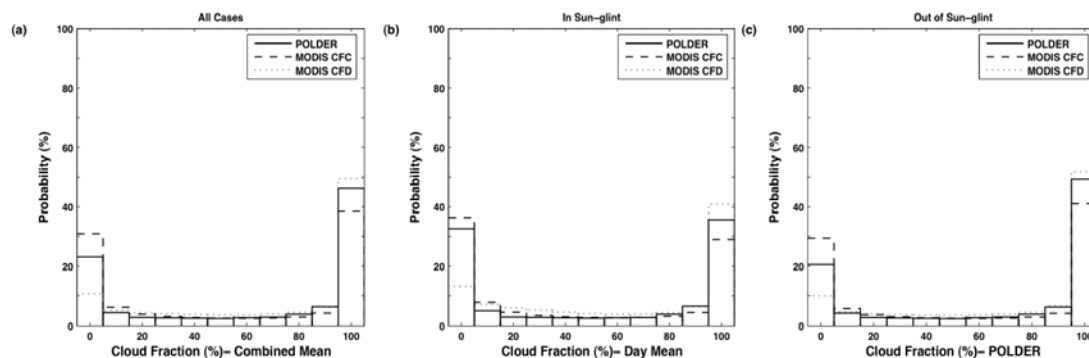
Figure 3.4-1 – *Histograms of the POLDER and MODIS cloud fractions for overall pixels (a), for pixels in MODIS sun-glint directions (b) and for pixels out of sun-glint regions (c). Histograms are for data between 30°N and 60°N during summer 2008.*

3.4.3 Impact of aerosols

Inversions of aerosols and clouds are inextricably connected and neglecting any one of them will lead to an inversion error. Certain simple tests taking advantage of IR and NIR channel information may be constructed by MODIS to indicate a presence of aerosol contamination such as heavy dust around Africa (Ackerman, 1997) and biomass burning/smoke over dark vegetated surface (Kaufman *et al.*, 2003). Without additional information from these IR and NIR channels POLDER probably classifies, in some directions, the heavy aerosol particles like biomass burning ones as clouds. This causes therefore an important positive difference in cloud fraction between POLDER and MODIS. It clearly appears in Figure 3.3-5 where large positive differences are found in the center of Africa during summer. These large positive differences coincide well with the high accumulation rates of fires detected by MODIS and available from the NASA rapid response web site (see Figure 3.4-2, a). They also correspond to a bad cloud detection quality index for POLDER (see Figure 3.4-2, b), which means that either the first part of the POLDER cloud detection scheme leaves the pixels undetermined or/and POLDER does not detect the same cloud fraction according to the direction. In these regions, the POLDER "Aerosols" processing line (Deuzé *et al.*, 2001) finds a large value of optical thickness for fine mode aerosol (see Figure 3.4-2, c). Moreover, as these aerosols are often non-spherical they are classified as ice clouds by POLDER (Goloub et al., 2000).

Consequently, large positive differences for total cloud as well as for ice cloud cover are associated to the presence of these aerosols as illustrated in Figure 3.3-5.
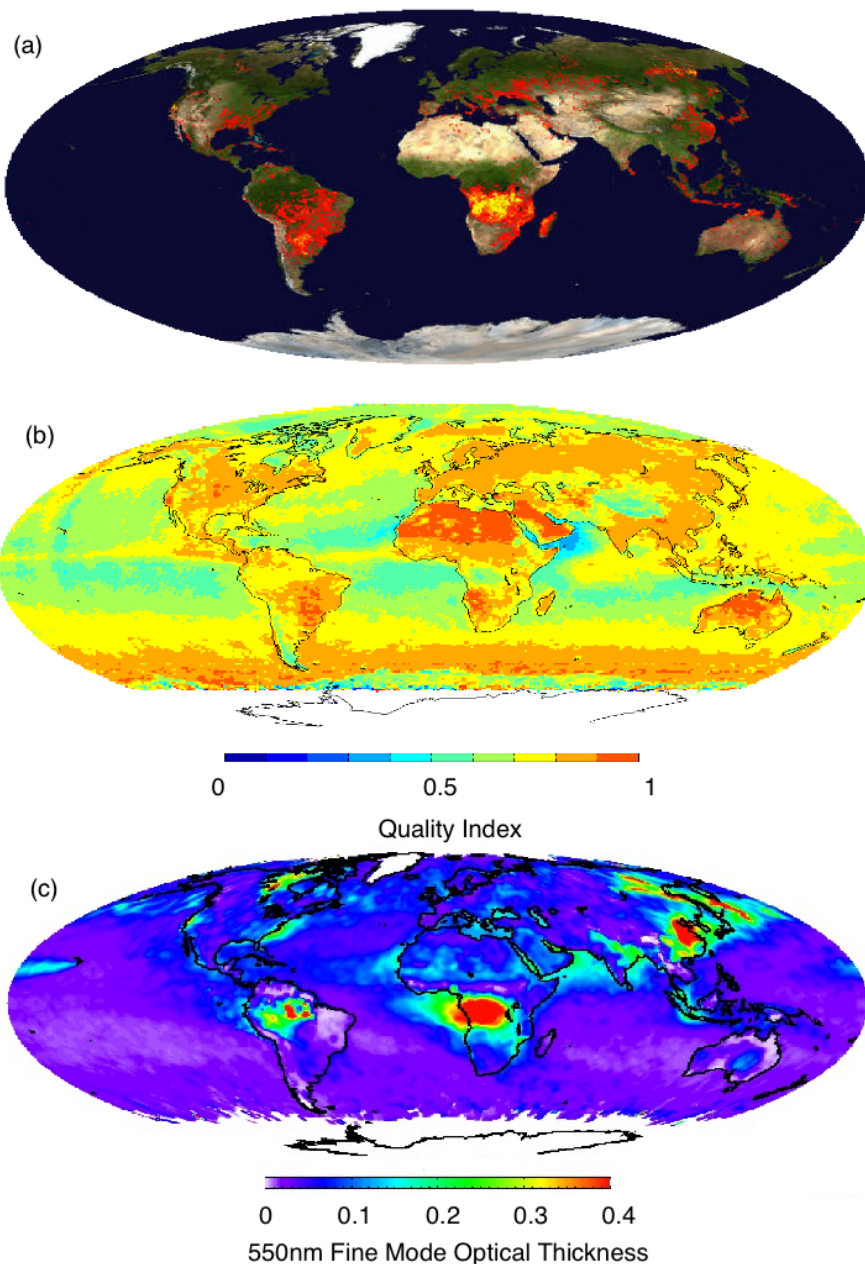
Figure 3.4-2 – *Geographical distribution of the active fires detected by MODIS for a period (09/07/2008-18/07/2008) in summer 2008 from NASA rapid response website (a), POLDER Quality index of cloud detection (b) and POLDER fine mode aerosol optical thickness (c) during summer 2008.*

3.4.4 Impact of cirrus

Cirrus detection is another complex situation in satellite remote sensing domain as cirrus may be optically very thin. MODIS developed its own method to identify very thin cirrus by using the 1.38μm channel (Gao *et al.*, 1993) and brightness temperature differences tests in split-window channels (Inoue, 1987). POLDER polarized radiance is also sensitive to cirrus but limited to the very thin cirrus. Again, as lack of additional NIR and IR information together with a larger resolution, POLDER has poor skill to cirrus detection. It is however worthy to note that some cirrus clouds are observed with oblique directions among the total of 16. Indeed, taking advantage of the oblique and extended path through the clouds may be also favorable to cirrus detection. Statistical results in Figure 3.3-5 show negative differences for ice cloud cover almost over the whole globe outside of aerosol regions. Negative values are even notable in the following regions: Indian monsoon area, Indonesia, west-central Pacific Ocean warm pool, equatorial central South America as well as mid-high latitude STs belts where active deep convection seems to generate many of cirrus (Wylie *et al.*, 1994; Sassen *et al.*, 2008). So, for one part, these negative ice cloud fraction differences between POLDER and MODIS may be due to POLDER cloud detection/mask limitations (see also Figure 3.3-8) for thin cirrus. For another part, they can be due to the sensitivity of thermodynamic phase determination to the very thin cirrus overlapping liquid clouds. Further studies need to be performed with the help of information from active sensors like the Cloud-Aerosol Lidar with Orthogonal Polarization (CALIOP) on CALIPSO platform. Preliminary results are presented in the next section.

3.5 The study of cloud cover with CALIOP

In the following, we will use the active sensor CALIOP to study the cloud detection and cloud cover, especially to quantify the missing cirrus from the two passive sensors. In Figure 3.5-1, we first use CALIOP to select 4 types of scene: all cloudy scenes, all single layered cirrus scenes, single layered cirrus over land and

over ocean. Then we calculate the occurrence frequencies of the POLDER/MODIS combined scene for each selected scene from CALIOP. Note, for the following study, we compare POLDER with MODIS CFD because MODIS CFC is not recorded in the CALTRACK data. From subfigure a, we see for all cloudy scenes determined from CALIOP, that about 86% of pixels are labeled as cloudy by both POLDER and MODIS CFD, which means the agreement between the three sensors is satisfactory. Only about 5% of the pixels are labeled as clear by both sensors, which suggest in these 5% cases, that the two sensors miss clouds. For the rest 8% of the pixels, only POLDER or MODIS misses clouds. Concerning the single layered cirrus (subfigures b, c and d), we find the agreement on cloudy scene between the passive and active sensors decreased to about 55% (subfigure b), even worse over land (48%, subfigure d) compared to over ocean (64%, subfigure c). POLDER and MODIS miss thin cirrus for about 22% of the cases (subfigure b). Cirrus detection over land is more difficult for both passive sensors. We also notice, although MODIS with IR channel should theoretically detect more cirrus than POLDER, it actually detects less cirrus over land. The possible reason is that POLDER pixel covers a lager FOV compared to MODIS and CALIOP pixels and thus could contain more clouds from the regions out of MODIS pixel. If the pixel size is exactly the same, POLDER may detect less cirrus than MODIS.
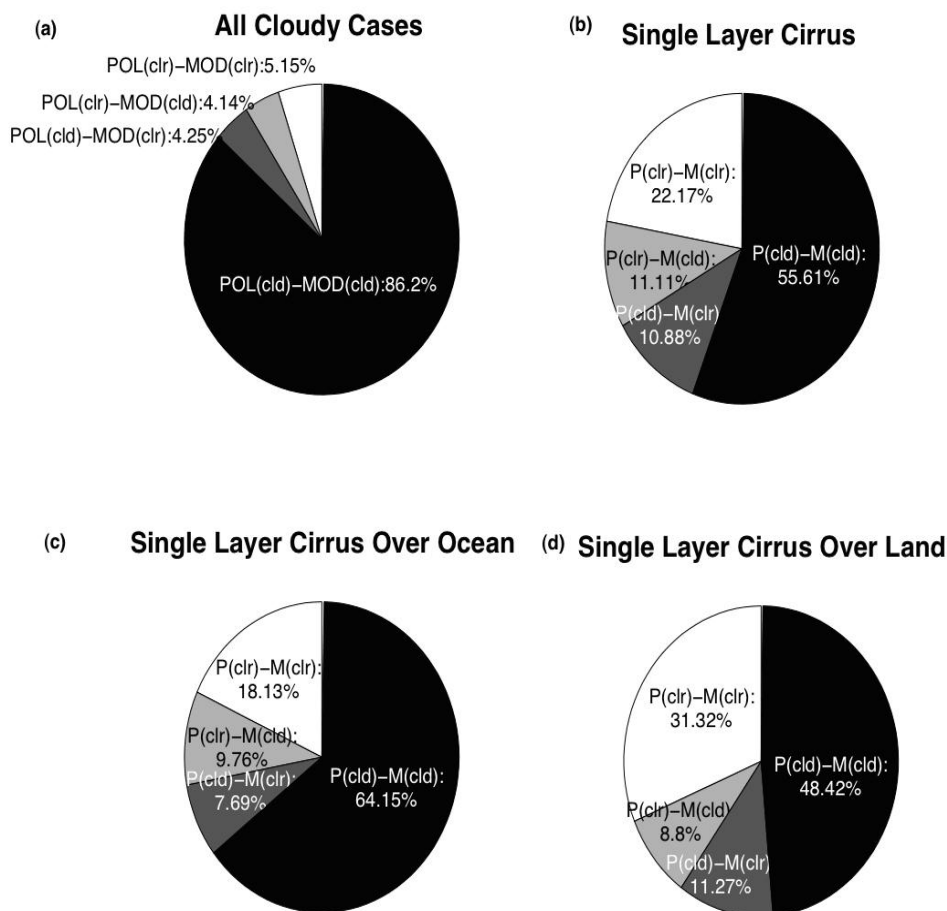
Figure 3.5-1 – *Occurrence frequencies for different POLDER–MODIS combined scenes for cloudy scenes (a), for single layered cirrus scenes (b), for single layered cirrus scenes over ocean (c) and over land (d) determined by CALIOP.*

In Figure 3.5-2, we continue to show the missing frequencies of the single layered cirrus as function of cirrus optical thickness of the uppermost layer (derived from CALIOP) for the two passive sensors. From subfigure c, we see that about 60% of the cirrus are missed by POLDER and MODIS (CFD) when their optical thickness is close to 0. As the optical thickness increases, the two sensors detect more cirrus. For an optical thickness more than 0.6, about 100% of the cirrus can be detected by the two passive sensors. We also notice that the cirrus missing frequencies are different over land and over ocean, for POLDER and for MODIS. Over ocean, when the optical thickness is greater than 0.3 for MODIS and 0.4 for POLDER, almost no cirrus is missed. Compared to ocean, over land thicker optical thickness is needed for cirrus to be 100% detected (MODIS: 0.6 and POLDER: 0.6). So we conclude that the cirrus detection over ocean is much better than over land. In addition, we see that

MODIS can detect thinner cirrus than POLDER, especially over ocean. Notice also that CALIOP optical thickness seems to be slightly underestimated (Lamquin *et al.*, 2009)
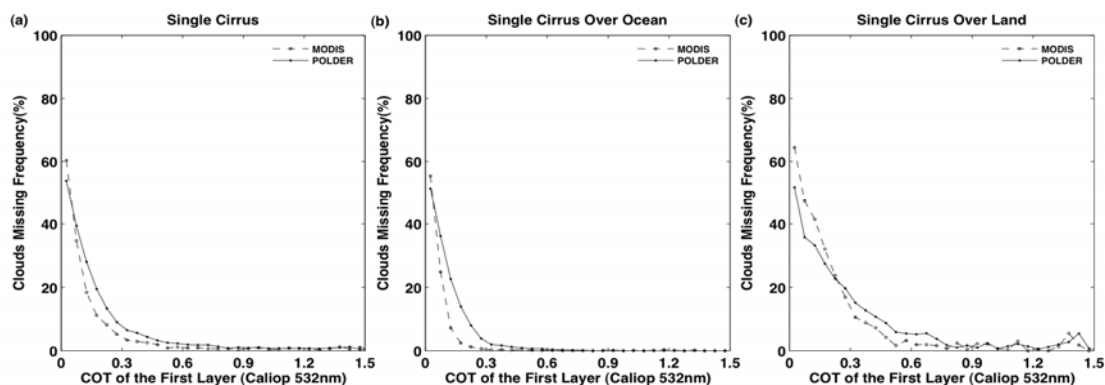
Figure 3.5-2 – *Missing frequencies of the single layered cirrus as function of cirrus optical thickness of the uppermost layer derived from CALIOP for all regions (a), for ocean regions (b) and for land regions (c).*

POLDER can detect thin cirrus possibly thanks to the multi-directional observations. It is easier for POLDER to see them in the more oblique directions because of the longer radiative path through them. In this case, the final cloud fraction by computing nadir and oblique directions is thus fractional. To see the cirrus impact on cloud fraction, we plot in Figure 3.5-3 the cloud fraction histograms for both POLDER and MODIS CFD and for the four CALIOP scenes shown in Figure 3.5-1. In the four cloudy scenes detected by CALIOP, both POLDER and MODIS detect some clear scenes, which again means to miss clouds. The cloud cover histograms are different for the two sensors. Compared to the all cloudy scenes (subfigure a), in case of single layer cirrus (subfigure b), POLDER (MODIS) finds about 5% (3%) more broken scenes and 35% (30%) less overcast scenes. Compared to the scenes of single cirrus over ocean (subfigure c), there are about 4% (0%) less broken scenes and 7% (17%) less overcast scenes to be found by POLDER (MODIS) over land (subfigure d).
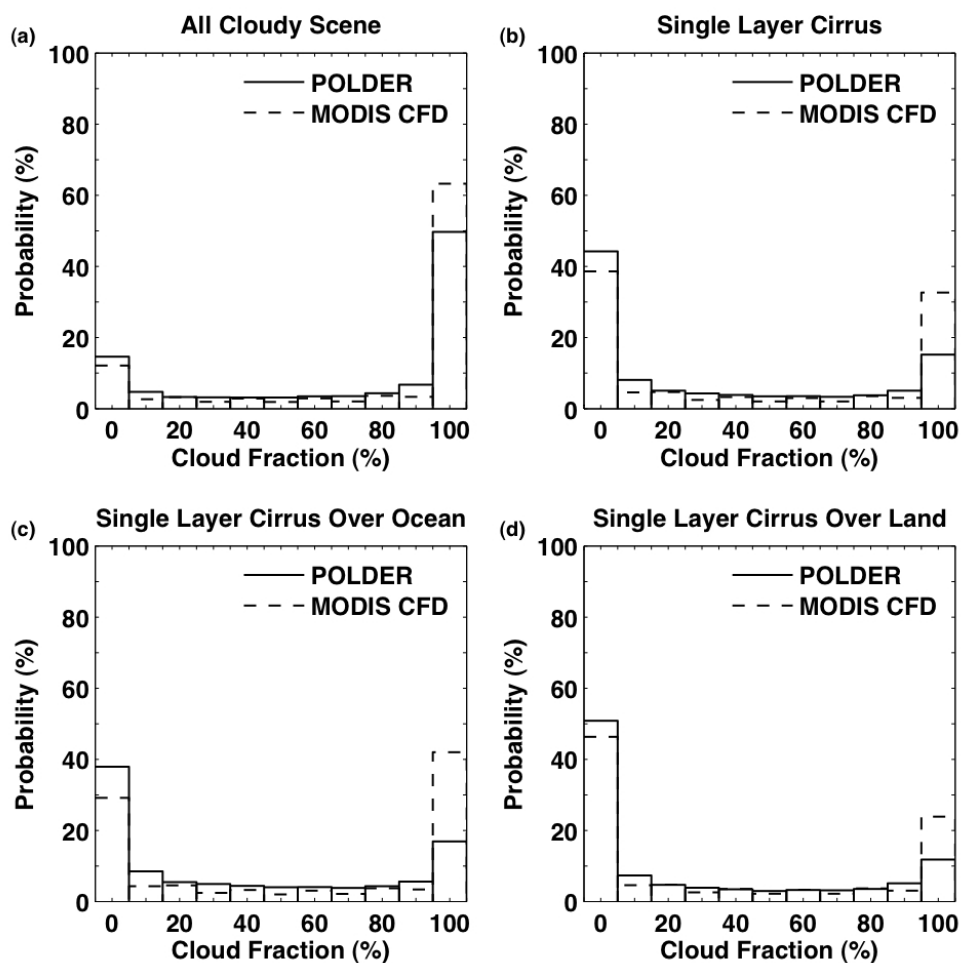
Figure 3.5-3 – *Histograms of the cloud fractions derived from POLDER and MODIS CFD for different CALIOP scenes: cloudy scenes (a), single layered cirrus scenes (b), single layered cirrus scenes over ocean (c) and single layered cirrus scenes over land (d).*

3.6 Conclusions

Cloud cover is an important cloud parameter, first because all the other retrieved cloud parameters result on it and secondly because it can be used for climate applications. In this chapter, we compare cloud fractions obtained from the two passive sensors, POLDER/PARASOL and MODIS/AQUA. Each of these sensors has its own particularities. MODIS is a multispectral radiometer with 36 channels ranging from visible to infrared wavelengths whereas POLDER measures multidirectional

total and polarized radiances in the solar range. To simplify and to handle correctly the comparisons, we use the PM Dataset. The advantage of this dataset lies in the coincident POLDER/MODIS observations over a common swath and at a scale of the POLDER super-pixel (20×20 km^2).

Although these different instruments have different characteristics and different spatial resolutions, we really observed an interesting consistency in cloud detection. We have shown that the spatial distributions as well as the seasonal variations of the cloud cover retrieved by the two sensors have similar behaviors. We noticed however a quasi-constant bias between POLDER and MODIS CFC (Cloud Fraction Combined) products being about 10% with POLDER detecting more confident clouds than MODIS and about -10% between POLDER and MODIS CFD (Cloud Fraction Day) products with POLDER detecting more confident clear sky. The confident cloud fraction differences between the two sensors (POLDER minus MODIS CFC) may come from the sensor resolution differences. In addition to this constant bias, we also focused on specific areas showing important positive or negative differences associated to typical cloud detection difficulties. For example, due to a lower resolution, POLDER badly detects very small clouds and classifies it as overcast cloud cover. Over snow, both sensors have difficulties in cloud detection and particularly POLDER, which underestimates cloud fraction mostly at low level because of the lack of efficient information in the visible bands. We also note important differences over the transition regions between desert and non-desert, which may be due to a better cirrus detection or a false desert detection in the MODIS algorithm. In sun-glint, besides the threshold problem of POLDER in northern Pacific during summer, which needs to be improved, POLDER with its multi-directional observations minimizes the sun-glint detection errors by averaging both in and out of sun-glint directions. We also report that, POLDER confuses heavy aerosols and clouds in some directions. Besides, POLDER misses some ice clouds because it has a bad skill to detect very thin cirrus with a lower resolution and a narrow range of detecting bands and also a bad skill to identify cloud water and ice phases with a presence of water clouds overlapped by cirrus.

With the advantage of detecting cirrus from CALIOP, we also see at the end of the chapter, the two sensors indeed miss thin cirrus, especially over land.

In summary, this work allows to exhibit a geographical localization of some problems in the cloud detection/mask algorithms and demonstrates that still some improvements can be done for both instruments in the future. Typically, concerning POLDER, the algorithm over snow surface and in the sun-glint directions needs to be improved to identify low clouds. And also discussions need to be done for POLDER to correctly identify very thin cirrus and to eliminate heavy aerosol panache. The MODIS algorithm shows also some uncertainties for example, in the transition region between desert and non-desert and also very thin cirrus over land as suggested by a comparison with the CALIOP cloud product. Further comparisons on different types of cloud are also of great interest in further studies to gain a better comprehension of limitations and advantages of each cloud detection/mask algorithm and specifically for a certain types of cloud.

Finally, this study of cloud cover provides the basis for further comparison studies of cloud thermodynamic phase and cloud optical properties from the two passive sensors in the following chapters.

Chapter 4

Thermodynamic Phase

4.1 Introduction

Cloud thermodynamic phase is an important parameter for studies of cloud microphysical and radiative properties and their effect on climate. The determination of cloud thermodynamic phase, in other words, the classification of cloud particles as being composed of liquid water, ice or a mixture of the two, is a critical first step in the process of inferring cloud optical and microphysical properties from satellite measurements. As seen in chapter 2, the derivation of cloud optical thickness, particle size and water content requires this parameter to be first determined because the absorption and scattering behaviors for ice crystals greatly differ from those of water droplets. The inversion quality of the optical properties that depends on the ability to match the precomputed using radiative transfer with the actual measurements is thus of poor value if we employed an erroneous phase assumption.

Many efforts have been recently made to automatically discriminate and to reasonably describe the cloud thermodynamic phase from satellite measurements. Great progresses have been made as a result of using various distinct techniques that are applied to the onboard-satellite instruments (Pilewskie and Twomey, 1987; Baum *et al.*, 2000; Goloub et al., 2000; Hu *et al.*, 2009; Riedi *et al.*, 2010). Many further studies have gone deeper into coupled studies of satellite observations and cloud physical-dynamic model prediction that may go further to study their relations with the complex atmosphere and environment (Doutriaux-Boucher and Quaas, 2004). In general, the distinction between ice and water clouds relies on three main categories of information.

1) The temperature. According to ice nucleation theory, it is hard for the supercooled droplets to remain in metastable state when the ambient temperature decreases to -40°C, and also ice crystals are no longer existing above the melting temperature (Pruppacher and Klett, 1997). So, the temperature is an important and efficient flag to discriminate the ice and water in clouds. The colder (warmer) clouds are assumed to be preferentially composed of ice crystals (liquid droplets).

2) The particle sizes and shapes. Typical water droplets are considered to have spherical shape and relatively small effective radius (ranging from 0.5 to 50μm and typically r_{eff} < 30 μm) (Hansen, 1971; Paltridge, 1974; Stephens *et al.*, 1978) while non-spherical particles (with extremely variable shapes: e.g. bullet rosettes, solid and hollow columns, plates, aggregates...) with relatively large effective radius (with extremely variable sizes: ranging from a few microns to 1000 μm and typically r_{eff} >30μm) characterize the ice crystals (Fu, 1996; Lawson *et al.*, 1998).

3) The spectral index of refraction. The indexes of refraction that characterize the scattering (real part) and absorption (imaginary part) capacity differ significantly between ice and liquid water at certain wavelengths. This nature of distinct radiative behaviors between ice and liquid water particles according to the wavelength is helpful for cloud phase retrieval and is widely used by satellite instruments. But measuring and analyzing the scattered and absorbed radiation from clouds lead to a determination of thermodynamic phase at the cloud top.

A technique combining all or some of the above discussed criteria is what current satellites can use to further improve cloud phase inversion.

Radiative (e.g. absorption, emission, scattering, and polarization) analysis of cloud phase has been widely accepted and demonstrated to be effective. The most widely known techniques include: (1) Visible/Near Infrared band ratio method (Pilewskie and Twomey, 1987). (2) Bi-spectral IR method (Baum *et al.*, 2000; Strabala *et al.*, 1994). These two methods (methods 1 and 2) are both based on the spectral differences of absorption between water droplets and ice crystals and are both employed by the MODIS operational algorithm (King *et al.*, 1997; Menzel *et al.*, 2006; Platnick *et al.*, 2003). (3) Angular polarization method. This method employed by the POLDER algorithm (Goloub et al., 2000) is based on the angular dependence of polarization at 865nm on scattering particle shape. Spherical water droplets and non-spherical ice crystals have different angular polarization features. (4)

Depolarization of backscattered light for active sensors (lidars). This method is employed by CALIOP (Hu *et al.*, 2009). The later two methods (methods 3 and 4) both use the polarization information and are based on what we refer as a shape determination technique. (5) Other auxiliary information from the cloud top. Like the four distinctions referred above, cloud top temperature (or vertical location) could also help to indicate the cloud top phase (e.g. cloud top temperature<-40°C suggests ice clouds) even though it is not so much useful in the supercooled temperature range where both liquid and ice can coexist. For satellites, cloud top temperature can be determined either from infrared emission (e.g. Brightness temperature at 11μm for MODIS low clouds) or from the couple information of cloud top pressure/altitude and the atmospheric profile (e.g. cloud top temperature derived from CALIOP and MODIS). In fact, no single method among those mentioned above can be considered as preferable to predict correct cloud phase for all cloud types and all ambient conditions. For example, the conditions such as for cloud top temperature between 240K and 273K where supercooled droplets or mixed phase can predominate, in multilayer or broken cloud systems, over snow/ice covered or temperature inversion regions, will make it difficult for some of these techniques to determine the cloud phase (Spangenberg *et al.*, 2005; Wolters *et al.*, 2008). In order to obtain more accurate information about cloud thermodynamic phase even in many of these complex and problematical conditions, the combination of more distinct and independent algorithm techniques is highly desirable as it helps to gather more useful information, benefit from their strengths and avoid their weaknesses. Taking MODIS as an example, the final cloud phase product (Cloud_Phase_Optical_Properties) is a result of 3 combined techniques (methods 1, 2, 5) with additional cloud mask information. After discriminating from each technique, a logical decision tree is required to connect different individual techniques and the final decision undergoes some "sanity check" to create a reasonable combined cloud phase (King *et al.*, 2004). This calls for a better understanding of the advantages and weaknesses of each retrieval technique. The A-Train satellites give us an unprecedented opportunity to study and compare several phase retrieval techniques. This is certainly helpful for our progressive understanding of cloud phase and the associated retrieval techniques and also helpful for the creation of a highly confident combined phase dataset that could be later use to benchmark cloud phase representation in models.

Recent comparisons of cloud phase especially with A-Train observations (POLDER, MODIS) mainly focused on individual case studies or radiative transfer simulations (Riedi *et al.*, 2007; Chylek *et al.*, 2006). From the inter-comparisons of phase among various sensors and techniques in an individual case, it has already been shown interesting information. In our work, we go further by providing a global assessment of cloud phase, using both passive and active sensors in the A-Train constellation. This statistic assessment could exhibit more representatively the potential issues and virtues in each algorithm compared to a particular case study. It can also help us to improve the phase inversion and to create a much needed high confidence cloud thermodynamic phase dataset.

Beside the radiative studies of cloud phase from satellites, the microphysical studies from cloud models show that cloud thermodynamic phase strongly depends on the local thermodynamic conditions (e.g. supercooling, supersatuation…) and the presence of impurities within the atmosphere (Pruppacher and Klett, 1997). The occurrence of ice crystals in nature is either directly from water vapor sublimation or through the condensation from vapor to liquid water and subsequent freezing from liquid water to ice crystals. The final crystal shape, size and concentration have therefore a tight relation with the cloud dynamics such as the atmospheric temperature and humidity (Miloshevich and Heymsfield, 1997). There are two ice nucleation mechanisms in the atmosphere, that are homogeneous and heterogeneous ice nucleation. Cirrus clouds can be formed by both homogeneous or heterogeneous ice nucleation mechanisms in the uppermost troposphere (temperature below 235K or 237K), studies show that they are generated predominately by homogeneous freezing of aqueous solution droplets (Heymsfield *et al.*, 2005; Kärcher and Lohmann, 2003). As reported, the homogeneous freezing of supercooled water droplets could take place at around -40°C with the precise value depending on temperature, droplet volume, carrier gas, ions state, and water activity within the liquid (Pruppacher and Klett, 1997). The impurities in cloud droplets could decrease the homogeneous freezing rate and permit them to exist for a longer time in liquid phase and at a colder temperature (Curran and Wu, 1982). For heterogeneous nucleation, the freezing saturation thresholds depend primarily on the ice nuclei size, composition, and molecular structure as well as particles history (Abbatt *et al.*, 2006). At atmospherically relevant conditions homogeneous and heterogeneous nucleation in clouds may exist at the same time; however a single mechanism dominates the freezing process. Modeling

studies suggest that homogeneous nucleation dominates in regions with updrafts stronger than 20cm s^{-1}, with the exception of heavy polluted areas which could be common in the northern hemisphere due to air traffic, where updrafts of the order 1m s^{-1} may be necessary to render heterogeneous nucleation unimportant (Gierens, 2003). Whether homogeneous or heterogeneous mechanism dominates calls for more careful studies of both ice nucleation processes and the competition between them. Recent efforts have been devoted to establish a critical concentration of heterogeneous ice nuclei as a function of temperature, updraft speed, ambient pressure and freezing supersaturation to efficiently define and describe this competition in cloud models (Barahona and Nenes, 2008). In short, as a result of the complexity of atmosphere and inadequate knowledge about ice nucleation, further studies on discussion about cloud thermodynamic phase that relates to the ice nucleation and the local dynamics are still needed, especially with the global scale and long-term observations from satellites. This study allows to confirm and support the cloud models and the ice nucleation theory behind those.

In this chapter, we first introduce each of the retrieval methods employed by POLDER, MODIS and CALIOP, compare their strengths and weaknesses. In the second section, the global assessments and comparisons of cloud phase are performed between passive sensors in order to locate the regions of consistent or inconsistent combined phases, and also point out the conditions when the potential problematical phase determinations are more likely to occur. A subsequent validation of cloud phase between the passive and active sensors is made separately for opaque and transparent clouds. The validation helps to better understand the different cloud phases derived from passive sensors especially in case of disagreement. With the confident combined phase cases identified above, studies are then performed on vertical ice-liquid transition. This vertical transition associated with ice nucleation indeed requires for a careful study with respect to the large-scale dynamics and cloud microphysical properties.

4.2 Theoretical Basis for Phase Determination

4.2.1 Physical Basis and Processing Description for POLDER

POLDER uses the angular characteristics of polarized reflectance at 865nm (where the molecule contribution is small) to discriminate the cloud phases (Goloub et al., 2000). This method is based on the strong dependence of polarized scattering behaviors on particle shape and size (r_{eff}) and therefore can be classified as a shape detection method. Unlike the total radiation and polarization degree, the polarized reflectance, L_p does not depend on the cloud optical thickness (τ_c) since it is saturated for τ_c greater than 2-3 depending on the cloud microphysics (the particle shape and r_{eff}) (Goloub *et al.*, 1994; Riedi, 2001 (Ph.D. Thesis)). Looking from satellites at a cloudy system, the polarized light is primarily formed in the upper cloud layer and less sensitive to multiple scattering effects. Its feature mainly corresponds to single scattering (about 80% of the single-scattered radiation reflected from the cloud layer arises from the first unity of optical depth). According to the single scattering approximation, the angular polarization depends therefore on the polarized phase function that is determined by the shape, size distribution and refractive index of the cloud particle. The simulations that suppose the liquid clouds are typically composed of spherical particles and ice clouds are composed of non-spherical particles show quite different polarized features for ice and liquid clouds (see Figure 4.2-1):

- Polarization in range 2 (the rainbow region for scattering angle around 140° with the exact position depending on r_{eff} and σ_{eff}) is 20 times greater for liquid clouds than for ice clouds (the polarization intensity increases slightly with r_{eff})

- In range 1, ice clouds have positive polarization with negative slope and liquid clouds have negative polarization for scattering angles less than about 90° and this polarization increases to positive with scattering angle.

- The neutral point (zero of polarization) exists for liquid clouds between 75° to 130° with its position depending on r_{eff}.

- Outside the range 1 and 2, the neutral point of ice clouds appears around 160° while the polarization for liquid clouds shows large dispersion because of "supernumerary bows" of spherical particles.

- Glory occurs around 180° for liquid clouds.
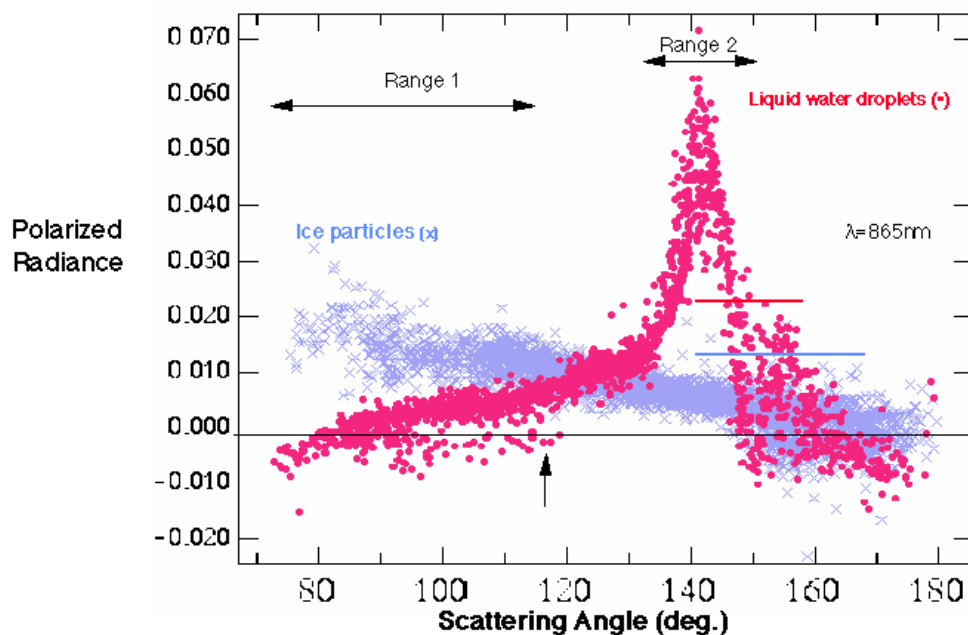
Figure 4.2-1 – *Angular Characteristics of Polarized radiance for both liquid (red) and ice clouds (blue) from Goloub (1997).*

In the operational processing, cloud phase is retrieved in super-pixel (3×3 pixels) using observations outside of sun-glint directions. POLDER phase flowchart is summarized in Figure 4.2-2 (Riedi, 2001). Four tests are included in its algorithm: (1) The existence of strong polarization in rainbow directions. (2) The slope sign of linear fit of P_p^{865} for Θ_{diff} <120°. (3) The existence of neutral point between 75°-130°. (4) The dispersion of linear fit of P_p^{865} for Θ_{diff} >140°. If none of four tests above is available, a supplementary test from the apparent pressure/Rayleigh pressure will control the final decision.
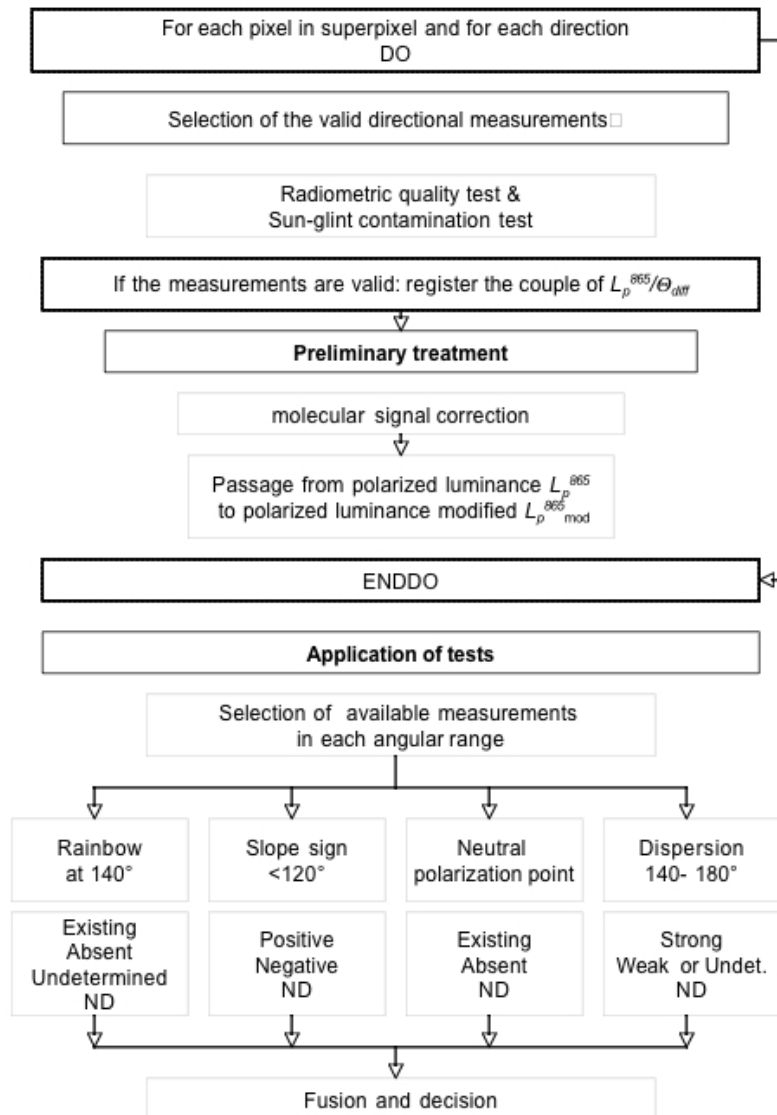
Figure 4.2-2 – *Flowchart of POLDER phase algorithm from Riedi (2001).*

4.2.2 Physical Basis and Processing Description for MODIS

As MODIS performs multiple spectral measurements, its phase retrieval takes advantages of this information. In its algorithm, three simple retrieval techniques (1. Visible/Near Infrared ratio method, 2. Bi-spectral Infrared method, 3. Cloud top

temperature method) are employed and two cloud phase products (Cloud_Phase_Optical_Properties (MODIS phase) and Cloud_Phase_Infrared (MODIS IR phase)) are produced. Two of the retrieval methods (method 1 and 2) rely on the basis that the absorption for ice and liquid clouds at one band is approximately equal but diverges at another band. The difference of the two methods relies on the selection of different couple of bands: one combines a visible and a near infrared band, another combines two thermal infrared bands. In fact, the selection of band is not random and requires to avoid the vapor absorption (to ensure that absorption occurred only or mostly in the clouds). In the following, we provide an introduction of each simple method contributing to MODIS phase retrieval.

a) Visible/Near Infrared ratio method (SWIR/VIS)

The physical principle of the SWIR/VIS method (short wave near infrared/visible) is based on different absorption features for liquid droplets and ice crystals in the solar band at $0.645\mu m$ and in shortwave infrared band at 2.13 μm or 1.64 μm (Curran and Wu, 1982; King *et al.*, 1997; Pilewskie and Twomey, 1987). In the visible band, the imaginary part of refractive index that dominates the absorption ability can be neglected for both liquid and ice water, but in near infrared bands, the imaginary part becomes non-negligible for both phases and is greater for ice than for liquid water for the two MODIS bands considered (see Figure 4.2-3). The absorption appears thus more marked after radiation has traveled through an ice cloud if all other microphysical properties in clouds (e.g. particle size, shape and density) are kept the same. With the experimental values (referred as thresholds) of reflectance ratio (1.64/0.654 or 2.13/0.654), we can successfully separate ice from water clouds, ice clouds usually exhibiting q significantly lower SWIR/VIS ratio compared to liquid clouds.
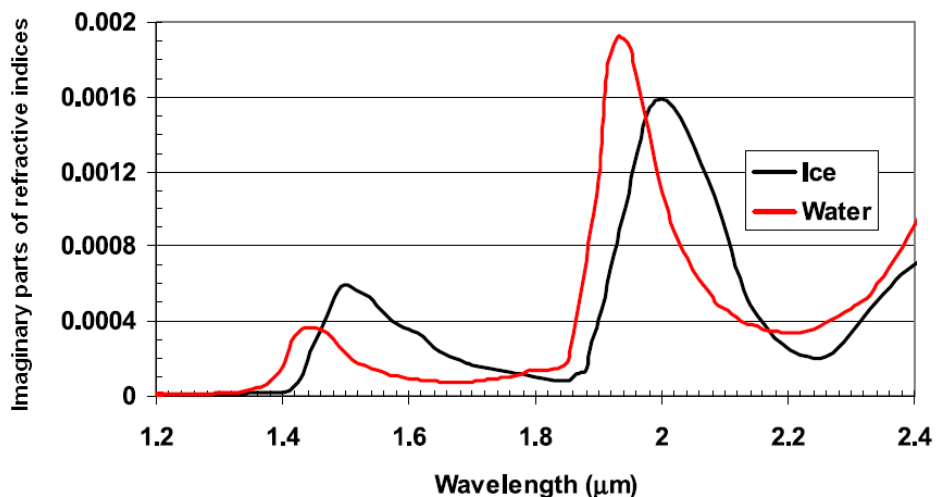
Figure 4.2-3 – *Imaginary parts of index of refraction for water and ice between 1,2 and 2.4 μm from Chylek et al. (2006).*

b) Bi-spectral Infrared method

The principle of the bi-spectral infrared method is also based on different spectral absorption for liquid droplets and ice crystals but in two infrared (IR) bands at 8.5μm and 11μm (Baum *et al.*, 2000; Menzel *et al.*, 2006). The imaginary parts of the refractive index at 8.5μm are approximately equal to each other for both liquid and ice but diverge significantly at around 11μm (see Figure 4.2-4) with ice having greater absorption. This IR bi-spectral method always combines with a cloud top brightness temperature from 11 μm to separate ice and liquid phases for clouds.
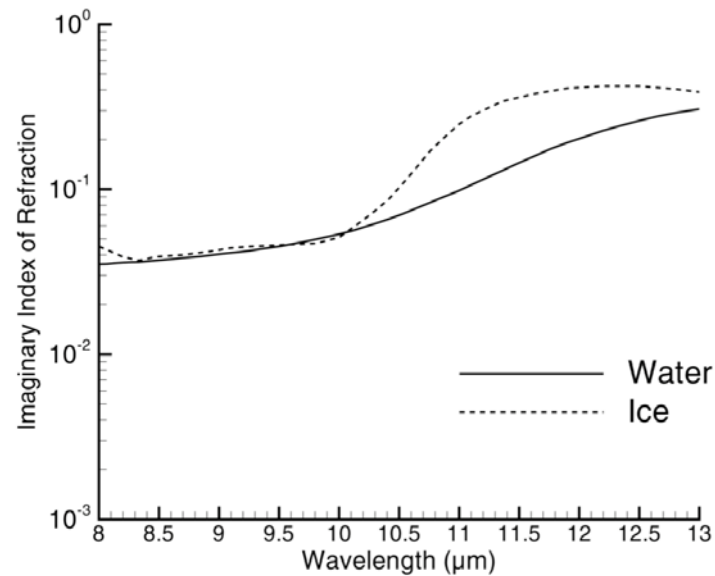
Figure **4.2-4** – *Imaginary parts of index of refraction for water and ice between 8 and 13 μm from Baum et al. (2000).*

Radiative transfer simulations for the two considered IR channels show different brightness temperature features for ice and liquid clouds (see Figure 4.2-5):

- The ice clouds exhibit positive BTD (Brightness Temperature Difference [$BT_{8.5}$-BT_{11}]) if clouds with COT > 0.5
- The water clouds of relative high optical thickness exhibit negative BTD with its value below -2K
- The water vapor could bias the BTD, because the BTD is also sensitive to the absorption of water vapor in the atmosphere. For those low clouds having an increasing loading current of water vapor absorption and larger particle sizes, the BTD becomes more negative.
- The clear sky exhibits negative BTD (like liquid clouds) because of the influence of water vapor absorption and emissivity of the surface (surface emissivity at 8.5μm tends to be much lower than at 11μm, especially for non-vegetation surface).
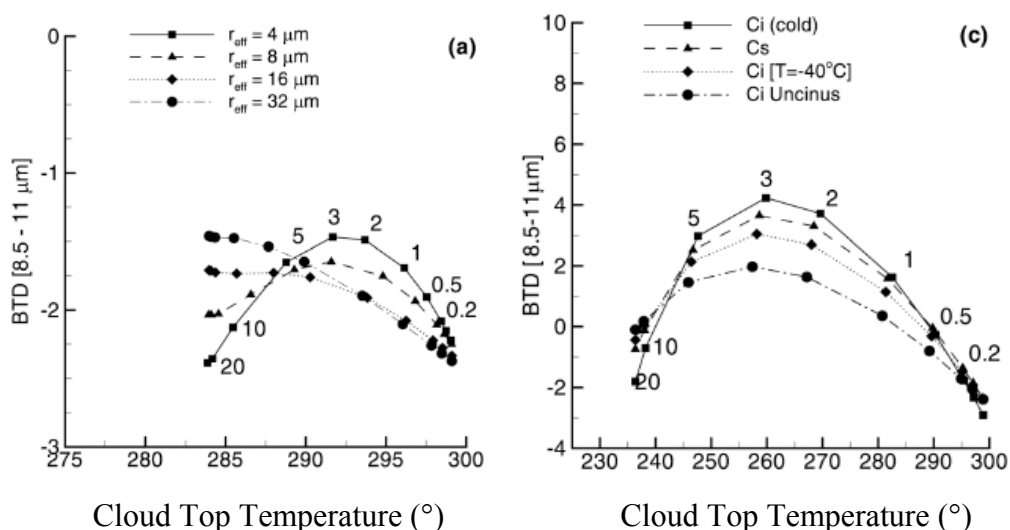
Figure 4.2-5 – *Transfer radiation simulation of BTD [8.5-11] for water (a), and ice clouds (b) from optical thin(COT=0) to optical thick (COT=20) clouds based on a mid-latitude summer temperature and humidity profile. Figure from Baum et al. (2000).*

c) Auxiliary method from Brighteness Temperature

MODIS also uses the brightness temperature at 11μm (BT_{11}) to help in cloud phase decision. Described in its algorithm, with BT_{11} above 275K (2°C), there are no more ice clouds allowed by the algorithm and below 233K (-45°C), there are no more supercooled water clouds.

d) Two cloud phase products

Two cloud phase products are derived from MODIS:

1) Cloud_Phase_Infrared, provided day and night at 5-km resolution is a result of the infrared method (IR bi-spectral & CTT).

2) Cloud_Phase_Optical_Properties, provided in daytime only at 1-km resolution is a result of combination of bi-spectral IR, SWIR/VIS, CTT methods and additional information from cloud mask tests.

The two phase processing flows and thresholds in tests are illustrated in Figure 4.2-6 for the Cloud_Phase_Infrared phase product and in Figure 4.2-7 for the Cloud_Phase_Optical_Properties phase product.
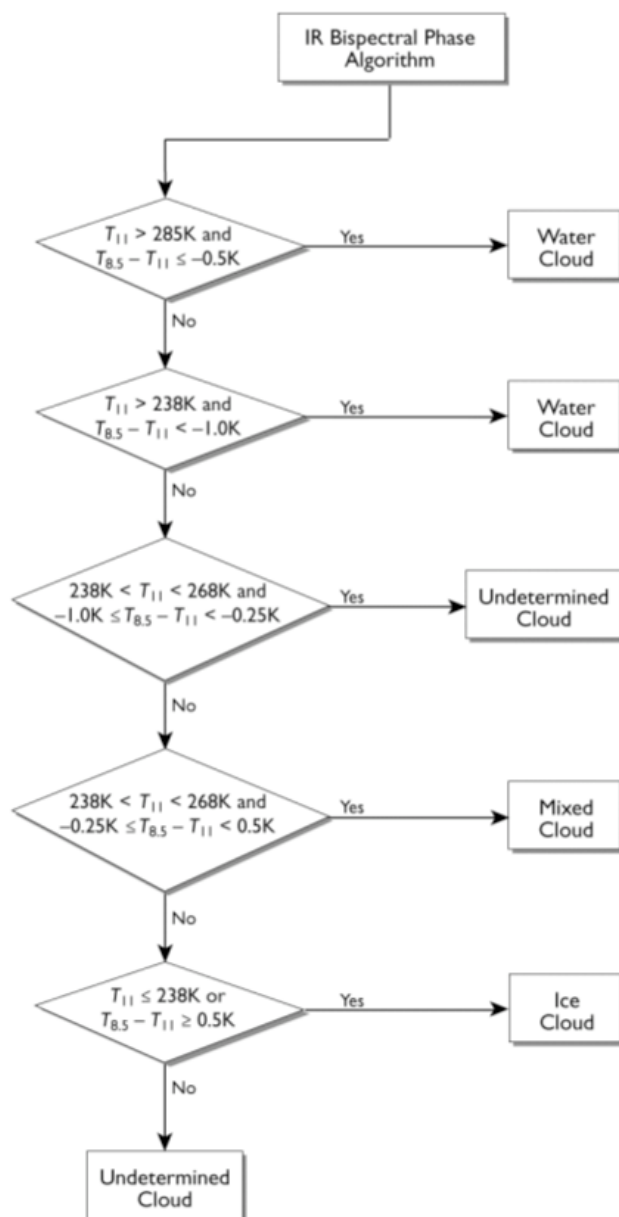
Figure 4.2-6 – *Flowchart for Cloud_Phase_Infrared determination in collection 5 MODIS products from Menzel et al. (2006).*
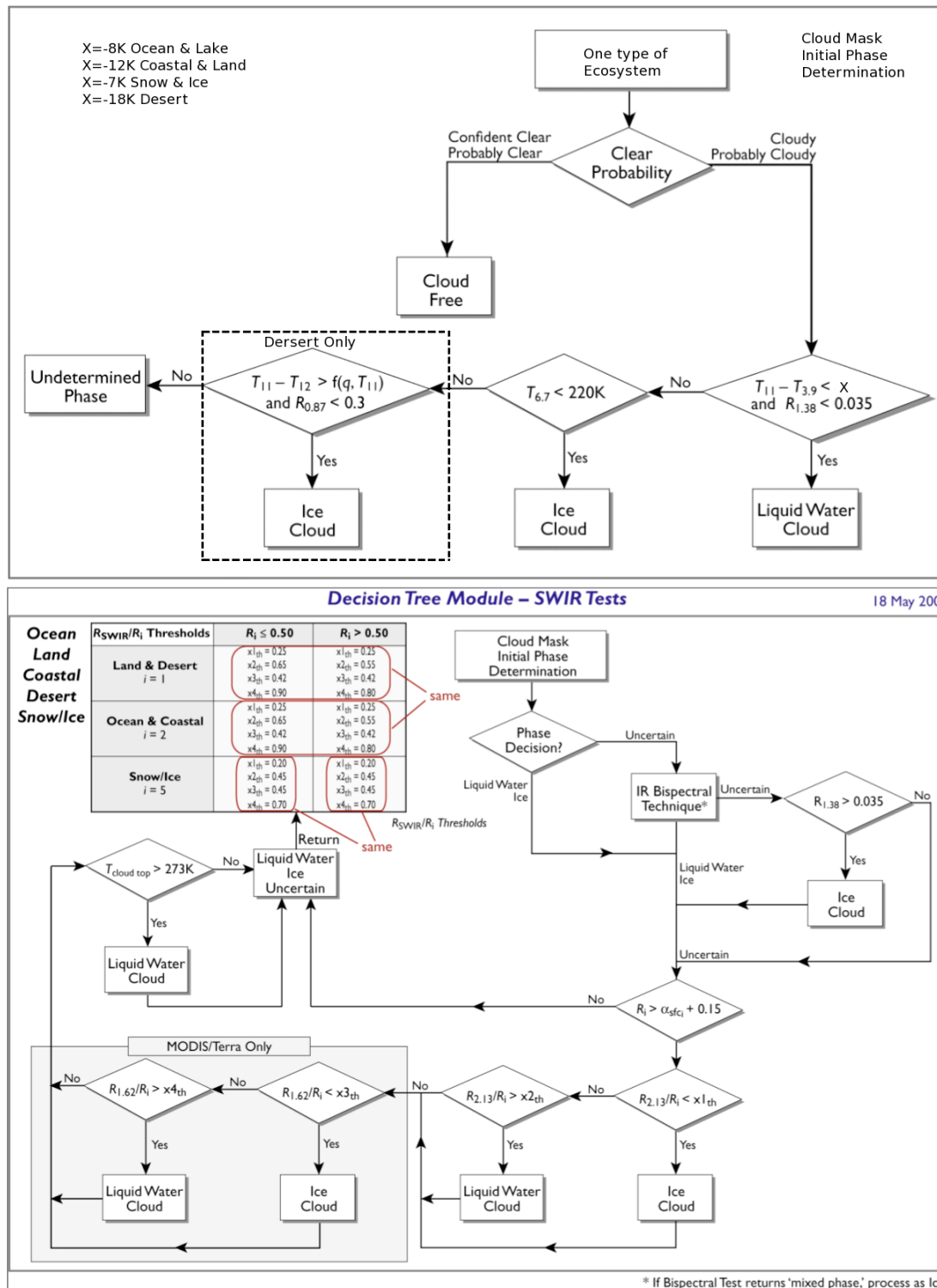
Figure 4.2-7 – *Flowchart for Cloud_Phase_Optical_Properties determination in collection 5 MODIS products from King et al. (2004).*

4.2.3 Physical Basis and Processing Description for CALIOP

CALIOP baseline Ice-Water Algorithm (IWA) primarily uses layer integrated depolarization of the backscattered light and cloud top temperature to classify cloud phase as ice or water. The detection of mixed phase requires vertical profiles of depolarization, which is currently an ongoing study and is not yet included in its operational algorithm (collection 2). The depolarization ratio and temperature methods are introduced in the following.

a)   The depolarization-attenuated backscatter method

The depolarization-attenuated backscatter technique employed by CALIOP to distinguish ice from liquid water is based on the different characteristics of backscattering and polarized scattering behaviors existing between spherical and non-spherical particles. When clouds are optically thin and single scattering dominates, the backscattered signal from spherical particles (e.g. liquid droplets and spherical aerosols) is not depolarized, making the perpendicularly polarized component of backscattered light very close to zero. For randomly oriented non-spherical particles (e.g. ice clouds, non-spherical aerosols), backscattering is highly depolarized (Hu *et al.*, 2009; Liu *et al.*, 2005; Vaughan *et al.*, 2005). The probability of having a particular phase is calculated from the layer-integrated depolarization ratio (δ) and its uncertainty ($\Delta\delta$) and layer-integrated attenuated backscatter (γ):

$$P_{ice}(\gamma,\delta_v,\Delta\delta_v) = (1+\exp(-2.3\frac{SNR}{\delta}(\delta-c_w))^{-1}$$

$$P_{water}(\gamma,\delta_v,\Delta\delta_v) = 1-(1+\exp(-2.3\frac{SNR}{\delta}(\delta-c_i)))^{-1}$$

(Eq. 4.2-1)

Where, SNR=$\delta/\Delta\delta$, represents the instrument noise. c_w and c_i are coefficients computed as a function of γ. $\delta = \int_{base}^{top}\beta_\perp'(r)dr / \int_{base}^{top}\beta_\parallel'(r)dr$. $\beta_\perp'(r)dr$ and $\beta_\parallel'(r)dr$ are

perpendicular and parallel components of the attenuated backscatter profiles and $\gamma = \int_{base}^{top} \beta'_{\perp}(r) + \beta'_{\parallel}(r) dr$ is an integral of attenuated backscatter.

The satellite measurements of γ and δ for ice and liquid clouds are well clustered into two distinct groups (see Figure 4.2-8 from Hu et al., 2006):

1) Water clouds have typical features of γ and δ around the green dashed line with positive slopes.
2) Ice cloud features are around the red solid line with mostly negative slopes:
   a) In the lower central and right area of the plot, ice clouds characterized by low backscatter and high depolarization are due to the inclusion of randomly oriented ice particles. In these clouds the depolarization is dependent primarily on ice crystal habit.
   b) In the upper left hand of the plot, ice clouds characterized by high backscatter and low depolarization are due to the presence of horizontally oriented plate crystals.
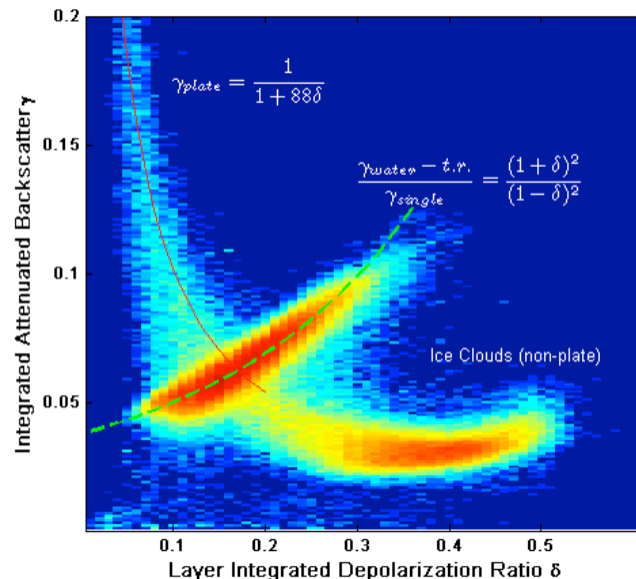
Figure 4.2-8 – *Features of layer-integrated attenuated backscatter and layer-integrated depolarization at 532nm for typical opaque ice and liquid water clouds in July 2006, from Hu et al., 2006. Opaque clouds are identified by the lack of a surface return signal beneath the cloud layer.*

b) Auxiliary method from Cloud Top Temperature

In cases where the depolarization ratio calculation from Eq. 4.2-2 fails to generate a high confidence classification (e.g. either P_{ice} < 0.5 or P_{water} < 0.5), a second probability test is performed based on the temperature at cloud top. The lidar profile provides unambiguous cloud height and the temperature is then determined using temperature profiles from a gridded analysis (Vaughan et al., 2005). In fact, if the temperature at cloud base is lower than -45°C, it can be assumed that the cloud is an ice cloud (Pruppacher, 1995). If the temperature at cloud top is higher than 0°C, then it can be assumed to be a water cloud. If the top/base temperatures fall between these extremes, both ice and water are potentially present with their respective probability depending on cloud top temperatures:

$$P_{water}(T) = 1 / (1 - \exp(-a(T_{top} - c) + d))$$
$$P_{ice}(T) = 1 - P_{water}(T_{top})$$

(Eq. 4.2-3)

The final phase is determined from a combination of these two methods, using a confidence value Q to present the final probability. See Figure 4.2-9, Q is calculated either as the maximum of the probability of the two methods or as the square root of the product of the two probabilities. If the final Q is greater than 0.25, water/ice phase is determined, or else, an unknown feature is labeled. These unknown features could be considered as mixed phase clouds, ambiguous cases with poor SNR, or mistakenly classified non-cloud features.
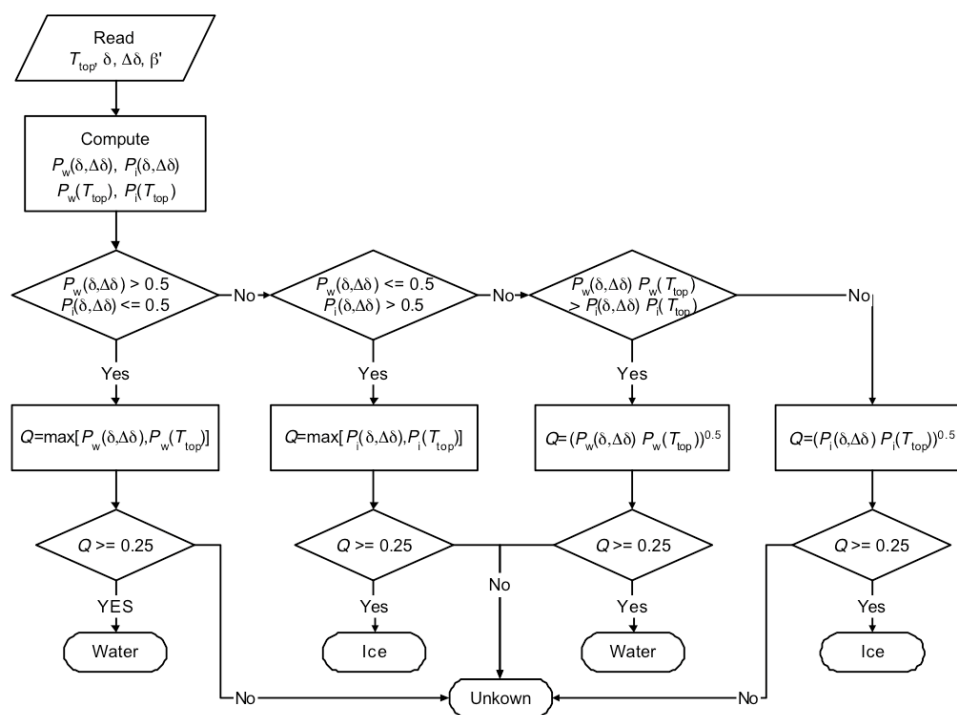
Figure **4.2-9** – *Flowchart of the baseline version of the CALIOP Ice Water Algorithm from Liu et al. (2005).*

4.2.4 Strength and limitation of each technique

a) SWIR/VIS ratio method

The strengths and weaknesses of SWIR/VIS method have been summarized by Pilewskie and Twomey (1987), Riedi et al. (2007), Chylek et al. (2006) and King et al. (2004). If the clouds are in one of the following conditions, the phase information may be incorrect:

- For very thin clouds with optical thickness less than 1 (King *et al.*, 2004), the optical path along which absorption can occur is too short to provide useful phase information.
- For clouds with large droplets or small ice crystals, the contrast of absorption between ice and liquid water is not large enough and make the separation difficult.

- Over surfaces where the albedo in near-infrared and visible bands are too different, the SWIR/VIS ratio could be biased by the surfaces (e.g. in sun-glint and over snow).

- The presence of mixed clouds makes the separation ambiguous as the absorption tends to an average value of the two parts.

b) Bi-spectral IR method

The limitations of the bi-spectral IR method are summarized in the following. Despite the numerous limitations listed hereafter, it is important to keep in mind that unambiguous cloud phase determination occurs in approximately 80% of the global data (Chylek *et al.*, 2006; Menzel *et al.*, 2006; Riedi *et al.*, 2007; Spangenberg *et al.*, 2005). The accuracy of phase separation will be affected by:

- The surface emission. Studies show that the surface emissivity at $8.5\mu m$ can decrease much more significantly than $11\mu m$ over non-vegetated land.

- The water vapor contained in the atmosphere.

- The particle size. Small particles tend to increase the BTD relative to large particles because of increased scattering.

- The presence of very thin cirrus, especially in multilayered cloud systems when thin cirrus overlaps water clouds.

- The presence of clouds with cloud top temperatures between 238K and 273K that may contain supercooled liquid droplets, ice crystals or a mixture of both. This issue often happens in Storm Tracks of each hemisphere.

- The presence of temperature inversion. In polar region, the detection difficulties from bi-spectral IR method are found as results of frequent temperature inversion and cold surface.

c) Angular polarization method

The strengths and weaknesses of the POLDER retrieval technique have been summarized from the comparison work with the active lidar and ISCCP measurements (Chepfer *et al.*, 1999; Riedi *et al.*, 2000; Riedi *et al.*, 2001), and also from studies of radiative transfer simulation (Goloub *et al.*, 1997; Goloub *et al.*, 2000; Riedi *et al.*, 2007).

- The quality of retrieved phase strongly depends on the number and nature of effective tests: the rainbow test around 140° and slope sign test for scattering angle <120° provide more confident information for the decision. This method is therefore dependent of available sampling of scattering angle that varies with season and region.

- Where the polarization signal is not saturated (e.g. cloud edges or thin clouds), the cloud polarization feature is not well defined, which could lead to misclassification.

- The low-water cloud edges are possibly classified as ice.

- In case of thin cirrus overlaying low liquid clouds, as the polarization feature mixes ice and liquid features, the final decision depends on the upper cirrus optical thickness. For COT > 2, ice flag is labeled; for COT<1, liquid flag is labeled; for 1< COT<2 the underlying liquid feature could pass through the cirrus and the mixed or undetermined flag may be labeled.

- In case of single layered cirrus, its polarization feature mixes the ice cloud and clear ground features. As the polarization feature of the ground (out of sun-glint) is similar to cirrus, the final decision is less biased.

- In transition zone of ice/water/mixed clouds, clear sky/clouds or aerosol/clouds, as one pixel corresponds to as large as 7km at ground, the mixing information from the neighboring pixels especially for oblique directions ambiguities the cloud phase derivations, and make the angular behaviors of phase detecting complex and ambiguous.

As a summary, not a single technique is perfect for detecting cloud phase in all situations. For example, according to Riedi (2007) and Chylek (2006), it seems that the SWIR/VIS method detects more ice and mix/undetermined clouds than bi-spectral IR method does, especially in a complex cloud system like the typhoon system. To simplify the understanding of later comparison work on cloud phase between satellite observations, Table 4.2-1 summarizes the main advantages and limitations of each method used by these satellites

Methods	Advantages	Limitations
POLDER (angular polarization)	(1) Insensitive to particle size (2) Insensitive to cloud top/surface temperature (3) Insensitive to atmospheric profiles	(1) Depends on the sampling of available scattering angle (2) Difficult for very thin clouds, broken clouds, cloud edges and aerosols over liquid clouds
MODIS (SWIR/VIS)	(1) Insensitive to cloud top temperature (2) Insensitive to atmospheric profiles	(1) Depends on particle sizes (2) Difficult for very thin clouds (3) Biased by the spectral difference of the surface albedo
MODIS (bi-spectral IR)	(1) Observations independent of solar light	(1) Depends on particle sizes (2) Difficult for very thin clouds (3) Depends on the ground/cloud top temperature (4) Depends on atmospheric profiles (both temperature and water vapor profiles)

Table **4.2-1** – *Summary of the advantages and limitations of phase retrieval methods employed by POLDER and MODIS.*

4.2.5 Ice nucleation Theory

Different from satellites that allow to study clouds on the basis of radiative transfer theory, cloud models focus on studies of cloud dynamics and describe the cloud phase in term of ice nucleation (Pruppacher and Klett, 1997; Heymsfield and Sabin, 1989; Fletcher, 1958). With the microphysical and thermodynamical conditions known, the cloud models allow to simulate and qualify the ice nucleation processes accounting for more or less details. In the real atmosphere, ice nucleation may result of either heterogeneous or homogeneous freezing or heterogeneous deposition. It is difficult to separate among them even though it is known that homogeneous nucleation occurs with much more difficulty from the pure substance. In simple terms, ice nucleation is a spontaneous process resulting of fluctuations in

time and space of temperature and density in the original phase, provided by a critical supersaturation of the vapor or a critical supercooling of the water drops. Accompanying this process, the water vapor is convergent while the latent heat is divergent, and also the effective particle size brutally increases while the concentration of germ and the supersaturation decrease rapidly.

4.2.5.1   Homogeneous nucleation in supercooled water

Homogeneous nucleation means that ice is formed by homogeneously freezing from pure vapor or water without need of ice-forming nuclei. Ostwald's rule of stages show that a supersaturated phase (water vapor) does not directly transform into the most stable state (ice), but rather into the next most stable or metastable state (supercooled water). In homogeneous vapor at temperatures below 0° C ice appears mostly via the freezing of supercooled water drops rather than directly from the vapor.

The process of ice nucleation from supercooled water then mostly occurs in the upper troposphere where fewer ice-forming nuclei are present and lower temperature (lower than -38°C) are encountered (Heymsfield and Sabin, 1989). During this process, growth is a matter of molecular reorientation involving the breaking of water-to-water bonds and the formation of water-to-ice bonds. The supercooling and supersaturation provide the driving force (free energy) for a water molecule must pass from its average equilibrium position of minimum potential energy in water to a new equilibrium position in ice (Pruppacher and Klett, 1997). Ice nucleation involves the two sub-processes mentioned above and concerns two terms: one for the volume transition and the other one for the surface formation. When supersaturation or supercooling occurs, it brings about a change in free energy per unit volume, G_v, between the liquid and newly created solid phase, which is balanced by the energy gain of creating a new volume ($3/4\pi r3$), and the energy cost due to creation of a new interface ($4\pi r2$) (see Eq. 4.2-4).

$$\Delta G = \frac{3}{4}\pi r^3 G_v + 4\pi r^2 \sigma \qquad \text{(Eq. 4.2-4)}$$

σ, is the interfacial energy between vapor/liquid, vapor/ice and liquid/ice. When the overall change of the free energy ΔG is negative, nucleation is favored. From Eq. 4.2-

3 and Figure 4.2-10, we note that it exists an extreme value for ΔG (happened when $d\Delta G/dr = 0$, the green curve) that corresponds to the critical nucleation size (see Eq. 4.2-5). If the supercooled nucleus is too small, the energy that would be released by forming the ice volume is not enough to create its surface. While surpassing this size, the nucleation proceeds automatically.

$$r^* = \overset{(1)}{\frac{-2\sigma}{G_v}} = \overset{(2)}{\frac{-2\sigma}{nkT\ln(\dfrac{e}{e_s})}} = \frac{-2\sigma T_m}{\Delta H_s \Delta T} \qquad \text{(Eq. 4.2-5)}$$

The corresponding energy at this extreme point is called the minimum energy needed for ice nucleation (see Eq.4.2-6):

$$\Delta G^* = \frac{32\pi}{3n^2}\left(\frac{\sigma}{kT\ln(\dfrac{e}{e_s})}\right)^2 = \frac{16\pi\sigma^3 T_m^2}{3\Delta H_s^2 (\Delta T)^2} \qquad \text{(Eq. 4.2-6)}$$

We note, e: water vapor pressure. e_s: saturated vapor pressure. n: water molecule number per volume. ΔH_s: the enthalpy per unit volume. T_m: freezing temperature. The process (1) in Eq. 4.2-4 applies the Kelvin equation and process (2) applies the Clausius-Clapeyron Equation.
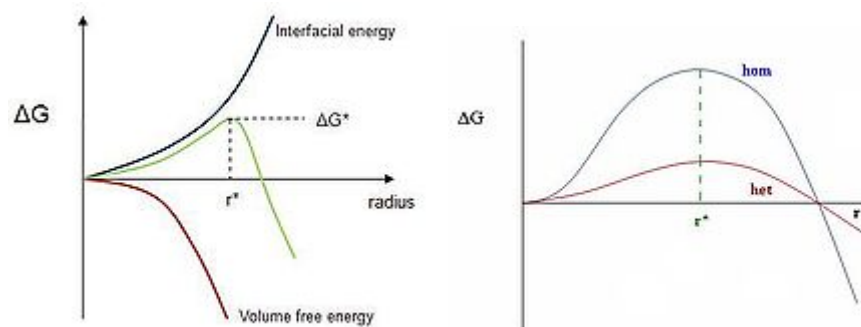
Figure 4.2-10 – *The free energy of a germ of the new phase as a function of the radius of the cluster for (a) homogeneous nucleation and (b) heterogeneous nucleation.*

Heymsfield (1989) concluded for homogeneous ice nucleation in this paper:
- Homogeneous freezing occurs at temperature lower than -38°C

- The size of the largest solution droplets decreases with decreasing temperature and increases with updraft velocity.
- Homogeneous ice nucleation occurs in a narrow temperature range
- Higher IN (ice forming nuclei) leads greater probability of the droplet freezing
- The relative humidity at the onset of appreciable ice nucleation decreases with temperature, but is independent of updraft velocity and IN

According to Heymsfield (1989), the fraction of unfrozen drops $N_u(T)/N_0$ can be estimated as a function of the nucleation rate J at temperature T, the droplet volume V_d and the cooling time t:

$$\ln(\frac{N_0}{N_u(T)}) = -JV_d t = \frac{V}{\gamma_c} \int_T^{T_0} J(T)dT \qquad \text{(Eq. 4.2-7)}$$

It can also be expressed as the right part of Eq. 4.2-7. γ_c: the rate of cooling (s^{-1}), $\gamma_c=dT/dt$. From the equation, it is easy to see that the unfrozen fraction of solution droplets depends on V, γ_c and J.

Larger the volume of a drop is, higher is the probability for a density fluctuation in the drop and, thus, higher is the probability that an ice germ will be produced.

For the median freezing temperature ($T_{sm} = T_0 - T_m$) where 50% of drops are still unfrozen ($N_u(T_{ms}) = 1/2N_0$), (Eq. 4.2-7) becomes:

$$\int_{T_{ms}}^{T_0} J(T)dT = 0.693\gamma_c V_d \qquad \text{(Eq. 4.2-8)}$$

4.2.5.2 Heterogeneous nucleation

Heterogeneous nucleation, freezing via foreign substrates (Ice Nuclei, IN), is assumed to happen when temperature is warmer than -38°C, although it is still active when colder than -38°C (Pruppacher and Klett, 1997). IN exhibit four basic modes of action:

1) The deposition mode: Water vapor at temperatures below 0°C is absorbed directly from the vapor phase onto the surface of the IN and is transformed into ice at low temperature.

2) The condensation freezing mode: An aerosol particle at temperatures below 0°C forms a drop which freezes at some time during the condensation stage.

3) The immersion mode: The IN becomes immersed into a drop at temperatures warmer than 0°C and freezing is subsequently initiated whenever the temperature of the drop has become sufficiently low.

4) The contact mode. The IN initiates the ice phase at the moment of its contact with the supercooled drop (Pruppacher and Klett, 1997). No matter which model, compared to homogeneous nucleation (see Figure 4.2-10 a), although the critical radius remains unchanged, the barrier energy needed for heterogeneous nucleation is reduced, which means less supercooling is needed (see Figure 4.2-10 b).

For heterogeneous nucleation of supercooled drops, experiments with water drops containing various impurities have revealed that their freezing temperature (usually expressed in terms of the median freezing temperature T_{sm} of a population of drops of volume V_d) is a function of the drop volume (Eq. 4.2-8, Pruppacher and Klett, 1997).

$$T_{sm} = A - B \ln V_d \qquad \text{(Eq. 4.2-9)}$$

T_{ms} is the median freezing temperature in °C. A and B are constants for a particular water sample.

In addition, above a certain temperature where the concentration of IN in the freezing mode rapidly decreases, the volume of a water sample which contains a particle that can nucleate ice will be progressively larger than that predicted by the T_{ms} -$\ln V_d$ law.

4.3 Global Statistics of the Phase Detection from POLDER and MODIS

For the first step of the study on cloud phase, we focused on the statistics of cloud phase at a global scale derived from POLDER and MODIS. By assessing the fraction of liquid, ice and mixed clouds, we intended to obtain a preliminary

evaluation on the capacity to detect cloud phase for each technique. This preliminary and statistical analysis helps for a second step on discussion of confident and non-confident cases derived from the combination of the two passive sensors. Going one step further, we will end this discussion by looking at relations between thermodynamic phase and other parameters accessible in cloud models.

As in previous chapters, the period chosen ranges from December 2007 to November 2008. The phase probability (or fraction, frequency) is calculated as the ratio of the pixel number labeled with one phase to the total number of cloudy pixels. Table 4.3-1 shows the annual, global probabilities of the three phases from different phase products and splits among different cloudy scenes. From this table we see:

● In condition of all cloudy scenes (overcast + broken), the ice fractions ordered from the most to the least are MODIS phase, POLDER phase to MODIS IR phase while for liquid phase are MODIS IR phase, POLDER phase to MODIS phase and for mixed phase are MODIS IR phase, POLDER phase to MODIS phase.

● Comparing the broken and overcast scenes, in overcast cloudy scenes, no matter which product, the ice fraction is more important than the liquid fraction. This phenomenon may be due to two reasons. First, broken clouds occur more frequently at low altitude and higher clouds often tend to be extended and overcast. Secondly, cloud inhomogeneities in broken clouds and the associated 3D effects could impact the cloud phase detection, which needs more careful attention in the future.

Probability(%)		Ice	Liquid	Mixed
Cloud_Phase_Optical_Properties **(combines IR and SWIR/VIS** **method, noted as MODIS phase)**	All	35	61	4
	Overcast	60	39	1
	Broken	20	76	4
Cloud_Phase_Infrared (uses IR **method, noted as MODIS IR** **phase)**	All	22	67	12
	Overcast	45	36	19
	Broken	13	82	5
POLDER (uses polarization **method, noted as POLDER** **phase)**	All	28	63	9
	Overcast	40	55	1
	Broken	21	67	12

Table **4.3-1** – *Probabilities of cloud phases (liquid, ice and mixed) for different phase products (MODIS phase, POLDER phase and MODIS IR phase) and for different cloudy scenes (all, overcast and broken).*

With the advantages of the PM dataset, not only we can assess the cloud phase from different phase products as done in Table 4.3-1 but also we can assess the pixel-to-pixel combined POLDER/MODIS phase in order to show the agreement and disagreement between these two passive sensors. In the following studies, unless otherwise stated, the combined phases mainly refer to the combination of MODIS phase (not MODIS IR phase) and POLDER phase. As each pixel could be classified as one of the three phases (ice, liquid or mixed) from one sensor, there is therefore 9 (3×3) combined phases determined from the combination of the two sensors. In the following, we will focus on these 9 classes of combined phases and qualify the agreement and disagreement in phase detection according to different environmental conditions and geographic locations.

In Figure 4.3-1 we plot the annual global percentages of the 9 combined phases according to different environments in order to see in which conditions POLDER and MODIS tend to present consistent or inconsistent phase determination.

From this figure (subfigure a), we found that over all cloudy scenes, the total frequency of agreement on phase between POLDER and MODIS reaches about 73% of all pixels with 50% of liquid clouds, 23% of ice clouds and about 27% of the pixels showing disagreement. Concerning the overcast scenes that are referred as overcast by both POLDER and MODIS, the agreement on phase raises to 77% (see subfigure c), but for the broken scenes that are determined as broken by both sensors, the overall agreement on phase decreases to 69% (see subfigure b). It shows an even better agreement in case of overcast single layered clouds (selected using MODIS multilayer flag), for which up to 93% of pixels show consistent phases decision between MODIS and POLDER. Not surprisingly, however the agreement on phase gets worse in case of overcast multilayer cloud systems with only 67% of pixels in agreement and even worse with only 64% of pixels over snow covered surface where both clouds detection and phase detection may be at issue for the two sensors.

In case of disagreement, the most frequent situation for all cloudy scenes (see subfigure a) corresponds to the POLDER-liquid & MODIS-ice class, which represents about 11% of the cloud cover; followed by the POLDER-liquid, MODIS-mixed class (about 5.6%), and the POLDER-ice, MODIS-liquid class (about 4.5%).

Comparing Figure 4.3-1 (b) and (c), we see again that the confident liquid (ice) clouds are relatively speaking more (less) frequent for broken scenes than overcast scenes, which agrees with Table 4.3-1. We also observe a greater percentage for

POLDER-ice (color: orange) or mixed (color: brown) & MODIS-liquid clouds (orange: 8.9% or brown: 9.9%) in broken scenes than in overcast scenes (orange: 0.8% or brown: 1.5%). In fact, scenes presenting mixture of clouds and clear sky (or aerosols) could complicate the broken clouds phase detection as we will see later.

If we now consider the multi-layered (see subfigure e) and single layered (see subfigure d for overcast cloud scenes, one can see that the POLDER-liquid & MODIS-ice (light orange, equal to 24%) clouds and POLDER-mixed & MODIS-ice (red, 6%) clouds represent a significant part of the multilayer cloud systems while these classes are barely observed for the single layer cloud systems. This tends to indicate that, in case of multilayer cloud systems, MODIS is sensitive to the upper layer cloud phase while POLDER signal is still impacted by the lower layers. It is fairly obvious that in case of multilayered systems, radiation that can pass through the upper thin layer will make the phase signal ambiguous and complicate the phase detection.

Over snow/ice (see subfigure f), POLDER-liquid & MODIS-ice class and POLDER-liquid & MODIS-mixed class take an important parts of percentage for about 18% and 7% of all cases. The specific atmospheric profiles (e.g. the inversion of temperature) over poles and the brighter and colder surface are most likely to cause issues in phase detection over snow/ice as explained earlier when we discussed the physical basis of each retrieval method.
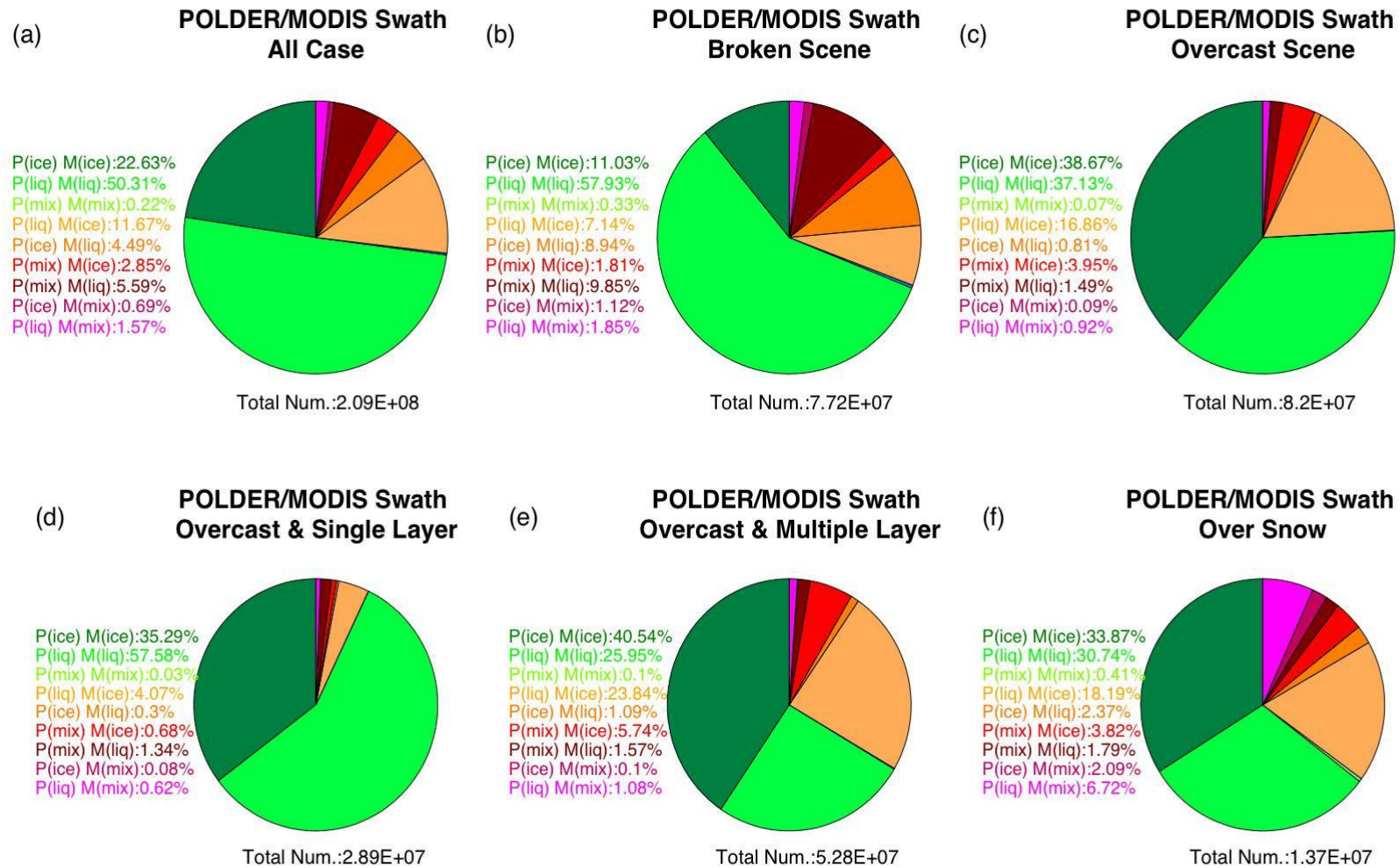
Figure 4.3-1 – *Pie chart of the percentage of 9 combined phases (POLDER-ice & MODIS-ice; POLDER-ice & MODIS-liquid; POLDER-ice & MODIS-mix; POLDER-liquid & MODIS-ice; POLDER-liquid & MODIS-liquid; POLDER-liquid & MODIS-mix; POLDER-mixed & MODIS-ice; POLDER-mixed & MODIS-liquid; POLDER-mixed & MODIS-mix) according to different cloudy conditions: all scenes (a), broken scenes (b), overcast scenes (c), overcast single layered scenes (d), overcast multi-layered scenes (e) and scenes over snow/ice (f).*

From the above study, we conclude that cloud phase detection shows a general satisfactory agreement although using different techniques, but also that they exhibit different sensitivity in detecting phase depending on types of cloudy scene. In the following, we will continue to plot the geographical distribution of the 9 classes of combined phases over the globe (see Figure 4.3-2) to visualize the location of the confident and ambiguous classes. This will help to associate different environmental phenomenons with the confident and ambiguous phases. In this figure, the map color presents the annual frequencies of each class of combined phase (the sum of the frequencies of the 9 combined phases is equal to 100%). From this figure, we can observe that:

- The confident ice clouds (consistent ice phase from POLDER & MODIS) are mostly located in the ITCZ and Storm Tracks, where can occur a great amount of thick high clouds because of the strong convection (subfigure, 1-1). The confident liquid clouds (consistent liquid phase from POLDER & MODIS) can be found mostly in subtropics subsidence regions where clouds often occur as broken and over ocean to the western coast of the continent where extended low stratocumulus are largely dominated (subfigure, 2-2). The confident mixed clouds are significant in Storm Tracks and in Polar regions (subfigure, 3-3).
- The clouds labeled as ice by POLDER but liquid by MODIS (see subfigure, 2-1) occur around Africa and China where there are often heavy aerosols over low water clouds (see analysis in chapter 4.4.5).
- The clouds labeled as liquid by POLDER and ice by MODIS (see subfigure, 1-2) occur in the ITCZ where often appear the multi-layered clouds and a great number of supercooled droplets associated to the strong convection in clouds (see analysis in chapter 4.4.3)
- The clouds labeled as liquid by POLDER and ice by MODIS (see subfigure, 1-2) also occur over snow covered surface and deserts where both the surface emission and atmosphere profile are extremely peculiar.
- The clouds labeled as mixed by MODIS and whatever by POLDER often occur over snow (see subfigures, 3-1, 3-2 and 3-3)

- The clouds labeled as mixed by POLDER and liquid by MODIS (see subfigure, 2-3) appear more frequently in regions where broken clouds are predominant or where clouds can be overlaid by aerosols such as around Africa
- The clouds labeled as mixed by POLDER and ice by MODIS (see subfigure, 1-3) occur in Storm Tracks and the ITCZ, similar to the situation in subfigure, 1-2, which is also associated to the multi-layered clouds and supercooled droplets in the strong convective clouds (see analysis in chapter 4.4.5)

It appears clearly from the above that the 9 combined phase classes are not randomly distributed and are most likely associated with particular environmental conditions which need to be further studied and described. In the next step, some other cloud properties will be used to help understanding these geographical distributions. Additionally, the active sensor CALIOP will be used for the interpretation of each combined phase detected by passive sensors. This will help us to assess how confident the phase could be found for each sensor and to confirm the potential bias for each technique.
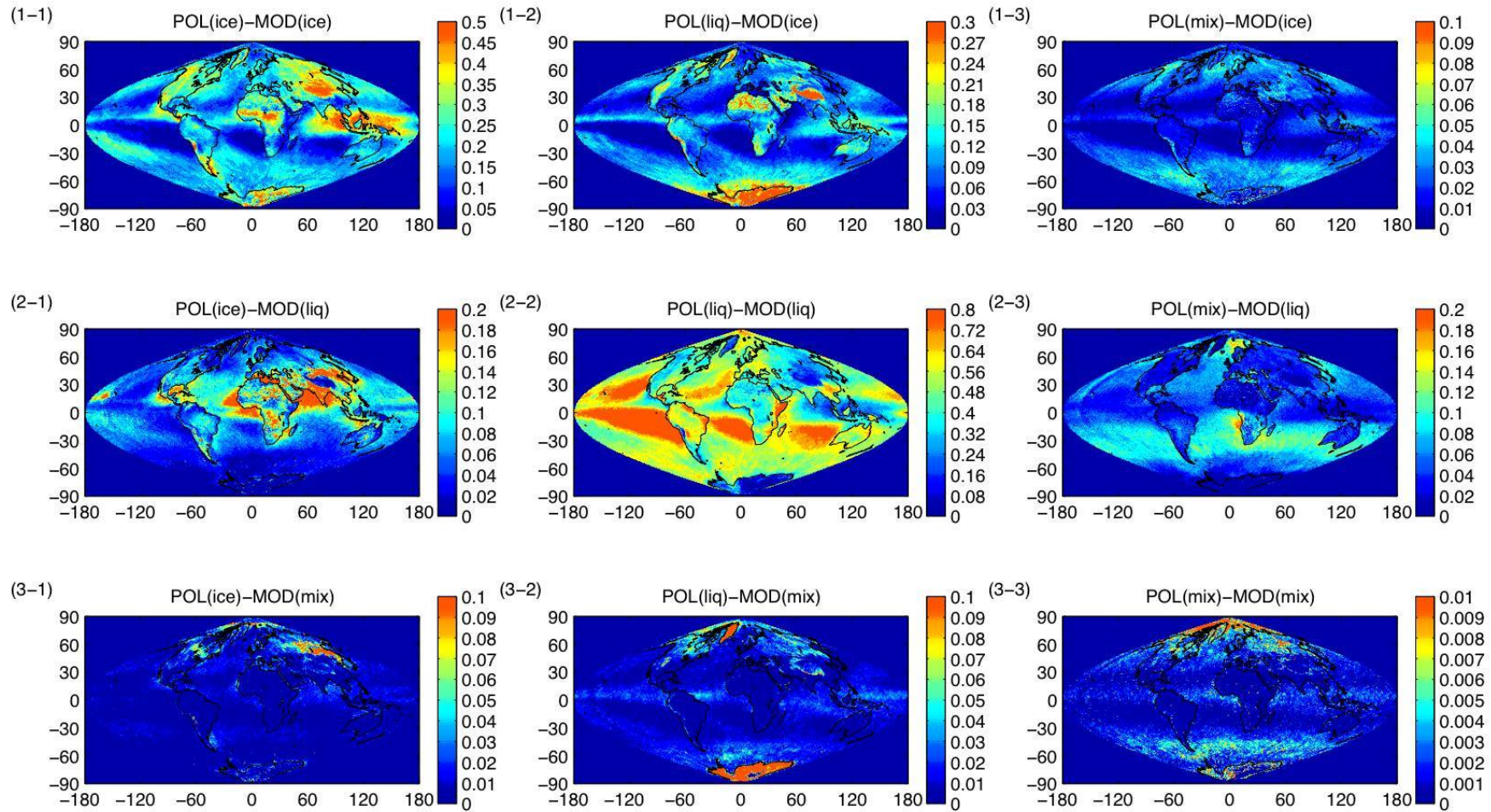
Figure 4.3-2 – *Geographical distribution of the occurrence frequencies of 9 combined phase: POLDER-ice & MODIS-ice (1-1); POLDER-liquid & MODIS-ice (1-2); POLDER-mixed & MODIS-ice (1-3); POLDER-ice & MODIS-liquid (2-1); POLDER-liquid & MODIS-liquid (2-2); POLDER-mixed & MODIS-liquid (2-3); POLDER-ice & MODIS-mixed (3-1); POLDER-liquid & MODIS-mixed (3-2); POLDER-mixed & MODIS-mixed. (3-3).*

To better recognize and understand these combined phases, we present hereafter histograms of cloud properties associated to the 9 classes, for example, the effective radii (derived from MODIS) in Figure 4.3-3, the cloud top temperature (derived from MODIS) in Figure 4.3-4 and the cloud top pressure (derived from MODIS & POLDER) in Figure 4.3-5 and Figure 4.3-6 These cloud properties play an important role in the ice nucleation process and could provide additional and important information to assess the quality of cloud phase detection. For example, clouds with the top temperature lower than -40°C and particle radii larger than 50μm are extremely likely to have ice phase. Studies with these cloud properties here, could first allow investigating the cloud properties according to different combined phases, and second help to check and improve the phase detection with only the limited information from the PM Dataset.

Figure 4.3-3 allows to confirm the following:

● The confident liquid clouds have significantly smaller particle sizes (the mean radius is equal to 15, subfigure, 2-2) compared to the confident ice clouds (the mean radius is equal to 26, subfigure, 1-1). For liquid clouds, the value of effective radius seems higher than other observations (Paltridge 1974), however no droplets are larger than 30.

● Except for the POLDER-ice & MODIS-liquid class, the mean radius corresponding to all clouds with inconsistent phase is between the confident ice crystals and the confident droplets. The POLDER-mixed & MODIS-liquid clouds has the closest radii distribution to that of confident liquid clouds with even smaller particles and not much particles effective radii larger than 30 micrometers. The POLDER-liquid & MODIS-ice clouds, POLDER-mixed & MODIS-ice clouds and POLDER-ice & MODIS-liquid clouds have comparable number of large and small particles.

Note, when the cloud phase is erroneously selected before retrieval of particle size (either mistaken as ice when it is liquid in reality or mistaken as liquid when it is really ice), the retrieved effective radius would be larger or smaller than it is in reality in order to balance the total absorption at the cloud top. For example, a real liquid

cloud would yield smaller particle size if it was retrieved assuming ice phase and contrarily, a real ice cloud would lead to larger retrieved effective radius if it is erroneously assumed to be liquid. In conclusion ambiguous phases will on average tend to produce a mean value of effective radius between those of confident liquid (15 microns) and confident ice (26 microns). With similar explication, the broken scenes tend to enlarge the radius as to balance the reduced reflection due to partly clear scenes, which is one of the well known effects due to 3D structure of clouds (Marshak *et al.*, 2006).
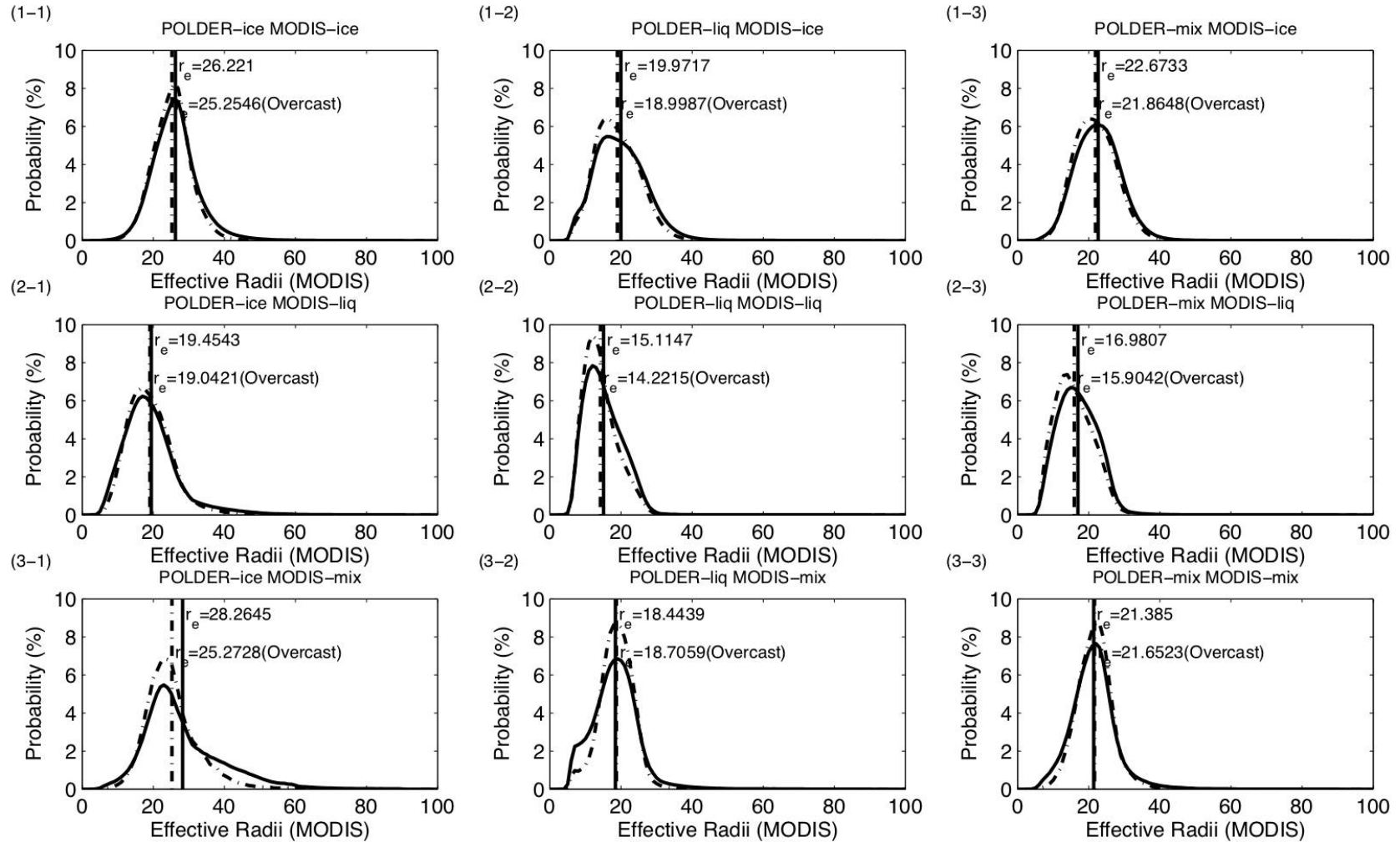
Figure 4.3-3 – *Histograms of cloud effective radii for 9 combined phases: POLDER-ice & MODIS-ice (1-1); POLDER-liquid & MODIS-ice (1-2); POLDER-mixed & MODIS-ice (1-3); POLDER-ice & MODIS-liquid (2-1); POLDER-liquid & MODIS-liquid (2-2); POLDER-mixed & MODIS-liquid (2-3); POLDER-ice & MODIS-mixed (3-1); POLDER-liquid & MODIS-mixed (3-2); POLDER-mixed & MODIS-mixed (3-3). Dashed line is for all cloudy scenes and Solid line for overcast scenes. Vertical lines correspond to the mean of the distribution.*

We now present in the following histograms of cloud top temperature corresponding to the 9 phase classes. Figure 4.3-4 shows that:

- The cloud top temperature of confident ice clouds (see subfigure, 1-1) is on average of -43.6°C (-46.8°C for overcast scenes); there are almost no ice clouds above 0°C.

- The cloud top temperature of confident liquid clouds (see subfigure, 2-2) is on average of 0.01°C (-7.4° for overcast scenes); there are almost no liquid clouds with temperature at cloud top below -40°C.

- The cloud top temperature of confident mixed clouds (see subfigure, 3-3) is on average of -11°C (-16° for overcast scenes) and distributes mostly between 0°C and -40°C for overcast scenes

- The cloud top temperature of POLDER-liquid & MODIS-ice clouds (see subfigure, 1-2) is on average of about -33°C and distributes over a wide range from liquid, supercooled liquid, to freezing temperature. The same applies to the POLDER-mixed and MODIS-ice class with an average cloud top temperature of -35°C.

- The distribution of cloud top temperature of POLDER-mixed & MODIS-liquid clouds (see subfigure, 2-3) is very much alike the confident liquid class with mostly warm clouds and marginal cold clouds below -40°C.

- The cloud top temperature of POLDER-ice & MODIS-liquid clouds (see subfigure, 2-1) is on average of -4° for all scenes, which means a level close to the ground, and on average of about -23.8°C for overcast scenes.

- Comparing the three figures in each column or line in figure, which means to fix the cloud phase from one sensor (column: fix POLDER phase or line: fix MODIS phase), the average temperature decreases from ice to liquid phase that is derived by the other sensor.

Overall, from this figure, we confirm that the cloud top temperature provides, on average, consistent and correlated information of the cloud phase. Also, not surprisingly, part of the ambiguous phase classes determined by combination of POLDER and MODIS are associated to the supercooled and low broken clouds.
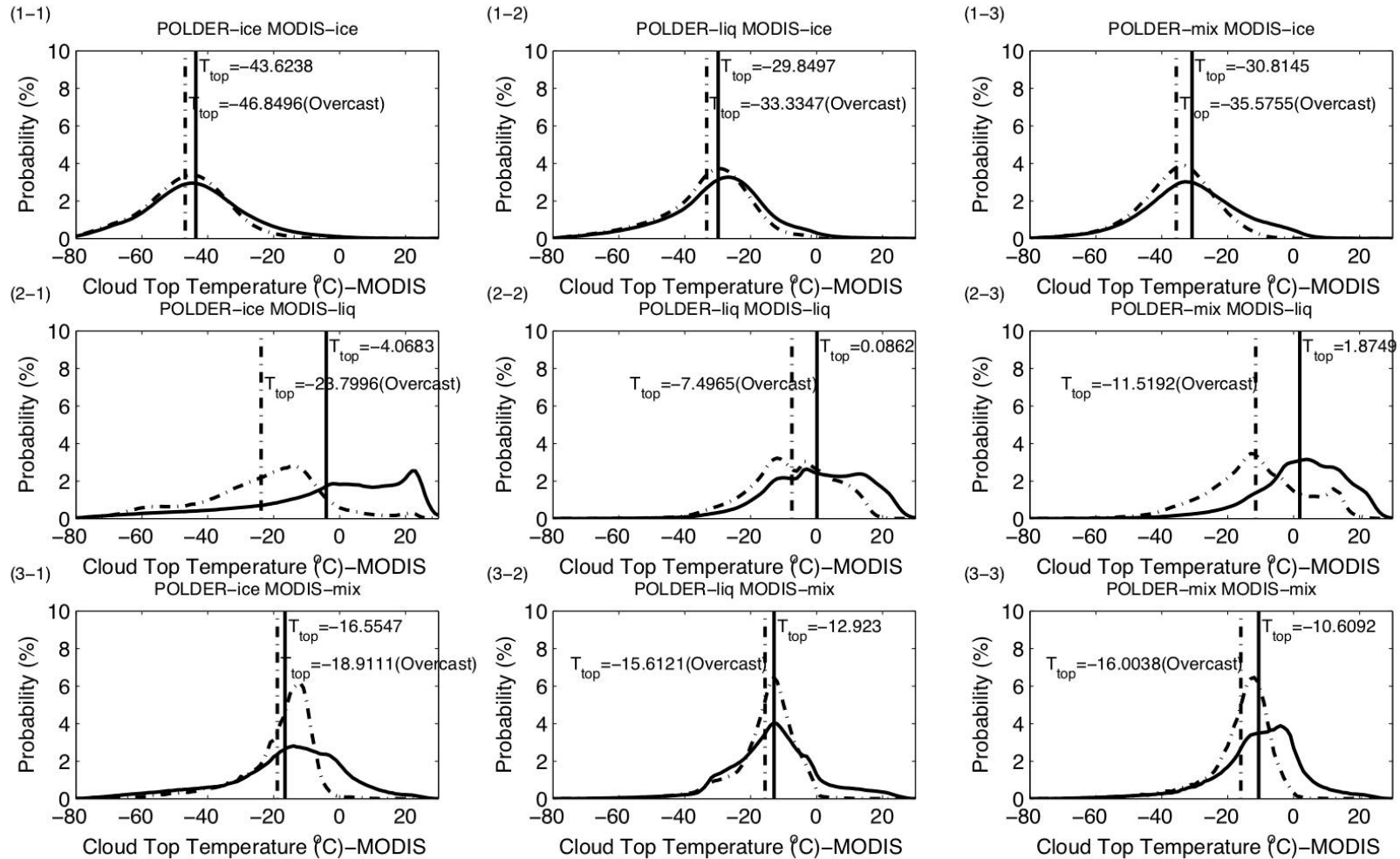
Figure 4.3-4 – *Histograms of the cloud top temperature for 9 combined phases: POLDER-ice & MODIS-ice (1-1); POLDER-liquid & MODIS-ice (1-2); POLDER-mixed & MODIS-ice (1-3); POLDER-ice & MODIS-liquid (2-1); POLDER-liquid & MODIS-liquid (2-2); POLDER-mixed & MODIS-liquid (2-3); POLDER-ice & MODIS-mixed (3-1); POLDER-liquid & MODIS-mixed (3-2); POLDER-mixed & MODIS-mixed (3-3). Dashed lines correspond to all cloudy scenes and solid lines to the overcast scenes.*

In Figure 4.3-5 and Figure 4.3-6, we now present the corresponding cloud top pressure (p_{co2} from MODIS, and p_{o2}, p_{ray} from POLDER) for these 9 combined phases in different cloudy conditions (all scenes and overcast scenes).

● In agreement with the cloud top temperature histograms in Figure 4.3-4, it is not surprising to see that the cloud top pressure is lower for the confident ice clouds and higher for the confident liquid clouds. In addition, clouds located below about 800hPa do not present the ice phase. Somehow more unexpected are some of the confident liquid clouds located in the upper atmosphere where we would usually expect only ice to occur.

● Again in accordance with the cloud top temperature analysis in Figure 4.3-4, the POLDER-mixed & MODIS-ice class and POLDER-liquid & MODIS-ice class are mostly associated to clouds located in the middle of atmosphere; POLDER-mixed & MODIS-liquid clouds correspond primarily to low clouds; the overcast POLDER-ice & MODIS-liquid clouds correspond to middle and high clouds while the broken POLDER-ice & MODIS-liquid clouds correspond to the low clouds.

● Similarly to the cloud top temperature analysis, cloud height is consistent with increasing confidence of cloud phase detection. When the phase determined from one sensor is fixed, the probability of finding ice (respectively liquid) from the other sensor increases when the clouds get higher (respectively low). This is especially true in case of overcast scenes.

● Since the combination of three pressures could also reveal the cloud and atmosphere structures, more information could be provided and confirmed with the combination of different phases and different pressures. For overcast confident ice clouds, co2 pressure is lower than Rayleigh pressure, and Rayleigh pressure is lower than oxygen pressure; for overcast confident liquid clouds, Rayleigh pressure and co2 pressure are about the same level and oxygen pressure is lower than these two especially for overcast scenes; for overcast confident mixed clouds, Rayleigh pressure is lower than the co2 pressure, and co2 pressure is lower than oxygen pressure. In fact, this combination analysis of cloud structure from pressure and phase needs further studies in the future.
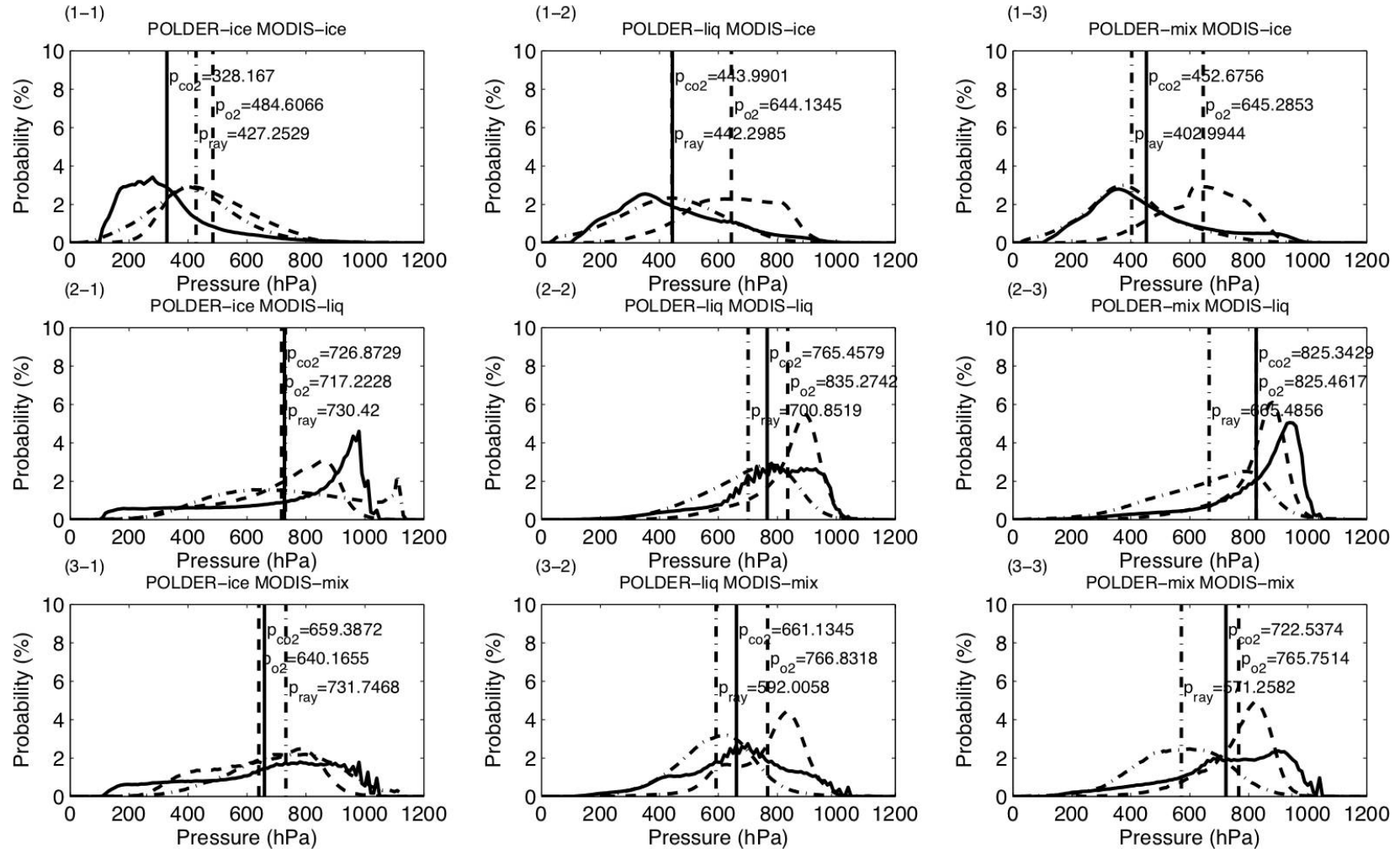
Figure 4.3-5 – *Histograms of the cloud top pressure for 9 combined phases: POLDER-ice & MODIS-ice (1-1); POLDER-liquid & MODIS-ice (1-2); POLDER-mixed & MODIS-ice (1-3); POLDER-ice & MODIS-liquid (2-1); POLDER-liquid & MODIS-liquid (2-2); POLDER-mixed & MODIS-liquid (2-3); POLDER-ice & MODIS-mixed (3-1); POLDER-liquid & MODIS-mixed (3-2); POLDER-mixed & MODIS-mixed (3-3). Dashed line is for Oxygen pressure from POLDER, dash-dot line is for Rayleigh pressure from POLDER and solid line for CO2 pressure.*
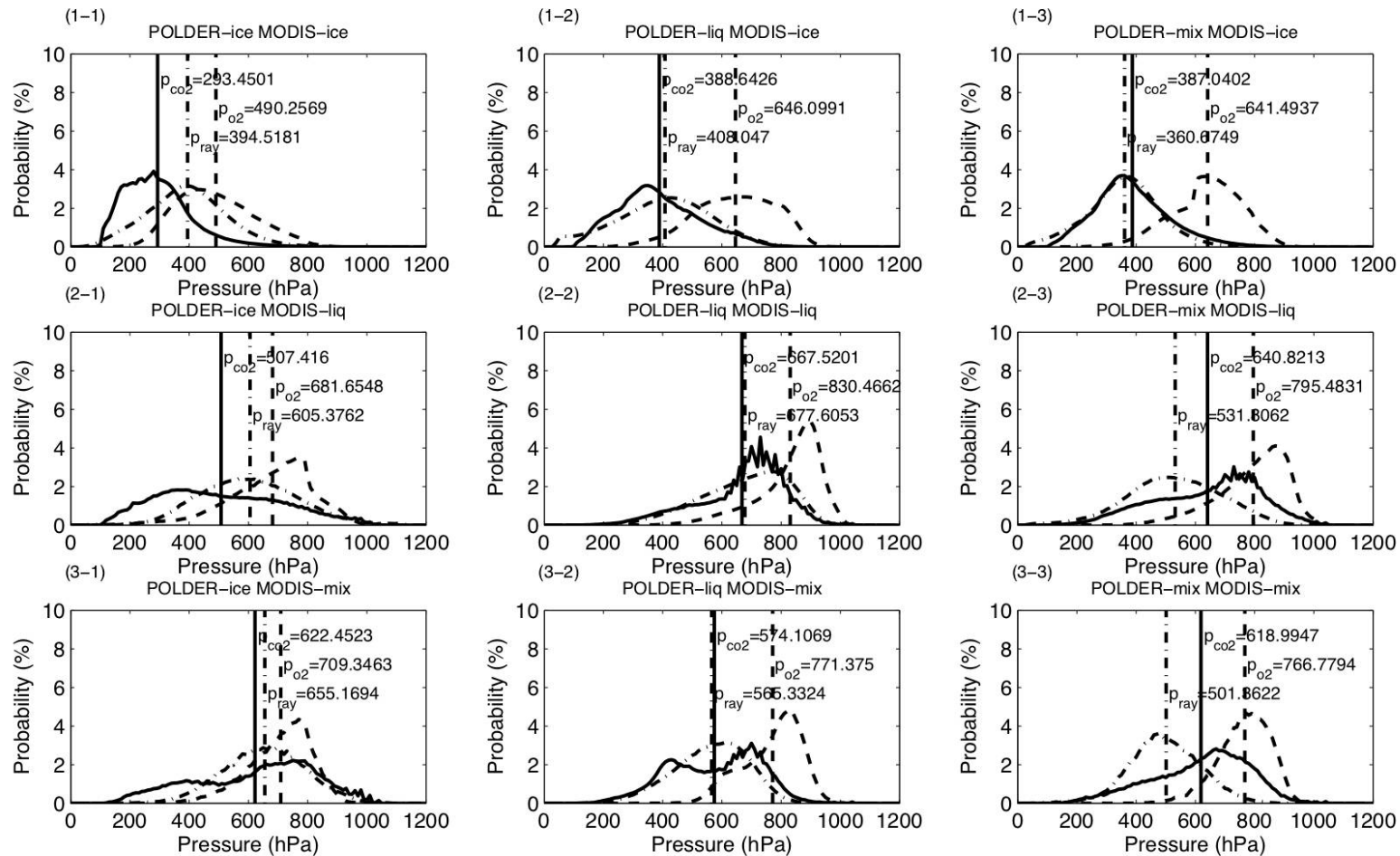
Figure 4.3-6 – *Histogram of the cloud top pressure for 9 combined phases in overcast scenes: POLDER-ice & MODIS-ice (1-1); POLDER-liquid & MODIS-ice (1-2); POLDER-mixed & MODIS-ice (1-3); POLDER-ice & MODIS-liquid (2-1); POLDER-liquid & MODIS-liquid (2-2); POLDER-mixed & MODIS-liquid (2-3); POLDER-ice & MODIS-mixed (3-1); POLDER-liquid & MODIS-mixed (3-2); POLDER-mixed & MODIS-mixed (3-3). Dashed line is for Oxygen pressure from POLDER, dash-dot line for Rayleigh pressure from POLDER and solid line for CO2 pressure from MODIS.*

Figure 4.3-7 illustrates the angular dependence of the occurrence frequencies (for all scenes) of 3 phase products (a) and 4 combined phase classes (b) derived from MODIS and POLDER. Note here, as MODIS is a scanning radiometer, its viewing angles represent roughly the distances to the orbit center, the pixels at nadir being located at the center of the orbit and oblique directions corresponding to the edges of the orbits. Negative viewing angles are associated to relative azimuth inferior to 90°, which means the sensor and the sun being on the same side with respect to satellite ground track, namely backward direction or the eastern side of the orbit. This figure intends to identify the angular bias of cloud phase retrieval in each algorithm:

- We notice again that MODIS IR phase detects the largest fraction of liquid phase in agreement with Table 4.3-1. This phase shows fairly smooth variations against the viewing angles and symmetric distribution for both backward and forward scattering directions. Liquid (ice) cloud fractions have a slight increase (decrease) with viewing angle. This slight increase of liquid clouds may be due to the longer absorption/emission path of water vapor above clouds in the more oblique directions.

- We also notice that both MODIS combined phase and POLDER phase show asymmetric variations against the viewing angle: POLDER detects more liquid fraction in the western of the orbit around 10°-20° of MODIS viewing angle (often corresponding to rainbow directions of POLDER); MODIS detects more ice fraction for the whole forward directions. As no obvious angular asymmetric characteristics of cloud cover have been detected for either MODIS or POLDER (see chapter 3, Figure 3.3-6), these asymmetric behaviors of cloud phase are most likely due to the angular dependent retrieval biases produced by POLDER and MODIS algorithm, both of which employ visible channels to retrieve cloud phase. This may be related to the fact that both the total and polarized radiation reflected in visible and SWIR present angular distribution different for the water and ice particles phase function which are not completely accounted for in both algorithms.

    - For MODIS that uses the ratio of reflected radiation in visible and near infrared (R_{NIR}/R_{VIS}<threshold is ice, see Figure 4.2-7), a constant threshold against viewing angle is not sufficient to classify the phase with the same sensitivity. This is because the cloud particles phase functions show a strong

scattering peak in the forward directions, although the peak is in a narrow angular width, the multiple interactions could broaden the solid angle through which radiation is primarily scattered and lead to a radiation maximum in a large range of forward directions (Bréon, 1992). As solar radiation in forward directions increases, it is easier to get smaller ratio in forward directions than backward direction, and thus classify more ice clouds and less liquid clouds in these directions

- For POLDER that uses angular variation of polarization in its algorithm, the strong polarization feature of liquid clouds (see Figure 4.2-1) in rainbow directions can be more easily captured and identified, even with a thin layer of cirrus overlapping. The rainbow test is therefore the most efficient test in the phase algorithm. At the same time, the probability to observe the rainbow directions (scattering angle around 140°) in the western orbit around 10°-30° of MODIS viewing angle (see Figure 4.3-8) is twice the probability in other parts of the orbit. As a consequence, POLDER tends to detect more easily liquid clouds in this region.
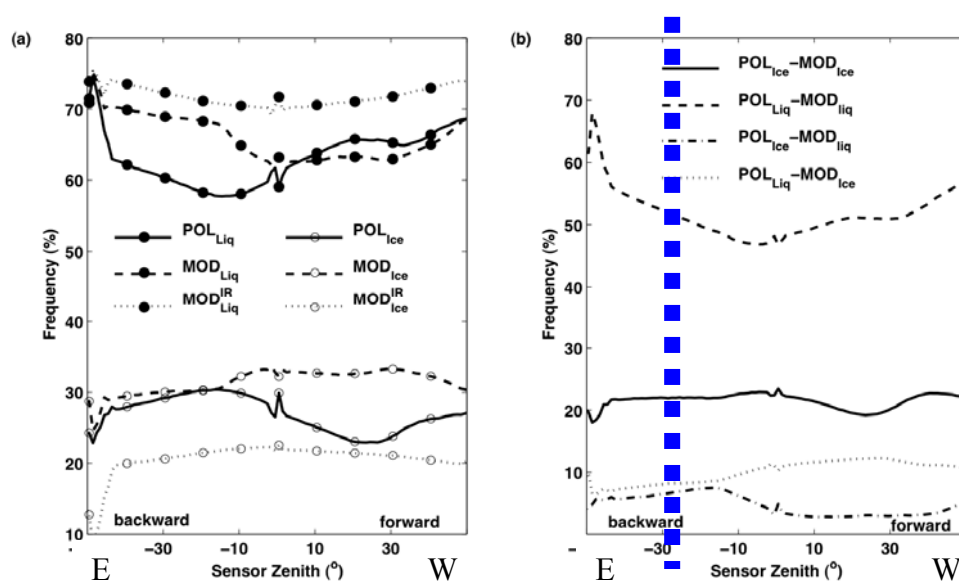
Figure 4.3-7 – *The occurrence frequency of 3 cloud phase products (a) and of 4 out of 9 combined phases (b) from POLDER and MODIS as function of MODIS viewing angle. Blue dashed line represents the CALIOP trace, which should be kept in mind in the following studies.*
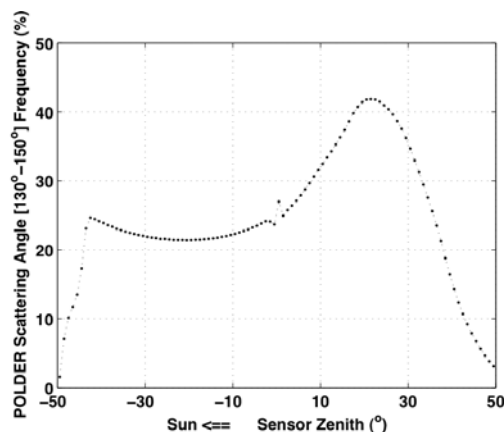
Figure 4.3-8 – *The occurrence frequency of POLDER rainbow directions (scattering angle between 130°-150°) against MODIS viewing angle.*

Note that, the combined phases also show an angular bias (see Figure 4.3-7, b) as a direct consequence of individual algorithm biases previously described. More important, it is worth keeping in mind that CALIOP orbit track actually allow to sample POLDER and MODIS pixels approximately located along the blue dashed line on the eastern part of the MODIS swath. Therefore, validation studies presented hereafter between passive and active sensors correspond to these angular regions and results should be mitigated in view of the intrinsic angular variability of POLDER and MODIS cloud phase products.

4.4 Validation between passive & active sensors

In the previous part, we presented and analyzed the pixel-to-pixel comparisons of cloud phase products derived from the two passive sensors POLDER and MODIS. It helped in identifying the confident and ambiguous cloud phase cases corresponding to different geolocations and environments. However, with these results, it is still difficult to evaluate quantitatively the performance of each sensor in correctly identifying the cloud phase, or under which precise circumstances the presence of cirrus could yield ambiguous phase decision. In order to assess the correctness of each cloud phase product and to reveal more information from the ambiguous phases, we have introduced in our analysis a third cloud phase product derived from the active sensor CALIOP. In the following sections, we present the results of the validation of

POLDER and MODIS phase products against the CALIOP observations and cloud phase product (referred as PC thereafter). This study will help to show how and when CALIOP agrees with the two passive sensors, how cirrus could impact the cloud phase and so on. Note that, in this and following sections, all comparisons between the active and passive sensors use the data from the CALTRACK Dataset (see chapter 2) and the analysis period is also chosen from December 2007 to November 2008.

4.4.1 The study of CALIOP γ-δ features for opaque clouds

As seen in section 4.2.3, CALIOP can identify the cloud phase mainly owning to the different features of layer-integrated depolarization (δ) and layer-integrated attenuated backscatter at 532nm (γ) between ice and liquid. In Figure 4.2-8, we have seen the distinct features between opaque ice and liquid clouds. In this section, we also select the opaque clouds from CALIOP (no signals return from the ground) and plot the γ-δ features for the 9 combined phase classes from passive sensors. Results are shown in Figure 4.4-1 (for all scenes) and Figure 4.4-2 (for overcast scenes). From these plots, we can see the following:

- **For confident classes** when both POLDER and MODIS are in agreement of phase detection (the subplots in the diagonal):

  - The confident ice clouds (Figure 4.4-1, 1-1 and Figure 4.4-2, 1-1) have typical γ-δ feature of ice clouds as shown in Figure 4.2-8: low backscattered radiation and high depolarization
  - The confident liquid clouds (Figure 4.4-1, 2-2 and Figure 4.4-2, 2-2) have typical γ-δ feature of liquid clouds as shown in Figure 4.2-8: relative high backscattered radiation and the depolarization increases with backscattered light
  - The confident mixed clouds (Figure 4.4-1, 3-3 and Figure 4.4-2, 3-3) have feature locating in the crossing region of liquid and ice clouds

In conclusion, for confident classes, the γ-δ features from CALIOP agree extremely well with the phases derived from passive sensors.

- **For inconsistent classes** when POLDER and MODIS phase decisions are in disagreement or present low confidence:

  - For POLDER-liquid & MODIS-ice (Figure 4.4-1, 1-2 and Figure 4.4-2, 1-2), POLDER-ice & MODIS-liquid (Figure 4.4-1, 2-1 and Figure 4.4-2, 2-1), POLDER-ice & MODIS-mixed (Figure 4.4-1, 3-1 and Figure 4.4-2, 3-1) and POLDER-liquid & MODIS-mixed (Figure 4.4-1, 3-2 and Figure 4.4-2, 3-2) clouds, CALIOP agrees with POLDER in a significant majority of the cases.
  - For POLDER-mixed & MODIS-ice (Figure 4.4-1, 1-3 and Figure 4.4-2, 1-3) and POLDER-mixed & MODIS-liquid (Figure 4.4-1, 2-3 and Figure 4.4-2, 2-3) clouds, CALIOP in majority agrees with MODIS most of the time.
  - The most important changes between overcast and all scenes appear for the POLDER-ice & MODIS-liquid clouds (Figure 4.4-1, 2-1 and Figure 4.4-2, 2-1). In this particular case, we clearly see that some pixels labeled as ice clouds by POLDER and liquid clouds by both MODIS and CALIOP, come partially from broken cloud scenes, corresponding to either broken liquid water clouds or thin aerosol layer above broken liquid water clouds (Waquet *et al.*, 2009).

In conclusion, CALIOP γ-δ features are very consistent with MODIS and POLDER phase products when those two agree. In cases where POLDER and MODIS have inconsistent decisions, CALIOP tends to agree with POLDER more often. This is most probably because both POLDER and CALIOP use somehow similar information content for their retrievals that are based on the polarization analysis and are in fact particle shape determination methods.
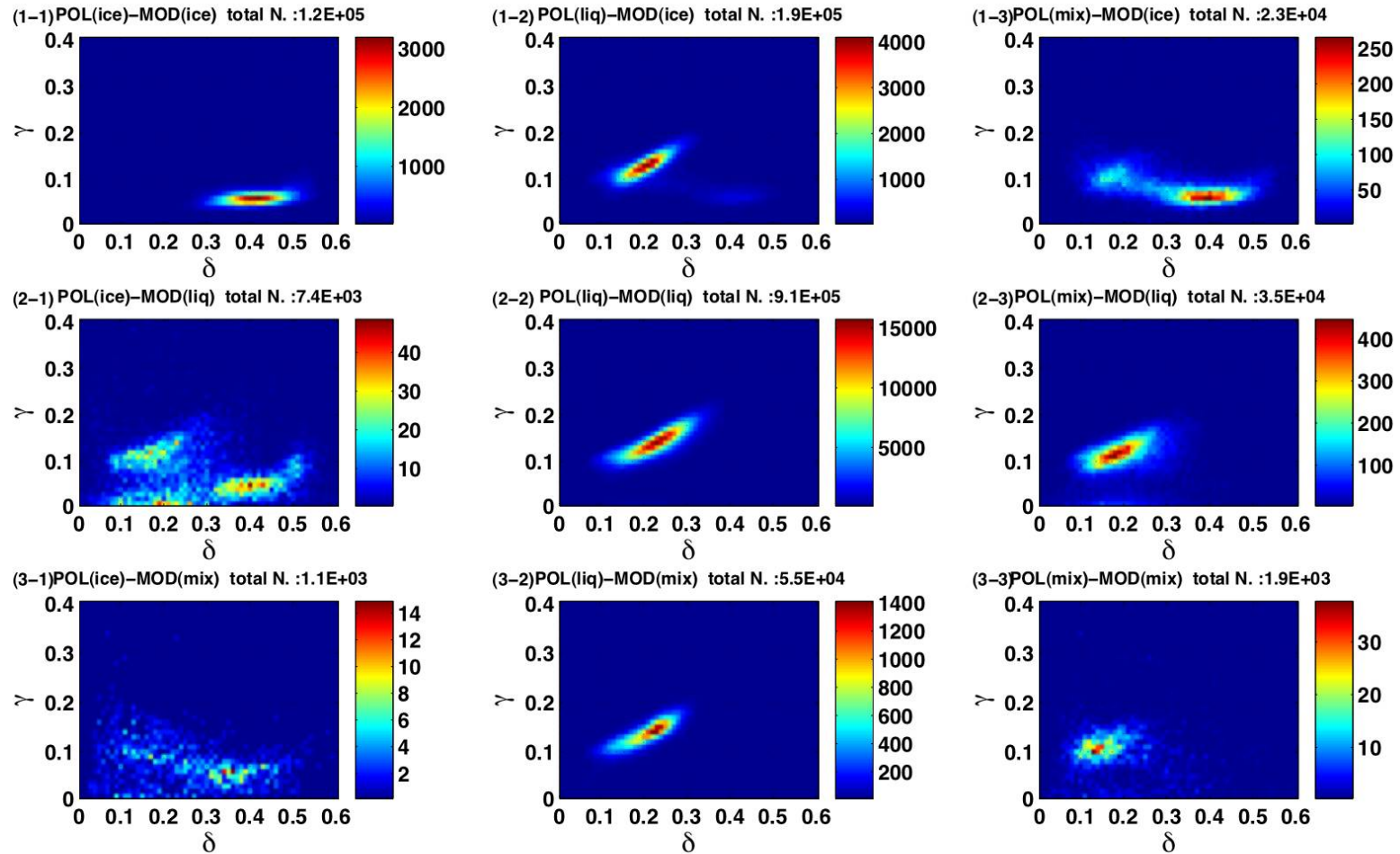
Figure 4.4-1 – *Statistical features of layer-integrated attenuated backscatter at 532nm (γ) and layer-integrated depolarization (δ) for opaque clouds of 9 combined phases determined by POLDER and MODIS: POLDER-ice & MODIS-ice (1-1); POLDER-liquid & MODIS-ice (1-2); POLDER-mixed & MODIS-ice (1-3); POLDER-ice & MODIS-liquid (2-1); POLDER-liquid & MODIS-liquid (2-2); POLDER-mixed & MODIS-liquid (2-3); POLDER-ice & MODIS-mixed (3-1); POLDER-liquid & MODIS-mixed (3-2); POLDER-mixed & MODIS-mixed (3-3).*
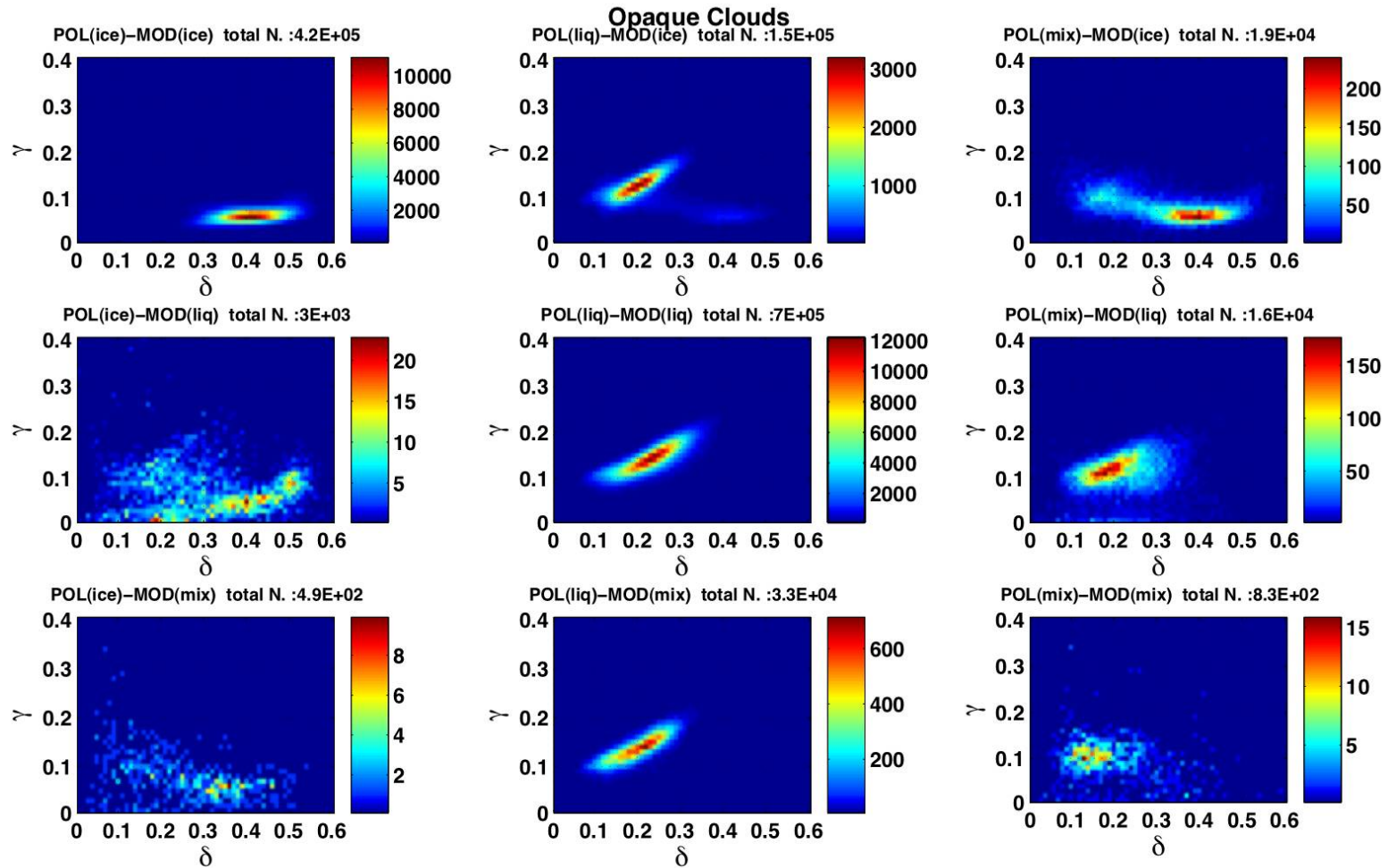
Figure 4.4-2 – *Statistical features of layer-integrated attenuated backscatter at 532nm (γ) and layer-integrated depolarization (δ) for overcast opaque clouds of 9 combined phases determined by POLDER and MODIS: POLDER-ice & MODIS-ice (1-1); POLDER-liquid & MODIS-ice (1-2); POLDER-mixed & MODIS-ice (1-3); POLDER-ice & MODIS-liquid (2-1); POLDER-liquid & MODIS-liquid (2-2); POLDER-mixed & MODIS-liquid (2-3); POLDER-ice & MODIS-mixed (3-1); POLDER-liquid & MODIS-mixed (3-2); POLDER-mixed & MODIS-mixed (3-3).*

4.4.2 Analysis of CALIOP phase product for opaque clouds

We have seen the observations of γ-δ features from CALIOP for the 9 combined phases. In the following presentations, we now analyze the CALIOP phase decisions for these 9 combined phases so as to exactly qualify the agreement between the active and passive sensors. In Figure 4.4-3 (for all opaque clouds), Figure 4.4-4 (for overcast opaque clouds), Figure 4.4-5 (for broken opaque clouds) and Figure 4.4-6 (for clouds over snow/ice), we computed the percentage of ice and liquid phase determined by CALIOP for each combined phase class (one year statistics over the globe) according to different cloudy and environmental scenes. In good consistency with CALIOP observations of γ-δ feature, the CALIOP cloud phase product shows similar tendencies when compared to POLDER and MODIS products. In particular:

For all opaque clouds (see Figure 4.4-3):

● For confident cloud phase classes: consistent phases from POLDER and MODIS (the pie charts in diagonal)

- For confident ice clouds (subfigure 1-1), more than 99% of pixels have ice phase determined by CALIOP.

- For confident liquid clouds (subfigure 2-2), about 95% of pixels have liquid phase determined by CALIOP

In conclusion, the agreement between CALIOP and passive sensors is up to 95% for the confident combined phases.

● For inconsistent cloud phase classes:

Again in good agreement with γ-δ features from CALIOP, CALIOP phase decision tends to agree preferentially with either POLDER or MODIS depending on particular situations:

1. For POLDER-ice & MODIS-liquid clouds (subfigure 2-1), CALIOP phases show more agreements with POLDER (64%).

2. For POLDER-liquid & MODIS-ice clouds (subfigure 1-2), CALIOP phases show more agreements with POLDER (80%).

3. For clouds detected as mixed from any one sensor, CALIOP phases show more agreements with the other sensor (the detailed percentages are shown in the charts).
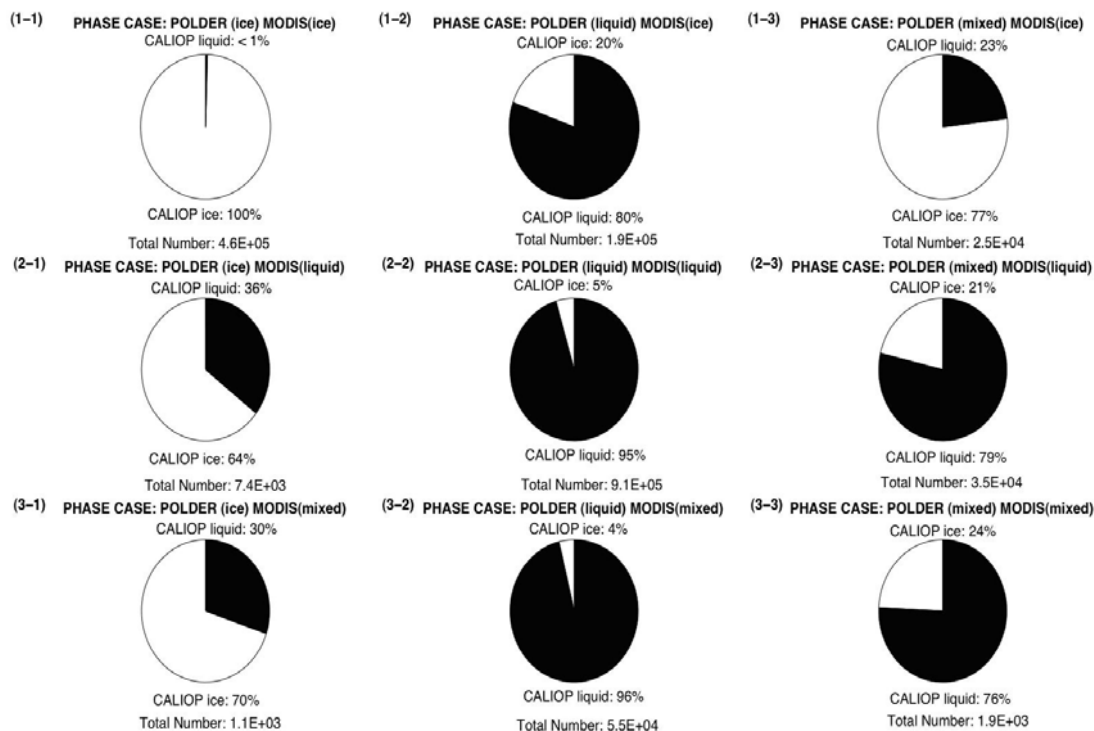
Figure 4.4-3 – *CALIOP liquid and ice cloud fractions for all opaque clouds of 9 combined phases determined from POLDER and MODIS: POLDER-ice & MODIS-ice (1-1); POLDER-liquid & MODIS-ice (1-2); POLDER-mixed & MODIS-ice (1-3); POLDER-ice & MODIS-liquid (2-1); POLDER-liquid & MODIS-liquid (2-2); POLDER-mixed & MODIS-liquid (2-3); POLDER-ice & MODIS-mixed (3-1); POLDER-liquid & MODIS-mixed (3-2); POLDER-mixed & MODIS-mixed (3-3). Black color denotes liquid cloud fractions and white color denotes ice cloud fractions.*

For different cloudy scenes: overcast in Figure 4.4-4 and broken in Figure 4.4-5, the agreements between passive and active sensors present noticeable differences:

- For confident cloud phase classes: (charts along the diagonal)
  - For confident ice clouds, more than 99% of agreements from CALIOP phase in overcast scenes compared to 93% of agreements in broken scenes.

- For confident liquid clouds, about 96% of agreements from CALIOP phase in overcast scenes compared to 79% of agreements in broken scenes.

In conclusion, the agreement between passive and active sensors decreases for broken scenes.

- For inconsistent cloud phase classes:
  - For POLDER-mixed & MODIS-ice clouds (subfigure 1-3) and POLDER-mixed & MODIS-liquid clouds (subfigure 2-3), fewer agreements between MODIS and CALIOP are found in broken scenes compared to overcast scenes.
  - For POLDER-liquid & MODIS-ice clouds (subfigure 1-2), POLDER-ice & MODIS-mixed clouds (subfigure 3-1), POLDER-liquid & MODIS-mixed clouds (subfigure 3-2) and POLDER-ice & MODIS-liquid clouds (subfigure 2-1), more agreements to MODIS from CALIOP are found in broken scenes compared to overcast scenes.

In conclusion, CALIOP shows most of the time a better agreement with MODIS in cases of broken cloud with inconsistent phases between the two passive sensors, which may be contributed to the higher spatial resolution of both MODIS and CALIOP compared to POLDER.
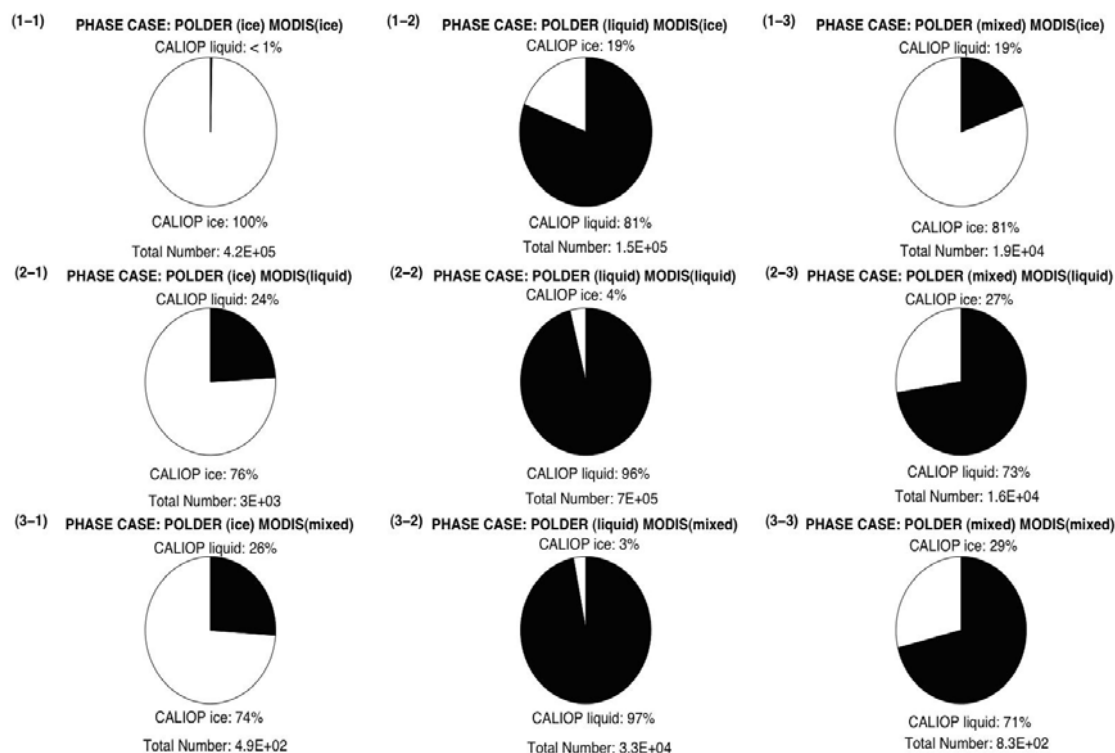
Figure 4.4-4 – *Same as Figure 4.4-3 but for overcast opaque clouds.*
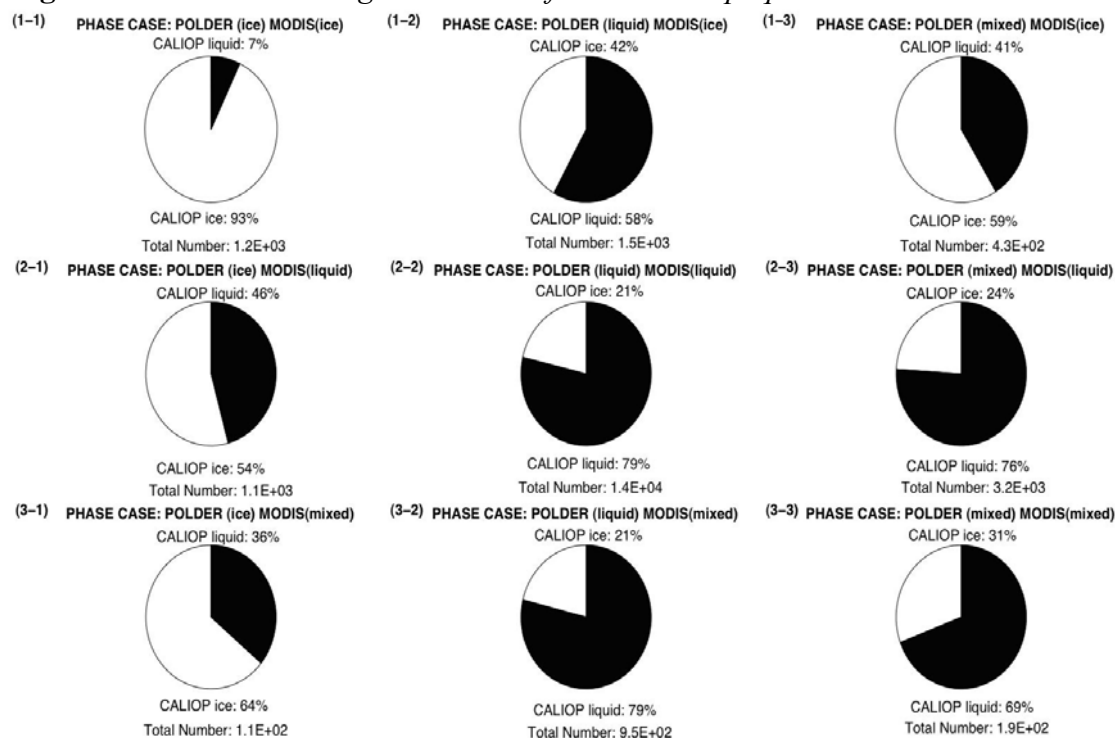
Figure 4.4-5 – *Same as Figure 4.4-3 but for broken opaque clouds.*

Over snow, cloud detections as well as any other cloud property retrievals face significant challenges. It is particularly true for the cloud phase detection in Polar Regions because of the minimal contrast between clouds and the surface, the frequent

occurrence of temperature inversion and the predominance of mixed-phase clouds (Spangenberg *et al.*, 2005). The comparison results between passive and active sensors over the snow (see Figure 4.4-6) therefore deserve special attention to see whether previous results are significantly modified above snow/ice covers. Note that POLDER can only detect the confident clouds over snow (seen in chapter 3, only some high clouds and liquid clouds with strong rainbow signal can be detected) because of its limited spectral range and the lack of thermal infrared channels.

- For clouds with consistent phases between POLDER and MODIS (subfigures in diagonal), good consistencies from CALIOP are also found.
- For other clouds with inconsistent phase decisions (subfigures outside of diagonal), more agreements between POLDER and CALIOP are found as previously.
- Compared to clouds over all surfaces, the agreements on cloud phase between passive and active sensors do not decrease.
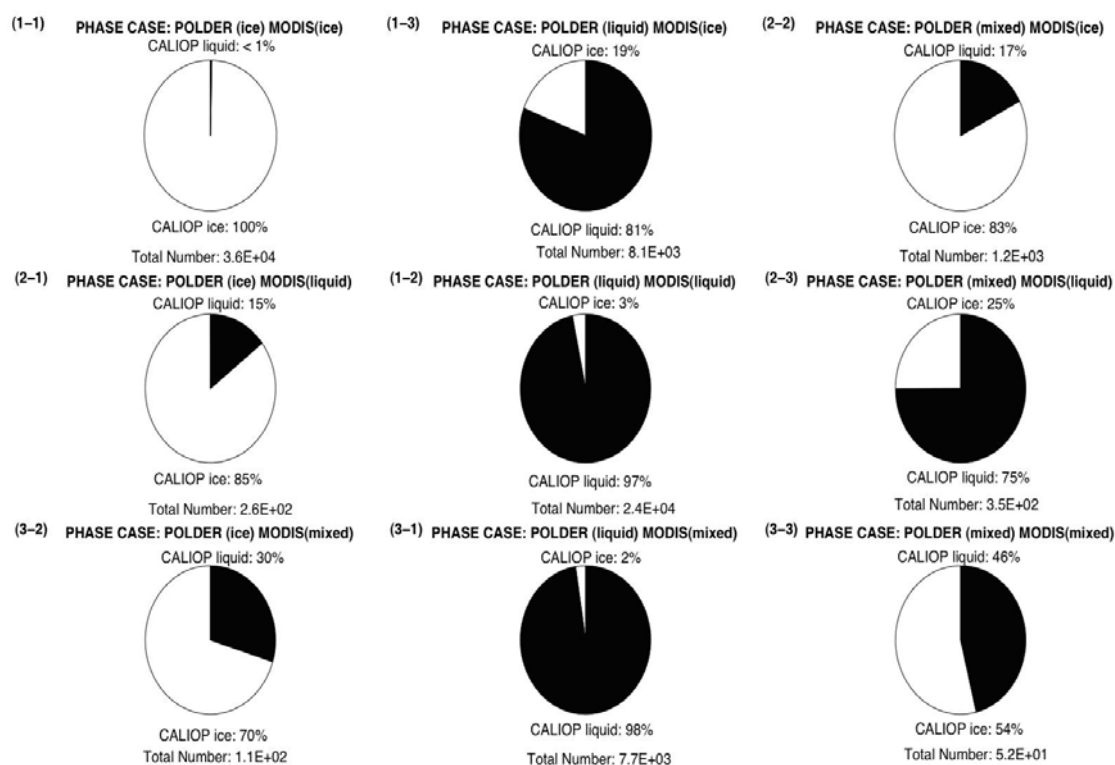
Figure 4.4-6 – *Same as Figure 4.4-3 but for opaque clouds over snow.*

4.4.3 The study of thin cirrus impact on cloud phase

In the previous sections, we have seen the comparisons of cloud phase between passive and active sensors for the opaque clouds only. However we still need to assess the impact of thin cirrus on cloud phase detection.

As we know, for the active sensor CALIOP, it is possible to detect the very thin cirrus. However, for the passive sensors, POLDER and MODIS, if the cirrus is too thin, the radiation from underlying surface may pass through the thin cirrus and bias the retrieved cloud phase toward the lower layer state (Nasiri and Kahn, 2008; Riedi *et al.*, 2010). For cirrus overlying water clouds, the underlying surface that impacts the cirrus radiation to be measured is the water clouds, which have strong polarization and can be much colder than the clear ground. For single layered cirrus, the underlying surface that impacts the cirrus is the clear ground, which has weak polarization and is usually warmer. The temperature of underlying surface could impact the phase derived from MODIS and the polarization of underlying surface could impact the phase derived from POLDER. So, the thin cirrus in multilayered and single layered cloud systems needs to be separately investigated.

In Figure 4.4-7, we used CALIOP observations to select the cirrus cases of interest. For different types of cirrus, we plotted the ice detection frequency against the cirrus optical thickness of the upper most layer derived from the CALIOP 532µm band. The upper two plots represent the ice fractions from one sensor and the lower two illustrate the fractions of the 9 combined phase classes against cirrus optical thickness. Note that, since the cirrus Optical Thickness (OT) can be confidently retrieved by CALIOP only if the clouds are constrained (Young *et al.*, 2008), we only investigated the impact from those thin cirrus having OT less than 1.4. From these plots, we can find that:

● The ice detection probability derived from both POLDER and MODIS increases with cirrus optical thickness for both cirrus in multilayered systems (subfigure a) and single layered systems (subfigure b). In other words, and not surprisingly, the thicker the cirrus, the easier it is to be classified as ice clouds in all cases.

● The probability to correctly identify the cirrus phase however depends strongly on both the cloud system type and the sensor considered:

- **For cirrus over liquid clouds**:

1. When cirrus OT reaches 1, about 90% of thin cirrus can be correctly identified as ice by MODIS

2. When cirrus OT is equal to 1.4, only about 60% of thin cirrus can be correctly identified as ice by POLDER. This is consistent with previous theoretical analysis (Goloub *et al.*, 2000; Riedi *et al.*, 2007) showing that, if cirrus OT is less than 2, POLDER can still see the underlying water clouds, as the strong polarization can still pass though the thin cirrus.

MODIS has a higher sensitivity to thin cirrus over water clouds and accordingly, the probability to detect ice phase in case of thin cirrus over liquid clouds increases with the cirrus optical thickness more rapidly than POLDER.

- **For single layered cirrus**:

1. For POLDER, when the cirrus OT is equal to 0.3, 80% of cirrus can be correctly identified as ice

2. For MODIS, when the cirrus OT is equal to 0.3, only 40% of cirrus can be correctly identified as ice; 80% of cirrus can be correctly identified as ice when cirrus OT reaches the value of 0.6.

POLDER is more likely to detect ice phase in case of thin cirrus in single layered systems, which again agrees well with the simulation from Riedi et al. (2007).

● For the fractions of 9 combined phase classes against the cirrus OT in Figure 4.4-7, c and d:

- The confident ice fraction increases with cirrus OT and confident liquid fraction decrease with cirrus OT; when the cirrus OT is greater than 1, the confident liquid cloud fraction decreases to about 10% (<5%) and confident ice cloud fraction increases to about 60% (>80%) in multilayer (single layer) cloud systems.

- The inconsistent phase classes occur significantly when the cirrus is thin.

1. In multilayer cloud systems, the fraction of MODIS-ice and POLDER-liquid clouds reaches to a maximum of 30% when cirrus OT is about 0.6; the fraction of MODIS-ice and POLDER-mixed clouds reaches 10% when cirrus OT is between 0.6 and 1.4.

2. In single layer cloud systems, the fraction of MODIS-mixed and POLDER-ice clouds reaches to a maximum of 10% when cirrus OT is about 0.2; the fraction of MODIS-liquid and POLDER-ice clouds reaches to a maximum of 30% when cirrus OT is about 0.3.

Note here that, in case of very thin cirrus, the cloud top detected by CALIOP may not correspond to the level where the POLDER/MODIS phase is retrieved. To make a coherent comparison between the cloud top level from CALIOP and the phase retrieval level from POLDER and MODIS, at least the thin cirrus with optical thickness less than 1 should be excluded from the analysis. This will be used in the later study of vertical ice-liquid transition with the cloud dynamics in section 4.5.
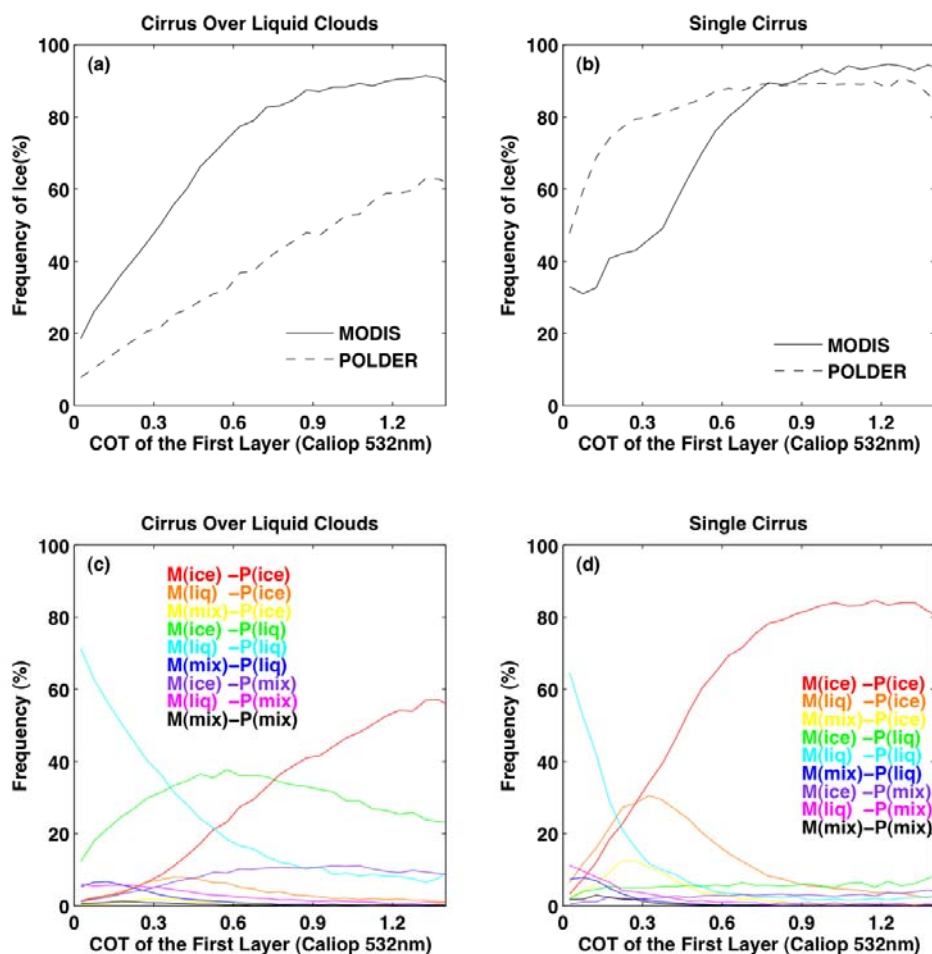
Figure **4.4-7** – *The fraction of cloud phase classes derived from POLDER and MODIS against the optical thickness of the upper most cirrus determined by CALIOP: cirrus over water clouds (a), single layered cirrus (b) and the fraction of combined phases derived from POLDER and MODIS against the optical thickness of the upper most cirrus determined by CALIOP: cirrus over water clouds (c), single layered cirrus (d).*

4.4.4 Impact of supercooled droplets

As mentioned above, difficulties in phase detection arise from the frequent occurrence of supercooled liquid clouds. For supercooled liquid clouds, MODIS by using IR brightness temperature or brightness temperature differences has troubles discriminating between ice and liquid phase due to the small contrast between supercooled and ice water. However CALIOP and POLDER by using polarization are less impacted by the supercooled droplets because the polarization and the retrieved phase decision depend only on the particle shape.

In Figure 4.4-10, we plotted the liquid fraction as function of cloud top temperature determined by CALIOP. The Data sample corresponds to a one year period when CALIOP sees only water clouds. From this figure we see that, when cloud top locates between 0°C and -40°C, the supercooled liquid cloud fraction predicted by MODIS is much less than 100% and increases with cloud top temperature. This result suggests that for MODIS, the supercooled droplets can be largely erroneously labeled as ice especially for higher level supercooled droplets. However for POLDER, liquid cloud fraction is saturated and close to 100% when cloud top temperature below -30°C, especially for overcast clouds, in other words, POLDER most probably correctly identify those supercooled droplets. In conclusion, POLDER detection technique appears much less biased by the occurrence of supercooled clouds compared to MODIS.

Moreover further studies are needed involving CloudSat to separately discuss the respective impact of a simple supercooled liquid cloud and a thin layer of supercooled liquid clouds over ice clouds to evaluate in which condition MODIS phase may be preferentially biased.
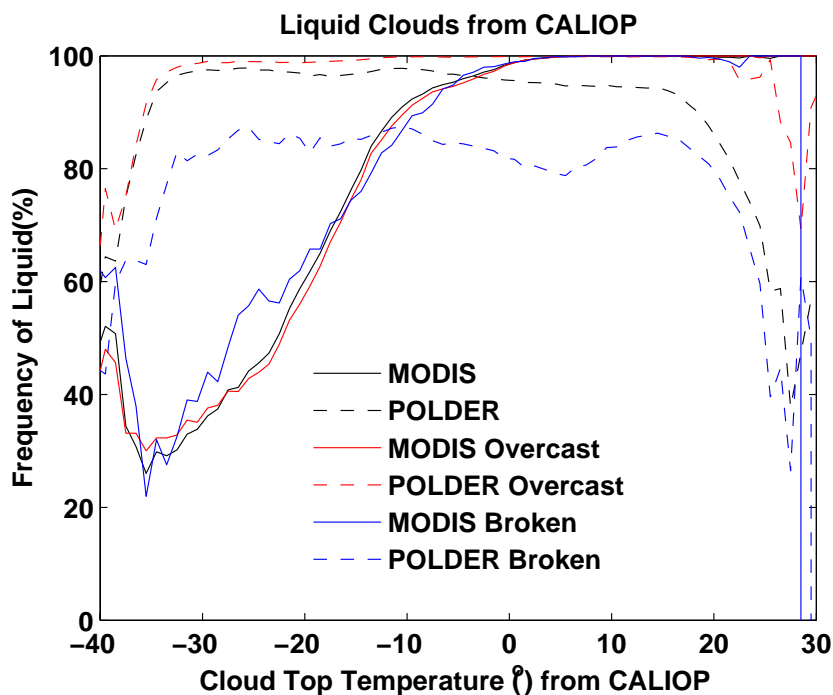
Figure 4.4-8 - *The fraction of liquid clouds for POLDER and MODIS as function of cloud top temperature derived from CALIOP for liquid clouds identified by the lidar depolarization technique.*

4.4.5 Impact of aerosols on cloud phase retrievals

POLDER uses the polarized radiance to discriminate cloud phase. This information and therefore the correctness of retrieved phase can be greatly affected by the presence of aerosols, which have small sizes and can produce strong polarization in visible bands. Some aerosols, such as desert dust, are often perceived and observed as non-spherical shape and their polarization features are therefore close to those produced by ice particles in clouds. Since aerosols are much smaller than ice particles, small optical thicknesses (e.g. 0.225) are required to shut out the signal from the underlying water clouds especially beyond the rainbow directions between 80° to 120° of scattering angle (see Figure 4.4-9, b yellow point; from Waquet *et al.*, 2009). So according to the available scattering angle in the retrieval, the ice or mixed phase could be obtained from POLDER when aerosols are present over the low water clouds (<120°: ice; >120°: liquid; both > and < 120°: mixed). For MODIS, some large

absorbing aerosols may act as ice crystals, however their contribution to total radiance is relatively much smaller than for polarization and can be neglected.
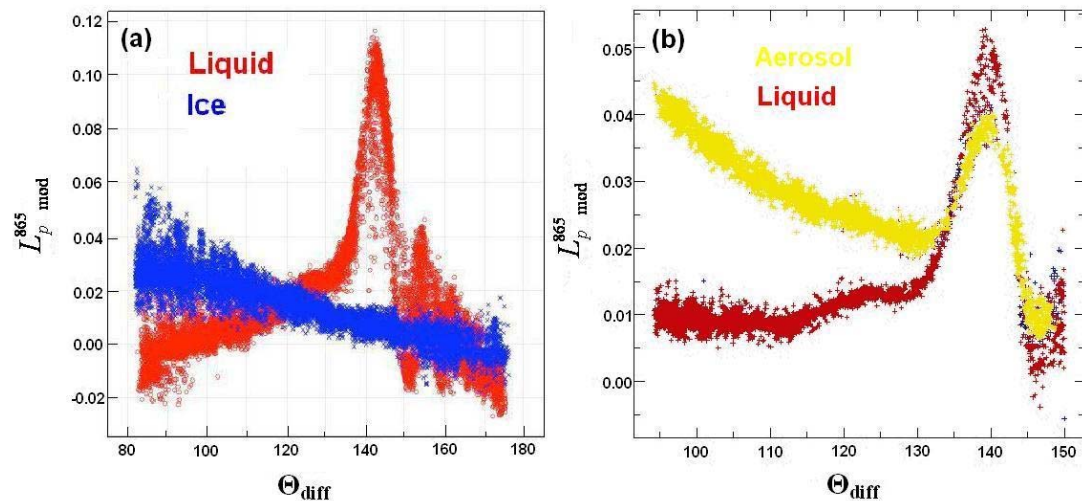
Figure 4.4-9 – *Polarized radiance measured by PARASOL at 0.865 μm as a function of the scattering angle for the two cases: only liquid or ice clouds are presented (liquid: subfigures a and b in red; ice: subfigure a in blue) and significant load of biomass burning was detected above the water clouds (subfigure b in yellow) from Waquet et al,(2009).*

We have already noticed above, the dominant regions of occurrence for POLDER-ice & MODIS-liquid clouds (Figure 4.4-10, c) and POLDER-mixed & MODIS-liquid clouds (Figure 4.4-10, d) are mostly around Africa, and coincide with regions of frequent occurrence of heavy aerosols and aerosols events over low water clouds (see Figure 4.4-10, a and b). In addition, we have also noticed that in Figure 4.4-10 POLDER detects erroneously the ice clouds in the warm atmosphere above 0°C that can be also linked to the aerosols. In conclusion, those aerosols with non-spherical shapes may cause troubles in detecting the phase of low clouds with the measurement of polarization from POLDER. However, on the other hand, the polarization information is a virtue to reveal the high aerosols over low clouds (e.g. Waquet et al., 2009).
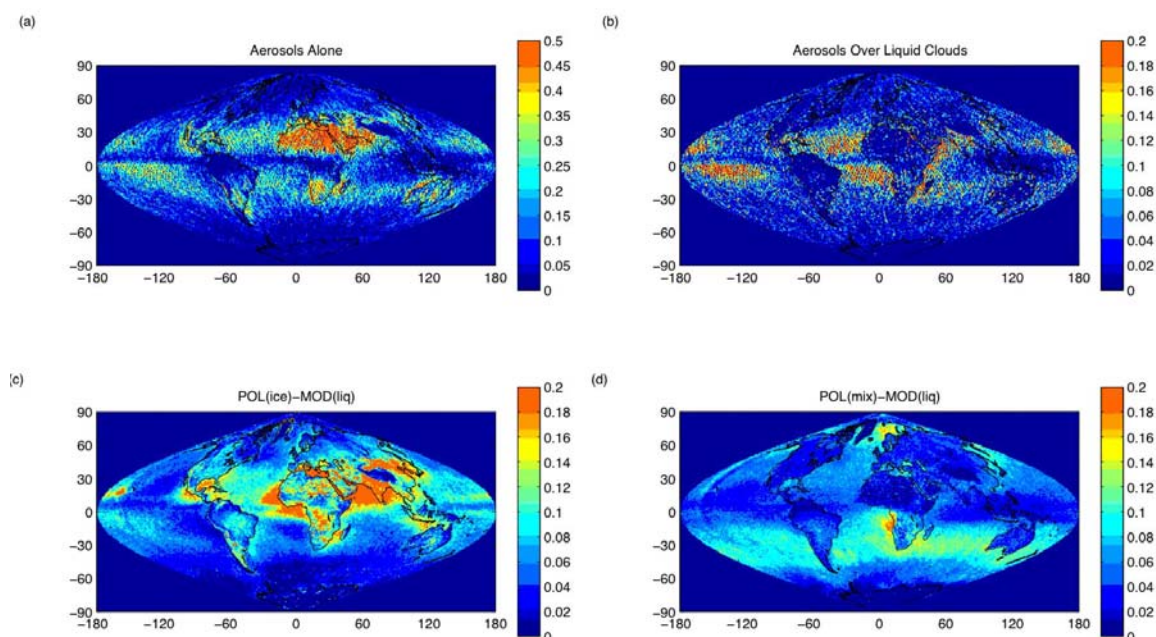
Figure 4.4-10 – *Occurrence frequency of aerosols (a), and aerosols over water clouds (b) derived from CALIOP; occurrence frequency of POLDER-ice & MODIS-liquid cloud (c) and POLDER-mix & MODIS-liquid clouds (d) from the PM dataset.*

4.4.6 Impact of Broken clouds

When the polarization signal is unsaturated, as is frequent for broken clouds, POLDER may give ambiguous phase decision. This is indeed what we observed when comparing Figure 4.4-1 and Figure 4.4-2. Broken clouds can be detected as ice for POLDER and as liquid for both CALIOP and MODIS. Again in Figure 4.4-10, we also note that the liquid fraction of POLDER for level of cloud top temperature above 0°C is less than 1 especially for broken clouds. About 20% of liquid broken clouds have ice or mixed phase decisions. Concerning MODIS, there is no such problem in its phase detection. Since the broken liquid cloudy scene is a mixture of liquid clouds and clear sky, the latter with a warmer brightness temperature and a negative brightness temperature will radiatively looks like liquid clouds when using MODIS detection method. However polarization angular feature of clear sky is similar to ice clouds and thus detected as ice by POLDER.

4.5 Relation between Vertical Water-Ice Transition and Cloud Dynamics, Thermodynamics and Microphysics

In the previous studies, it has been demonstrated that the agreement on ice or liquid phase detection from POLDER and MODIS provides a subset of high confident retrievals, as CALIOP agrees for more than 95% of them, especially for overcast opaque clouds. With these confident cases found above, we try to study the vertical water-ice transition and its relationship with the cloud dynamics, thermodynamics and microphysics. Indeed, these parameters are linked to the ice nucleation processes and can be further evaluated in cloud models and GCMs. This study could help us understand the ice nucleation processes in the real atmosphere at globe scale and improve the presentation of cloud phase, especially the cloud phase at the water-ice transition level in cloud models.

4.5.1 Vertical distribution of cloud phase and properties

The first important parameter in the ice nucleation process is the temperature. Because temperature tends to decrease with altitude, the vertical development of clouds trigger the ice nucleation. At the same time, the other cloud microphysical properties will also change with the development of the clouds. So, in a first stage, we looked at the vertical distribution of cloud phase and effective radius and evaluated the consistency of these distributions with what we understand theoretically about cloud development.

In Figure 4.5-1, the fractions of 9 phase cases as a function of cloud top temperature (derived from CALIOP) are plotted for a whole year of data from December 2007 to November 2008 at global scale. In Figure 4.5-1 (a), all clouds are selected including also very thin cirrus; in Figure 4.5-1 (b), cloud with OT greater than 1. As already mentioned, for the very thin cirrus, cloud top may not correspond to the equivalent mean radiative altitude where the combined phases are retrieved (see section 4.4.3). This explains why 40% of the clouds at temperature below -80°C are still detected as liquid clouds: the phase retrievals are insensitive to the upper thin

cirrus overlaying low water clouds. If we strictly eliminate the thin cirrus with OT less 1, fractions close to about 100% of combined ice (liquid) phase are found when the temperature T<-40° (T>0°). Between 0°C and 40°C, water transits slowly to ice and ice fraction non-linearly increases with the decrease of cloud top temperature.

Figure 4.5-1 (b) again confirms that POLDER-liquid & MODIS-ice (green points) clouds correspond to either supercooled water or the thin cirrus overlaid system while the POLDER-ice & MODIS-liquid (yellow points) clouds are most probably corresponding to the low broken clouds or the aerosols.
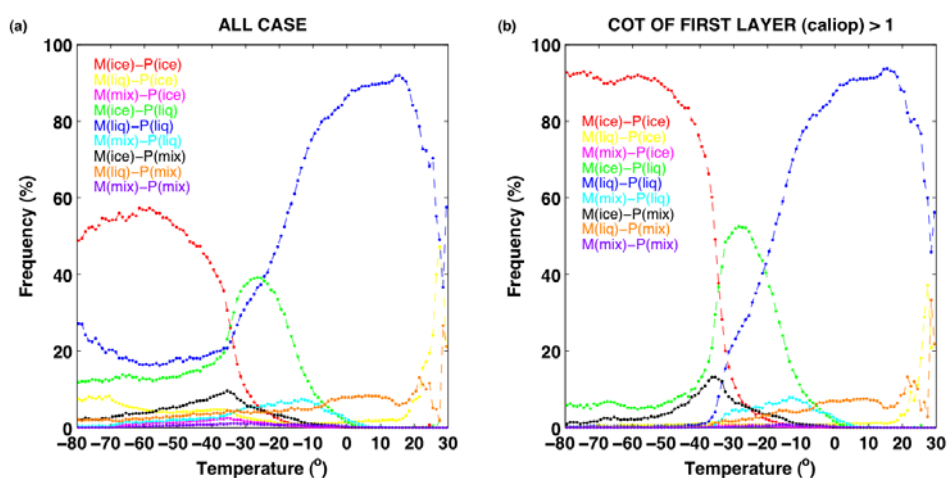
Figure 4.5-1 – *Occurrence frequencies of 9 combined phase classes as a function of cloud top temperature derived from CALIOP for all clouds (a) and for clouds with COT of upper most layer greater than 1 (b). M: MODIS, P: POLDER, liq: liquid.*

As the cloud development and freezing process have an important relation with particle sizes, we analyze in the following the vertical distribution of the cloud effective radius determined by MODIS (see Figure 4.5-2).

In Figure 4.5-2 (a), it appears that the cloud particle size distribute around two distinct modes corresponding to either phase: at low temperature, the ice crystals have a mean radius of about 25; at warm temperature, the water droplets have a mean radius of about 15. In the water-ice transition zone, the mean effective radius increases with temperature as more and more ice crystals are produced.

If we separate ice from liquid clouds (see Figure 4.5-2, b), the mean radius of ice crystals increases with increasing cloud top temperature that agrees with both the observations and the model parameterizations (Donovan and Lammeren, 2002;

Heymsfield and Platt, 1984). For liquid clouds, however, the mean radius of water droplets decreases with cloud top temperature when clouds are colder than 0°C but increases with the decrease of cloud top temperature when clouds are warmer than 0°C that also agrees with other studies (Rogers and Yau, 1989; Martin *et al.*, 1994; Miles *et al.*, 2000).

The decrease of ice crystal radius with temperature is a consequence of combining factors, for example, the fall of large crystals when lacks of strong vertical dynamics in the high atmosphere and also the evaporation due to the decrease of vapor content with altitude (Houze, 1994).

For water droplets, the observed variation of the mean radius with temperature results from two competitive processes: first, the water droplets could grow as a result of condensation and collision when they are lifted in strong updraft air; second, when temperature decreases below the freezing point, large particles tend to deposit to solid phase with only smaller particles remaining in liquid phase, which tend to produce a decrease of the remaining water droplets radius (Houze, 1994). In warm water clouds, droplet sizes grow as the first process dominates and in cold water clouds, droplets decrease as the second process dominates.

In this figure we also see that the zonal means effective radius present significant differences: ice crystals and water droplets in polar regions are smaller than elsewhere, and especially smaller than the tropical regions at any temperature or altitude). This observation agrees with other studies (Boudala *et al.*, 2002; Heymsfield, 2003). The different freezing mechanisms occurring at different latitudinal zones may be one reason for the differences of the maximum radius among latitudinal zones, but availability of water vapor is certainly another major influence (Stubenrauch *et al.*, 2004).

If we now concentrate on Figure 4.5-3, we see the vertical distribution of droplets (subfigure a) and crystals (subfigure b) sizes grouped by range of effective radius. As it has been shown in subfigure a, the smallest droplets with radius between 1 and 5 distribute between -40°C and 20°C, with most droplets occurring around -20°C. When the droplets become larger, both their distribution and the peak of the histogram shift toward warmer temperature. This distribution variation agrees with Figure 4.5-2 and confirms that the largest droplets tend to freeze first and that smaller droplets may remain in supercooled liquid phase at very low temperature. For ice crystals (subfigure b), we also see that the distribution and the peak of the histogram

shift slightly toward warmer temperature when their sizes increase, which again agrees with Figure 4.5-2. This vertical distribution may be due to the strong evaporation at cloud top in the higher atmosphere and the strong uplift in the lower atmosphere.
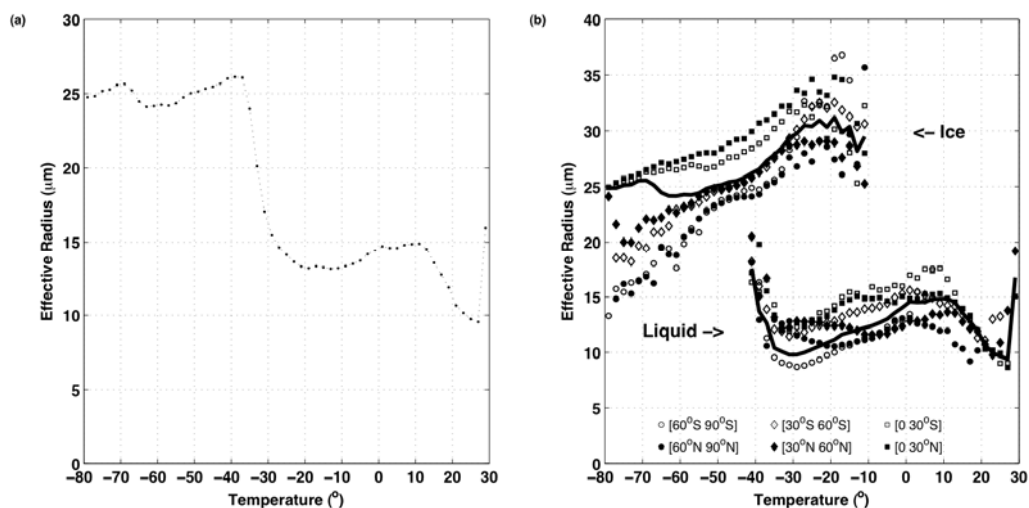
Figure 4.5-2 – *Vertical distribution of mean particle sizes for all clouds (a) and with separation of ice and liquid phase for 6 latitudinal zones (b), the solid line represents the global mean value.*
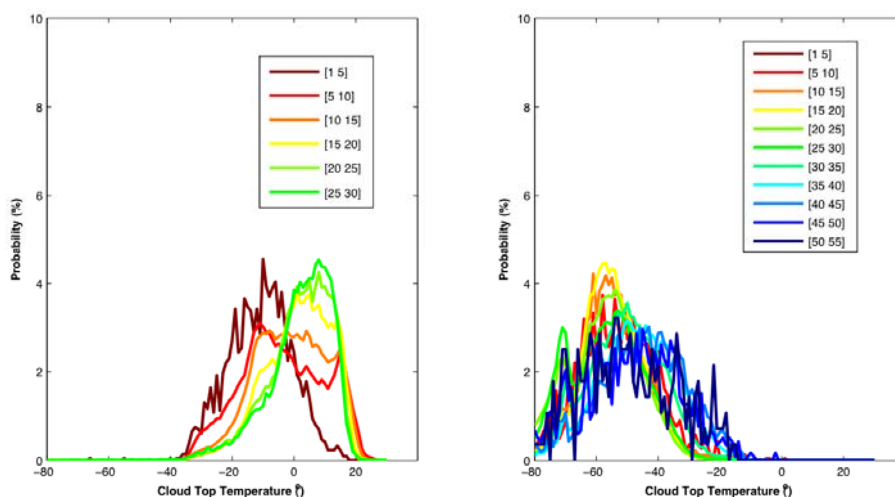
Figure 4.5-3 – *Histograms of particle number for different droplets (a) and crystals (b) radius range against the cloud top temperature.*

4.5.2 Global and regional water-ice transition

In cloud models, the ambient temperature at a certain level is often used to define the liquid and ice fractions. In a GCM, the occurrence frequency of cloud phase (ice or water) in the water-ice transition zone between T_m (freezing temperature, below which there are no liquid droplets. e.g. T_m=-40°C) and T_0 (above which there are no ice droplets. e.g. T_0=0°C) is a simple one-to-one relationship to the cloud top temperature T. Many studies show that the freezing temperature (T_m) of supercooled water droplets is near -40°C, but the precise temperature for homogeneous ice nucleation depends on lots of microphysical and dynamical factors.

In the following, we examine the one-to-one function of cloud phase frequency and cloud top temperature by using our confident phases derived from combination of POLDER and MODIS. In this study, we did not try to adopt the exponential function of frequency and temperature employed by CALIOP, nor any other functions used in cloud models (e.g. Le Treut and Li, 1991; Del Genio *et al.*, 1996). Instead, we use a simple hyperbolic tangent function to fit the satellite observations:

$$X_{liq,ice} = (1 + \tanh(a_1 * T + a_2))/2 \qquad \text{(Eq. 4.5-1)}$$

The underlying mechanisms of ice nucleation may not be well described by this hyperbolic tangent fitting, and some other functions may fit better the one-to-one relationship. Using the hyperbolic tangent function here however presents a number of significant advantages:

- The shape of this function is quite close to the real observations (see Figure 4.5-1 b and Figure 4.5-4), which can make sure that above T_0, liquid fraction tends to 100% and below T_m, ice fraction tends to 100%.
- The hyperbolic tangent function has particular properties: the constant a_1 controls the flatness of the curve which means the speed of the water-ice transition (small absolute of a_1 means a slow transition from 100% liquid to 100% ice); the other constant a_2 controls the shift of the curve which means the 50% frozen temperature (negative a_2 means a left side movement of the transition curve, namely the 50% frozen temperature moves to the warmer

side). The shift and flatness constants together could control the freezing temperature T_m and T_0. After all, this fitting function could realize and simplify the study of water-ice transition with the cloud dynamics. By studying and comparing the two constants (a_1 and a_2) we can investigate and visualize the regional and seasonal variations of water-ice transition, we can also better understand the different water-ice transition according to various dynamical and microphysical conditions. This numerous study of the two constants makes it possible to apply in cloud models and improve the phase description in them.

- For liquid and ice fractions, a_1 and a_2 are the same absolute values with the opposite signs (a_1 and a_2 are positive for liquid clouds and negative for ice clouds).

Note, the hyperbolic tangent function fitting has been performed strictly and only for the confident liquid and ice clouds as referred above. We exclude from this analysis the mixed phase and less confident phase clouds to ensure that:

1. The sum of ice and liquid fractions is equal to 100%.
2. The problematical phase determination occurring in broken, thin cloud scenes, low aerosols and ground surfaces are mostly excluded.
3. The retrieved microphysical properties from satellites (e.g. the effective radius) are not impacted by phase detection biases.

With these limitations, the annual observations and simulations of ice fraction as a function of cloud top temperature for the whole globe and for different surfaces are shown in Figure 4.5-4, and the hyperbolic tangent fitting for the whole globe is shown in (Eq. 4.5-2). From Figure 4.5-4 we find, T_0 (the 100% liquid temperature) is between -10°C and -20°C, and T_m (the 100% ice temperature) is between -40°C and -50°C.

$$f_{ice} = (1 + \tanh(-0.23171 * T - 7.3058)) / 2 \qquad \text{(Eq. 4.5-2)}$$

The hyperbolic tangent fitting reconciles well the satellite observations and can be considered to be acceptable. In this figure, we also see, water-ice transition is different over ocean, land and snow: over ocean and snow, more supercooled clouds are found.
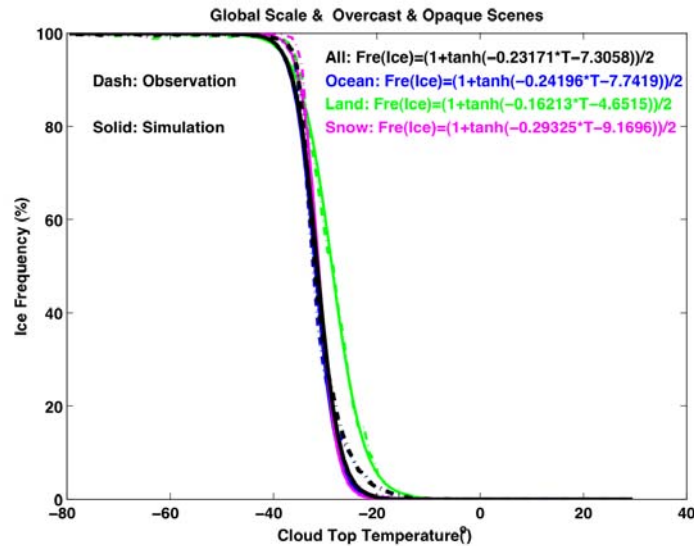
Figure 4.5-4 – *Ice fraction as function of cloud top temperature (dashed lines) and the corresponding hyperbolic tangent fitting (solid lines) for the globe (black curve), for the ocean (blue curve), land (green curve) and snow covered regions (rose curves).*

The derivation of the phase-temperature function has been done only from those confident cloud cases in attempt to understand the water-ice transition in the atmosphere using only high confidence cloud phase samples. By doing so, we obviously excluded all ambiguous cases among which real mixed phase clouds are nevertheless of clear importance in understanding the transition process between liquid and ice. Therefore, we should still keep in mind and wonder if these relationships can as well represent what happens for those unconfident phase clouds, for which more work is needed, especially regarding identification between real mixed phase clouds and other conditions that may lead to mixed signal (multilayer, clouds, broken clouds…). To improve our understanding of such transition, we present in Figure 4.5-5 the standard deviation associated with each temperature bin and also relationships from different sensors to evaluate the potential range of uncertainties. From this figure, we clearly see, using cloud phase from only one

sensor will make the function much more variable since it is clearly impacted by individual shortcomings of each method (short dashed lines). Both POLDER and MODIS miss the very thin cirrus while CALIOP cannot well see the low water clouds. For those high clouds, CALIOP as seeing thin cirrus, its function is in the credible regions of the relationship of those confident cases, for those middle-to-low clouds, the function from POLDER locates in the credible regions and for near ground, MODIS as separating well the aerosols is in credible regions. Excluding broken clouds and thin cirrus, CALIOP or POLDER itself is in credible regions; however MODIS represents quite different relationship due to problems to detect supercooled clouds. In conclusion, before the creation of more confident combined phase is render possible by new instruments and observations, our approach using only confident cloud cases represents a first and credible attempt to understand better liquid/ice phase transition.
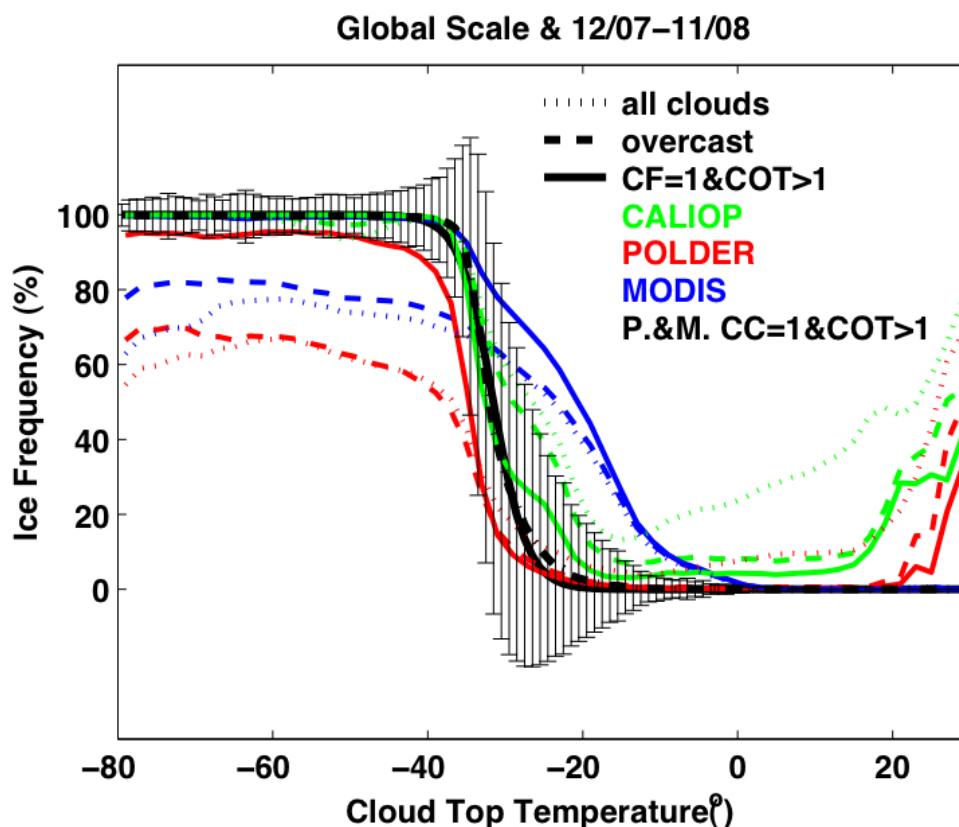
Figure 4.5-5 – *Uncertainties associated with relationship between cloud phase and cloud top temperature. Error bars represent the standard deviation of ice fraction as function of cloud top temperature for the confident cases using combined POLDER and MODIS phase with cirrus optical thickness greater than 1 (black curves). Short dashed lines are from all clouds, long dash lines only from the overcast clouds and solid lines only from overcast thick clouds with cirrus optical thickness greater than 1. Green color is for cloud phase only determined by CALIOP, red color for POLDER and blue color for MODIS.*

We continue to look at the regional variations of water-ice transition. For different regions, the atmospheric dynamics and environmental conditions are quite different (e.g. the sources of ice nucleus, the convection mechanics, the solar energy received, the water vapor content…), which may greatly affect the local vertical water-ice transition. Figure 4.5-6 shows the ice fraction against cloud top temperature for 6 different latitudinal zones (a) and the corresponding hyperbolic tangent fitting (b). From these figures, we see that:

1. In both hemispheres, water-ice transition becomes more rapid from tropical to polar zones.

2. The freezing temperatures T_0 are between -10°C and -30°C and T_m are around -40°C. T_0 are higher in north hemisphere, which may be related to the polluted air in North Hemisphere. The polluted air could lead to more heterogeneous ice nucleation occurring in warmer atmosphere in North Hemisphere (Gierens, 2003). In South hemisphere the freezing temperature T_0 becomes higher from polar to the tropics while in North hemisphere the freezing temperature T_0 is highest in middle latitude.
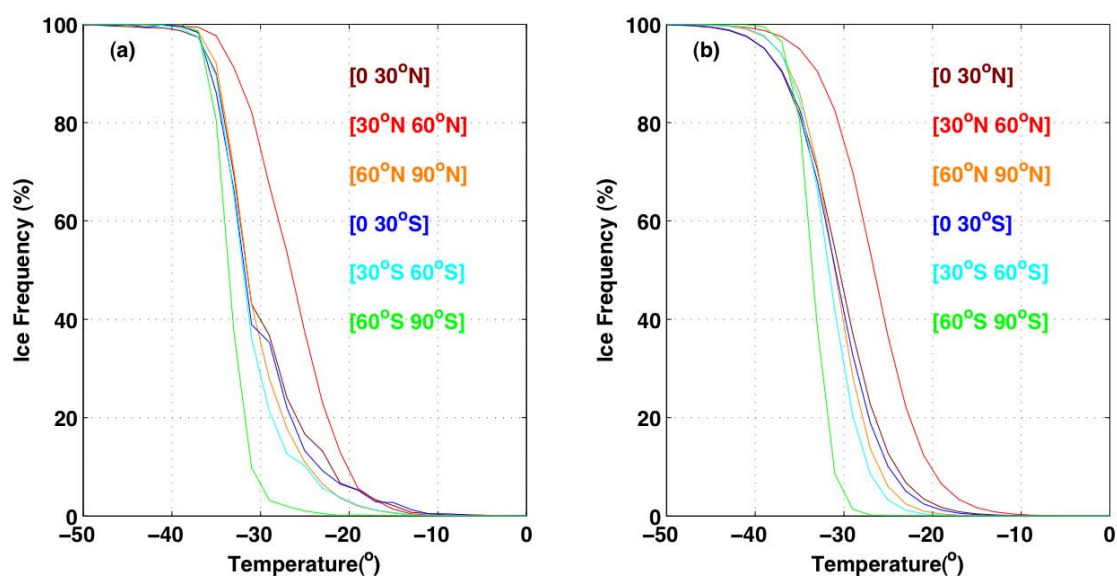
Figure **4.5-6** – *Ice fraction as function of cloud top temperature derived from CALIOP (a) and the corresponding hyperbolic tangent fitting (b) for 6 latitudinal regions: [0° 30°S], [0° 30°N], [30°S 60°S], [30°N 60°N], [60°S 90°S] and [60°N 90°N].*

In order to better visualize the latitudinal variations of water-ice transition, study the freezing temperature (T_m and T_0) and transition speed, we reduced the latitudinal interval from 30° to 5°. In each 5° latitudinal zone, the simulations of water-ice transition with the hyperbolic tangent fitting are done as before. Two year latitudinal variations of the two constants a_1 and a_2 are shown in Figure 4.5-7. Known from above, the greater absolute value of a_1 (flatness) means the more rapid transition and the greater absolute of value a_2 (shift) means the lower 50% frozen temperature.

The freezing temperature (T_0) is thus lower if both a_1 and a_2 are small. From this figure we see:

- In the tropics between 10°N and 20°N where the vertical convection is strong and the vapor content is abundant that may lead to small effective size (Beam *et al*, 2005), a_1 and a_2 are greater, especially in winters. It means that the water-ice transition is rapid and 50% frozen temperature moves to the colder atmosphere, which conducts a lower freezing temperature T_0.

- In subtropics where vertical convection is week, a_1 and a_2 are small. It means that the water-ice transition is slow and the 50% frozen temperature moves to the warmer atmosphere, which lead to a warmer freezing temperature T_0.

- In Polar Regions, a_1 and a_2 are greatest. It means that the water-ice transition is quite rapid and 50% frozen temperature moves to the colder atmosphere.

- Comparing the Polar Regions and subtropics, there are more supercooled clouds in Polar Regions and the ice-water transition is more rapid (with larger a_1 and a_2), especially in South Polar Regions. Comparing South and North Hemisphere, there are more supercooled clouds in South Hemisphere where air seems cleaner compared to the North Hemisphere.
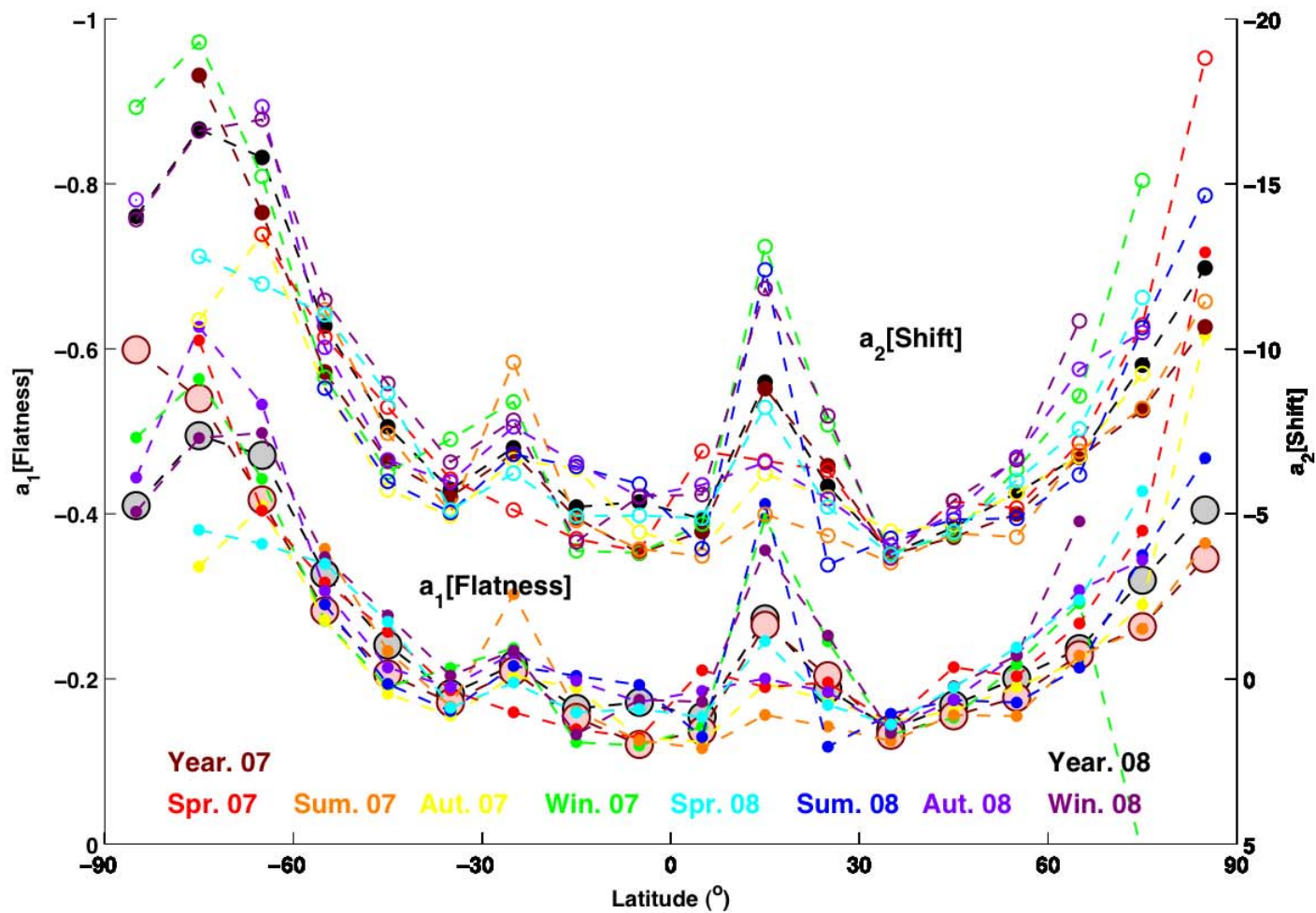
Figure 4.5-7 – *Latitudinal variations of the two constants in the hyperbolic tangent fitting. Different color means different seasonal statistics. The annual statistics are represented with solid circles, in brown for 2007 and in black for 2008.*

From the figure above, we have also seen for different seasons, these two constants have slight variations. Next, we investigate the seasonal variations of the vertical water-ice transition in Figure 4.5-8 over ocean and in Figure 4.5-9 over land for two years from 2007 to 2008. As in Polar Regions for certain seasons, POLDER has no data for analysis because of polar night, the evolution is limited for latitudes between 60°S and 60°N.

From these figures, we see that a_1 and a_2 show irregular and unnoticeable seasonal variations of water-ice transition over the two years. We note that in some regions like northern tropics and southern middle latitudes, during winter (Dec-Jan-Feb) more supercooled clouds are found.
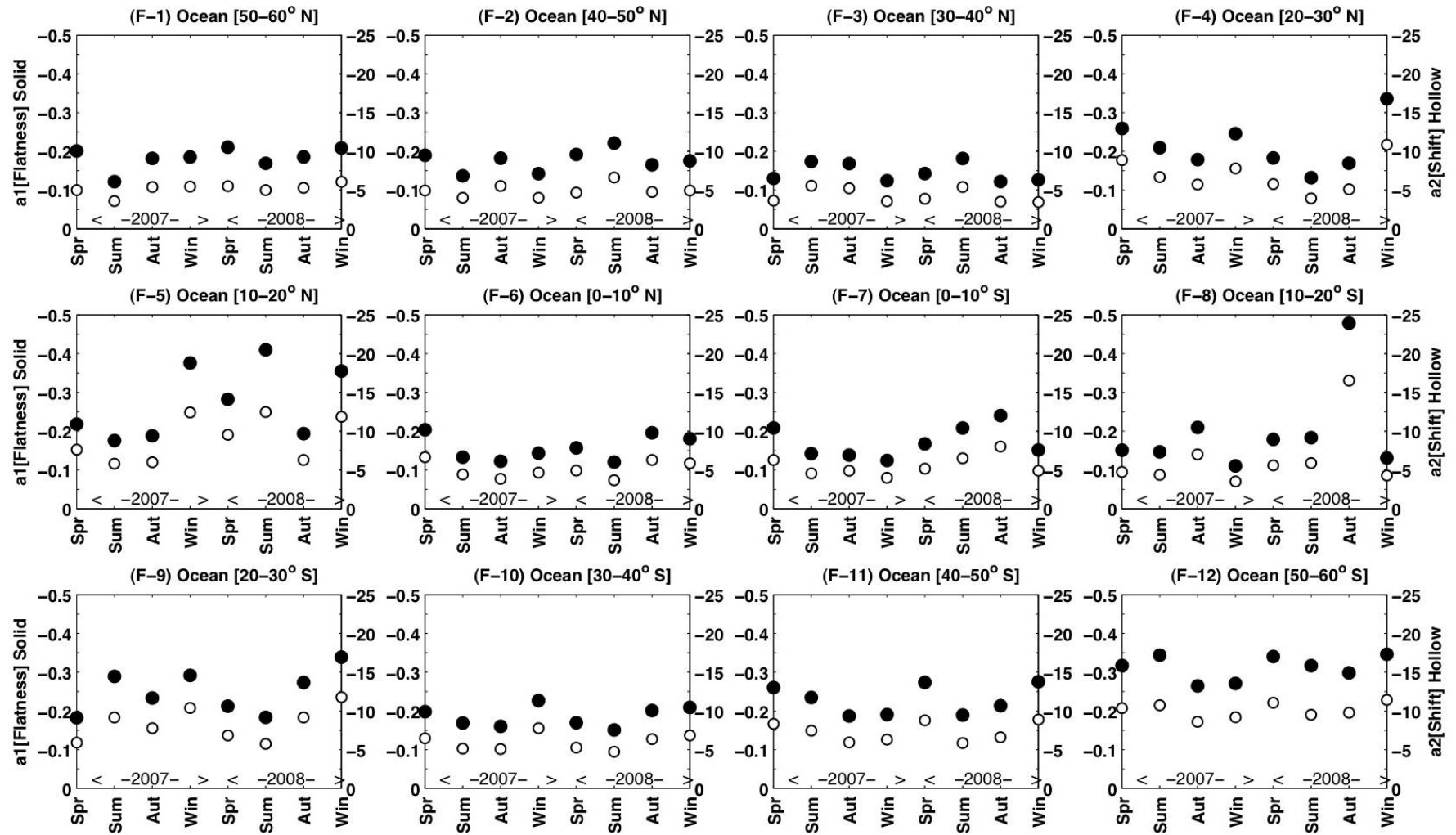
Figure 4.5-8 – *Seasonal variations of the two constants of the hyperbolic tangent fitting for every 10° interval latitude over ocean.*
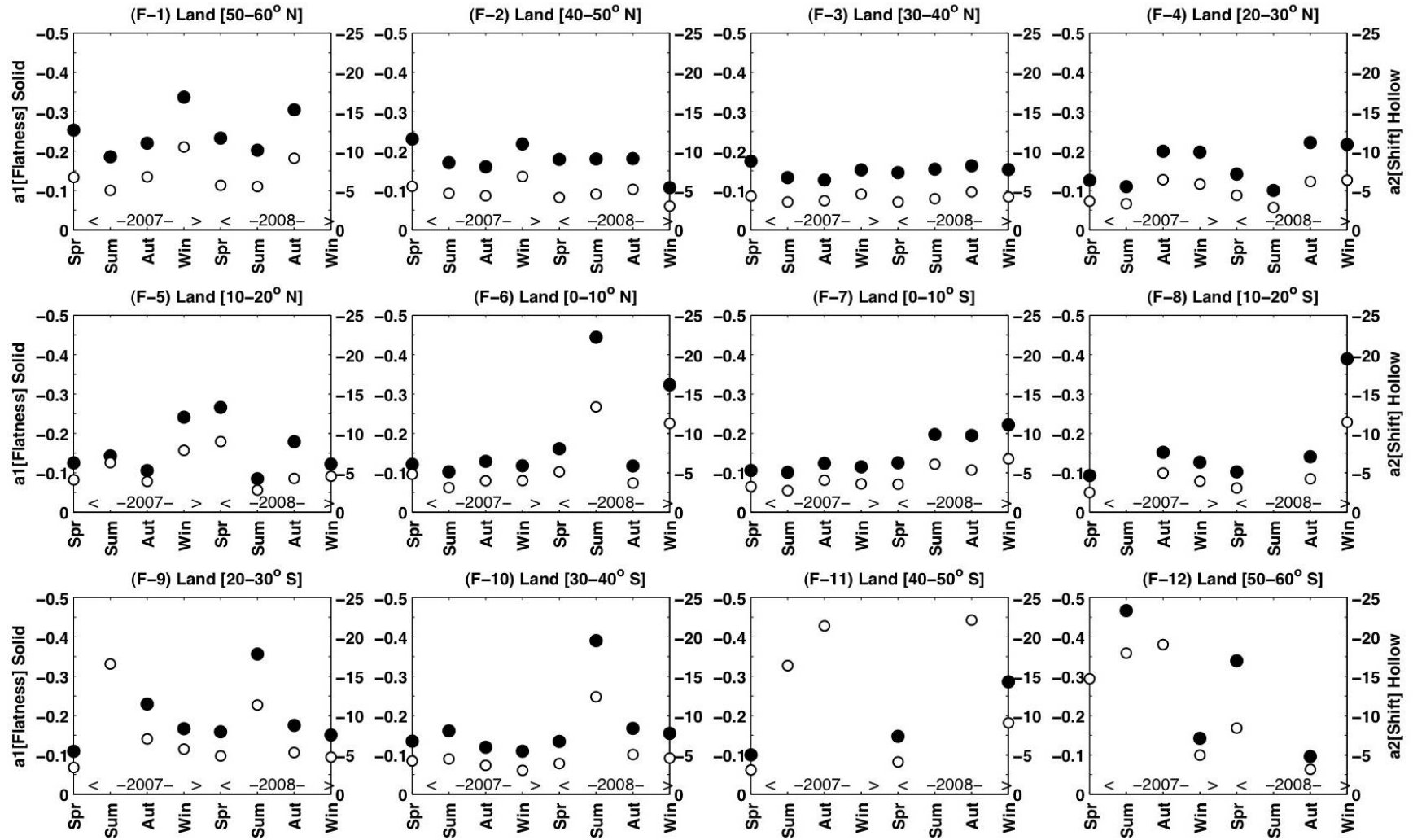
Figure 4.5-9 – *Seasonal variations of the two constants of the hyperbolic tangent fitting for every 10° interval latitude over land.*

4.5.3 Impact of Effective Radius & Vertical Velocity

According to ice nucleation theory, freezing temperature and nucleation rate greatly depend on the size of supercooled solute droplets, the supersaturation and the cooling rate that relates to the large scale of vertical motion of air mass. So in this subsection, we tried to study water-ice transition in relation with cloud microphysics and atmospheric dynamics, represented here by the effective radius derived from MODIS and the vertical velocity from meteorological reanalysis data ECMWF. As seen previously, the smallest particles have lowest freezing temperature (Houze, 1994), which means the smaller particles can travel longer into the upper atmosphere and remain supercooled (see Figure 4.5-3 and Eq.4.2.6).

In Figure 4.5-10, for each group of droplets (classified by effective radius, each group corresponds to radius of 5µm), water-ice transitions were studied. We see that water-ice transition curves have been distinctly separated according to the droplet size. The smaller particles have lower freezing temperature and more rapid transition, which tend to indicate that the dominant freezing process acting is the homogeneous ice nucleation. When droplets grow, freezing temperature becomes warmer and water-ice transition becomes slower. In agreement with Figure 4.5-10, in Figure 4.5-11, we see that both a_1 and a_2 decrease with effective radius. The vertical water-ice transition strongly depends on effective radius.
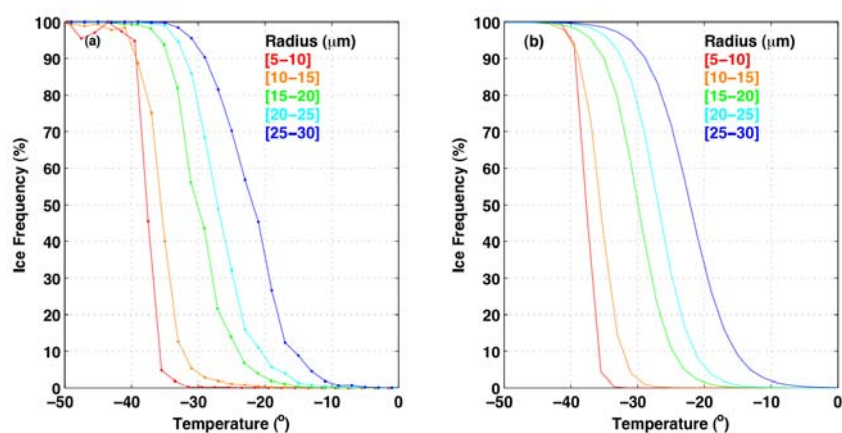
Figure 4.5-10 – *Relations of ice frequency as function of cloud top temperature from CALIOP (a) and the corresponding hyperbolic tangent fitting (b) according to different particle radiuses derived from MODIS.*
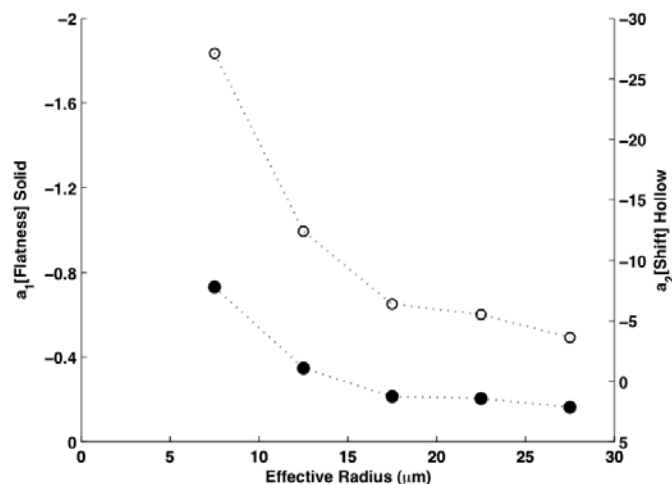
Figure 4.5-11 – *The two constants a_1 and a_2 as function of effective radius.*

Another important dynamic parameter driving freezing processes and therefore cloud phase is the vertical velocity. Analysis of the vertical velocity at 500hPa is a relevant indicator of vertical atmospheric motion at large scale. Large updraft velocities partially associated with strong convection could lead to a rapid cooling rate and can potentially impact significantly the associated microphysical properties (e.g. more and larger particles could be supported and injected at higher altitudes). Measurements have shown that the tropical cirrus formed near centers of deep convection in meso-scale systems tend to contain more particles of larger size than the synoptically-generated cirrus that forms in the midlatitudes due to the relatively low updraft velocities in the ice cloud layer (Heymsfield and Iaquinta, 2000). The manner in which ice is formed in the atmosphere is of interest and related to the cloud formation processing. There is therefore an obviously great interest in observing and understanding the impact of vertical velocity on cloud phase evolution and other microphysical properties as it may provide valuable information to better characterize the processes taking place during cloud formation and evolution.

In Figure 4.5-12, we present the observed water-ice transition and the corresponding hyperbolic tangent fitting curves for different vertical velocity ranges as determined by ECMWF model. From this figure we see, the phase transition curves associated with updraft regime are clearly distinct from those associated with downdraft or weak updraft. In the weak conversion regimes, smaller vertical velocities lead to lower cooling rates and the freezing temperature (T_0) is found colder

than for the stronger convection regimes, while the complete freezing temperature (T_m) remains at -40°C in all cases.
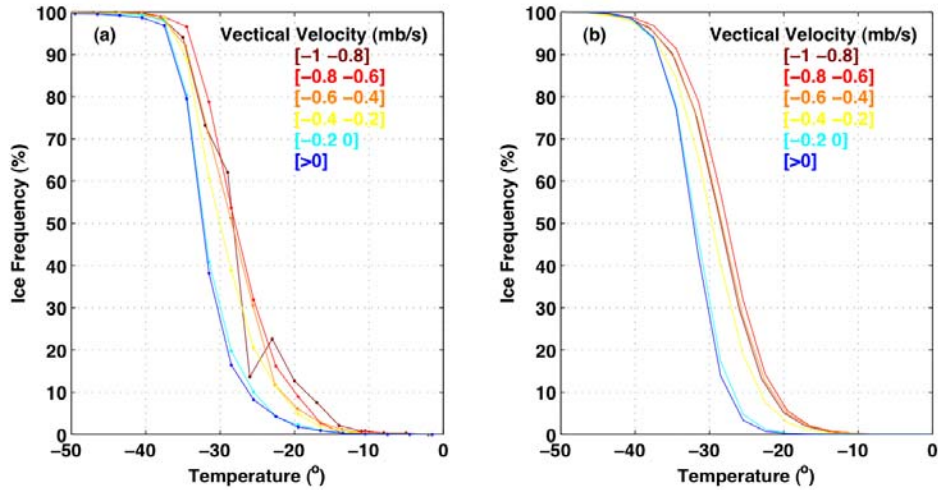
Figure 4.5-12 – *Distribution of ice frequency as function of cloud top temperature from CALIOP (a) and the corresponding hyperbolic tangent fits (b) according to different vertical velocities decided by ECMWF model.*
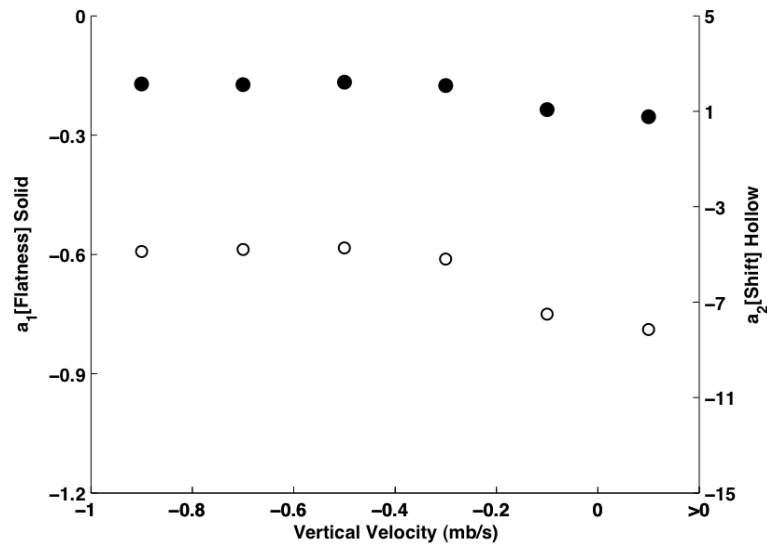
Figure 4.5-13 – *The two parameters a_1 and a_2 as function of vertical velocity.*

4.6 Conclusions

Cloud phase is a critically important cloud parameter for cloud observation and modeling. Whether the clouds are ice or liquid is associated to the cloud formation and development processes which have important relation with the cloud dynamics and microphysics. As a consequence, changes in cloud phase could greatly impact the cloud radiation and feedback to the climate system. In this chapter, we have concentrated on the study of this key parameter. In view of the advantages and limitations of different phase retrieval methods used by POLDER, MODIS and CALIOP, we compared the phase products from the passive sensors, and validated the combined phases from passive sensors with the phases derived from the active sensor CALIOP. The validation and combination of 3 different cloud phase products allow to provide a more confident cloud phase. This in return allows us to perform a robust study of water-ice transition at global and regional scale and analyze its relations with the cloud dynamics and microphysics.

The first part of our study regarding comparison and validation of cloud phase products provided a much better understanding of the cloud phase as determined from POLDER and MODIS. We identified, located and explained the consistent and inconsistent phase cases and also qualified the angular bias in cloud phase detection existing in MODIS SWIR/VIS and POLDER polarized methods. The inconsistent phase decision may inform of the presence of broken clouds, thin cirrus, heavy aerosols, snow or supercooled water. From this study we have seen that POLDER could falsely detect the broken scenes and the aerosols with underlying water clouds as mixed or ice phase. However it correctly identifies cloud phase in case of single layered thin cirrus, water clouds over snow and supercooled water clouds. Compared to POLDER, MODIS detects better the ice phase in case of thin cirrus overlying water clouds or broken clouds. CALIOP agrees for more than 95% in the confident phase cases while for inconsistent and less confident phases, CALIOP partially agrees with either POLDER or MODIS, but preferentially with POLDER certainly because of similar retrieval methods.

A study of the cloud water-ice transition with cloud top temperature, large scale dynamics and cloud microphysics has been performed as a second part by using the confident phase cases identified from the first part of our studies. Results confirm that the ice-freezing process has land-ocean and latitudinal distributions. It also reveals the important variations with relation to the droplet radius and the 500hPa vertical velocity. The smaller droplets have colder freezing temperature and rapid transition speed, most of which therefore locate in the upper atmosphere. The smaller vertical velocities lead to colder freezing temperature. This study may suggest some possible improvements that could be applied in cloud models and in GCMs.

In the future, a lot of work could be continuously done. For example, as the merged phase has been created from the PM Dataset (Riedi *et al.*, 2007), more investigations are needed for this new phase product, which helps to understand the combination of POLDER and MODIS retrieval techniques. Improvements for individual POLDER and MODIS phase algorithms and combination of the two are also required. In addition, the study of cloud water-ice transition need further processing. For example, the impact of vapor content on cloud phase has not been better understood. Whether the results from this study could improve the cloud models and GCMs need to be intensively verified. In addition, what other useful information about the structures of cloud and atmosphere could be revealed from the combined passive and active observations need more continuous studies.

Chapter 5

Cloud Optical Thickness

5.1 Introduction

The cloud optical thickness (referred hereafter as COT), which is another key parameter to characterize cloud optical properties, plays an important role in the determination of cloud radiative forcing (Jensen *et al.*, 1994, Kristiansen and Kristjansson, 1999). This parameter is defined as the vertical integration of the extinction coefficient over cloud geometrical thickness and expresses the quantity of light removed from a beam by scattering and absorption during its path through clouds. The cloud optical thickness increases linearly with liquid water content (Liou, 2002). Many early GCM simulations showed that the changes in cloud optical thickness in response to a doubling CO_2 result in a negative radiative feedback (Roeckner et al., 1987; Mitchell et al., 1989) because water content increases with temperature. However, recent observations from satellites (Tselioudis and Rossow, 1994, Chang and Coakley, 2006) suggests that some clouds increase in optical thickness with temperature consistent with adiabatic behaviour, but other clouds primarily show decreases in optical thickness with temperature, which leads to an overall positive feedback as climate warms. Long records of space-borne measurements at global scale are actually needed in order to correctly map the cloud optical thickness and better understand its radiative effect on climate changes especially in response to anthropogenic activities and natural variations (Rossow and Schiffer, 1991).

Cloud optical thickness is derived from the so-called solar reflective approach which uses a non-absorbent (for water or ice) band in the visible (MODIS conjuncts it with a near infrared band to retrieve together the effective radius). A number of recent studies show this popular approach to retrieve cloud optical thickness achievable and effective (King, 1987, Nakajima and King, 1990, Nakajima and Nakajima, 1994). The underlying principle of the method is that the reflectance in a non-absorbent channel is a one-to-one non-linear function of cloud optical thickness (and particle absorption is proportional to particle effective size). The relationship between cloud reflectance and optical thickness is inherently more sensitive over dark surfaces where the cloud-surface contrast is large enough for the retrievals. Over bright surfaces such as snow and sea ice, any errors in the measurement of visible reflectance and uncertainty in the variation of underlying albedo can increase the errors on optical thickness. To simplify the calculations and limit the computation time, pre-calculated look-up tables (LUTs) are built for different spectral bands using a forward radiative transfer model with a separation of surface types (ocean, land and snow) and for different microphysical models (thermodynamic phase, particle size and habits). The final cloud optical thickness is usually retrieved by matching the measured reflectance with that contained in the LUT for the corresponding geometries and surface condition.

However the real atmosphere is complicated and thus causes many retrieval problems that need careful investigations. Due to the uncertainties in any inputs of the LUT or potentially erroneous assumptions during LUT production, COT retrievals can be easily biased. For example, errors can come from the spectral radiation calibration, the radiative impact of upper molecules, gas and aerosols, the statistical representation of clear-sky albedo, the cloud cover (e.g. broken clouds), the cloud phase identification (e.g. mixed phase), misfit in the description of cloud microphysics (effective radius, particle size distribution and shapes), the cloud horizontal and vertical inhomogeneities that bias the Plane Parallel Homogenous (PPH) approximation (referred as 3D effects), and so on. Some of these uncertainties have been well qualified while some are not. Past studies have shown for example that the departure in cloud phase function observed can lead to an uncertainty in cloud optical thickness of approximately 2 (Malkova, 1973). Concerning liquid water clouds, an error of a factor 2 in the droplet radius can induce an error in cloud optical thickness of about 10% (Han *et al.*, 1994). Concerning cirrus clouds, the use of a wrong particle shape model (sphere instead of crystal) can result in an over-estimation

of cloud optical thickness by a factor that can exceed 3 (Mishchenko *et al.*, 1996; Zhang *et al.*, 2009). In case of thick clouds, small uncertainty in reflectance can induce large errors in cloud optical thickness while the uncertainty from the surface can be ignored. For thin clouds, the TOA reflectance has little sensitivity to cloud optical thickness and uncertainty from the surface dominates the errors (Platnick and Valero, 1995). The vertical stratification can induce an error of no more than 3% (Nakajima and King, 1990). In addition, great efforts have been devoted to understand the optical thickness bias associated to the horizontal cloud heterogeneity. Many studies from both Monte-Carlo simulations and satellite observations argue about the cloud optical thickness bias due to cloud 3-D effect. This bias depends on cloud type, sensor resolution and observation geometry. Observations from POLDER have shown that for liquid clouds, the deviation from the PPH assumption can induce an underestimation of cloud optical thickness in the forward directions especially for higher clouds and for large sensor views at oblique sun (Buriez *et al.*, 2001). For elevated sun geometries, the tilted cloud surface that reflects the photons in off-nadir direction and darken the near nadir reflectance, can result in negative bias in near nadir direction while for low solar angles, the cloud-side shadowing tends to lead to a negative bias in forward scattering viewing geometry and the cloud-side illumination to a positive bias in backscattering viewing geometry (Iwabuchi and Hayasaka, 2002). Studies with MODIS version 4 observations have found, that the optical thickness retrievals give remarkably consistent results against the sensor views for homogeneous clouds while for inhomogeneous clouds, cloud optical thickness is higher for the oblique sensor views (of both backward and forward directions) than the overhead views in view of cloud edges, especially when the sun is fairly oblique (Várnai and Marshak, 2007). The cloud optical thickness bias due to 3-D effect is found more pronounced when cloud top is heterogeneous compared to the heterogeneity from internal volume extinction (Loeb *et al.*, 1998; Várnai and Davies, 1999).

A better understanding of possible uncertainties can of course promote improvement for cloud optical thickness retrievals. For instance, over the most problematical surface such as snow covered surface, the adoption of a NIR band instead of a visible band for the optical thickness retrievals shows satisfactory improvements in obtaining a correct optical thickness (Platnick *et al.*, 2001). A more sophisticated representation of the microphysics in ice clouds can gradually complete

the light scattered by ice crystal and thus improve the retrievals of the optical thickness for ice clouds (C.-Labonnote *et al.*, 2001; Baum *et al.*, 2005).

In the future, plenty of work remains in order to assess and improve cloud optical thickness retrieved from space borne measurements. More supports from airborne and grounded-based measurements, particularly from inter-comparisons of different space-borne instruments are needed. As already presented in chapter 1, different instruments have different characteristics and retrieve cloud optical thickness with different strengths and limitations, which allows to assess one and another over the whole globe. Many satellites such as the Advanced Very High Resolution Radiometer (Heidinger *et al.*, 2005), Spinnig Enhanced Visible and Infrared Imager (SEVIRI) (Roebeling *et al.*, 2006), MODIS (Platnick *et al.*, 2003), and POLDER (Buriez *et al.*, 1997) have already developed their own algorithms to retrieve the cloud optical thickness. In the framework of our studies, we will present the analysis of cloud optical thickness derived from the two sensors: MODIS and POLDER in the A-Train constellation.

The chapter 5 is organised as follows. First, we present the basic method to retrieve cloud optical thickness and summarize the main differences between POLDER and MODIS for liquid and ice clouds respectively. With this reminded basic knowledge, we study the cloud optical thickness from the two sensors, show the geographical, vertical, seasonal distribution as well as pixel-to-pixel comparisons. The potential uncertainties are further analysed to discuss the cloud optical thickness bias, which in return can help in establishing a more confident global representation of cloud optical thickness. After that, we also studied the cloud inhomogeneity and angular distributions of the cloud optical thickness to evaluate the impact of the 3D radiative transfer and microphysics on cloud optical thickness retrievals. Conclusions and perspectives are provided in the closing subsection.

5.2 Principle of COT retrieval (POLDER & MODIS)

5.2.1 COT retrieval principles

Both POLDER and MODIS operational algorithms employ 1-D (Plane parallel

hypothesis) solar reflective method to determine the cloud optical thickness (COT, τ). The official COT product for POLDER is derived from 0.67μm band over land and 0.865μm band over ocean while for MODIS COT is retrieved from 0.645μm band over land, 0.858μm band over ocean and 1.24μm band over sea ice or snow covered surfaces. Both algorithms use pre-calculated Looking Up Tables (LUTs) which contain the bi-directional reflectance and cloud optical thickness for different viewing geometries, thermodynamic phases and surfaces. Figure 5.2-1 summarises the underlying principle of the processing line to build the LUTs which can be used to retrieve cloud optical thickness through simple multidimensional interpolation.
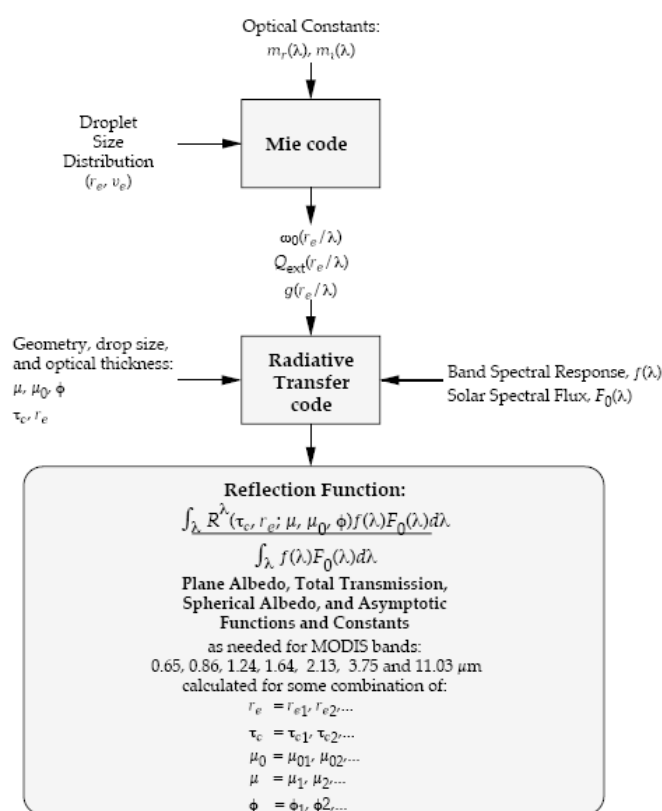
Figure 5.2-1 – *Schematic of cloud optical thickness retrievals processing line.*

Two codes are included in the processing line: the scattering code and the radiative transfer code. The scattering code links cloud microphysics to cloud optical properties (extinction coefficient, single scattering albedo and phase function from which is derived the asymmetry factor). The radiative transfer code resolves how the radiation interacts with the atmosphere and gives the reflectance in one observation direction at the top of the atmosphere as it is captured and measured by the sensors. In the following, more details concerning the assumption used for the direct calculation

used in the POLDER (Buriez *et al.*, 1997) and MODIS COT (Platnick *et al.*, 2003) retrieval algorithm are presented.

The scattering code is based on scattering theory, which employs different particle models and enables to simulate the particle scattering and absorption behaviors. For liquid droplets, which can be considered as spheres with sizes comparable to the wavelength in the visible range, the Mie theory is suitable to resolve the Maxwell Equations and obtain the optical parameters of liquid droplet distributions used for both algorithms. Ice crystals have more complex shapes and their sizes are larger. More complex theory such as ray-tracing method or finite-difference time domain methods (FDTD,Yang and Liou, 2000) are required and adopted to resolve scattering problems posed by ice crystals of various habits.

5.2.2 Differences between POLDER and MODIS COT retrieval

a) Microphysical and surface reflectance assumptions

Table 5.2-1 summarizes the main differences in the inputs and assumptions in the scattering code used for each of the two sensors. Concerning liquid clouds, MODIS uses different particle sizes that are obtained from the water absorption channel in the near-infrared range while POLDER, which has no information on particle size, assumes that clouds are composed of water droplets with a constant effective radius (9μm over land and 11μm over ocean) (Buriez *et al.*, 1997, Buriez *et al.* 2005, Parol *et al.*, 1999). For ice clouds, MODIS employs the Baum05 Models (Baum *et al.*, 2005) which are a mixture of different ice crystal habits. It uses 12 size distributions of crystals composed of mixed habits (droxtals, aggregates, bullet rosettes, hollow columns, solid columns and hexagonal plates) with the fraction of each habit depending on particle size. These habits employed are based on in situ observations from the FIRE-II experiment. POLDER, on the other hand, uses the IHM Model (C.-Labonnote *et al.*, 2000; C.-Labonnote *et al.*, 2001), which assumes that light is scattered by randomly oriented hexagonal ice crystals containing air bubbles with effective radius of 1μm. The IHM model is found to be in good agreement with both total and polarized reflectance measurements of POLDER and in

situ observations.

	POLDER	**MODIS**
Liquid		
Model	Mie	Mie
Effective Radius	Land: 9 μm Ocean: 11 μm	Depend on the retrieval from the NIR band
Size distribution	Gamma distribution	log-normal
Effective variance	0.15	0.13
Ice		
Model	IHM	Baum05
Shape	Hexagonal ice crystals containing air bubbles	Mixed of droxtals, aggregates, bullet rosettes, hollow columns, solid columns and hexagonal plates, fraction of each depends on particle size
Size parameter:	L/2R : 220μm /44μm $<l>$:15μm r_{eff}-v_{eff} 30μm-0.1 N: 82 l^{-1} (Mid level) 255 l^{-1} (Top level)	Depend on the retrieval from the NIR band 12 size distributions
Ground albedo		
	Ocean: Cox and Munk model (Cox and Munk, 1956) Land: clear albedo from the "land surface" processing line	MOD43 Product which provides 16-day 1-km composites of clear-sky albedo
Radiative transfer code		
	Discrete ordinate method (Stamnes et al., 1988)	Discrete ordinates Method (Nakajima and Tanaka, 1986 or Stamnes *et al.*, 1988)

Table **5.2-1** – *Summary of cloud microphysics and assumptions in cloud optical thickness retrieval algorithm for POLDER and MODIS.*

Concerning the radiative transfer code, the calculations of reflectances for

different solar geometries and view angles are both performed using the discrete ordinates method formulated by Stamnes et al. (1988). The final bi-directional cloud reflection function (normalized reflectance) observed by the satellites is simply defined using the following formula (Liou, 2002):

$$R(\tau, \tilde{\omega}_o, P_{11}, \theta_o, \theta_v, \phi_v - \phi_o) = \frac{\pi I(\theta_v, \phi_v)}{F_o \times \cos(\theta_o)}$$

(Eq. 5.2-1)

where $\theta_o(\phi_o)$ and $\theta_v(\phi_v)$ denote respectively the solar and sensor zenith (azimuth) angles; $\tilde{\omega}_o$ is the single scattering albedo, F_o is the solar flux density in W.m^{-2}, I is the radiance observed by the satellites in W.m^{-2}.Sr^{-1}, τ is the total optical thickness, P_{11} is the scattering phase function of cloud particles.

As cloud absorption in the visible range can be ignored ($\tilde{\omega}_o$ is close to one) and F_o is a known constant, given an observation geometry, the one-to-one function of R versus τ based on the homogeneous cloud assumption depends for thick clouds only on the phase function P_{11}, in other words on the cloud microphysics. However for thin or broken cloud, this function depends also on the surface albedo. For POLDER, the surface albedo over land is obtained from surface parameters previously retrieved from POLDER observations under clear-sky conditions by the POLDER "Land surfaces" processing line (Leroy *et al.*, 1997) while over ocean it is calculated using the Cox and Munk (1956) model depending on the surface wind velocity derived from ECMWF analysis. For MODIS, the surface albedo is from 16-day 1-km composites of clear-sky observations in MOD43 products (Strahler, 1999; Moody et al., 2005). An example of the R-τ relationship at 0.67μm and 2.13μm band is shown in Figure 5.2-2.

b) Sensor resolutions and cloud detections

Beside the different cloud microphysics and inputs used in the processing line that can impact the retrieved cloud optical thickness from POLDER and MODIS, bias can also be directly linked to the different sensor characteristics, such as the spatial resolution and the multi-angular observations.

Cloud optical thickness is retrieved from the two sensors only for the cloudy pixels. POLDER has a lower spatial resolution (6×7km^2) and thus smoothes more the

sub-pixel cloud holes and inhomogeneities compared to MODIS ($1\times1km^2$). Consequently, at the POLDER resolution ($6\times7km^2$) in case of sub-pixel cloud free area, POLDER tends (chapter 3) to find larger cloud fraction but lower cloud optical thickness compared to MODIS for the same spatial resolution because cloud optical thickness of POLDER is retrieved by setting sub-pixel clear sky part to 0 (see section 5.4.1). In order, to limit and account for the impact of sub-pixel cloud free area in the following analysis, we introduce later the product cloud optical thickness times cloud cover (COT×CF). This parameter in fact represents the linear mean optical thickness of both clear and cloudy parts in a POLDER super-pixel by setting the values of clear parts to 0.

Note also that, POLDER takes advantage of the 16 viewing directions to average angularly the optical thickness and to assess the angular consistency. Indeed, a large angular dispersion can be attributed to the departure of POLDER observations from the microphysical assumptions or from the one layer PPH cloud model (Parol *et al.*, 2000).

c) Statistical average and PPH bias

Mainly for rapidity and simplicity reasons, the COT retrieval is based on the plane-parallel assumption for both sensors. However, several studies had shown that the non-linear relationships between visible reflectance and optical thickness leads to the so-called plane parallel homogeneous (PPH) bias (e.g. Cahalan *et al.*, 1994; Davis *et al.*, 1997; Oreopoulos and Davies, 1998; Szczap *et al.*, 2000; Pincus *et al.*, 1999).

Looking at Figure 5.2-2 issued from Marshak et al. (2006), the convex nature of the reflectance-COT relationship implies that the linear mean COT of two cloudy pixels (X-axis) is larger than the effective COT derived from the mean reflectance of the two pixels (Y-axis). Since PPH bias increases with the spatial resolution (Davis *et al.*, 1997; Zinner and Mayer, 2006), the POLDER COT would tend to be smaller than the MODIS one. In the following, we should keep in mind that, MODIS and POLDER having different spatial resolutions, their PPH biases resulting of the different initial sensor spatial resolution are studied at the PM dataset resolution ($20\times20km^2$) from the comparisons of the two linearly averaged COTs. In Figure 5.2-3c, we present the comparison between the linear average of MODIS and

POLDER COT for overcast water cloud and we clearly notice that, POLDER COT is indeed smaller than the MODIS one.

As the solar reflectance is a linear function of the logarithm COT over a wide range of optical thickness (Cahalan *et al.*, 1994; Rossow *et al.*, 2002), in the MODIS official product, the logarithmic average of COT is also computed (Hubanks *et al.*, 2008). Different to the MODIS logarithmically averaged COT, in the POLDER official dataset the COT is also derived from the mean spherical albedo that is called the radiative optical thickness (Rossow *et al.*, 2002). These two optical thicknesses are logically smaller than the linear average values (Figure 5.2-3 a and b). As they account for the logarithmic dependence of the solar reflectance to the optical thickness, they should be more similar than the linear averages. However, we see in Figure 5.2-3 c and d that their relationship is not really improved compared to the relationship of linear average COTs. This may come from the weighted angular average done in the computation of the spherical albedo (Buriez et al., 2001). The mean COT presented thereafter, unless particularly noted, results from a linear averaging.

d) Limitations of the COT values

Another difference between the two COT can come from the fact that in the official dataset, the MODIS COT product has been bounded by an upper limit of 100 while for POLDER COT, the COT value is not limited and can reach up to 200 when seeing very bright clouds. To match what is being done for MODIS, we also bounded POLDER COT with an upper limit of 100. Not too much pixels are concerned and this limitation improves logically the relationship between the two COTs.

Overall, MODIS and POLDER have similar retrieval principles but with different microphysical assumptions and input during the processing lines. MODIS takes advantage of higher resolution that can account more realistically for particle size variations while POLDER takes advantage of the 16 viewing directions to average angularly the optical thickness and to assess the angular consistency. These two products will be compared in the following.
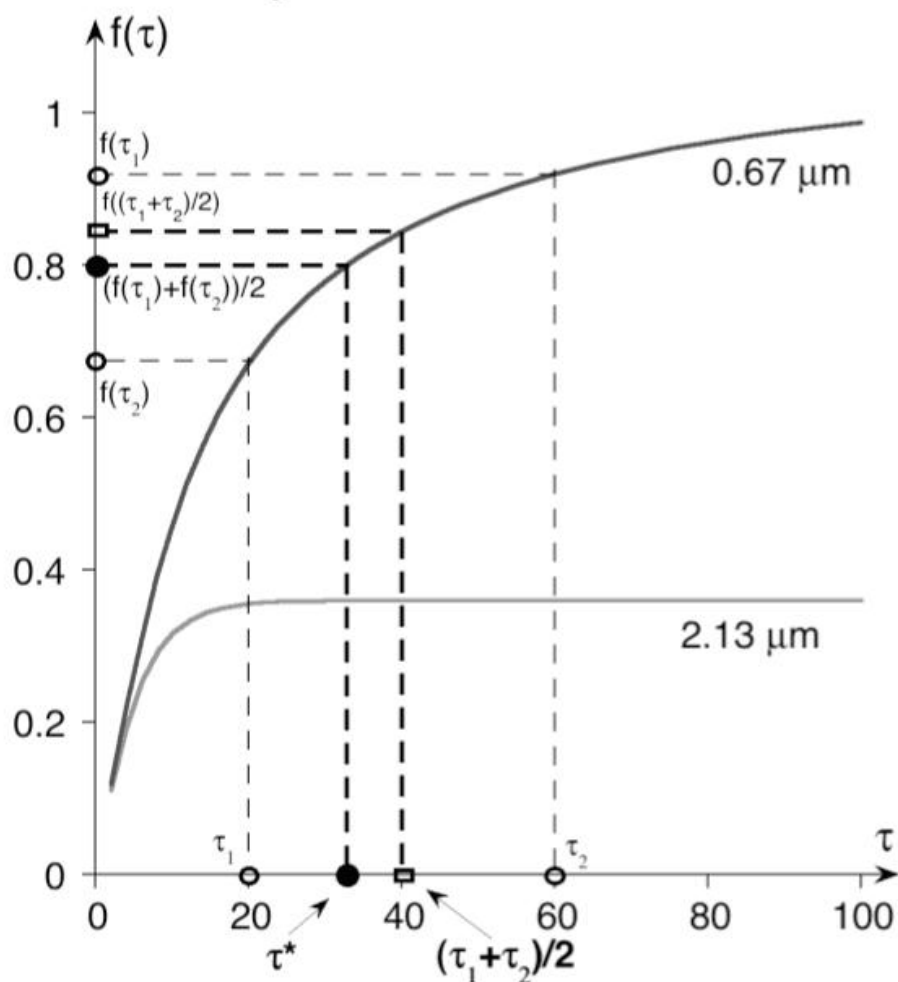
Figure 5.2-2 – *Illustration of the effects of the no-linear relationship between reflectance and optical thickness. Nadir reflectances at 0.67 and 2.13 μm versus optical thickness, τ; Cloud droplet effective radius, $r_e=10\mu m$. Solar zenith angle $\theta_0=41°$; viewing is from nadir $\theta=0°$, surface is absorbing. From Alexander Marshak et al. (2006).*
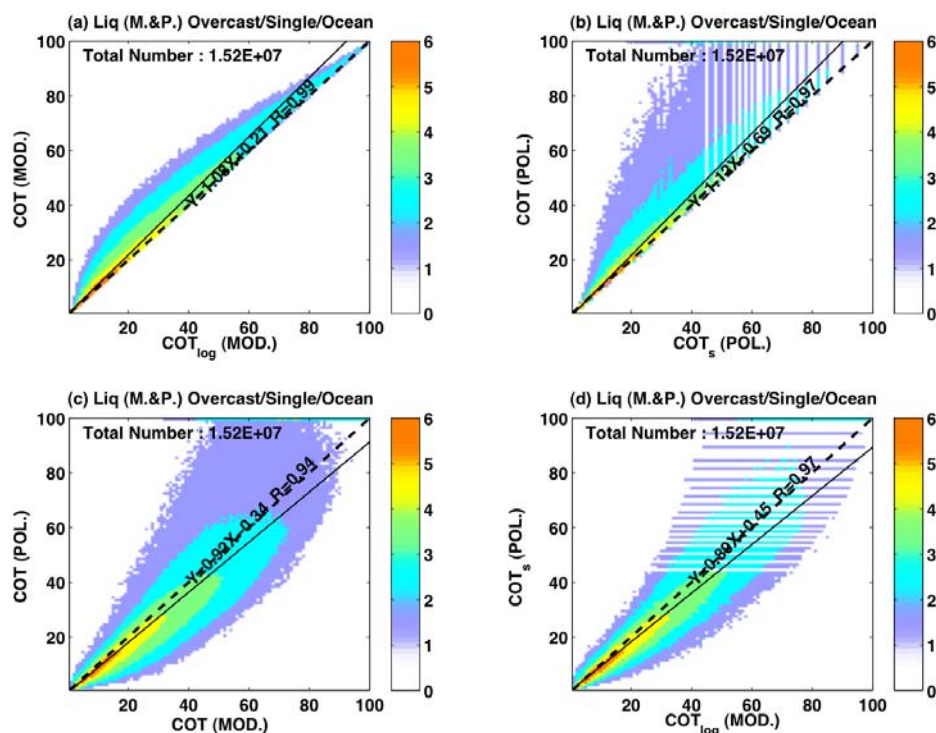
Figure 5.2-3 – *Pixel-to-pixel comparisons between MODIS linearly and logarithmically averaged COTs (a)*，*between POLDER linearly averaged COTs and the ones derived from the spherical albedo (b), between POLDER and MODIS linearly averaged COTs (c) and between MODIS logarithmically averaged COTs and POLDER COTs derived from the spherical albedo (d).*

5.3 Comparisons between POLDER and MODIS COT

As in previous chapters, the optical thickness comparisons presented in the following are made at the POLDER super-pixel scale $(20 \times 20 \text{km}^2)$ using the PM Dataset created for this work.

5.3.1 Pixel-to-Pixel comparison

First, we show pixel-to-pixel comparisons between the COTs derived from the two sensors, which indeed present linear relationships between them. The slope and the correlation coefficient of the linear relationship are indicated to assess the similarity between POLDER and MODIS COTs. The slope corresponds to the ratio between the two optical thicknesses and should be equal to one for perfect relation. The correlation coefficient is a measure of the pertinence of the linear relationship between the two products. In the following, comparisons are made separately according to thermodynamic phase, cloud cover, surface type and cloud structure in order to discuss the variations of the relationship in response to the changes of clouds and environmental conditions. This study is hence performed from the simplest condition cases to the least favorable. Among all conditions, overcast scenes over ocean can be considered as the simplest one. By selecting clouds in such condition, we plot the one-year statistical relationship between POLDER and MODIS COTs for four different combined thermodynamic phase classes in Figure 5.3-1. Overcast is determined as before from combination of POLDER and MODIS CFM (both CF=1). This relationship for overcast oceanic clouds thereafter can be considered as a reference for the other pixel-to-pixel comparisons presented. In this figure, we note that for the four phase classes, the correlation coefficients are quite important with values greater than 0.8 and even above 0.92 for confident ice and confident liquid clouds. As a consequence, we see a strong linear relationship between POLDER and MODIS COTs. The slope is very good with a value close to unity for confident water clouds but only about 0.74 for confident ice clouds. For clouds with inconsistent phases between the two sensors (see subfigures b and c), both slopes and correlation coefficients are worse compared to subfigures a and d. We may also notice that the slope of the POLDER ice and MODIS liquid clouds (see subfigure b) is below unity which means that MODIS COT is larger than POLDER one. This slope value is even smaller than in case of confident ice clouds. On the contrary, the slope of the POLDER liquid and MODIS ice clouds (see subfigure c) is greater than one, which means in this case, that POLDER COT is larger than MODIS one.

These results, of course, help us to understand more about cloud optical thickness retrieval. We first stress out that the correctness of phase identification is

very important. Indeed, cloud phase at first order determines the cloud microphysics model used for the retrieval, which greatly impacts the cloud reflectances. Backward scattering for ice crystals is much stronger than for water droplets ($g_{ice} < g_{water}$). Thus, to reflect the same quantity of radiation back to satellites, COT of ice clouds need to be smaller compared to water clouds. This being stated, it is not difficult to understand that in Figure 5.3-1 the slope for POLDER-ice MODIS-liquid clouds (subfigure b) is below one and the slope for POLDER-liquid MODIS-ice clouds (subfigure c) is larger than one.

For overcast clouds with confident phases over ocean (see subfigures a and d), the smallest bias are expected from cloud detection, phase identification and surface impact. COT will therefore be retrieved with higher correctness and confidence from the two sensors and COT relationships between them should appear better with both slope and correlation coefficient close to one. That is true for confident liquid cloud cases. However for confident ice cloud cases, the correlation coefficient is good but the slope value is biased away from one, which means that significant and systematic differences exist between the two COTs. The main COT differences for ice clouds come from microphysical hypothesis used for retrievals while for liquid clouds this impact is minimal. We will discuss these differences in section 5.4.2.
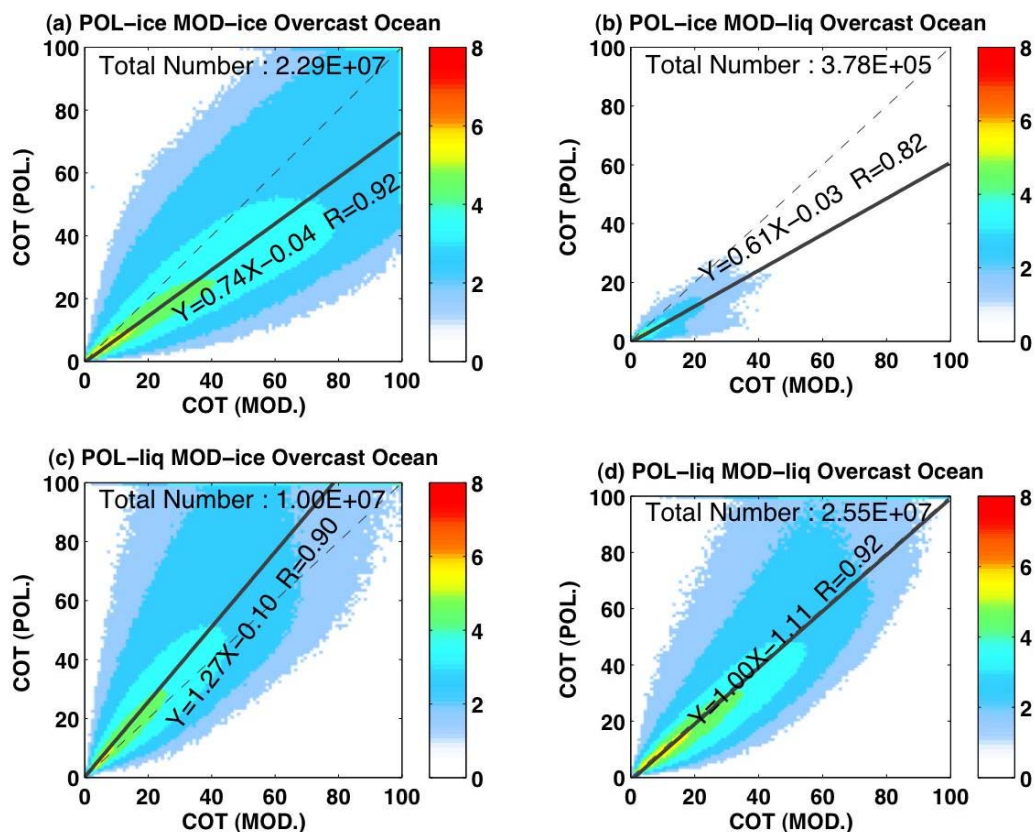
Figure 5.3-1 – *Pixel-to-pixel comparisons between POLDER and MODIS COT for overcast clouds and separated by cloud combined phase: POLDER-ice & MODIS-ice (a), POLDER-ice & MODIS-liquid (b), POLDER-liquid & MODIS-ice (c), POLDER-ice & MODIS-ice (d). Different colors represent logarithmic number of pixels. Solid lines represent linear regression of POLDER and MODIS COT and dashed lines are diagonal lines corresponding to y=x.*

We next present comparisons for clouds in more complex situations. First, we investigate the COT relationships between single layer and multilayered cloud systems identified using the MODIS multilayer flag (Wind *et al.*, 2010). Results are presented by cloud phase in Figure 5.3-2. The correlation coefficients are of the same order for mono or multi layer situations. For both ice and liquid clouds we find a slightly better correlation coefficient for the single layer cloud system. For ice clouds, the slope for multilayer systems (0.72) is smaller than the one for single layer systems (0.76) which suggests larger differences between the two sensors in multilayer cloud systems. For liquid clouds, the slope is smaller than one in single layer systems and larger than one in multilayer systems. This means that POLDER COT is smaller than

MODIS one in single layer systems and greater than MODIS one in multilayer systems. The worse relationships in multilayer systems suggest less confidence on COT retrieval due to the large vertical variations of cloud structures (Nasiri *et al.*, 2004). This may be attributed to either the increased probability of finding multiple phases for the different layers or the larger impact of various 3D effects in case of multilayer systems.
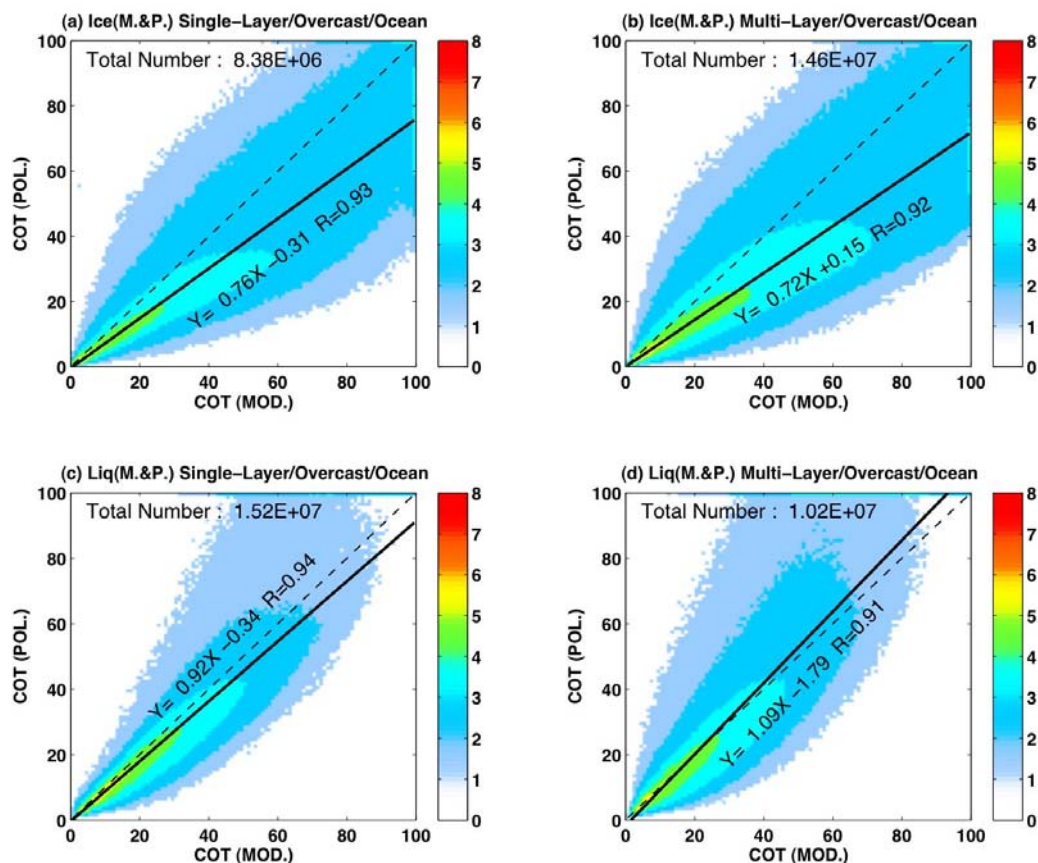
Figure **5.3-2** – *Pixel-to-pixel comparisons for overcast clouds separated by combined cloud phase and cloud structure: single layer ice clouds (a), multilayer ice clouds (b), single layer liquid clouds (c) and multilayer liquid clouds (d).*

In Figure 5.3-3, we present the same relationships for overcast single layer clouds over land. Whatever the cloud thermodynamic phase, the slope of the linear relationship between POLDER and MODIS COT is smaller than 1 for the two surface types (land and ocean) but smallest for clouds over land. However, surprisingly, the correlation coefficient is slightly better over land than over ocean, which may be due to smaller sampling of very bright clouds with POLDER COT $\geq$ 100 over land

compared to ocean. Both sensors use statistic clear-sky reflectance to account for and exclude the impact of surface reflectance in the COT retrieval, which may potentially complicate the COT retrieval and change the relationships. More detailed discussion about the impact of ground reflectance on COT is given in section 5.4.3.
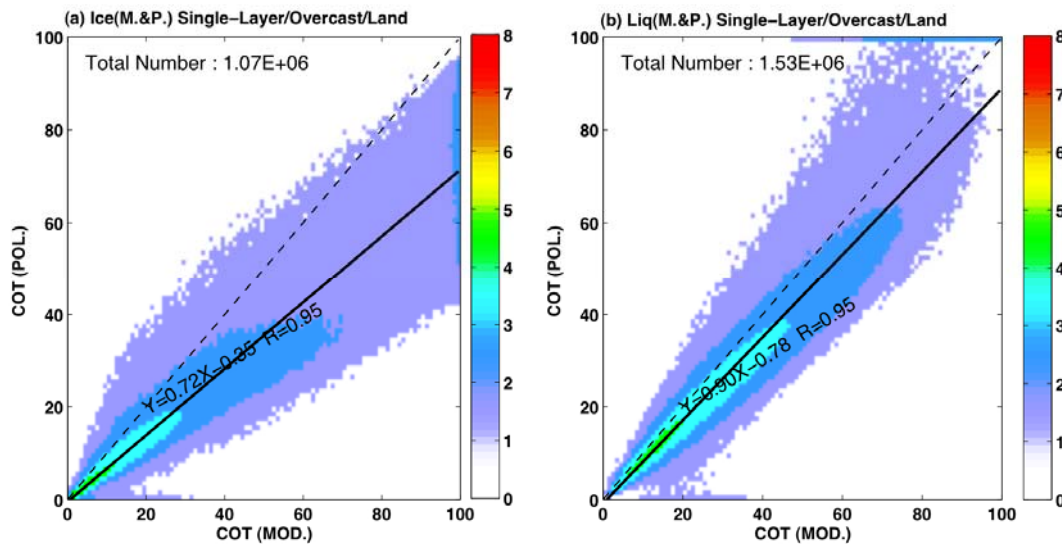
Figure 5.3-3 – *Pixel-to-pixel comparisons for overcast single-layer clouds over land: for confident ice clouds (a) and for confident liquid clouds (b).*

Comparisons for broken clouds, corresponding to the cases where both sensors indicated broken clouds (0<CF<1), are shown in Figure 5.3-4. Broken clouds correspond often to small clouds or cloud edges that contain more sub-pixel cloud holes, so the retrieved cloud optical thickness especially for POLDER is logically smaller than the one from overcast cloud systems. From this figure, we find out for broken clouds that whatever the thermodynamic phase, the correlation coefficients are typically less than 0.7 which means poor relationships between POLDER and MODIS COTs. The slopes are exclusively biased away from 1 with POLDER detecting much smaller COT. Compared to the overcast scenes, the relationships between COTs from the two sensors seem to be much worse. In fact in Chapter 3, we saw that cloud detection is more difficult to operate in broken cloud scenes and that some disagreements on cloud fraction are due to the different spatial resolutions of the two sensors. The impact of sensor spatial resolution and the consequences of cloud cover and 3D effects differences on COT retrieval for broken clouds will be discussed later in section 5.4.1.
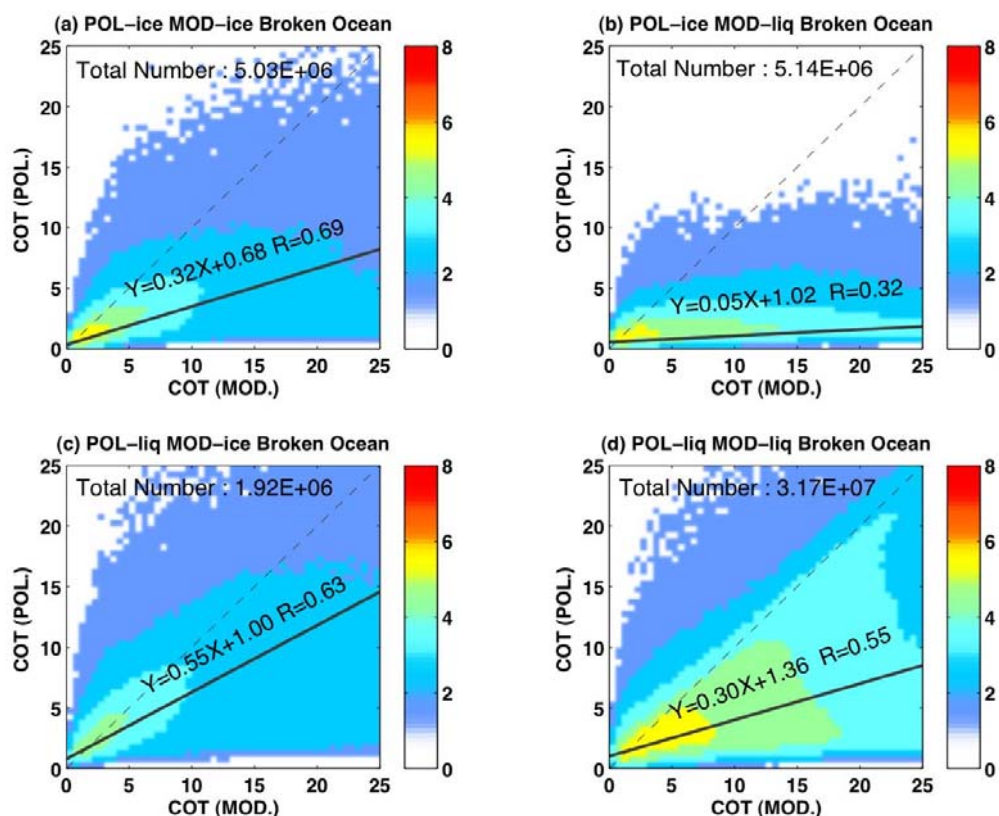
Figure 5.3-4 – *Same as Figure 5.3-1 but for 4 broken clouds. Note that COT values are limited to 25.*

5.3.2 Histogram comparisons

Different from pixel-to-pixel comparisons, which give information on the relations between POLDER and MODIS COT, in this section, we show the Probability Distribution Functions (PDFs, also called histograms) of the COT derived from the two sensors. PDFs are from one-year statistic over the whole globe and are shown with the separations of cloud phase and underlying surfaces in Figure 5.3-5 for overcast clouds and in Figure 5.3-6 for broken clouds. These histograms show the mean and dispersion of COT for each sensor and COT differences between the two sensors according to cloud cover, cloud phase and the underlying surface types. The mean and standard deviation values are indicated on each histogram.

Main findings in Figure 5.3-5 for overcast clouds are:

- Comparing COT over ocean (subfigures from a to h) and over land (subfigures from i to p), independently of cloud phase, the mean and dispersion of COT are not surprisingly larger over land.

- Over ocean, we see that the mean and dispersion of COT for POLDER and MODIS are larger for confident ice clouds (respectively $\tau=16$ and $\tau=22$) than for confident liquid clouds ($\tau=14$ and $\tau=15$) certainly because ice cloud classes often represents convective or multilayered cloud systems with higher COT. We note again that the agreement between the two sensors for liquid cloud is quite good with mean difference smaller than 1 (subfigure h) while for ice cloud a bias of almost 6 exists between the two values (subfigure e).

- Over land, POLDER and MODIS do not agree so well: for POLDER, liquid clouds ($\tau=23$) are on average thicker than ice clouds ($\tau=17$) while for MODIS the mean COT of ice clouds ($\tau=25$) and liquid clouds ($\tau=25$) are almost the same. This leads to a bias and a standard deviation between the two sensors higher over land than over ocean with a mean difference close to 2 for liquid clouds and to 8 for ice clouds (subfigures p and m respectively).

- For clouds with inconsistent phase, it is interesting to note that in case of POLDER-ice and MODIS-liquid clouds, the mean optical thickness is quite small (POLDER/MODIS: 4/6 over ocean and 6/11 over land) compared to others classes. In case of POLDER-liquid and MODIS-ice clouds, the mean COT is greater than confident ice clouds for POLDER (23 compared to 16) and smaller than confident ice clouds for MODIS (18 compared to 22). This is possible due to the uncertainty in phase detection, leading to higher (lower) retrieved COT by erroneous use of liquid (ice) cloud model. And also it may be because MODIS seems to detect better thin cirrus.

- Negative differences are more pronounced for confident ice clouds with almost no positive differences (subfigures e and m), and also for POLDER-ice and MODIS-liquid clouds (subfigures f and m) with differences and dispersions more pronounced over land. For confident liquid clouds, the differences are distributed on both sides of zero with

mean value near zero or slightly negative. For POLDER-liquid and MODIS-ice clouds the differences are also distributed on each side of zero but with a positive mean value.

These results agree well with those from the pixel-to-pixel comparisons in the previous sections, but show them in a different way.
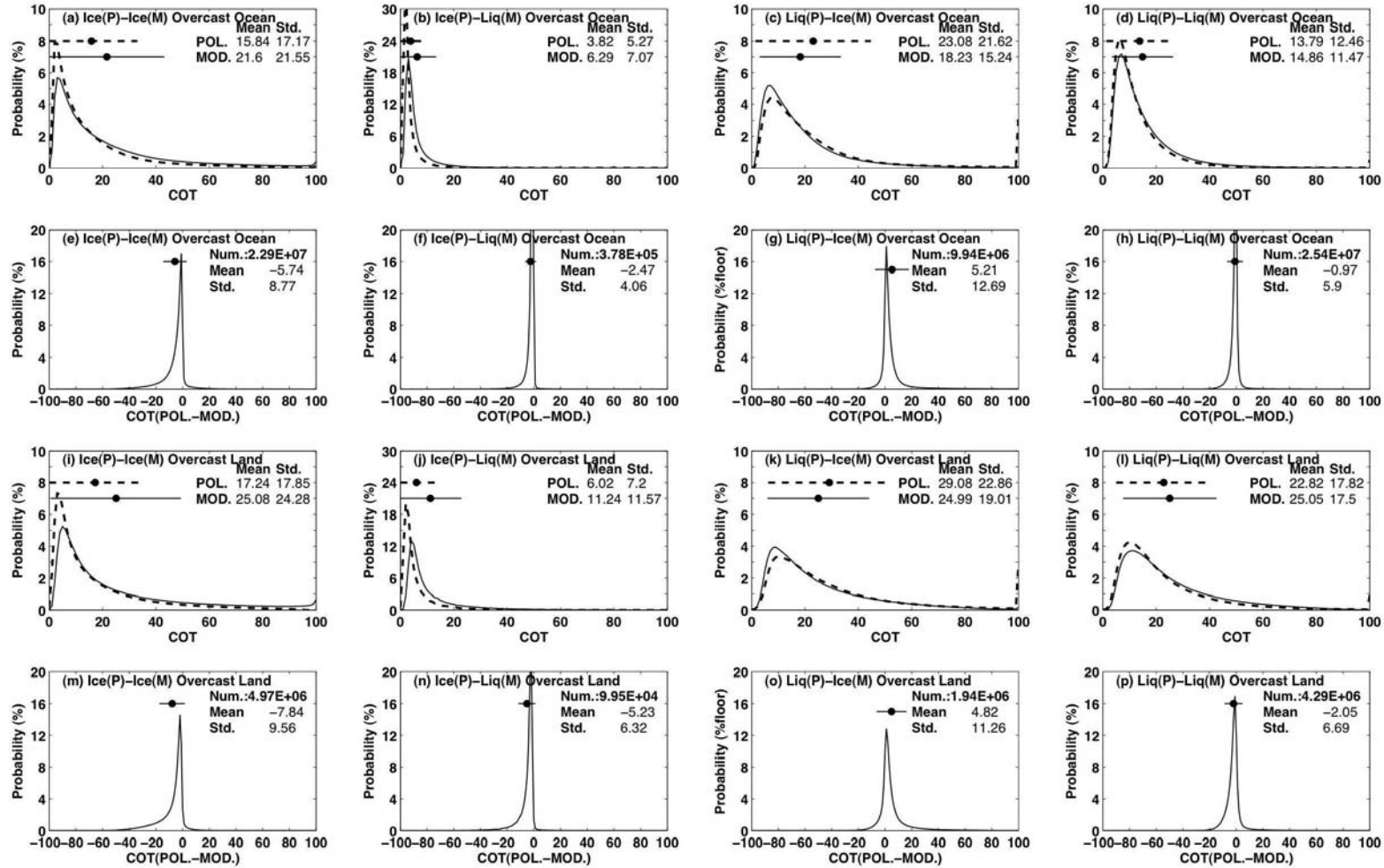
Figure 5.3-5 – *Histograms of COT derived from both sensors for the overcast clouds over ocean (first line) and over land (third line) and histograms of the differences over ocean (second line) and over land (fourth line) for different combined phases: POLDER-ice & MODIS ice clouds (first column), POLDER-ice & MODIS-liquid clouds (second column), POLDER-liquid & MODIS-ice clouds (third column) and POLDER-ice & MODIS-ice clouds (forth column).*

For broken clouds, main findings from Figure 5.3-6 are compared to overcast clouds above and we observe that:

- Compared to overcast clouds, broken clouds have small COT, especially for POLDER with mean value not exceeding 5, which is consistent with the fact that the mean optical thickness at the super pixel scale is computed by setting cloud free pixels to zero.

- In agreement with overcast clouds case, larger COT is found over land whatever the phase class.

- POLDER COT is almost always smaller than the MODIS one with a smaller dispersion. As we will see in section 5.5.1, this is consistent with the cloud fraction differences observed in chapter 3.

- For both sensors, we note that broken ice clouds have smaller COT than liquid clouds and that the negative COT differences between the two sensors are less pronounced for confident ice clouds compared to other cases.
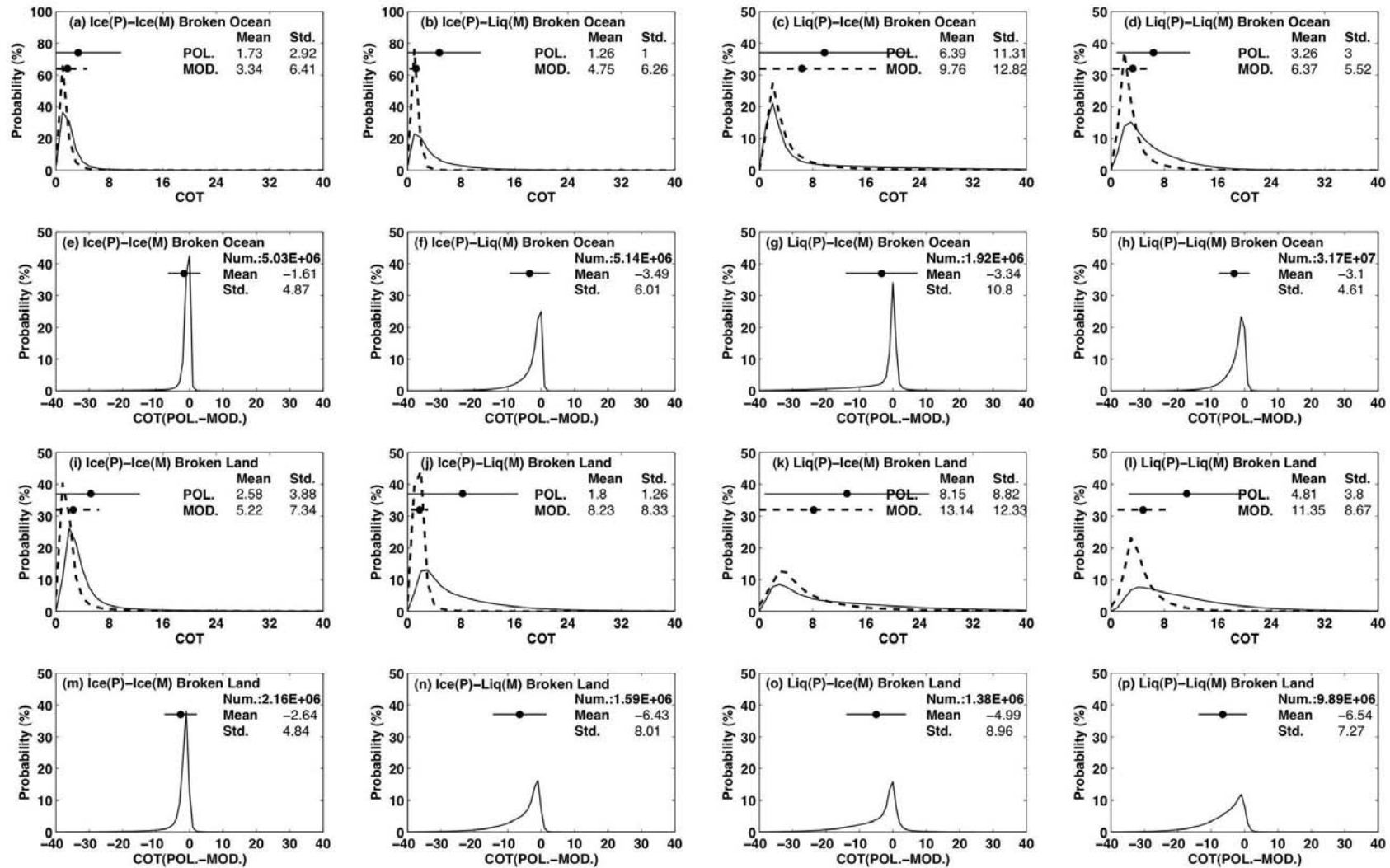
Figure 5.3-6 – *Same as Figure 5.3-5 for broken clouds.*

5.3.3 Latitudinal variations and geographical distributions

We now present latitudinal variations and geographical distributions of COT and COT differences, which allow to analyze and associate them to the local environmental conditions as done in chapter 3 for cloud cover and chapter 4 for cloud phase. Latitudinal variations for overcast clouds are shown in Figure 5.3-7 and for broken clouds in Figure 5.3-8 while geographical distributions for overcast clouds are shown in Figure 5.3-9 and for broken clouds in Figure 5.3-10.

In Figure 5.3-7, we plotted the latitudinal variations of MODIS and POLDER COT and of the scaled COT. Scaled optical thickness is defined as the product of COT by the factor 1-g and better represents the radiative impact of clouds independently of microphysical assumptions (see section 5.4.2). Note that the asymmetry parameter (g) can take only 3 fixed values for POLDER but increases with particle size for MODIS. The variations are plotted for overcast clouds and for different combined phases. The latitudinal distributions of COT for ice or liquid clouds have similar trends with large values in the Storm tracks zones (STs) and small values in the subtropics agreed with other cloud climatologies (Rossow and Lacis, 1990; Rossow and Schiffer, 1999; Minnis *et al.*, 2004; Loyola R. *et al.*, 2010). However, ice clouds and liquid clouds COT have a different behavior in the ITCZ with a peak for ice clouds as for cloud cover (see Figure 3.3-2), which does not appear for liquid clouds. This is possibly because the confident liquid clouds without overlying ice clouds in the ITCZ are rarely occurring and thus results in statistically small liquid COT in this zone.

In agreement with the pixel-to-pixel comparisons, COT of confident liquid clouds derived from POLDER is almost equal to the MODIS one (see Figure 5.3-7, a). For confident ice clouds, POLDER COT is on average smaller than MODIS one with rather systematic bias of 5 (subfigure d). For clouds with inconsistent phases determined by combination of the two sensors, we see again that the sensor using the liquid cloud model always retrieves larger COT than the other using ice cloud model. In case of POLDER-liquid and MODIS-ice clouds, the latitudinal variations of the COT and the COT differences tend to increase with latitude.

Concerning the latitudinal variations of the scaled COT, we note an important reduction of the differences between the two COTs. Explanations will be given in section 5.4.2.

For broken clouds determined by the two sensors (see Figure 5.3-8), we plotted the COT of both POLDER and MODIS and also the COT times the cloud fraction (CF) value to account for the cloud cover differences of the two sensors as function of latitude. The COT values are again reduced compared to overcast clouds. Differences between the two COTs are reduced a lot when COT is multiplied by CF. We will discuss this point in section 5.4.1. Looking at the variations, we note that POLDER COT presents smaller latitudinal variations than MODIS COT, which increase from mid-latitudes to high latitudes.
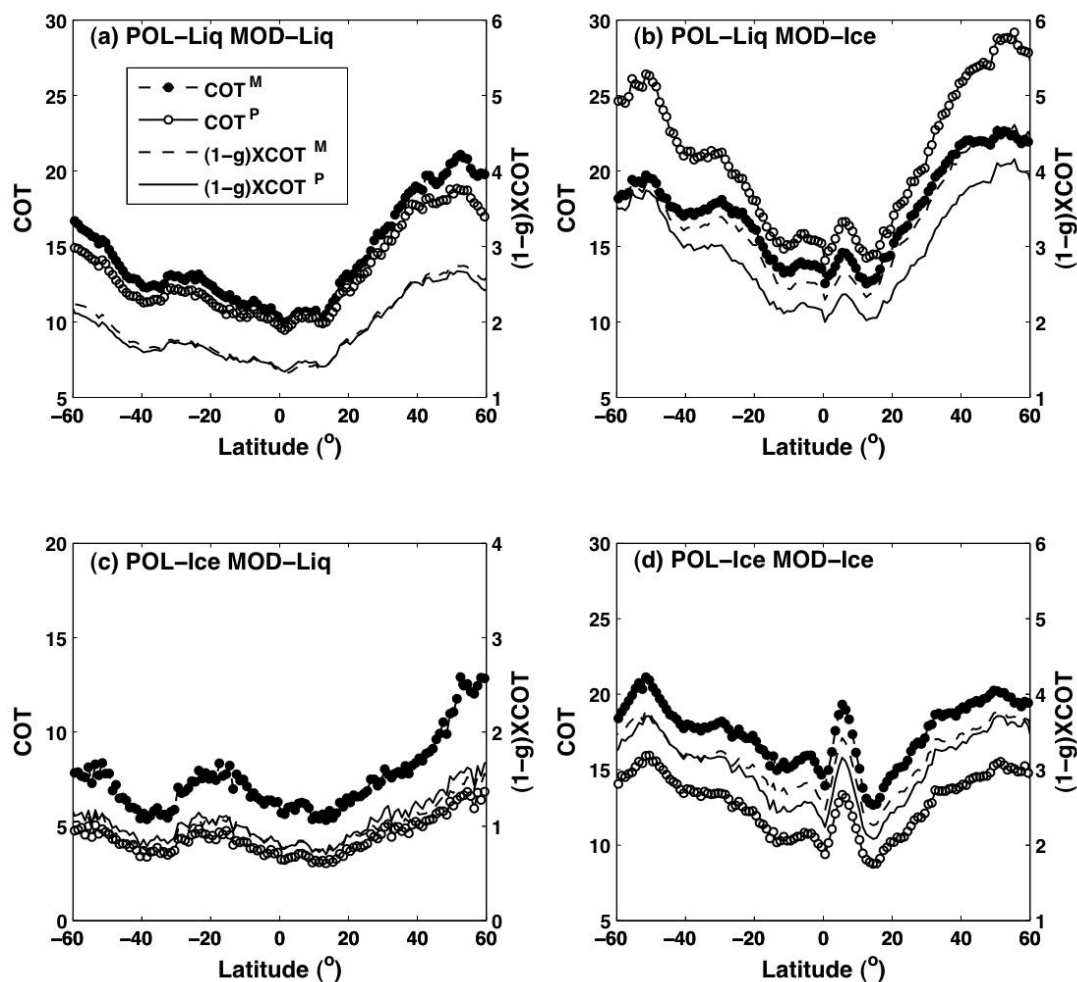
Figure 5.3-7 − *Latitudinal variations of MODIS and POLDER COT (left axis) and the scaled COT (defined as (1-g) × COT, right axis) for 4 different overcast clouds classes determined by cloud combined phase: POLDER-liquid & MODIS-liquid (a),*

POLDER-liquid & MODIS-ice (b), POLDER-ice & MODIS-liquid (c), POLDER-ice & MODIS-ice (d).
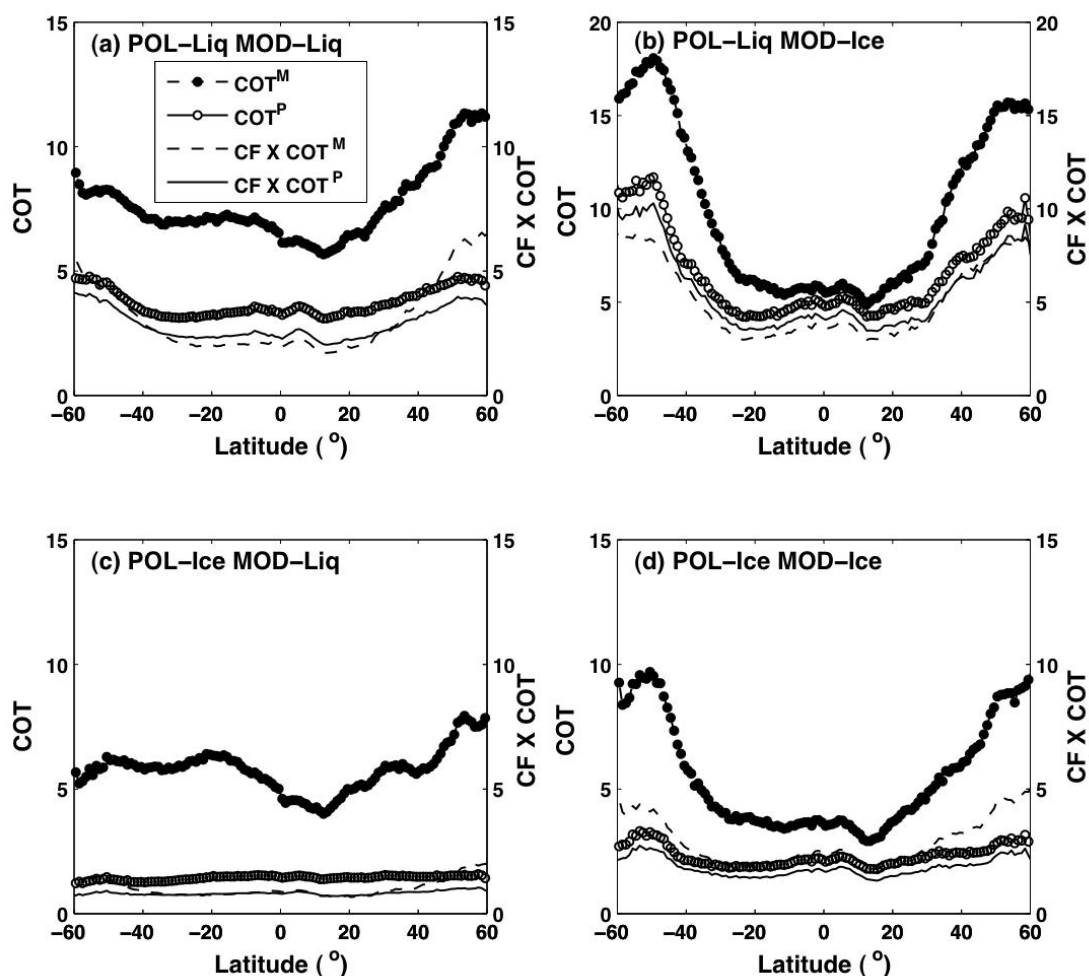
Figure 5.3-8 – *Latitudinal variations of MODIS and POLDER COT (left axis) and the product CF ✕ COT (right axis) for 4 different broken clouds classes determined by cloud combined phases (same as Figure 5.3-7).*

Looking at the geographical distributions of COT in Figure 5.3-9 for overcast clouds and in Figure 5.3-10 for broken clouds, we get more precise information about the COT zonal distributions and their local differences.

For overcast clouds, we can note that:

- In general, POLDER and MODIS show similar COT geographical distributions whatever the cloud phase class, and especially for confident liquid and ice clouds.

- The confident thick ice clouds (COT ≥ 20) are found mostly in the ITCZ and the STs zones over ocean and over Northern South America, Southern South Africa, Southern Asia and Eastern North America and principally over land. The confident thick liquid clouds (COT ≥ 20) are also found in these regions except in the ITCZ. No matter liquid or ice phases, thicker clouds are found over continent for both POLDER and MODIS which agrees with ISCCP C product (Rossow and Schiffer, 1999). The land-ocean contrast of COT has been removed in ISCCP D product primarily because a significant increase in the amount of detected thin cirrus has been found over land with the lower IR threshold. The detection of thin cirrus directly impacts statistics of COT. Also, thin cirrus over liquid clouds can cause problem in phase identification which in turn will impact COT statistics through the use of microphysical models with different asymmetry factors depending on which phase is detected. Finally, low-level clouds over land may extent to larger heights thus to larger optical thickness than low-level clouds over ocean (Warren *et al.*, 1986;Warren *et al.*, 1988).

- For the well-known stratocumulus zones in the western coast of the continents, liquid COT is rather small at about 7. Meanwhile, we note in these zones a relatively high COT in the POLDER-ice and MODIS-liquid phase class. This is most probably due to the occurrence of aerosols over the stratocumulus which can lead to erroneous phase determination by POLDER (Waquet *et al.*, 2009).

- Among the four phase classes, the case POLDER-liquid and MODIS-ice clouds have the largest COT and the case POLDER-ice and MODIS-liquid clouds have the smallest COT, which agrees with Figure 5.3-5. This again can suggest the combined POLDER-liquid and MODIS-ice phase always associated with thick clouds, or multilayer systems in deep convection and POLDER-ice and MODIS-liquid phase associated with thin clouds or aerosols over low clouds.

- Concerning the COT differences, for confident ice clouds, they are negative over the whole globe. The larger differences appear over land, in the ITCZ and the STs. For confident liquid clouds the differences are also negative in the STs and over land but are mostly around zero over ocean in tropics and

middle latitudes with slightly positive differences in ITCZ and around the continents where it is possible to be associated with polluted air and smaller effective radius thus more cloud nucleation nuclei (CNN). For POLDER-ice and MODIS-liquid clouds, COT differences are slightly negative almost all over the globe with quasi-zero values found over some tropical ocean. For POLDER-liquid and MODIS-ice clouds, in agreement with previous results, the differences are almost positive over the globe, especially in the STs.

For broken clouds (see Figure 5.3-10), both sensors present also similar COT distributions for the four different clouds cases. The main observations are that:

- Again we find the COT of broken clouds are significantly smaller than overcast clouds, especially for POLDER, with COT quite small over the whole globe and for all cloud phase classes.

- As for overcast clouds, COT of broken clouds is larger over land and also in the ITCZ and STs over ocean.

- The COT differences between POLDER and MODIS for POLDER-liquid and MODIS-ice clouds are close to zero in tropics over ocean and negative in middle-high latitudes. The COT differences of confident ice clouds, liquid clouds and POLDER-ice and MODIS-liquid clouds are negative over the globe with smaller value over the tropical ocean.
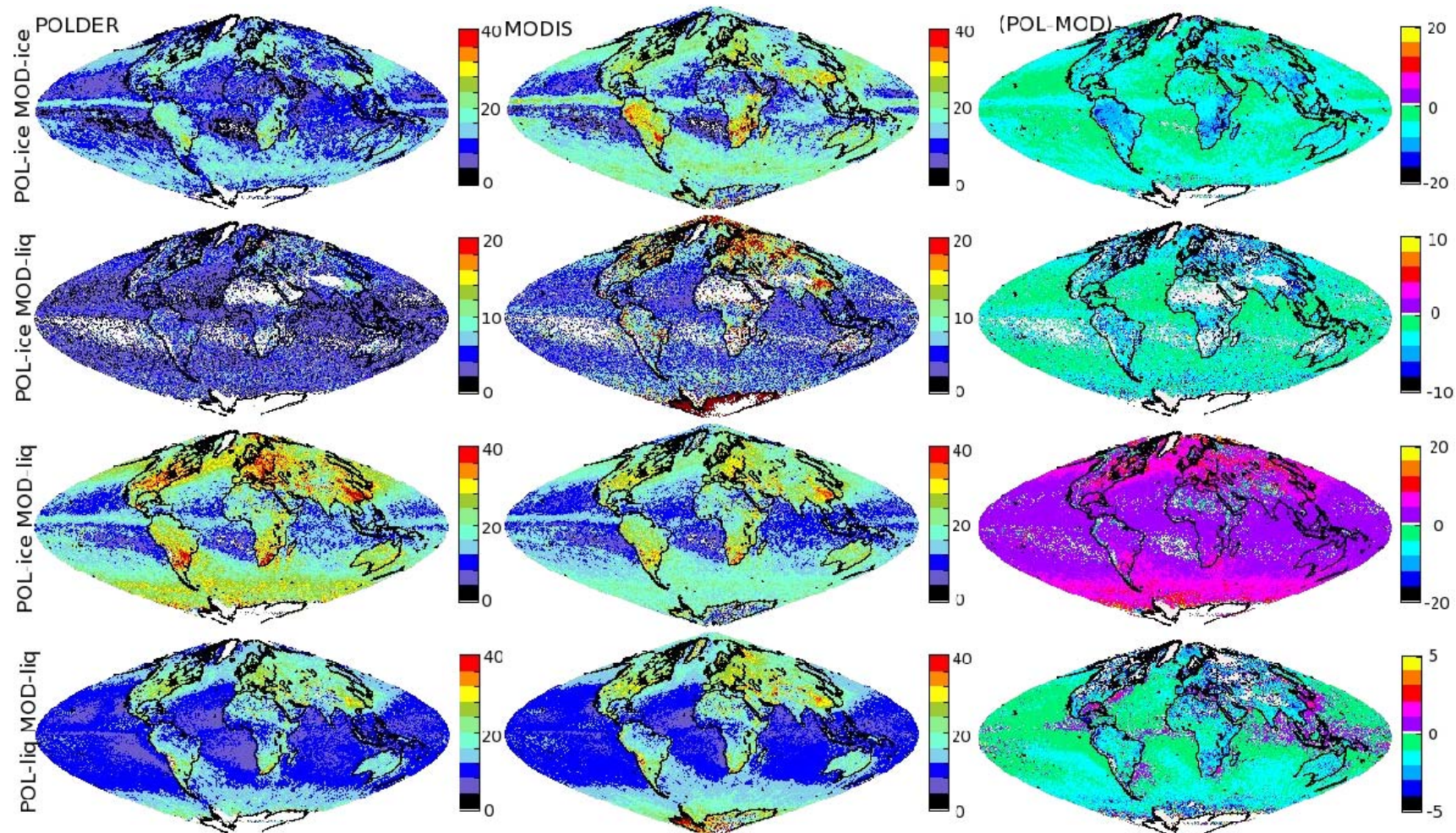
Figure 5.3-9 – *Geographical distribution of POLDER overcast COT (first column), MODIS overcast COT (second column) and the corresponding COT differences (POLDER-MODIS) (third column) for 4 different phases: POLDER-ice MODIS-ice (first line), POLDER-ice MODIS-liquid (second line), POLDER-liquid MODIS-ice (third line) and POLDER-liquid MODIS-liquid (fourth line).*
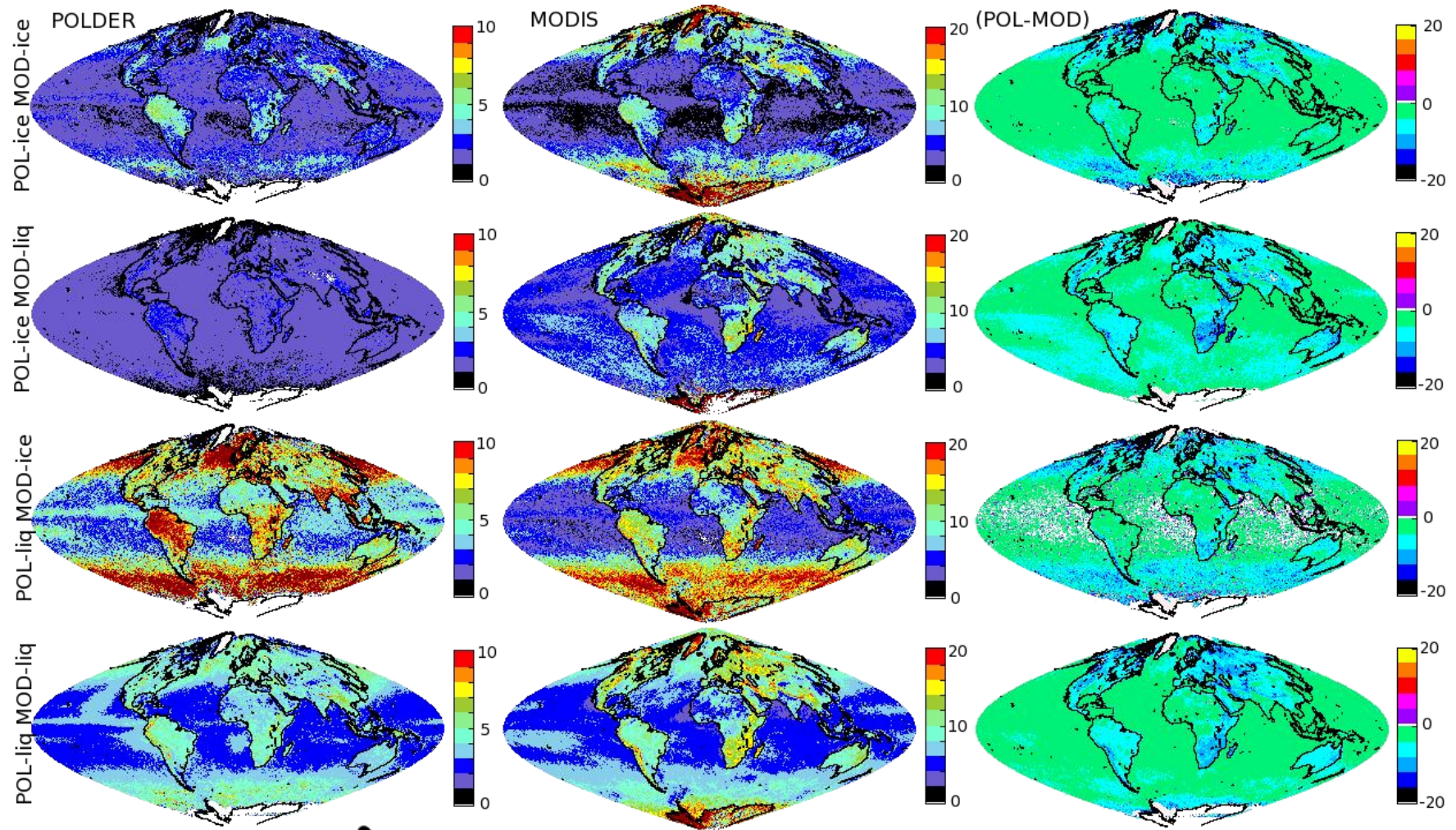
Figure 5.3-10 – *Geographical distribution of POLDER broken COT (first column), MODIS broken COT (second column) and the corresponding COT differences (POLDER-MODIS) (third column) for 4 different phases: POLDER-ice MODIS-ice (first line), POLDER-ice MODIS-liquid (second line), POLDER-liquid MODIS-ice (third line) and POLDER-liquid MODIS-liquid (fourth line).*

5.3.4 Vertical variations

Previously, we looked at the geographical distributions of COT. However, clouds in different levels have different cloud microphysics, such as cloud phase, particle radius and shape. Knowledge of the vertical distributions of COT that may be associated with the vertical cloud properties and water content is also important. To see statistically the COT dependence on vertical location, we plot in Figure 5.3-11 the COT against cloud top temperature (CTT) derived from MODIS (determined by the CO_2 pressure and the atmospheric profile for high clouds and by 11µm brightness temperature for low clouds) for four latitudinal regions and for the four combined phase classes.

In the figure, we see that for different locations and phases, vertical distributions of COT are significantly different:

- For liquid clouds and POLDER-ice & MODIS-liquid clouds, no matter the region and the sensor, COT is on average greater over land than over ocean at any level of temperature. In another word, for a same temperature level at cloud top, clouds are optically thicker over land than over ocean. First, the impact of thin cirrus over land can bias the cloud phase detection to liquid and consequently bias high the optical thickness (see chapter 4). Secondly, the atmosphere profiles can be quite different from a region to another and from ocean to land, especially in the lower boundary layer. We note that land and ocean differences are less pronounced for ice clouds.

- For both sensors, the vertical distributions of COT present similar distributions for the two hemispheres with a different behavior according to the latitude zones (tropics and mid-altitudes).

- Concerning the vertical trend of COT for liquid clouds, COT increases almost linearly with CTT to a maximum (about 0/10°C over land and 0/-20°C over ocean) that are consistent with temperature variation of the adiabatic cloud water content (Tselioudis *et al.*, 1992; Tselioudis and Rossow, 1994). This increase is more rapid over tropics, subtropics

compared to middle latitudes and over land compared to ocean. Over ocean, the maximum of COT is reached at a colder level of about -20°C in mid-latitudes compared to about -5°C in the tropics. Over land, COT increases more rapidly with the CTT compared to clouds over ocean and has two maximum values with one appearing around 15°C and the other around -15°C. COT then decreases slowly with CTT for colder water clouds.

- For ice clouds, COT increases slightly when the CTT decreases in middle latitudes and independent of CTT in subtropics and tropics, but near -60 °C both the increase is more pronounced that does not agree with what has been observed by Tselioudis and Rossow (1994).

- For POLDER-ice and MODIS-liquid clouds, COT is larger at warmer levels while smaller with constant variations at colder levels.

- For POLDER-liquid and MODIS-ice clouds, the vertical variations of COT at colder levels are similar to the ice ones and at warmer levels are similar to the liquid clouds.
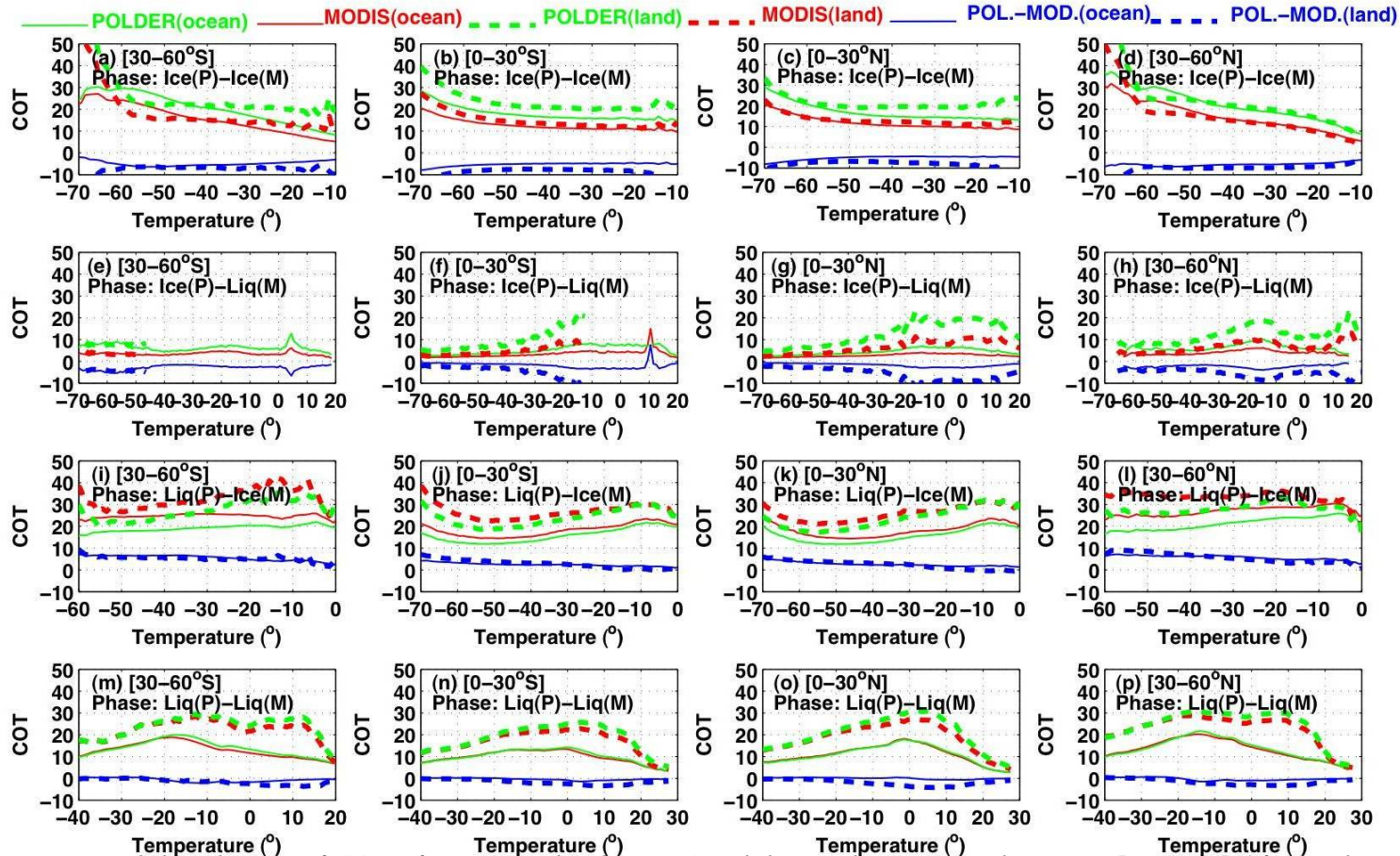
Figure 5.3-11 – *Vertical distribution of COT of overcast clouds over South hemisphere tropical regions [0°-30°S] (first column), mid-latitude regions [30°-60°S] (second column), North hemisphere tropical regions [0°-30°N] (third column) and mid-latitudes regions [30°-60°N](fourth column) for 4 different phases : POLDER-ice MODIS-ice (first line), POLDER-ice MODIS-liquid (second line), POLDER-liquid MODIS-ice (third line) and POLDER-liquid MODIS-liquid (fourth line). Solid lines correspond to Ocean data while dash lines represent Land. Green stands MODIS data and red for POLDER.*

5.3.5 Seasonal variations

The seasonal cycle of COT is plotted in Figure 5.3-12 in the same way as section 3.2.2 for cloud cover that is by subtracting the annual COT average from the monthly average in order to avoid the systematic bias between the two COT datasets. The seasonal cycle is calculated for overcast clouds for both POLDER and MODIS sensors according to cloud occurrence regions (subtropics and middle latitudes over ocean and land in each hemisphere) and to their combined thermodynamic phases.

From the figure, we first see that the COT from the two sensors depends logically on the seasons and regions agreed with other cloud climatologies (Rossow and Lacis, 1990; Minnis *et al.*, 2002; Stubenrauch *et al.*, 2006).

For a same region and with consistent thermodynamic phase, MODIS and POLDER COTs have quite similar temporal variations, especially for clouds with consistent liquid phase (subfigures m to p). Note that in the case of confident ice clouds and POLDER-ice MODIS-liquid clouds, the absolute COT differences were quite important but their seasonal variations are quite similar.

For liquid clouds (subfigures m to p), COT show almost asymmetrical characteristics in South and North hemisphere over both land and ocean, with thicker clouds in winter in each hemisphere excepted over land in the mid-latitude of south hemisphere because of less sample. The larger COT in winter for both hemispheres agrees with ISCCP climatology (Rossow and Schiffer, 1999; Rossow *et al.*, 1989).

For ice clouds (subfigures a to d) in both hemispheres, seasonal variations are more marked with differences between ocean and land. Thicker ice clouds appear in winter over ocean. Over land thicker ice clouds appear predominantly in summer.

For POLDER-liquid and MODIS-ice clouds (subfigures i to l), thicker clouds are found in winter over ocean.

For POLDER-ice and MODIS-liquid clouds (subfigures e to h), the seasonal variations are less pronounced compared to other phase cases, especially over ocean. Over land in middle latitudes thinner clouds are found in summer.
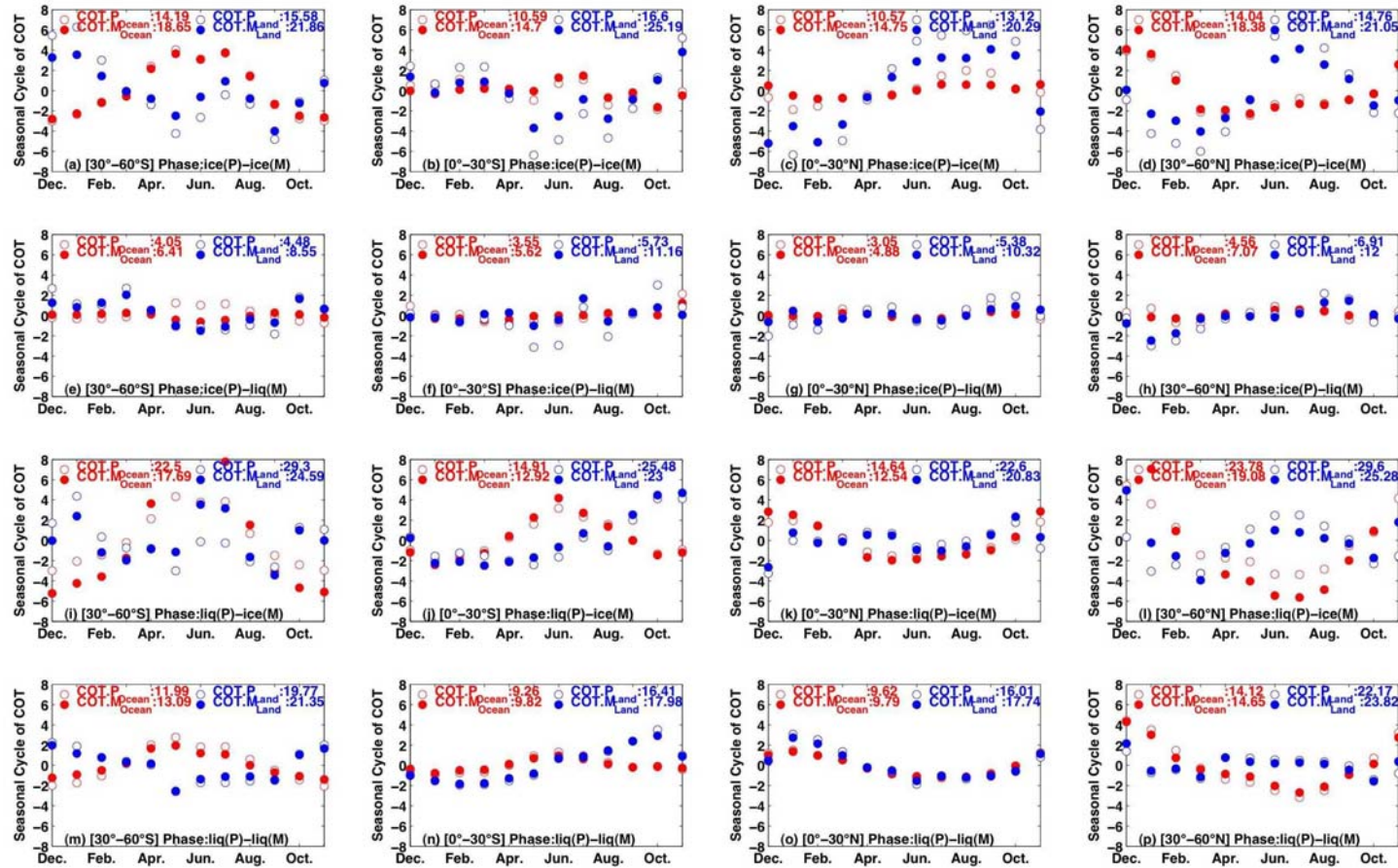
Figure 5.3-12 – *Seasonal cycles of COT for overcast clouds over South Hemisphere mid-latitude regions [30°-60°S] (first column) and tropical regions [0°-30°S] (second column), over North Hemisphere tropical regions [0°-30°N] (third column) and mid-latitudinal regions [30°-60°N](fourth line) with different combined cloud phases: POLDER-ice & MODIS-ice (first line), POLDER-ice & MODIS-liquid (second line), POLDER-liquid & MODIS-ice (third line) and POLDER-liquid & MODIS-liquid (fourth line). Ocean data are in red and land data are in blue. The solid circles present data from MODIS and the hollow circles from POLDER.*

5.4 Factors impacting the COT retrieval

In previous sections, we presented in different ways the POLDER and MODIS COT and the results of their comparisons. Accuracy of COT retrievals and derived statistics depend strongly on the correctness of cloud detection and phase identification, but also on many other factors controlling the quality of COT retrieval. In this section, we will discuss the main factors impacting the COT retrieval and try to explain COT differences observed between POLDER and MODIS.

5.4.1 Impact of sensor spatial resolution

As seen in chapter 3, the sensor spatial resolution (6km×7km for POLDER and 1km×1km for MODIS) impacts the cloud heterogeneity and the cloud detection ability therefore the estimate of cloud cover. Many studies have been done to account for the impact of sensor spatial resolution on COT retrieval (Marshak *et al.*, 2006; Deneke *et al.*, 2009). In this section, we continue to discuss how it can impact the COT retrieval and produce biases between POLDER and MODIS COT.

a. Role of cloud detection differences in COT retrieval

As already described, COT is only retrieved for the pixels detected cloudy and the final COT is averaged over the cloudy part of the super-pixel. The correctness of cloud identification and the decision to retrieve or not COT for a given pixel can therefore strongly impact the COT retrieval and statistics. MODIS with a higher spatial resolution can identify much smaller clear scenes among clouds than POLDER and overall, as we saw in chapter 3, the fraction of pixels for which COT retrieval is performed represent a higher cloud cover for POLDER than MODIS. However except over bright surface, the reflectance used for the POLDER COT retrieval is reduced by the small sub-pixel holes among clouds and the derived COT is consequently usually smaller compared to the MODIS one. This bias directly associated to cloud

identification can be attributed to the sensor resolution differences and is clearly visible in Figure 5.3-4 where POLDER COT is much smaller than MODIS one.

To evaluate the cloud optical thickness of the two sensors disregarding the sub-pixel holes among clouds, we present, in Figure 5.4-1 a pixel-to-pixel comparison of the product COT×CF for broken clouds. Compared to Figure 5.3-4, which show pixel-to-pixel comparisons of COT for the same clouds, it is clear that both the correlations and the slopes of the relationship between POLDER and MODIS are greatly improved for all phase categories: linear regressions with higher confidence are much closer to y=x. This not surprisingly confirms that the sensor resolution affects the COT retrieval and statistics via cloud cover differences and that COT cannot be used independently from a coherent estimate of CF.
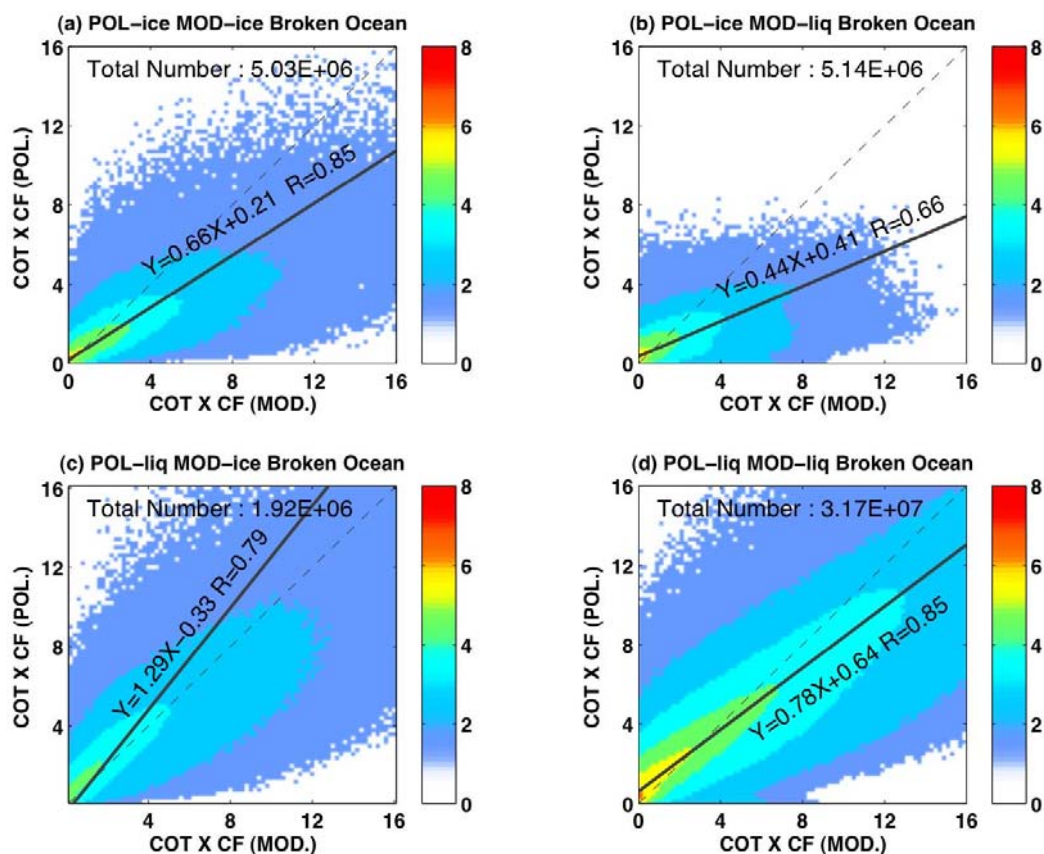
Figure 5.4-1 – *Same as in Figure 5.3-4 but for the product COT×CF of 4 different broken clouds separated by cloud phase case.*

To further confirm this, we also plot for liquid oceanic clouds the two coefficients (slopes and correlation coefficients) of the relationship between COT and between

COT×CF as function of MODIS cloud cover in Figure 5.4-2. It is clear that both the slope and the correlation coefficient for the COT relationships increase with cloud cover almost linearly. The smaller the cloud cover, the larger the dispersion is with decreasing correlation between the two sensors. Concerning the product COT×CF, we see that the slope is significantly improved (closer to one) and becomes independent of the cloud cover. The correlation coefficient is only slightly improved and still increases with cloud cover.
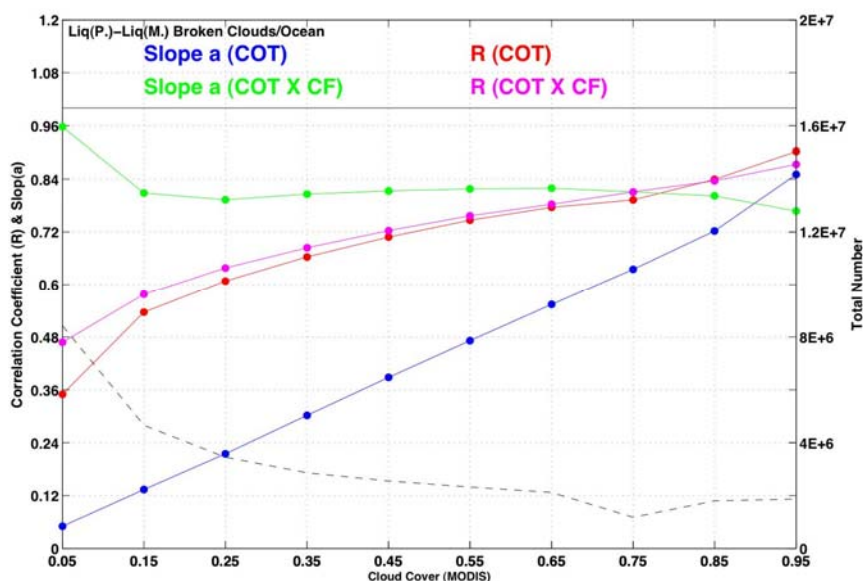
Figure 5.4-2 – *The slopes and correlation coefficients of the relationship between POLDER and MODIS COT and between POLDER and MODIS (COT ×CF) as function of MODIS cloud cover. Dashed line corresponds to the pixel number.*

b. Role of the sub-pixel cloud inhomogeneities in COT retrieval

Since sensor spatial resolutions of POLDER and MODIS are different, POLDER with a lower resolution not only ignores the sub-pixel cloudiness but its COT retrievals are also more directly impacted by sub-pixel clouds inhomogeneities compared to MODIS. When POLDER considers a cloudy pixel as a plan-parallel homogeneous (PPH) cloud, MODIS accounts for a part of variability as the POLDER pixel contains several MODIS pixels considered as PPH clouds. As explained in Figure 5.2-2, cloud optical thickness of heterogeneous clouds retrieved from the sensors with a lower resolution is thus reduced. This has been reported by other studies (Cahalan *et al.*, 1994; Oreopoulos and Davies, 1998; Marshak *et al.*, 2006;

Deneke *et al.*, 2009). Since POLDER does not account for sub-pixel heterogeneity, its COT is expected to be smaller compared to the MODIS one. This is indeed what we observe, for example, in the pixel-to-pixel comparisons for single layer overcast clouds with confident phase (see Figure 5.3-2 and Figure 5.3-3).

To see more clearly the impact of cloud heterogeneity on the retrieval of COT, in Figure 5.4-3, we present correlation coefficients and slopes between POLDER and MODIS COT for different ranges of cloud inhomogeneous values, determined as the ratio of the standard deviation to the mean cloud optical thickness derived from MODIS. We see for homogeneous clouds (inhomogeneity parameter close to 0), that both the correlation coefficients and the slopes values are high and close to one. When clouds become more inhomogeneous, these two constants decrease rapidly. It means that the more inhomogenous the clouds are, the larger differences are found between POLDER and MODIS COT, and their correlation becomes weaker. From this figure, we also note a decrease of MODIS COT when clouds become more inhomogeneous. For inhomogeneous clouds, MODIS COT distributes between 0 and 50 but for homogeneous clouds, it distributes between 0 and 100. This is a consequence that for the more inhomogeneous cloud that contains a large and a small COT with sharper contrast between the two, the mean COT is a moderate value. And also, as the subpixel cloud inhomogeneity is important for the two sensors, the COT retrieved is underestimated. Note in addition that for the very thick convective clouds, as the reflectance saturates near a COT of 100, the contrast due to cloud inhomogeneity will not appear thus the inhomogeneity parameter will be small.
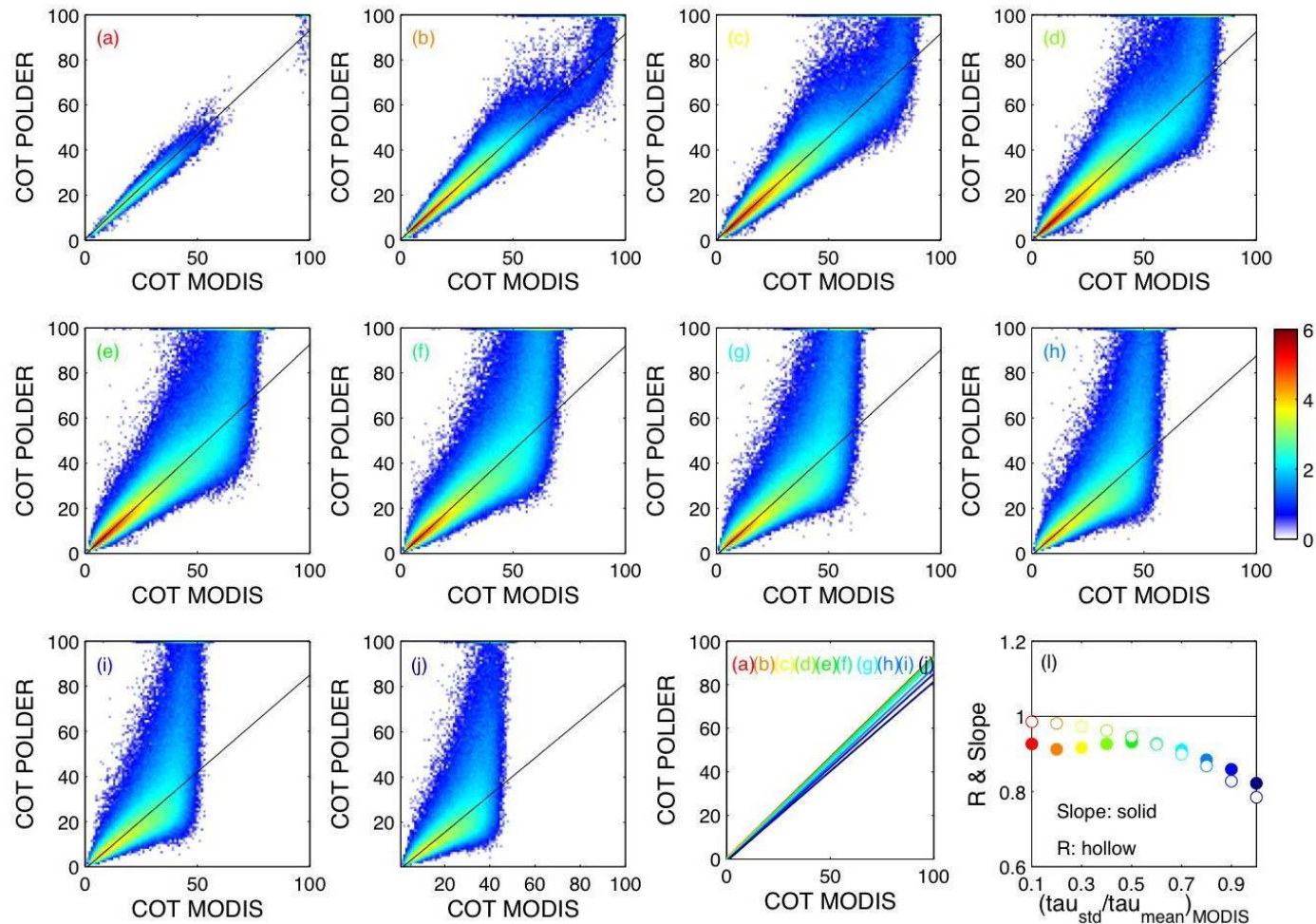
Figure 5.4-3 – *Pixel-to-pixel comparisons of POLDER and MODIS COT for different inhomogeneity parameter values determined by the standard deviation to the mean COT from MODIS: 0 to 0.1 (a), 0.1 to 0.2 (b), 0.2 to 0.3 (c), 0.3 to 0.4 (d), 0.4 to 0.5 (e), 0.5 to 0.6 (f), 0.6 to 0.7 (g), 0.7 to 0.8 (h), 0.8 to 0.9 (i), 0.9 to 1 (j) and a summary of the slopes and correlation coefficients as function of cloud inhomogeneity (l). Colorbar means logarithmic pixel number.*

5.4.2 Impact of cloud microphysics

Cloud reflectance depends explicitly on the scaled optical thickness and implicitly on the phase function (King, 1987). "Scaled" means that the optical thickness is multiplied by the factor (1-*g*) where g is the asymmetry coefficient (Eq. 5.5-1). It allows to account in a first order for the assumed phase function used for the retrievals. Hence, the retrieved scaled optical thickness will still depend on surface albedo and cloud reflection but less on cloud microphysical hypotheses (cloud phase, cloud particles radius and shapes). To assess the potential optical thickness bias associated to uncertainties associated with the scattering model, we compared the scaled optical thickness between the two sensors (see Figure 5.4-4).

$$\tau^* = (1-g)\tau \qquad \text{(Eq. 5.5-1)}$$

As seen in chapter 4, POLDER and MODIS may have inconsistent phase decisions and even in case of consistent phases, they have different assumptions in particle microphysics used to retrieve cloud optical thickness especially for ice clouds. The different assumptions in particle microphysics between POLDER and MODIS are summarized in Table 5.2-1. For liquid clouds, both sensors employ a Mie scattering model. However POLDER has no real-time effective radius retrievals but uses a fixed value of 9 μm over land and 11 μm over ocean whereas MODIS can simultaneously retrieve the effective radius and the optical thickness. As the sensitivity of visible reflectance of liquid clouds to microphysics assumption is small, the impact of particle radius bias on POLDER COT deviation can be mostly ignored except for particular scattering angles, such as the rainbow and backward directions (Parol *et al.*, 2000, Buriez *et al.*, 2001). We obtain thus, for liquid clouds, a good statistical relationship between the COT of the two sensors as shown in Figure 5.3-1 (d). For ice clouds, a recent study from Zhang et al. (2009) has discussed ice COT differences between POLDER and MODIS. Among many potential reasons, the microphysical assumption differences appear to be the main reason of ice COT differences between the two sensors. The slope derived from Figure 5.3-1 (a) through the whole year at the global scale (0.74) is close to the value found by Zhang for only

one granule (0.68). The better slope (0.74 compared to 0.68) and correlation coefficient obtained are due to an improvement in the matching of POLDER and MODIS coincident pixels in the PM data and potentially to the larger dataset considered here.

As scaled optical thickness referred above is less dependent on cloud microphysics, closer relations between the two sensors are found whatever the cloud phase classes in Figure 5.4-4 compared to the relations observed in Figure 5.3-1. Better agreement between the two sensors is found especially for ice clouds and clouds with inconsistent phases where one sensor uses ice crystal model and the other uses liquid droplet model. In this case, although clouds with inconsistent phases are associated to complicated situations shown in chapter 4, as for example, the presence of aerosols (biomass burning) over low water clouds or multilayer cloud systems, the slopes of scaled optical thickness are much closer to 1 compared to the slopes of the two optical thicknesses shown in Figure 5.3-1. The slope is also improved for ice clouds. This confirms with significant statistics, that the bias in ice cloud optical thickness between POLDER and MODIS comes primarily from different cloud microphysical assumptions as reported by Zhang et al. (2009). The correlation coefficients of the two optical thicknesses and scaled optical thicknesses remain almost unchanged independently of the cloud phase category considered.
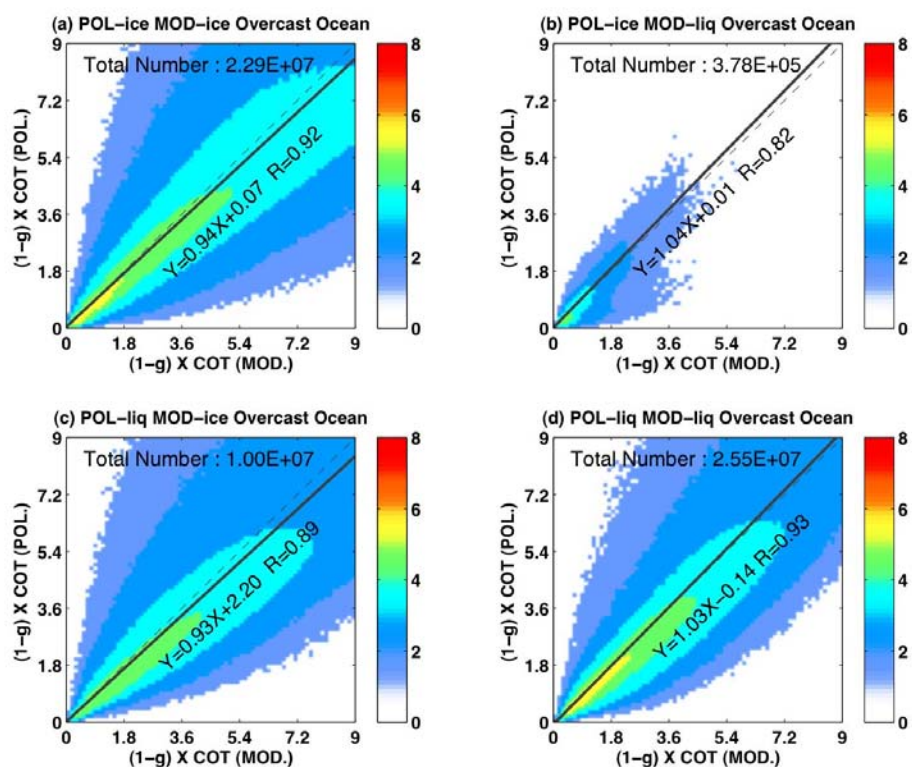
Figure 5.4-4 – *Pixel-to-pixel comparisons of COT ×(1-g) for the 4 different overcast clouds separated by cloud phase.*

As mentioned above, the effective radius is one of the main cloud microphysics differences in assumptions used in POLDER and MODIS COT retrievals. The asymmetry factor (*g*) depends strongly on the effective radius according to a simple increasing relationship (King, 1987, Baum *et al*, 2005). To further study the impact of cloud microphysics on COT, we plot in Figure 5.4-5 the slopes and correlation coefficients between the two optical thicknesses and the two scaled optical thicknesses respectively as function of cloud effective radius derived from MODIS for liquid (subfigure a) and ice (subfigure b) clouds. The correlation coefficients remain quasi-unchanged with a variation limited to 0.01%. On the contrary, we note a large improvement for the slope value. We notice also that the correlation coefficients remain quasi-constant as function of the effective radius for liquid clouds while they slightly increase with the effective radius for ice clouds. The slope for liquid clouds decreases from small droplets (slope >1) to large droplets (slope <1) with logically a slope close to 1 for effective radius around 11 as used by POLDER retrieval. Clouds with smaller effective radius reflect more radiation to satellites if other cloud microphysical properties are kept unchanged. To reflect the same radiation back to

satellites, clouds with small particle effective radius need consequently smaller COT compared to the large one. However, it is a little surprising that the slope increases for droplets superior to 16. This is possibly because the dependence between the asymmetry factor and the effective radius is less important for large effective radius and thus other impacts may dominate the relationship. But this needs to be further studied. Compared to the cloud optical thickness slopes, the scaled optical thickness slopes are closer to 1 for all effective radii. For liquid clouds with effective radius around 11 corresponding to POLDER effective radius assumption in the retrieval, the slope remains logically unchanged for optical thickness and scaled optical thickness. For ice clouds, the cloud optical thickness slope decreases with effective radius and is a lot improved (close to 1) for scaled optical thickness with value remaining almost constant as function of the effective radius. The better slopes obtained for liquid and ice clouds for the scaled optical thickness show that accounting for the asymmetry factor allows to explain an important part of the differences between POLDER and MODIS COT, calling for a good understanding of microphysics assumptions when comparing COT retrievals from various instruments.
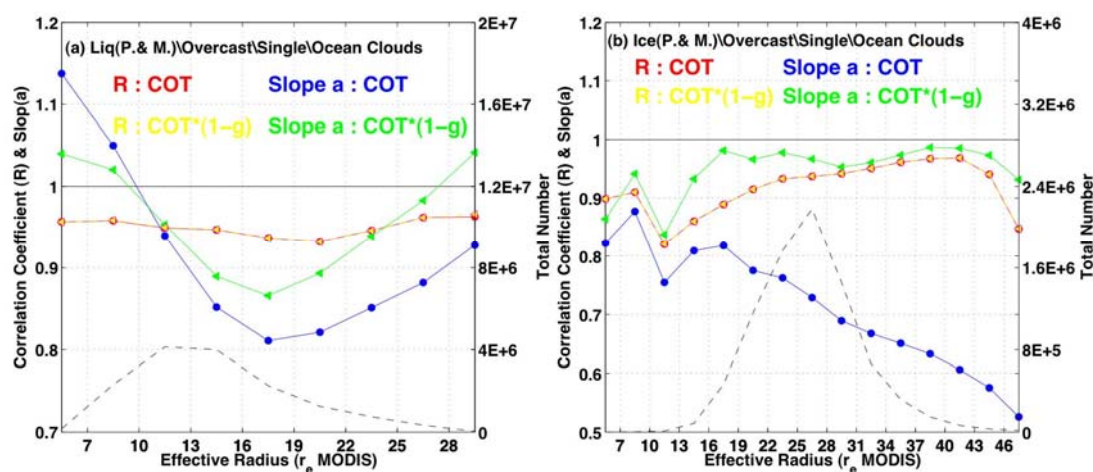
Figure 5.4-5 – *Slopes and correlation coefficients obtained between POLDER and MODIS COT and scaled COT as function of cloud particle effective radius for liquid clouds (a) and ice clouds (b). The corresponding pixel numbers are in dash line.*

5.4.3 Impact of ground albedo

To correctly retrieve cloud optical thickness, the ground reflectance is accounted for in the building of the LUT or during retrieval when reconstructing TOA signals from LUT and ancillary data such as surface albedo. Therefore, an error in the surface reflectance value may impact the LUT, the theoretical TOA signal simulation used and thus the COT retrieval. Platnick and Valero (1995) assessed this sensitivity to surface reflectance for the COT retrieval (see Figure 5.4-6). An error of 0.04 in surface albedo biases the retrieved optical thickness especially for the thinner clouds. For example when optical thickness is equal to 1, the error can reach up to 90% and is still about 10% for a COT of 5. As POLDER and MODIS use different surface reflectance inputs (both use the statistical clear sky albedo derived from their own algorithm, see Table 5.2-1), this uncertainty due to the surface reflectance needs to be carefully studied.
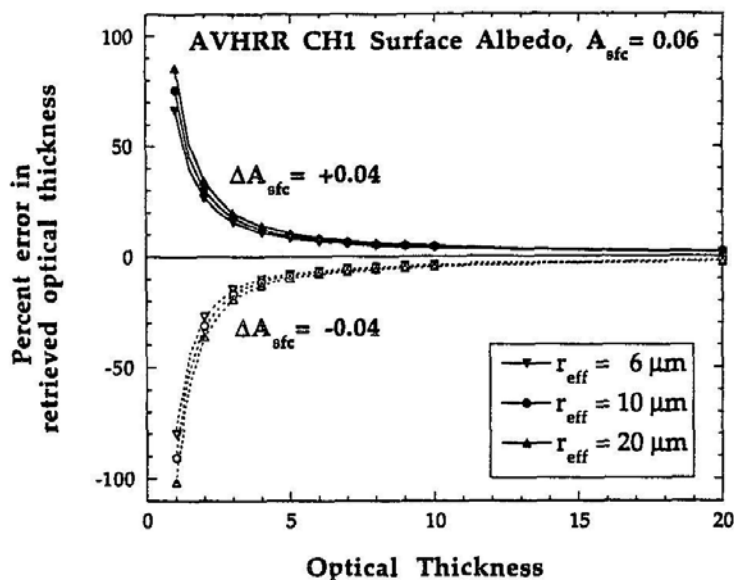
Figure 5.4-6 – *Error in retrieval of cloud optical thickness for various radii as a function of optical thickness for an uncertainty in surface albedo of ±0.04 from Platnick and Valero (1995). A_{sfc}=0.06 is typical value of the ocean surface albedo.*

In Figure 5.4-7, we present the correlation coefficients and the slopes of POLDER and MODIS COT relationship as function of surface albedo (derived from POLDER) in bins of a width of 0.03. Overall, we notice that surface albedo impact less the relation between the two COTs compared to cloud fraction or microphysics assumption. For both liquid (subfigure a) and ice (subfigure b) clouds, the correlation

coefficients and the slopes are worse for thin clouds compared to all clouds. For all clouds, the correlation coefficient decreases when surface albedo increases, which means a degraded relationship between POLDER and MODIS COT over brighter surfaces. The decrease of the correlation coefficient is more pronounced for thin clouds (thin clouds in hollow circles are identified when MODIS COT is less than 5). Looking at the slope, for albedo lower than 0.06, where the impact of surface can be ignored for COT retrieval, the value approaches unity for liquid clouds and is about 0.67 for ice clouds. As the surface becomes brighter, the slope values increase for ice clouds and show slight decrease or no significant change for liquid clouds. This means that for ice cloud, POLDER COT is closer to the MODIS one over bright surface and suggests that errors in surface albedo compensate other differences. In practice, it is consistent with the fact that bright surface reflects more radiation to satellites compared to dark surfaces acting similarly to the small particles reflecting more backward radiation.
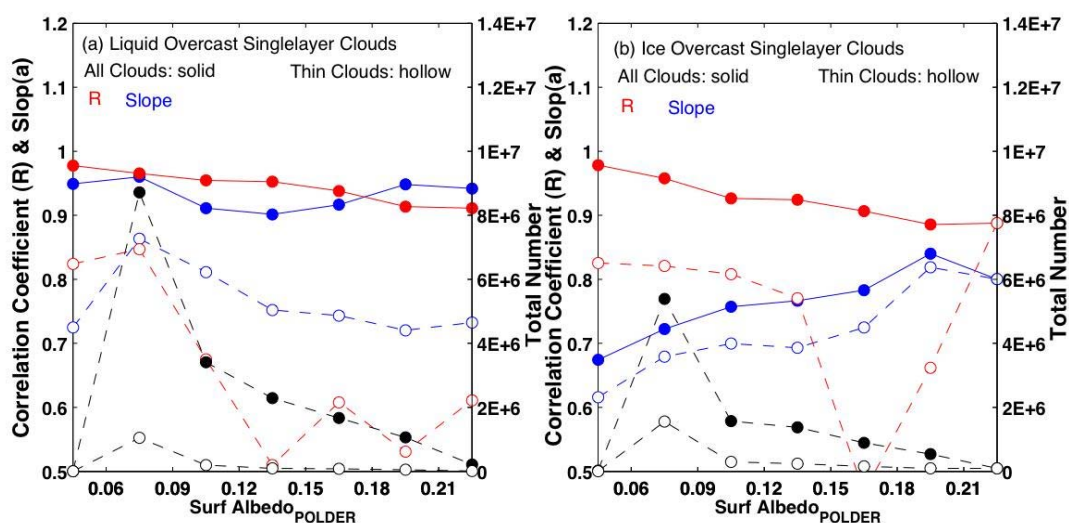
Figure 5.4-7 – *The slope a (in blue, left axis) and correlation coefficient R (in red, left axis) between POLDER and MODIS COT as function of the surface albedo derived from POLDER clear sky albedo: for liquid clouds (a), ice clouds (b). Thin clouds (dashed line) means COT derived from MODIS less than 5. Black lines indicate the number of pixel used (right axis).*

.

5.5 Cloud inhomogeneity

Cloud inhomogeneities are directly linked to cloud formation and may cause errors referred as plane-parallel bias (see section 5.2.2). It is important to better know cloud inhomogeneities at a global scale in order to improve cloud parameterization in global and regional climate models. Many parameters can be used to characterize cloud inhomogeneities, which can be separated at least in two terms: cloud top inhomogeneities (cloud structure) and inhomogeneity from internal volume extinction (Loeb *et al.*, 1998). Loeb et al. (1998) and Vàrnai and David (1999) suggested that the variation of cloud-top heterogeneity affects the reflection more than the internal volume extinction heterogeneity. Many studies with satellite observations have tried to parameterize cloud inhomogeneity and have shown their global geographical and seasonal distribution (e.g. Rossow *et al.*, 2002: Oreopoulos and Cahalan, 2005).

As Oreopoulos and Cahalan (2005) and Oreopoulos (2005) described in their publications, cloud inhomogeneity can be parameterized either by the ratio of logarithmic to linear average of a cloud optical thickness distribution (see Eq. 5.5-1) (Cahalan *et al.*, 1994; Barker *et al.*, 1996) or by the ratio of mean to standard deviation of the optical thickness distribution (see Eq.5.5-2).

$$\chi = \frac{e^{\overline{ln\tau}}}{\overline{\tau}} \quad , 0 < \chi \le 1, \quad \text{(Eq. 5.5-1)}$$

$$\upsilon_{MOM} = \frac{\sigma_{\tau}}{\overline{\tau}} \quad \text{(Eq. 5.5-2)}$$

Histograms of these two inhomogeneity parameters for both POLDER and MODIS from the PM data (at $20 \times 20 km^2$) are shown in Figure 5.5-1. In the same figure, we also show other cloud inhomogeneity parameters, such as the ratios of angular standard deviation to the mean of optical thickness, oxygen and Rayleigh cloud top pressure for POLDER and the ratio of standard deviation to the mean of cloud top temperature for MODIS. The geographical distributions of different cloud inhomogeneity parameters are shown and compared in Figure 5.5-2 for overcast liquid clouds and in Figure 5.5-3 for overcast ice clouds and we present also the seasonal variations of these parameters.

Looking at Figure 5.5-1, we see that the histograms are different according to the inhomogeneity parameter used. For example, the ratio of mean to standard deviation of COT for POLDER (subfigure a) is mostly between 0 and 1 while for MODIS (subfigure b) it is mostly between 0 and 1.6. The ratio of logarithmic to linear average of COT, which by definition being ≤ 1, is mostly between 0 and 0.4 for POLDER (subfigure c) while for MODIS between 0 and 0.6 (subfigure d). We note thus that for the two inhomogeneity parameters MODIS values are more dispersed with higher values certainly because of the higher spatial resolution of MODIS. From these histograms, we note also that we do not have a clear separation between homogenous and inhomogeneous clouds. The standard variation of the angular optical thickness is another way to measure the inhomogeneity and can be also sensitive to the vertical variation of the optical thickness, as each viewing angle does not sample the same side of the cloud and thus can be sensitive to the shadowing and brightening effects. The values are slightly smaller than the spatial variation and also less dispersed.

The other cloud inhomogeneity parameters (see subfigures f to h) measure rather the inhomogeneity of the cloud top as they are derived from parameters, which vary with cloud top. We see that for the overall clouds, those values are quite small certainly as the resolution of these parameters (5hPa for POLDER pressures and 0.01K for MODIS temperature) allows to resolve only large cloud top variations but no variations of few hundred meters or less.
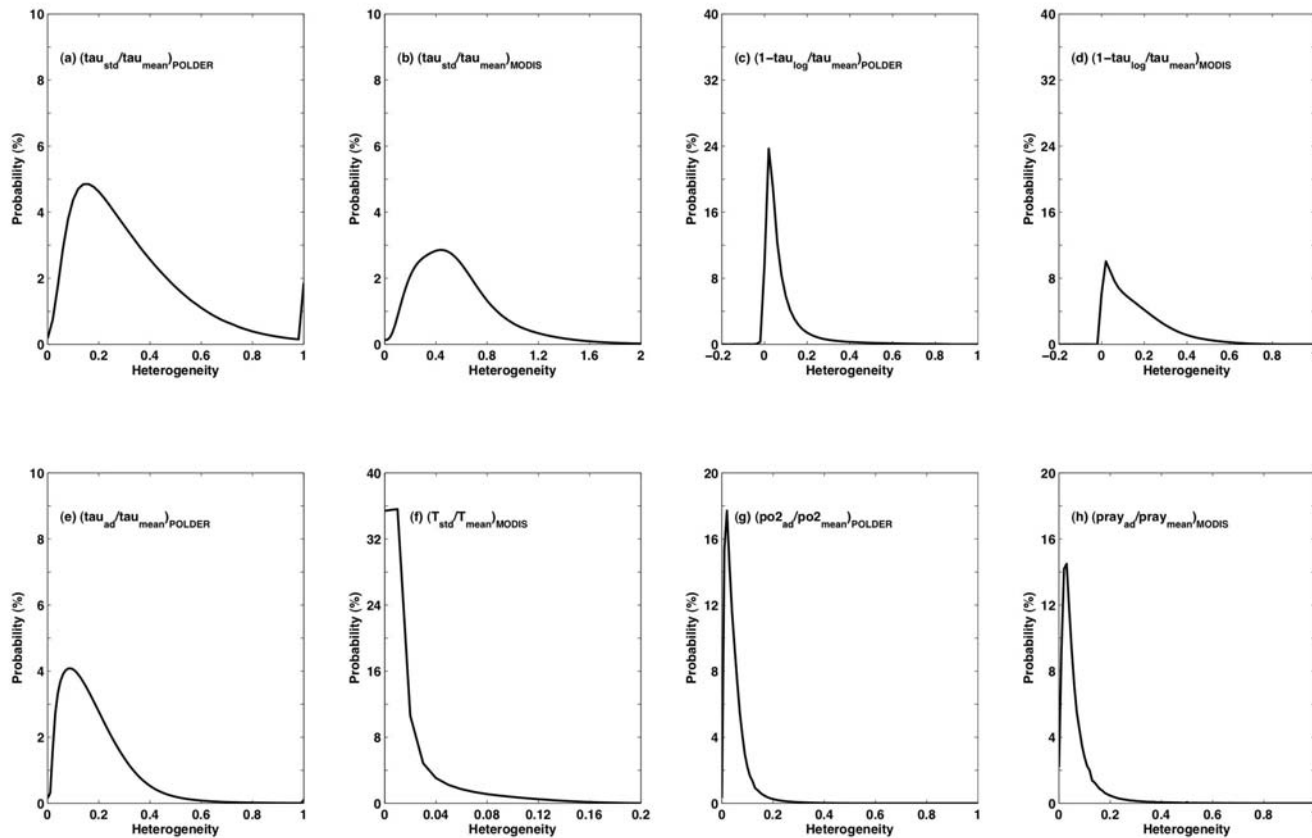
Figure 5.5-1 – *Histograms of different cloud inhomogeneity parameters from all clouds (overcast and broken with liquid and ice phase): ratio of the standard deviation to the mean optical thickness for POLDER (a) and for MODIS (b); ratio of the logarithmic and the linear average of optical thickness for POLDER (c) and for MODIS (d); ratio of the angular standard deviation to the mean optical thickness for POLDER (e); ratio of the standard deviation to the mean of cloud top temperature for MODIS (f); ratio of the standard deviation to the mean of angular cloud oxygen pressure (g) and of angular cloud Rayleigh pressure for POLDER (h).*

The geographical distributions of these inhomogeneity parameters for liquid and ice clouds are presented respectively in Figure 5.5-2 and Figure 5.5-3. At first glance, we see, no matter what sensor, that inhomogeneity parameter mainly sensitive to internal volume extinction differences or mainly due to cloud top differences are not coincidently located. However among the same type of inhomogeneity parameters, rather coincident distributions appear. Cloud inhomogeneities for ice and liquid clouds are distributed differently.

For liquid clouds, we find that:

- Looking at the inhomogeneity parameters describing rather the internal extinction variabilities (subfigures a to e), homogeneous liquid clouds are mostly located at the west coast of the continent where often appear low stratocumulus clouds while inhomogeneous liquid clouds seem mostly located over land where often appear convective clouds. Surprisingly, over deep convection regions like the ITCZ, clouds appear more inhomogeneous than above the west coast of the continent but less than above some land area. This may be due to the fact that saturation of reflection at large optical thickness makes it difficult to identify the cloud inhomogeneity.

- Looking at the inhomogeneity parameters describing the cloud top inhomogeneities (subfigures f to i), we now clearly see that the inhomogenous liquid clouds are mostly located in the tropics and in the Pacific Ocean.

For ice clouds, we find that:

- The values are almost of the same order as values for liquid cloud but we need to keep in mind that for ice clouds inhomogeneity, the microphysics model can play an important role in these values.

- The agreement between the different inhomogeneity parameters distributions is worse than for liquid clouds.

- The most inhomogeneous cloud (linked with internal extinction inhomogeneity) seems to be located over land and in high latitudes where often appear convective clouds but which can also be an artifact due to surface albedo effects (presence of desert or snow).

- From the parameters linked with cloud top inhomogeneity, we note that inhomogenous ice clouds are mostly located in the tropics.
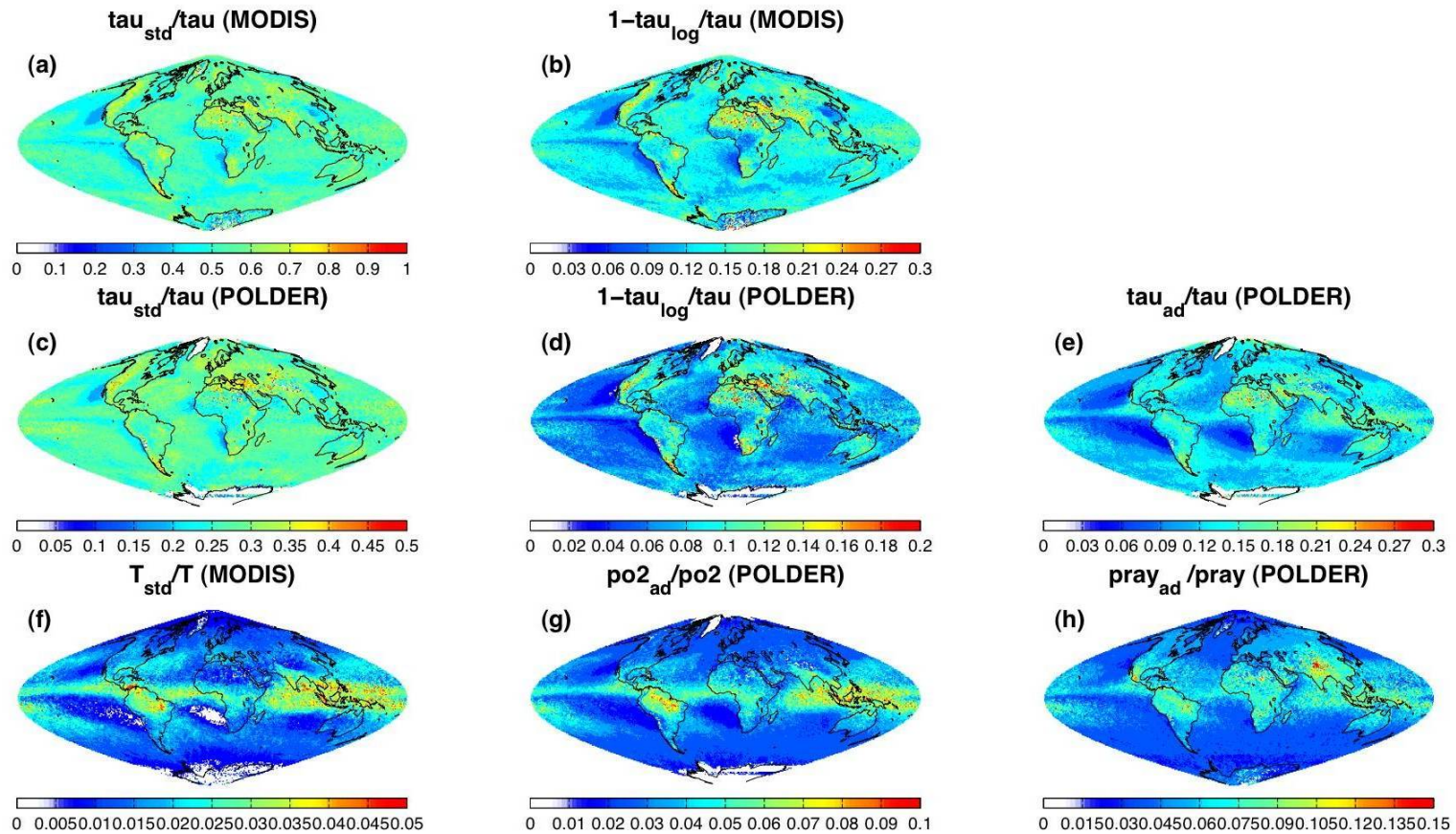
Figure 5.5-2 – *Geographical distribution of different inhomogeneity parameters for liquid clouds parameters: ratio of the standard deviation to the mean optical thickness for MODIS (a) and for POLDER (c); ratio of the logarithmic and the linear average of optical thickness for MODIS (b) and for POLDER (d); ratio of the angular standard deviation to the mean optical thickness from POLDER (e); ratio of the standard deviation to the mean cloud top temperature for MODIS (f); ratio of the standard deviation to the mean of angular cloud oxygen pressure (g) and of angular cloud Rayleigh pressure for POLDER (h).*
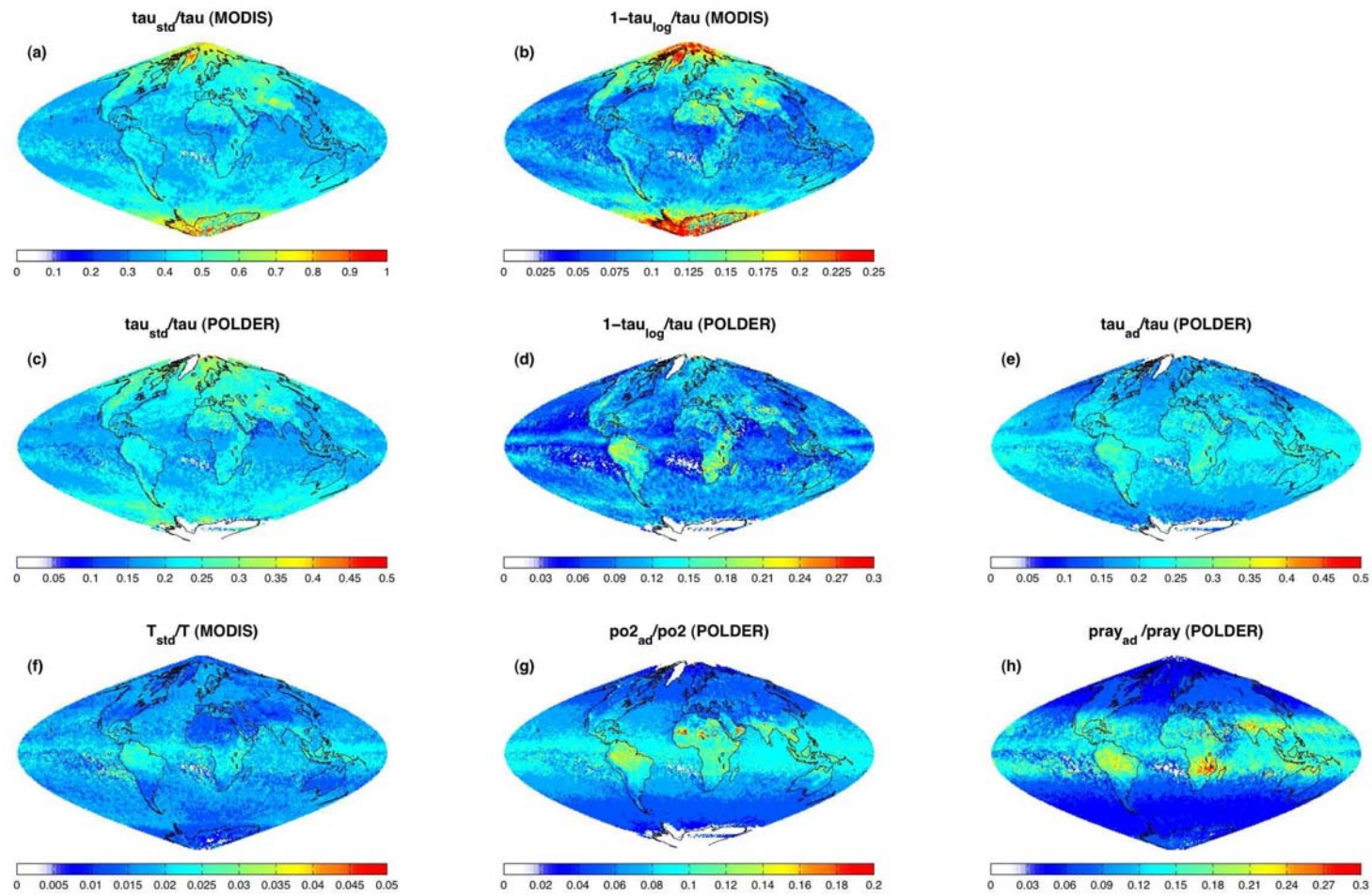
Figure 5.5-3 – S*ame as in Figure 5.5-2 for ice clouds.*

In Figure 5.5-4 we also present the seasonal variations of latitudinal distribution of cloud inhomogeneity parameters for overcast liquid clouds and in Figure 5.5-5 for overcast ice clouds. For liquid clouds, the distribution of parameters linked with cloud internal extinction inhomogeneities agrees well with the results of Oreopoulos and Cahalan (2005) that find liquid clouds more inhomogeneous in fall and winter of each hemisphere. Concerning the parameters linked with the cloud top inhomogeneities, seasonal variations are less marked except the parameters built from the Rayleigh pressure, which shows more inhomogeneous liquid clouds in summer in each hemisphere possibly because convective cells development is more frequent in summer than in winter. Again in ITCZ, clouds are not so inhomogeneous according to parameters describing the internal extinction inhomogeneities while they appear inhomogeneous according to parameters linked with cloud top inhomogeneities independently of the season.
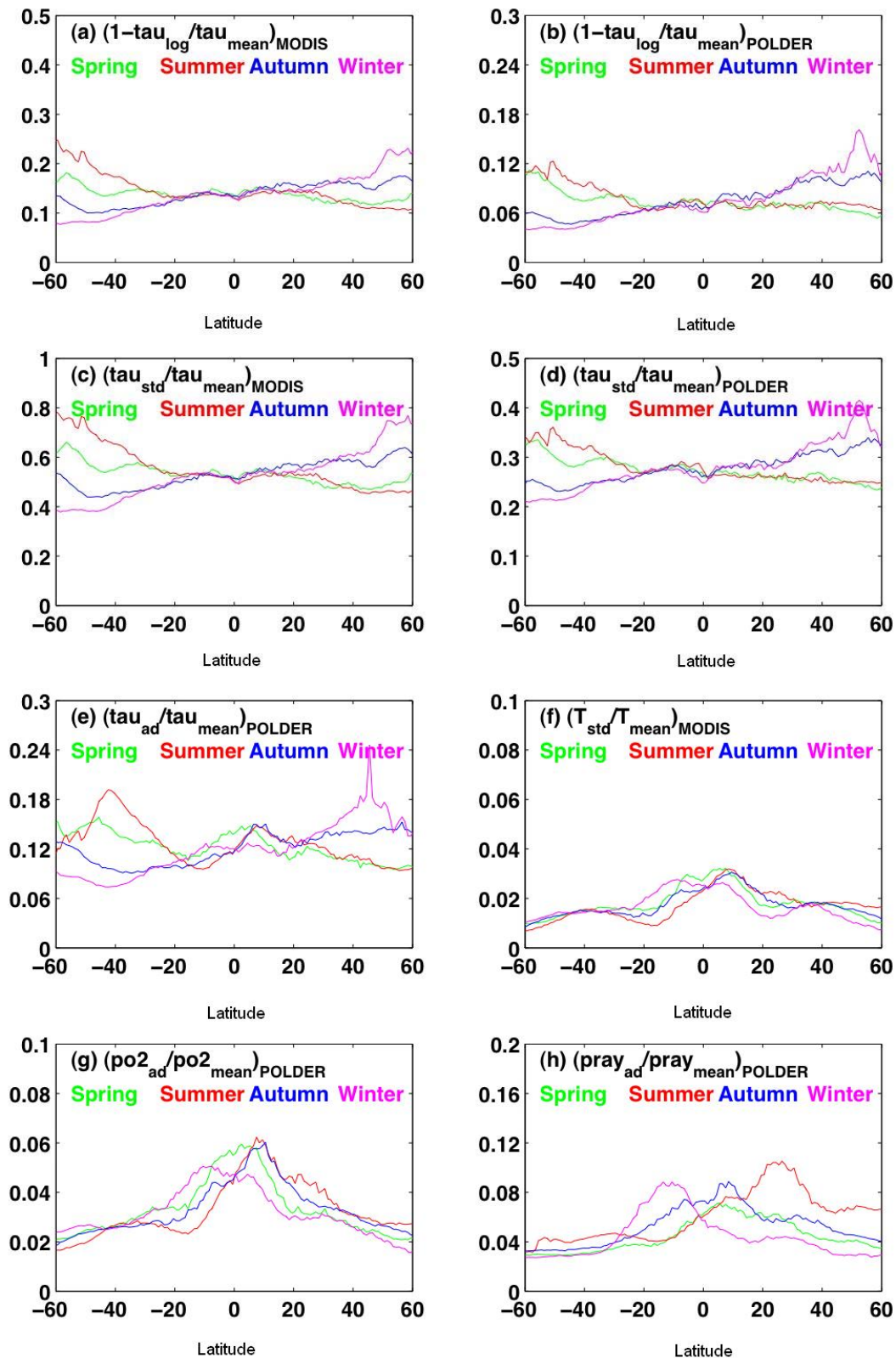
Figure 5.5-4 – *Seasonal variations for liquid clouds of latitudinal distributions of the different inhomogeneous parameters presented in Figure 5.5-1.*

For ice clouds, seasonal variations of the inhomogeneity parameters are similar and even more pronounced than those of liquid clouds: clouds are more inhomogeneous in winter in each hemisphere. Compared to the other parameters, the ratio of the angular variation to the mean COT from POLDER (e) has a different behavior and clouds seem to become slightly more homogeneous at higher latitudes.
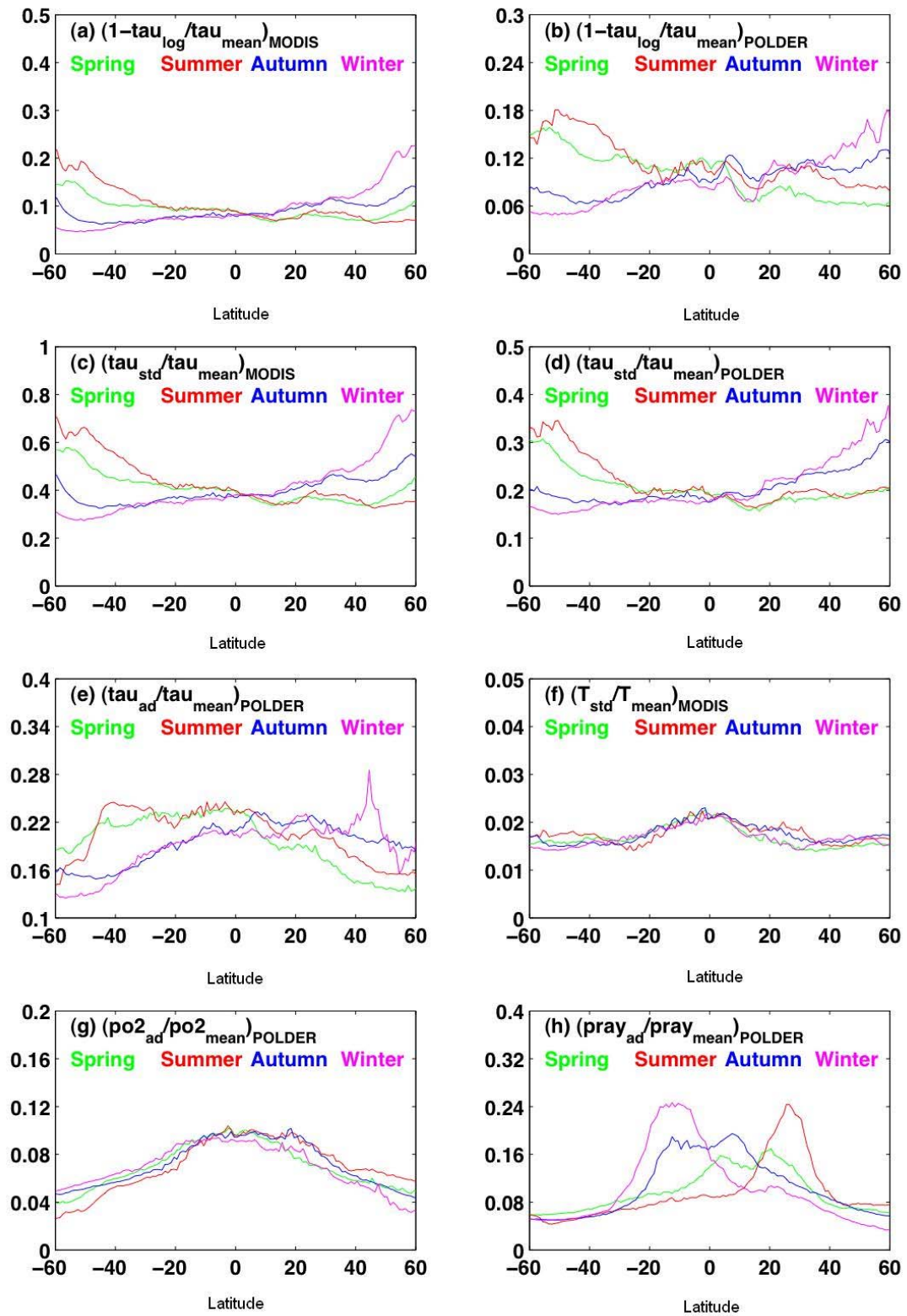
Figure 5.5-5 – *Same as Figure 5.5-4 for ice clouds.*

5.6 Angular variations

In this section, we study the angular variations of COT, which allow to illustrate errors due to the assumption of 1D homogeneous cloud model or to inadequate cloud microphysics model. As well known, for computation time reason, operational algorithms mostly usually employ the 1D theory (plane parallel) to simulate radiative transfer. 3D development could in the future improve the retrieval of COT (Cornet and Davies, 2008), but so far they cannot be operationally implemented. Several studies have been devoted to the 3D effects on COT retrieval (Loeb and Davies, 1997; Loeb and Coakley, 1998; Buriez *et al.*, 2001). They found that for low Sun, 3-D effects such as shadowing make clouds appear too dark for oblique views facing the Sun, and thus make 1-D retrievals underestimate COT while an opposite influence exists for oblique views facing away from the Sun. Theoretical studies (Bréon, 1992; Kobayashi, 1993) also indicated that cloud inhomogeneities could enhance reflection through cloud sides into oblique side scatter directions relatively to cloud reflection into overhead direction. Várnai and Marshak (2007) analyzed MODIS data and found that, optical thickness retrievals give remarkably consistent results for all view directions if clouds are homogeneous but they give much higher COT values for oblique views if clouds are inhomogeneous and facing to a fairly oblique sun.

Note that the angular comparisons presented in this section are not strictly comparable to the coincident pixel-to-pixel comparisons made in previous sections because of sampling differences. Indeed, an increase of MODIS viewing angle corresponds to locations from the center to the edges (western/eastern side) of the swath, with each pixel observed only in one direction while for POLDER, one pixel can be seen up to 16 directions. This implies that the same scattering (or viewing) angle for POLDER and MODIS may be sampled from different latitudes (or longitude) leading to the observation of different cloud systems. In addition, the scattering angles sampling are biased by the fact that solar angles variations are linked to latitudes as A-Train satellites are sun-synchronous.

In Figure 5.6-1, we present statistics of COT against sensor viewing angles separated by solar elevation. Negative sensor zenith values correspond to backward scattering direction (relative azimuth angle<90°). These angular variations are plotted according to cloud cover and thermodynamic phase determined from a combination

of POLDER and MODIS retrieval. As we have seen in Figure 3.3-6, cloud cover varies also with viewing angle. We will use these previous results to analyze the figures and understand the angular variations of COT.

For liquid clouds:

● For overcast liquid scenes for the two sensors and for broken scenes for MODIS, we see that COTs increase with solar angle and cloud cover as can be seen in Figure 3.3-6. This behavior has already been observed (Loeb and Davies, 1996) and has been reproduced with simulations of reflectances from 3D clouds with bumpy cloud top (Loeb *et al.*, 1997). However as we have seen in chapter 3, the zonal sampling can also lead to this increasing trend as solar elevation decreases and cloud fraction increases with latitude. We also note that for overcast scenes except for low solar elevations for POLDER, COT almost does not change with viewing angle (see subfigures a and e). On the contrary, for low solar elevations observed by POLDER and for broken scenes, we see an important decrease of COT when the viewing angle increases, especially in forward directions that are primarily impacted by cloud shadow (subfigures e, c and g). This bias agrees with what Buriez *et al.* (2001) and Varnai and Marshak (2007) found for all clouds situations.

● For broken cloud scenes, COT decreases with viewing angle for both sensors in both forward and backward directions, agreeing with results by Maddux et al. (2010).

For ice clouds:

● Except for broken ice clouds observed by MODIS (subfigure d), COT does not show an increasing trend against solar elevations as it does for liquid clouds. The COT seems to be smaller for solar angles between 30° to 60°, which may be associated to latitudinal distribution. Secondly, we note that the angular variations of COT for ice clouds are quite different between POLDER and MODIS and can certainly be explained by the use of different ice microphysics models: For POLDER, it shows a decreasing trend against the viewing angle in forward directions while an increasing trend in backward directions for oblique suns while for overhead suns COT decreases with viewing angle for both forward and backward directions. For MODIS, angular variations of COT are very confused and it is hard to find any significant tendency. This can be explained again by the fact that MODIS uses a different microphysics model for each retrieval. We can

however conclude that the microphysical representations of ice clouds still need to be further investigated and can probably be improved for both sensors.
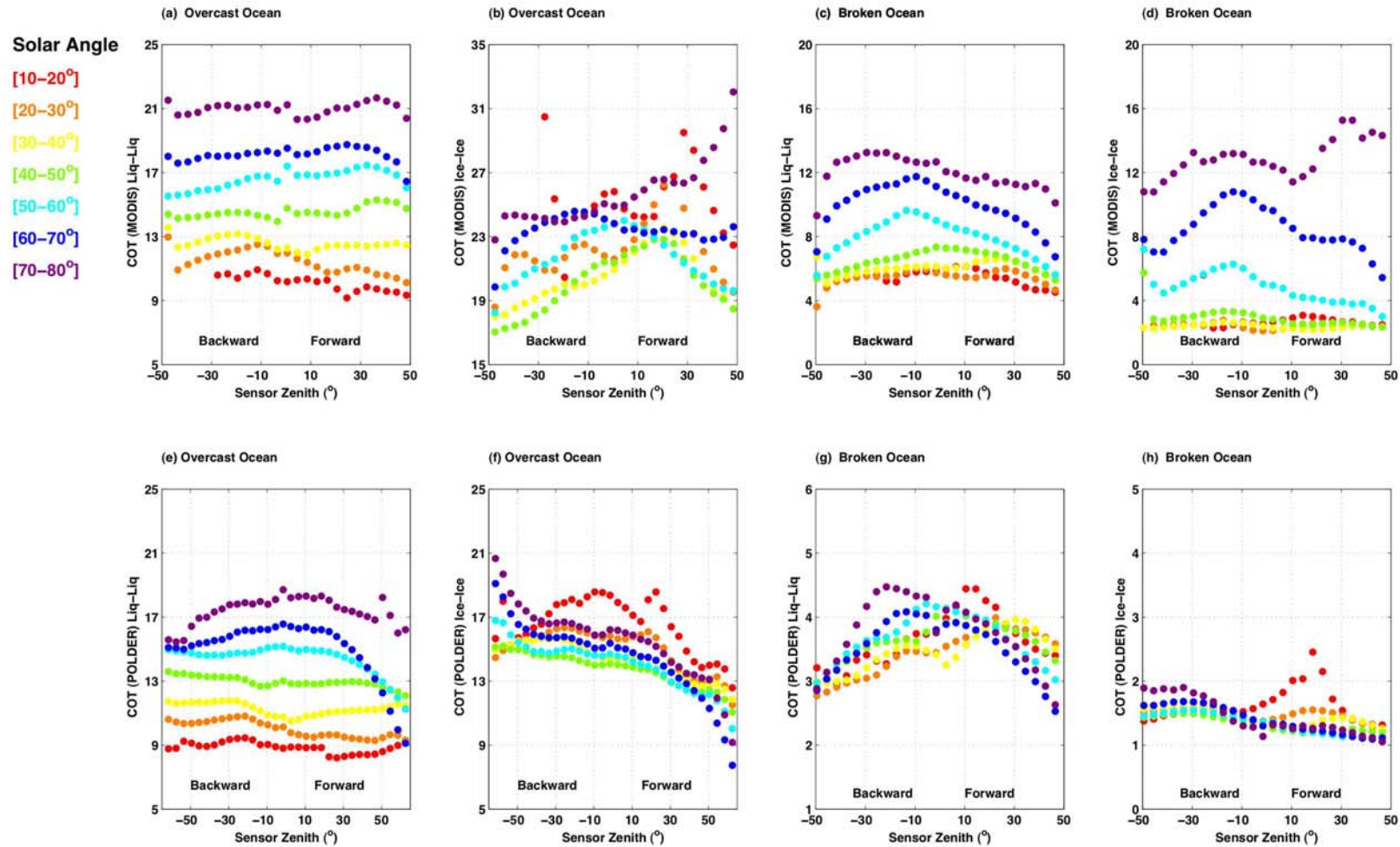
Figure 5.6-1 – *COT against viewing zenith angle for both MODIS and POLDER sensors separated by cloud phase and cloud cover over ocean. MODIS: first line, POLDER: second line. confident overcast liquid clouds: first column, confident overcast ice clouds: second column, confident broken liquid clouds: third column and confident broken ice clouds: fourth column.*

In Figure 5.6-2 we show COT against the scattering angle calculated from Eq. 5.6-1. Each subplot corresponds to one class of combined phase and three curves are presented individually: MODIS COT against MODIS scattering angle (hollow circle, referred as curve 1), directional POLDER COT against POLDER scattering angle (solid circle, referred as curve 2) and finally the mean POLDER COT against MODIS scattering angle (hollow rectangle, referred as curve 3). Note that curve (1) and (2) are not from coincident pixels as explained above, and then may show bias due to different zonal samples. However curve (1) and (3) are from coincident samples.

$$\cos\Theta = \cos\theta_v \cos\theta_s - \sin\theta_v \sin\theta_s \cos\phi_r \qquad \text{(Eq. 5.6-1)}$$

Looking first at the directional POLDER COT (curve 2), we see that one-year statistics of angular COT variations in Figure 5.6-2 show similar angular trends for both liquid and ice clouds as previous studies realized in a shorter period (Buriez *et al*. ,2001; C.-Labonnote *et al*., 2000). As reported for liquid clouds, POLDER finds smaller COT in rainbow and forward directions. For ice clouds, a quasi-constant variation against the scattering angle is observed with smaller value in forward directions. One interesting observation is for the case of POLDER-liquid and MODIS-ice clouds, where the decrease of COT in backward and rainbow directions is more pronounced compared to confident liquid clouds. Buriez *et al*. (2001) presumed that the smaller rainbow value is not simply related to cloud particle radius but seems to have some relations with cloud top pressure as the decrease is less pronounced for low clouds. Result here supports in one sense this assumption, as cloud top pressure is also linked partially with cloud thermodynamic phase. High clouds have a higher probability of erroneous liquid phase detection, which lead to a lower rainbow value for COT. Indeed, if ice clouds are falsely labeled as liquid in the rainbow direction, where liquid phase function presents a peak, it results in a smaller retrieved optical thickness. In addition, as phase functions of mixed phase clouds are not well defined, in case of clouds identified with different phases by the two sensors, angular variations of COT can be impacted by mixed phase clouds. As a consequence, cloud phase impacts directly COT, and in turn, we can speculate that angular consistency of COT could help to assess the correctness and confidence of cloud phase.

We look now at the final POLDER COT averaged at the superpixel resolution over 16 directions. It may contain forward and backward directions and thus minimize the angular bias from 1D radiative transfer. This final POLDER COT is plotted against MODIS geometries (curve 3) and compared with MODIS COT (curve 1). They do not show constant variations as function of scattering angle and abnormally large COT in forward directions that is opposite to the directional POLDER COT behavior (curve 2). However compared to MODIS COT (curve 1), the averaged POLDER COT (curve 3) shows similar angular trends with an increase of both COT in forward directions. As the MODIS observing geometry depends strongly on the latitude, the increase of COT in forward directions may be due to a more frequent sampling of thick clouds in certain regions. Concerning the COT differences between curve 1 and 3, the coincident differences increase logically linearly with COT because of the linear relationship between the two COTs observed above. This is verified except that for confident liquid clouds almost null COT differences between 140°-170° are found and that for POLDER-liquid & MODIS-ice clouds small COT differences in MODIS rainbow directions are found.
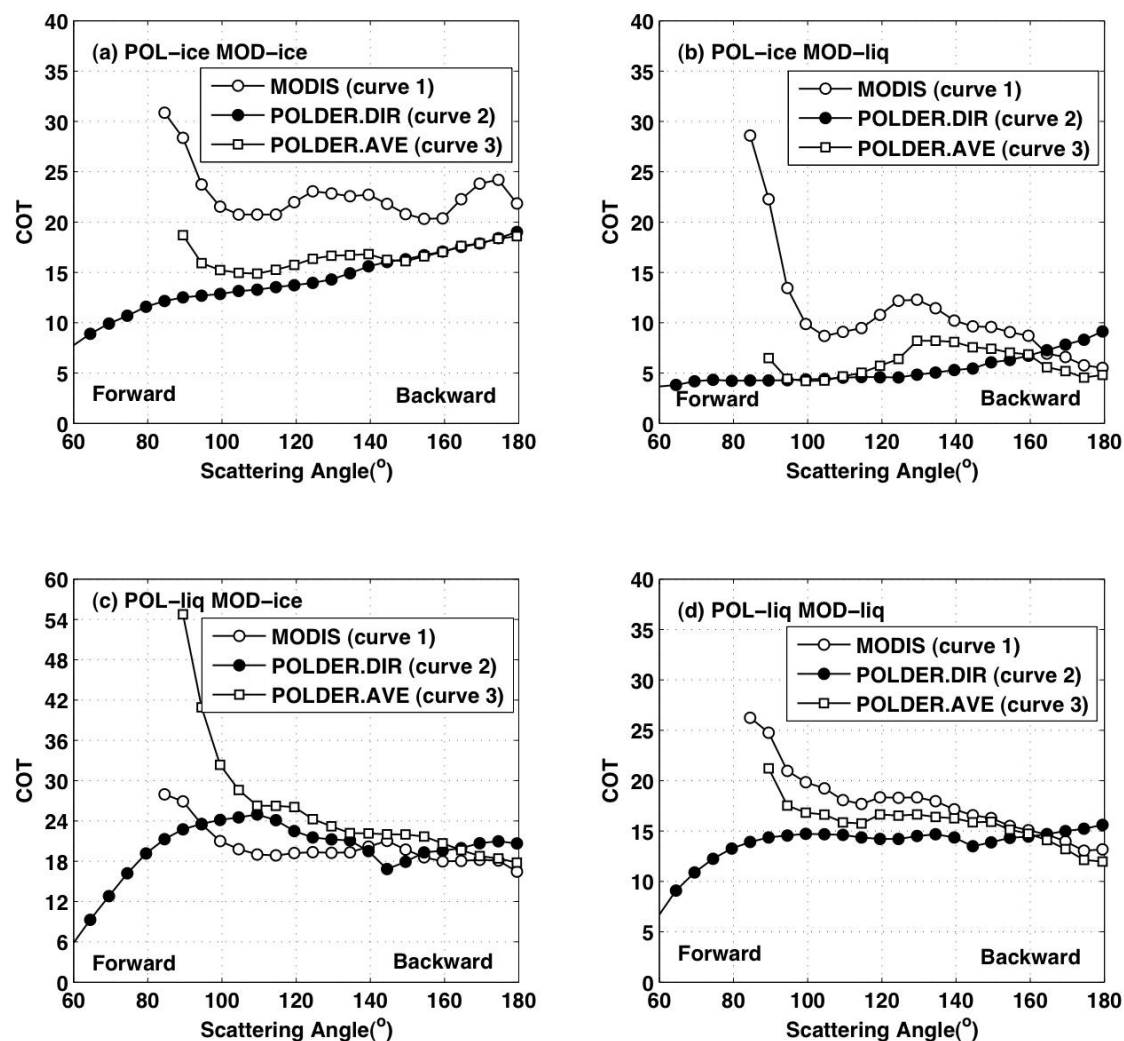
Figure 5.6-2 – *COT of overcast clouds over ocean according to scattering angles for directional POLDER COT (solid circles, curve 2), for average POLDER COT (hollow squares, curve 3) and for MODIS COT (hollow circles, curve 1). The 4 panels present results by cloud phase combination: POLDER-ice MODIS-ice (a), POLDER-ice MODIS-liquid (b), POLDER-liquid MODIS-ice (c) and POLDER-liquid MODIS-liquid (d).*

Above, we have analyzed COT variations against the viewing angle and scattering angle. Here we go a little further to study POLDER and MODIS angular signature by looking at polar plots of optical thickness for the two sensors. If the cloud model is perfect and the geographical changes are excluded, optical thickness values should be constant with viewing angle. The polar plot allows then to identify some deviations due to the inappropriate cloud model used for the retrieval. Moreover, it can help to establish a reference to select a suitable weighted average method in order to better

determine the final COT from the directional COT and then avoid some systematical errors from 3D effects such as shadow effect.

The COT polar graph as function of the sensor viewing angle and relative azimuth for different solar elevations is presented in Figure 5.6-3 for POLDER overcast liquid clouds, in Figure 5.6-4 for MODIS overcast liquid clouds, in Figure 5.6-5 for POLDER broken liquid clouds and in Figure 5.6-6 for MODIS broken liquid clouds. The zero relative azimuth direction corresponds to backward scattering direction.

In the four groups of figure as observed above, we note that optical thickness increases with solar zenith angle even for overcast cloud which are not supposedly biased by an increase of cloud cover.

Comparing Figure 5.6-3 and Figure 5.6-4, we clearly see that MODIS has limitations in sampling different relative azimuth angles (mainly around 60° and 120° for the low sun) as it observes only in one direction. The figures are thus not very informative except maybe a small decrease of optical thickness in the forward scattering direction for sun zenith angles lower than 30°. We however note that whatever the solar angle, COT seems to be almost constant with the viewing zenith angle for the overcast cloud case (also seen in Figure 5.6-1). Thus the effects of cloud inhomogeneity seem to be statistically limited for MODIS due to its limitation in sampling of relative azimuth angles. This behavior of MODIS COT agrees with the simulation: for lower sun COT may be overestimated in backward directions and underestimated in forward directions; however between them and on average, COT retrieved from 1D radiative transfer may be correct. Figures built from POLDER cover more geometries thanks to the 16 observations. Looking at Figure 5.6-3 for overcast clouds, we see that COT decreases in forward directions and more significantly for oblique sun. This may come from cloud shadows that decrease the retrieved COT. We also see smaller COT in the rainbow direction at lower sun, which may be associated to both particle radius assumption and cloud inhomogeneities.

For broken clouds, we see that COT retrieved from MODIS decreases with viewing angle independently of the relative azimuth (see Figure 5.6-6). This decrease behavior may come from the cloud detection. As we have seen in chapter 3, MODIS cloud fraction (CF) depends more seriously on the viewing angle due to the change of resolution as it scans at different viewing angles. CF increases with the viewing angle because MODIS sees more cloud sides and as a consequence the COT decreases with the viewing angle. This decrease of COT can be also explained by 1D radiative

transfer bias. In case of broken clouds for POLDER, we clearly see high values of COT in the sun-glint directions. It may point out that the limitation to prevent COT retrieval in sun glint regions is not enough restrictive especially in case of broken clouds (see Figure 5.6-5). We also see consistent underestimations of COT in the backward and rainbow directions, which are certainly due to the microphysics issue that POLDER effective radius is set to a constant value.
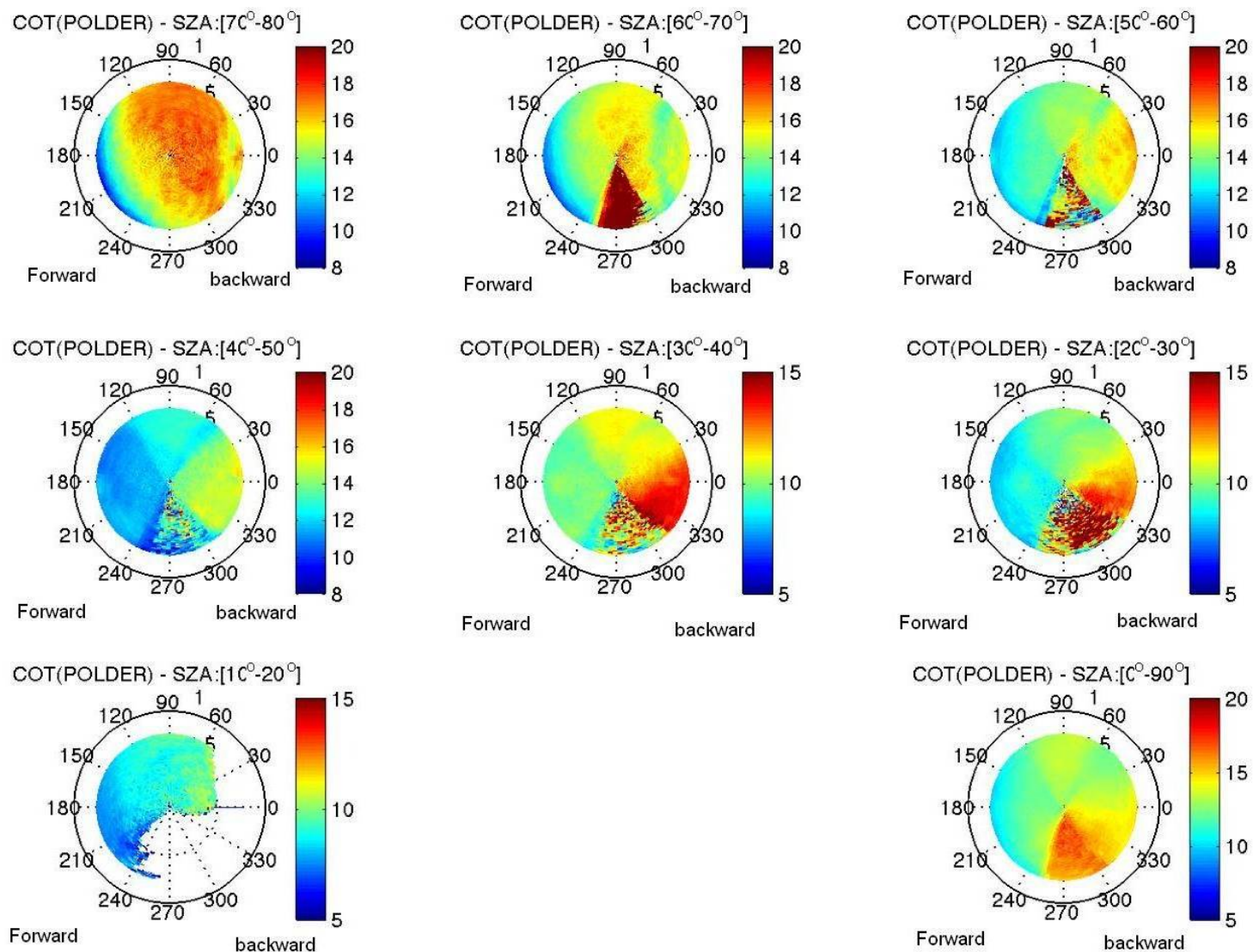
Figure 5.6-3 – *Polar graph of POLDER COT for overcast oceanic clouds and for different solar elevations.*
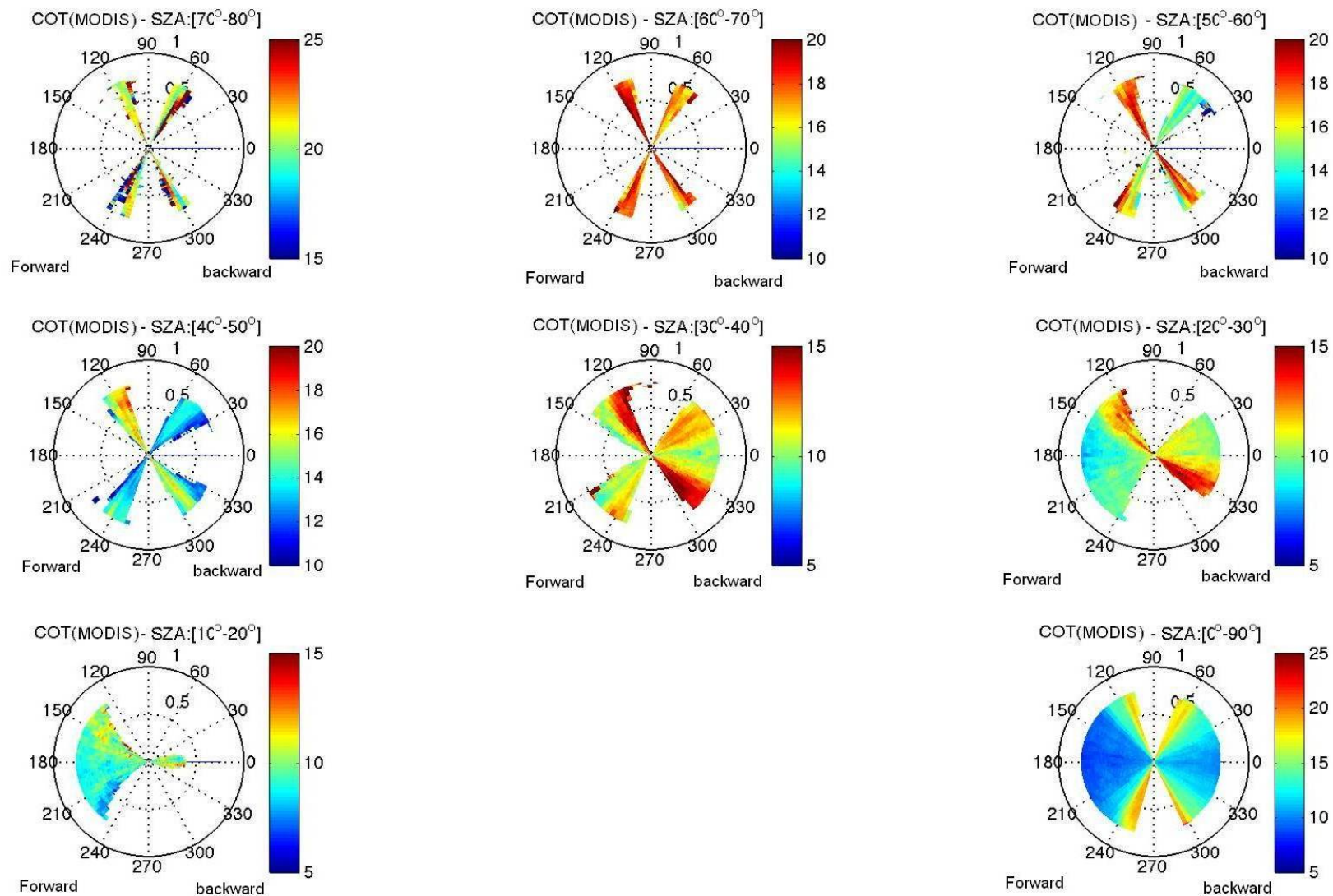
Figure 5.6-4 – *Polar graph of MODIS COT for overcast oceanic clouds and for different solar elevations.*
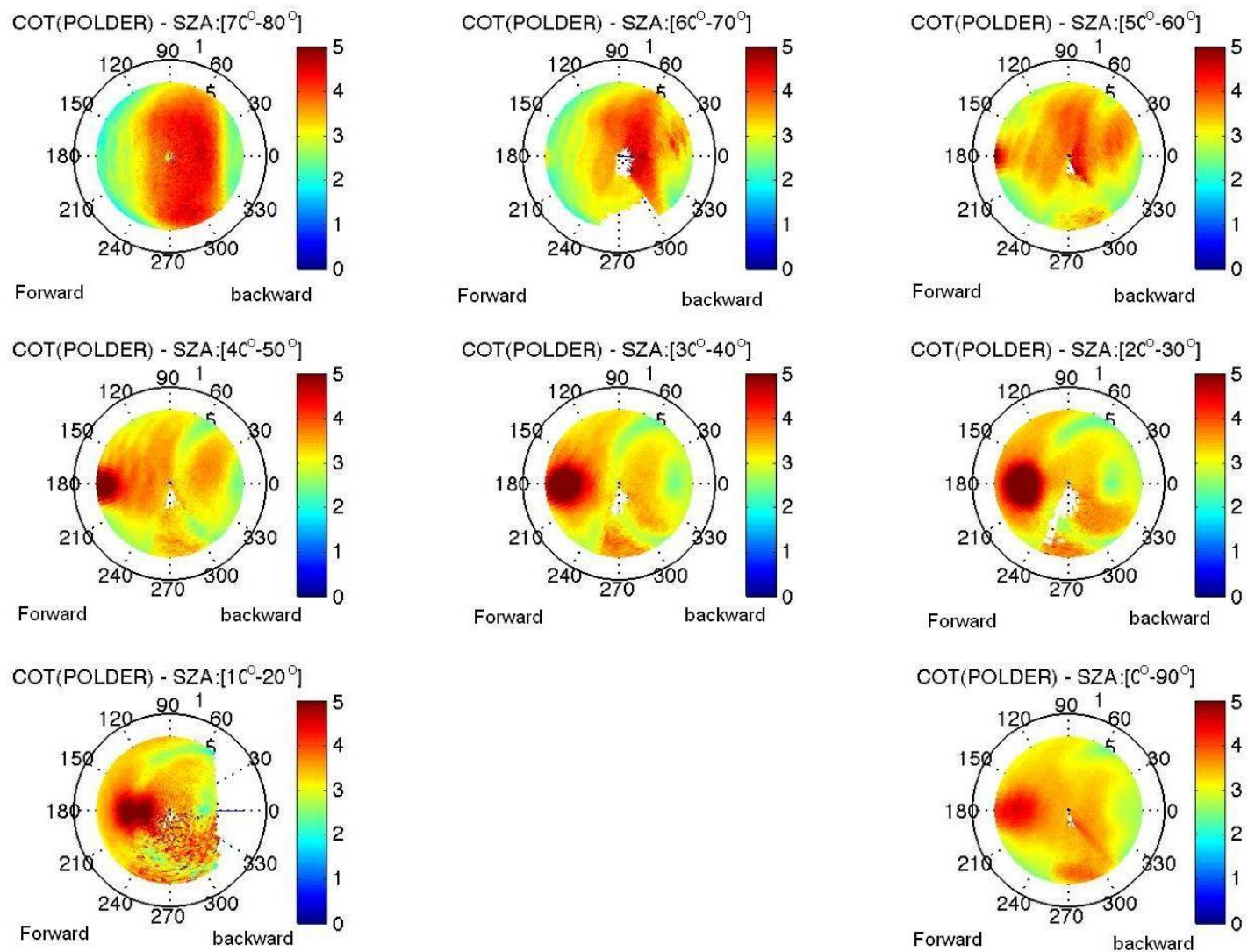
Figure 5.6-5 – *Polar graph of POLDER COT for broken oceanic clouds and for different solar elevation.*
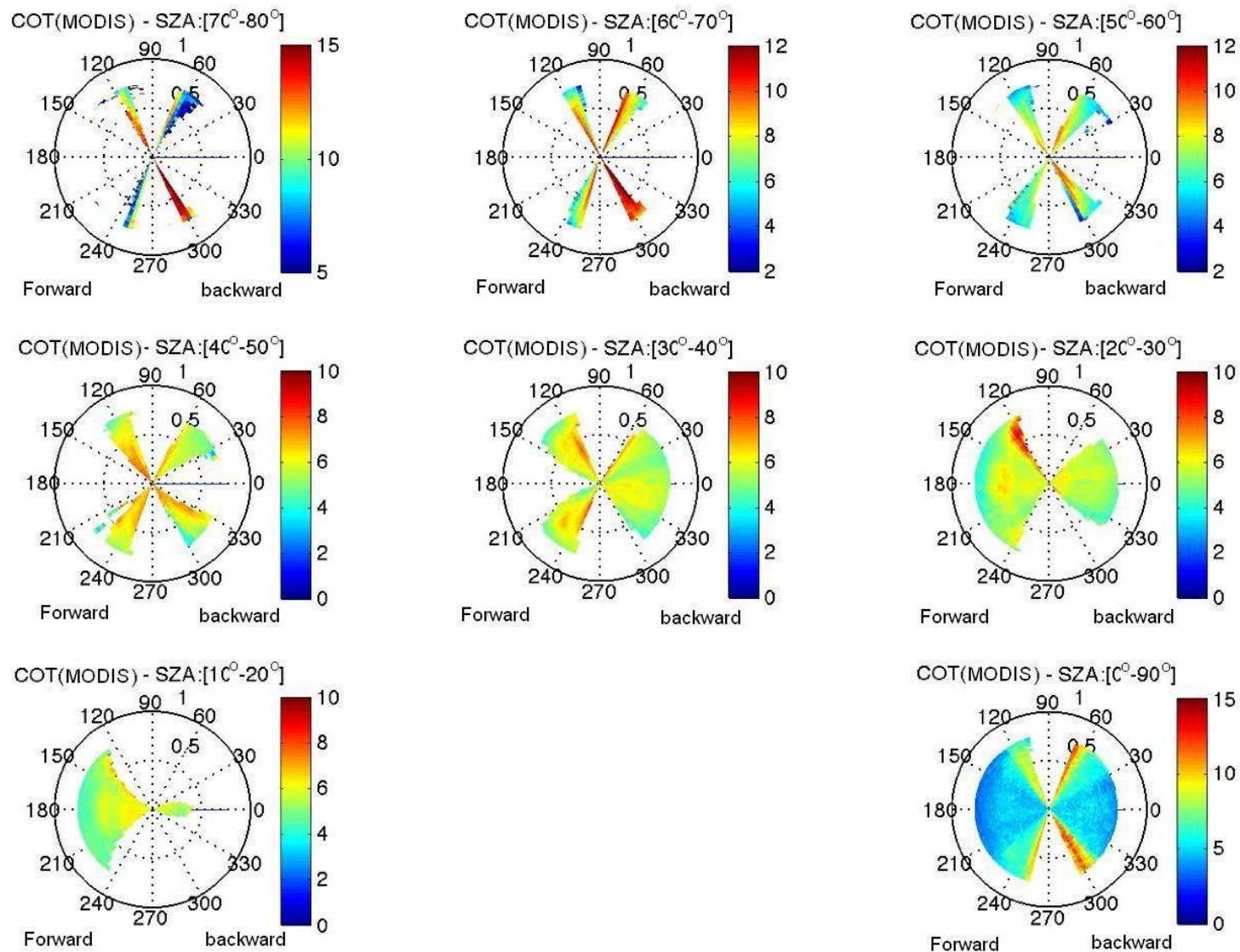
Figure 5.6-6 – *Polar graph of MODIS COT for broken oceanic clouds and for different solar elevation.*

5.7 Conclusion

In this chapter, we studied cloud optical thickness, one of the most important cloud properties. The retrieval of this parameter is not simple as it strongly depends on many cloud and environment factors such as cloud cover and thermodynamic phase. We start this chapter by presenting the underling principles of COT retrieval in the POLDER and MODIS algorithms. The comparison of COT between the two sensors was first done for the simplest cloudy situations, the cases of overcast oceanic clouds. The comparison is made separately for different phases determined from a combination of POLDER and MODIS. Our results show that, for clouds with confident cloud phases, there exists a strong correlation between the optical thicknesses of the two sensors. For confident liquid clouds, MODIS and POLDER COT have similar values while for the confident ice clouds, MODIS COT is larger than the POLDER one. For the clouds with inconsistent phases, the sensor that employs a liquid phase model retrieves logically larger optical thickness. These comparisons are then extended to broken clouds, multilayered and single-layered clouds. Compared among different cloudy scenes, we have concluded not surprisingly that the COT relationships between the two sensors are much stronger in overcast scenes compared to broken cloud scenes and stronger for single layer cloud systems compared to multilayer cloud systems. These results between the two optical thicknesses help in identifying the conditions where the COT retrieval can be considered as suitable. Beside this relationships analysis, we also plotted latitudinal variations, global geographical distributions, vertical distributions and seasonal evolutions that help to reveal the specific uncertainties in cloud optical thickness retrievals.

As a second part of this chapter, we discussed many uncertainties and impacts from various factors in COT retrieval processes. Among all those factors, the sensor spatial resolution is an important one and is first discussed. Through its impact on cloud detection, the spatial resolution differences can bias cloud cover (see chapter 3) and thus cloud optical thickness. Indeed, satellites with lower spatial resolution tend to detect larger cloud cover and as a consequence smaller retrieved optical thickness. In addition, the spatial resolution differences lead to different plane-parallel biases

due to inhomogeneous clouds. By neglecting the sub-pixel cloud inhomogeneities, satellites with lower spatial resolution tend to retrieve smaller optical thickness.

Other uncertainties presented are associated to the cloud microphysics and its models used in algorithm. The cloud microphysics issues for COT retrieval include thermodynamic phase, cloud particles size and shape. Using a liquid model instead of an ice model leads to an overestimation of the optical thickness of ice clouds. The influence of particle size for liquid clouds can be ignored, however for ice clouds, the differences of cloud particle sizes and shapes conduct the main bias of cloud optical thickness.

In addition, we also studied the impact of the ground albedo on cloud optical thickness retrievals: over brighter surface, larger uncertainties are found, especially for thin clouds.

In this work, we also showed cloud inhomogeneity parameter distributions, which are consistent with previous studies. We present angular variation of optical thickness, where we clearly see the underestimation of cloud optical thickness in forward directions due to shadow effect especially for the lower sun and also the underestimation of cloud optical thickness from POLDER in rainbow and backward directions due to the cloud microphysics assumption.

In the future, comparisons of cloud top reflectance and clear sky reflectance between POLDER, MODIS and CERES are still needed in order to evaluate the impact of radiative biases on COT retrieval. In addition, in order to improve the COT retrieval, 3-D effect on cloud optical thickness needs to be accounted for and a better representation of ice clouds microphysics is still needed.

Chapter 6
Summary and Future Works

Clouds cover permanently an important part of the Earth and are essential components of the atmosphere. They influence the Earth's climate by virtue of their radiative properties both in the solar and thermal-infrared spectral regions and also because of their role in the hydrological cycle. Long records of observations on clouds from the onboard satellite instruments have the advantage of a global coverage with a high space-time resolution. Among which, the A-Train satellites and sensors, provide an unprecedented opportunity to make effort on the study of clouds. This group of satellites provides within minutes of each other, thorough information about our atmosphere from a set of passive and active sensors with broad performances and application ranges. As parts of the A-Train, Aqua carrying MODIS and PARASOL carrying POLDER fly both in ascending orbit and give thus coincident observations. Their noticeable instrumental characteristics are, concerning MODIS a relatively high spatial resolution as well as a wide spectral coverage from solar, near infrared, to thermal infrared spectrum, while the virtues of POLDER reside in its multi-polarization, multi-directionality and multispectal capability. These different characteristics conduct each sensor to identify clouds and retrieve cloud properties in different ways. In this work, we studied and compared the cloud properties obtained from these two passive sensors POLDER/PARASOL and MODIS/AQUA and from an active sensor CALIOP/CALIPSO in order to better qualify statistically and globally the cloud cover, cloud thermodynamic phase and cloud optical thickness. We also discussed the biases in retrieved cloud properties, which are due to the advantages or disadvantages of each instrument and to specific assumptions used in retrieval algorithm. These results should help to remove or correct some erroneous

retrievals in recent operational algorithms, as well as to give worthily suggestions to data users.

6.1 Major Findings

In this work, we studied some main cloud properties derived from POLDER/PARASOL and MODIS/AQUA and intended to identify the consistent cloud observations and the differences between them through an extensive comparison work. In order to help at these comparisons, we also used observations of the active sensor CALIOP/CALIPSO, which provides an indication on the cloud vertical structure. The main results can be summarized as follows:

1. Concerning cloud cover, although POLDER and MODIS instruments have different characteristics and different spatial resolutions, we observed a consistent cloud distribution and a quasi-constant bias between POLDER and MODIS CFD (Cloud Fraction Day) products of about 10% with POLDER detecting less clouds than MODIS and also about 10% between MODIS CFC (Cloud Fraction Combined) and POLDER with MODIS CFC being lower. These constant biases come mainly from the sensor resolution and sensitivity differences, and also because of MODIS CFC and POLDER cloud fraction only corresponding to pixels for which cloud properties retrieval has been attempted. In addition to these constant biases, we also focused on specific areas showing important positive or negative differences associated to typical cloud detection difficulties. For example, due to a lower resolution, POLDER badly detects the very small clouds and classifies it as overcast cloud cover. Over snow, both sensors have difficulties in the cloud detection and particularly POLDER, which underestimates more cloud fractions because of the lack of efficient information in the visible bands. We also note important differences over transition region between desert and non-desert, which can be due to a better cirrus detection or a falsely desert detection in the MODIS algorithm. In sun-glint, besides the threshold problem of POLDER in northern Pacific during summer, POLDER with its multi-directional observations

minimizes the sun-glint detection errors by averaging both in and out of sun-glint directions. We also report that POLDER confuses heavy aerosols as clouds in some directions and misses very thin cirrus because of its lower resolution and its narrow spectral range of channels available for cloud detection.

2. The second cloud parameter studied in this work was the cloud phase. The methods used to classify ice and liquid clouds are completely different for the two instruments: POLDER uses the angular signature of the polarized reflectance and MODIS uses the absorption difference in the visible and near-infrared bands and in two window thermal IR bands. We globally identified, located and explained the consistent and inconsistent phase decisions between the two instruments. We also qualified the angular biases in cloud phase detection existing in MODIS SWIR/VIS and POLDER polarized methods, which need to be improved in future algorithms. The inconsistent phase decision gives often information on the presence of broken clouds, thin cirrus, heavy aerosols, snow or supercooled water droplets. From this study, we reported that POLDER can falsely detect the broken scenes and the aerosols overlaying water clouds as mixed or ice phase but can correctly identify the single layered thin cirrus, water clouds over snow and also some supercooled water clouds. Compared to POLDER, MODIS detects better thin cirrus overlaying water clouds and broken water clouds. Further validation of phase from CALIOP shows quite good agreement to the passive sensors with more than 95% of the consistent combined phase cases being in agreement with CALIOP. For inconsistent or less confident phase decisions, depending on the situations, CALIOP agrees with either POLDER or MODIS, but in overall preferentially with POLDER which we attribute to the use of polarization based technique for both POLDER and CALIOP.

3. With the confident ice and liquid phase identified above, we continued by studying the cloud vertical water-ice transition and its relationship with cloud top temperature, large-scale dynamics and cloud microphysics. These relationships can be important to help in development or validation of GCM. Results show that the ice-freezing process has land-ocean and latitudinal

distributions. We also reveal important variations in relation with the droplets radius and the vertical velocity. The smaller droplets tend to have colder freezing temperature and sharper transition, most of them therefore located in the upper atmosphere. The smaller vertical velocities (corresponding subsidence regime) seems also to lead to colder freezing temperature but these results need to be verified in GCM models or with more detailed studies.

4. In the last chapter, we studied the cloud optical thickness. The principles used by the two algorithms to retrieve this parameter are quite similar with the use of pre-computed look-up table based on the plane-parallel homogeneous cloud assumption. They differ mostly by their cloud microphysics assumptions. The comparisons show that, for overcast clouds with consistent combined phase, the COT relations between the two sensors are strong (high correlation coefficient) with small bias for liquid clouds but quite large bias for ice clouds. For clouds with inconsistent combined phase, larger differences and weaker relationships are logically found as for broken clouds where the relationships are much weaker with larger differences between the two sensors. We discussed then the potential reasons explaining these differences as the uncertainties in COT retrieval associated to the sensor spatial resolution, which can directly impact the cloud cover and also the sub-pixel cloud inhomogeneity effects. Compared to MODIS, POLDER with a lower resolution tends to retrieve optical thickness for a larger part of the total cloud fraction and thus smaller optical thickness because it cannot identify sub-pixel broken cloud covers. Moreover, as it also neglects more sub-pixel cloud inhomogeneity, it logically retrieves smaller optical thickness. We also discussed the uncertainties associated to the different cloud microphysics used in the algorithm. No matter the departure of cloud microphysics is in cloud phase, cloud effective radius or cloud particle shape, the retrieved cloud optical thickness is impacted. A use of ice cloud model instead of liquid one leads to an overestimation in optical thickness. The effective radius can also slightly impact the retrieved optical thickness for liquid clouds especially in the rainbow and backward directions. The main differences for ice clouds are explained by effective radius and particle shape. The ground reflectance can also bias the retrieved optical thickness especially for thin clouds, but the

impact is not as important as others. Looking afterwards at the angular distribution of retrieved COT, we observed a 3D radiative transfer bias for POLDER with strong shadowing effects in forward directions for oblique sun (COT decreases with viewing angle). But, apart from the forward directions, COT is almost constant as function of sensor views in case of overcast clouds. In case of broken clouds, 3D effects are more marked as well as surface reflectance effects. To conclude this part, we can say that the best improvements in COT retrieval can be done in the microphysics assumptions especially for ice clouds and the account of the 3D effects especially for low sun.

6.2 Future work

The work done during this thesis mainly focuses on statistical studies of cloud cover, cloud phase and cloud optical thickness. Other cloud properties such as cloud top pressure have not been studied but are also important. This study would first allow to understand the different cloud top pressures such as the oxygen and Rayleigh pressures from POLDER and the CO_2 slicing derived pressure from MODIS. In addition, as differences between these cloud top pressures are directly linked to vertical structures, their studies may reveal information on cloud and atmosphere structures such as cloud geometrical thickness (Ferlay *et al.*, 2010), presence of aerosols over water clouds (Waquet *et al.*, 2009) and temperature inversion by using a combination of POLDER and MODIS data. Indeed, vertical information from passive sensors would allow to have spatially more extended products compared to active sensors such as CALIOP or Cloudsat. However, the current understanding of these cloud top pressures especially from statistics is not sufficient and thus needs more researches. With a better knowledge of the cloud top pressures and cloud optical thicknesses, we could also better qualify and understand the nine types of clouds classified by ISCCP criteria. The cloud occurrence of each cloud type is indeed directly linked to the cloud detection and the retrievals of cloud pressure and optical thickness.

In addition, as one reason to retrieve cloud properties concerns their radiative impacts, it would be interesting to compare also the shortwave albedo derived from the cloud optical thickness and the ground reflectance, with data from the Cloud and the Earth's Radiant Energy System (CERES/AQUA) which measures the broadband reflectances that can be converted to fluxes. And also over land, the angular effect of the ground reflection in cloud detection and consequent retrievals of cloud property requires more detailed studies.

Once the difficulties in retrieving the cloud parameters are well identified, we can also conduct studies concerning the relationships between the parameters as we have done for cloud phase and the ice-water transition levels. This study needs also further researches, as for example the verification of the global and regional ice-water transitions (cloud phase parameterization) in cloud and climate models and also, further discussions about the impact of CCN on cloud ice-water development. To go further, we could also study, for example, the relation between cloud optical thickness and effective radius or cloud top pressure (cloud vertical extension or effective radius may be modified by anthropogenic impacts).

From the work done during this thesis, we also showed that for each cloud parameter derived from the two passive sensors, some improvements are possible in the algorithms. For example in the cloud detection algorithm, POLDER may be improved in sun-glint, by resetting the threshold of oxygen pressure of clear sky in northern Pacific Ocean during summer in order to better detect low clouds. Heavy aerosols may be excluded by setting a threshold in cloud detection index in aerosol frequent occurrence regions. Concerning very thin cirrus as well as very low clouds identification over snow, more studies and improvements are needed for both sensors especially POLDER. For MODIS, improvements seem needed in the separation of clouds and desert over transition region between desert and non-desert. In cloud phase identification, the mixed phase class of POLDER and MODIS requires a better understanding and classification to be either thin cirrus overlying water clouds, supercooled water clouds, broken scenes or a real mixture of ice and liquid water. In addition, the angular bias in the algorithms of both sensors needs more studies.

At last, as we also showed the advantages and disadvantages of each instrument and potentially their complementarity, this study can thus be a first step toward a better passive radiometer taking advantages of the two instruments considered here. The future "dream" radiometers are expected to have a high spatial resolution of

about one kilometer or less with multi-directional and polarized observations not only in the visible band range but also in the near infrared and infrared range, so as it can give more correct information about clouds, for example, in the identification of ice and water content, broken clouds, cirrus clouds and clouds over snow and desert.

References

Abbatt, J. P. D., S. Benz, D. J. Cziczo, Z. Kanji, U. Lohmann, and O. Möhler, 2006: Solid ammonium sulfate aerosols as ice nuclei : A pathway for cirrus cloud formation. *Science*, **313,** 1770-1773.

Ackerman, S. A., 1997: Remote sensing aerosols using satellite infrared observations. *J. Geophys. Res.*, **102,** 17069-17079.

Ackerman, S. A., K. I. Strabala, W. P. Menzel, R. A. Frey, C. C. Moeller, and L. E. Gumley, 1998: Discriminating clear sky from clouds with MODIS. *Journal of Geophysical Research*, **103,** 32,141-32,157.

Ackerman, S. A., R. E. Holz, R. Frey, E. W. Eloranta, B. C. Maddux, and M. McGill, 2007: Cloud Detection with MODIS. Part II: Validation. *Journal of Atmospheric and Oceanic Technology*, **25,** 1073-1086.

Ackerman, S. A., R. A. Frey, K. I. Strabala, Y. Liu, L. E. Gumley, B. Baum, and W. P. Menzel, 2010: Discriminating clear sky from clouds with MODIS. *J. Geophys. Res.*, **103,** 32,141-32,157.

Albers, F., A. Reuterl, U. Maixnerl, L. Levkovl, E. Raschke, and I. Sednev, 1999: Horizontal Inhomogeneities in Clouds and Particle Measurements. *Phys. Chem. Earth (B)*, **24,** 197-202.

Albrecht, B., 1989: Aerosols, cloud microphysics, and fractional cloudiness. *Science*, **245,** 1227- 1230.

Barahona, D. and A. Nenes, 2008: Parameterization of Cirrus Cloud Formation in Large Scale Models: Homogeneous Nucleation. *J. Geophys. Res.*, **113,** D11211, doi:10.1029/2007JD009355

Barker, H. W., B. A. Wielicki, and L. Parker, 1996: A parameterization for computing grid-averaged solar fluxes for inhomogeneous marine boundary layer clouds. Part II: Validation using satellite data. *J. Atm. Sci.*, **53,** 2304–2316.

Baum, B. A., P. F. Soulen, K. I. Strabala, M. D. King, S. A. Ackerman, W. P. Menzel, and P. Yang, 2000: Remote sensing of cloud properties using. MODIS airborne simulator imagery during SUCCESS, II, Cloud thermodynamic phase. *J. Geophys. Res.*, **105,** 11781-11792.

Baum, B. A., P. Yang, A. J. Heymsfield, S. Platnick, M. D. King, Y.-X. Hu, and S. T. Bedka, 2005: Bulk Scattering Properties for the Remote Sensing of Ice Clouds. Part II: Narrowband Models. *J. Appl. Meteor.*, **44,** 1896-1911.

Bony, S., R. Colman, V. M. Kattsov, R. P. Allan, C. S. Bretherton, J.-L. Dufresne, A. Hall, S. Hallegatte, M. M. Holland, W. Ingram, D. A. Randall, B. J. Soden, G. Tselioudis, and M. J. Webb, 2006: How Well Do We Understand and Evaluate Climate Change Feedback Processes? *J Climate*, **19,** 3445-3482.

Boudala, F. S., Q. Fu, and G. A. Issac, 2002: A GCM Parameterization of Ice Particle Mean Effective Sizes for High Latitude Cirrus Clouds and It's Comparison with Mid-Latitude Parameterization *Twelfth ARM Science Team Meeting Proceedings*.

Bréon, F.-M. and M. Doutriaux-Boucher, 2005: A comparison of cloud droplet radii measured from space. *IEEE Trans Geosc. Rem. Sens.*, **43,** 1796-1805.

Bréon, F.-M. and CNES Parasol Team, 2006: Parasol Level-1 Product: Data Format and User Manual. *http://www.icare.univ-lille1.fr/products/download/Parasol_Level-1_format.pdf*.

Bréon, F. M., 1992: Reflectance of broken cloud fields: simulation and parameterization. *J. Atmos. Sci.*, **49,** 1221-1232.

Buriez, J.-C., M. Doutriaux-Boucher, F. Parol, and N. J. Loeb, 2001: Angular Variability of the Liquid Water Cloud Optical Thickness Retrieved from ADEOS-POLDER. *J. Atm. Sci.*, **58,** 3007-3018.

Buriez, J., C. Vanbauce, F. Parol, P. Goloub, M. Herman, B. Bonnel, Y. Fouquart, P. Couvert, and G. Seze, 1997: Cloud detection and derivation of cloud properties from POLDER. *International Journal of Remote Sensing*, **18,** 2785-2813.

C.-Labonnote, L., G. Brogniez, M. Doutriaux-Boucher, and J. C. Buriez, 2000: Modeling of light scattering in cirrus clouds with inhomogeneous hexagonal monocrystals. Comparison with in-situ and ADEOS-POLDER measurements. *Geophys. Res. Lett.*, **27,** 113-116.

C.-Labonnote, L., G. Brogniez, J. C. Buriez, M. Doutriaux-Boucher, J. F. Gayet, and A. Macke, 2001: Polarized light scattering by inhomogeneous hexagonal monocrystals. Validation with ADEOS-POLDER measurements. *J. Geophys. Res.*, **106,** 12139-12153.

Cahalan, R. F., W. Ridgway, W. J. Wiscombe, and T. L. Bell, 1994: The albedo of fractal stratocumulus clouds. *J. Atmos. Sci.*, **51,** 2434-2455.

Cess, R. D., G. L. Potter, J. P. Blanchet, G. J. Boer, S. J. Ghan, J. T. Kiehl, H. L. Treut, Z.-X. Li, X.-Z. Liang, J. F. B. Mitchell, J.-J. Morcrette, D. A. Randall, M. R. Riches, E. Roeckner, U. Schlese, A. Slingo, K. E. Taylor, W. M. Washington, R. T. Wetherald, and I. Yagai, 1989: Interpretation of Cloud-Climate Feedback as Produced by 14 Atmospheric General Circulation Models *Science*, **245,** 513-515.

Chang, F.-L. and J. A. Coakley, 2006: Relationships between Marine Stratus Cloud Optical Depth and Temperature: Inferences from AVHRR Observations. *J. Climate*, **20,** 2022-2036.

Chepfer, H., P. Goloub, L. Sauvage, P. H. Flamant, G. Brogniez, J. Spinhirne, M. Laborato, N. Sugimoto, and J. Pelon, 1999: Validation of POLDER/ADEOS data using a ground-based lidar network: preliminary results for cirrus clouds. *Phys. Chem. Earth (B)*, **24,** 203-206.

Chylek, P., S. Robinson, M. K. Dubey, M. D. King, Q. Fu, and W. B. Clodius, 2006: Comparison of near-infrared and thermal infrared cloud phase detections. *J. Geophys. Res.* , **111,** Doi:10.1029/2006JD007140.

Cornet, C. and R. Davies, 2008: Use of MISR measurements to study the radiative transfer of an isolated convective cloud: Implications for cloud optical thickness retrieval. *J. Geophys. Res.* , **113,** D04202, doi:10.1029/2007JD008921.

Council, N. R., 2003: Understanding climate change feedbacks: panel on climate change feedbacks.

Cox, C. and W. Munk, 1956: Slopes of the sea surface deduced from photographs of the sun glitter. *Bulletin of the Scripps Institute of Oceanography*, **6,** 401-488.

Curran, R. J. and M. L. C. Wu, 1982: Skylab Near Infrared Observations of Clouds Indicating. Supercooled Liquid Water Droplets. *J. Atmos. Sci.*, **39,** 635-647.

Curry, J. A., C. D. Ardeel, and L. Tian, 1990: Liquid Water Content and Precipitation Characteristics of Stratiform Clouds as Inferred from Satellite Microwave Measurements. *Atmos. Phys.*, **51,** 203-229.

Davis, A., A. Marshak, C. R. F., and W. Wiscombe, 1997: The landsat scale break in stratocumulus as a three-dimensional radiative transfer effect: Implications for cloud remote sensing. *J. Atmos. Sci.*, **54,** 241-260.

Del Genio, A. D., M.-S. Yao, W. Kovari, and K. K.-W. Lo, 1996: A prognostic cloud water parameterization for global climate models. *J Climate*, **9,** 270-304.

Deneke, H., R. Roebeling, E. Wolters, A.Feijt, and C. Simmer, 2009: On the Sensitivity of Satellite-Derived Cloud Properties To Sensor Resolution and Broken Clouds. *AIP Conf. Proc.*, **1100,** 376-379.

Deschamps, P., F. Breon, M. Leroy, A. Podaire, A. Bricaud, J. Buriez, and G. Seze, 1994: The POLDER mission: instrument characteristics and scientificobjectives. *Geoscience and Remote Sensing, IEEE Transactions on*, **32,** 598-615.

Dessler, A. E., 2010: A Determination of the Cloud Feedback from Climate Variations over the Past Decade. *Science*, **330,** 1523-1527.

Deuzé, J. L., F. M. Bréon, C. Devaux, P. Goloub, M. Herman, B. Lafrance, F. Maignan, A. Marchand, F. Nadal, P. G., and D. Tanré, 2001: Remote sensing of aerosols over land surfaces from POLDER-ADEOS-1 polarized measurements. *J. Geophys. Res.*, **106,** 4913-4926.

Donovan, D. P. and C. A. P. V. Lammeren, 2002: First ice cloud effective particle size parameterization based on combined lidar and radar data. *Geophys. Res. Lett.*, **29,** 1,1006, doi:10.1029/2001GL013731.

Doutriaux-Boucher, M. and J. Quaas, 2004: Evaluation of cloud thermodynamic phase parameterizations in the LMDZ GCM by using POLDER satellite data. *Geophys. Res. Lett.*, **31,** 06126.

Dufresne, J.-L. and S. Bony, 2008: An assessment of the primary sources of spread of global warming estimates from coupled atmosphere-ocean models. *J Climate*, **21,** 5135-5144.

Feigelson, E. M., 1978: Preliminary radiation model of a cloudy atmosphere. Part I structure of clouds and solar radiation. . *Contrib. Atmos. Phys.*, **51,** 203-229.

Ferlay, N., F. Thieuleux, C. Cornet, A. B. Davis, P. Dubuisson, F. Ducos, F. Parol, J. Riédi, and C. Vanbauce, 2010: Toward new inferences about cloud structures from multidirectional measurements in the oxygen A band: Middle-of-cloud pressure and cloud geometrical thickness from POLDER3/PARASOL. *J. Appl. Meteor. Climatol.*, **49,** 2492-2507.

Fletcher, N. H., 1958: Size effect in heterogeneous nucleation. *J. Chem. Phys.*, **29,** 572-576.

Frey, R. A., S. A. Ackerman, Y. Liu, K. I. Strabala, H. Zhang, J. R. Key, and X. Wang, 2008: Cloud Detection with MODIS. Part I: Improvements in the MODIS Cloud Mask for Collection 5. *Journal of Atmospheric and Oceanic Technology*, **25,** 1057-1072.

Fu, Q., 1996: An accurate parameterization the solar radiative properties of cirrus clouds for climate models. *J. Climate*, **9,** 2058-2082.

Gao, B.-C., A. F. H. Goetz, and W. J. Wiscombe, 1993: Cirrus cloud detection from airborne imaging spectrometer data using the 1.38 micron water vapor band. *Geophys. Res. Lett.*, **20,** 301-304.

Gierens, K., 2003: On the transition between heterogeneous and homogeneous freezing. *Atmos. Chem. Phys.*, **3,** 437-446.

Goloub, P., J. L. Deuze, M. Herman, and Y. Fouquart, 1994: Analysis of the POLDER polarization measurements performed over cloud covers. *IEEE Transactions on Geoscience and Remote Sensing*, **32,** 78-88.

Goloub, P., H. Chepfer, M. Herman, G. Brogniez, and F. Parol, 1997: Use of polarization for cloud study. SPIE, Doi:10.1117/12.283865

Goloub, P., M. Herman, H. Chepfer, J. Riedi, G. Brogniez, P. Couvert, and G. Seze, 2000: Cloud thermodynamical phase classification from the POLDER spaceborne instrument. *Journal of Geophysical Research*, **105,** 14,747-14,759.

Han, Q., W. B. Rossow, and A. A. Lacis, 1994: Near-global survey of effective droplet radii in liquid water clouds using ISCCP data. *J. Climate*, **7,** 465-497.

Hansen, J., M. Sato, and R. Ruedy 1997: Radiative forcing and climate response. *J. Geophys. Res.*, **102,** 6831–6864.

Hansen, J., A. Lacis, D. Rind, G. Russell, P. Stone, I. Fung, R. Ruedy, and J. Lerner, 1984: Climate sensitivity: Analysis of feedback mechanisms. In Climate Processes and Climate Sensitivity, AGU Geophysical Monograph 29, Maurice Ewing Vol. 5. J.E. Hansen and T. Takahashi, Eds. American Geophysical Union, pp. 130-163. **,** 5.

Hansen, J. E., 1971: Multiple scattering of polarized light in planetary atmospheres. Part II. Sunlight reflected by terrestrial water clouds. *J. Atmos. Sci.*, **28,** 1400-1426.

Harrison, E. F., P. Minnis, B. R. Barkstrom, V. Ramanathan, R. D. Cess, and G. G. Gibson, 1990: Seasonal Variation Of Cloud Radiative Forcing Derived from the Earth Radiation Budget Experiment. *J. Geophy. Res.*, **95,** 18.687-18.703.

Hartmann, D. L., M. E. Ockert-Bell, and M. L. Michelsen, 1992: The Effect of Cloud Type on Earth's Energy Balance: Global Analysis. *J. Climate*, **5,** 1281-1304.

Heidinger, A. K., M. D. Goldberg, D. Tarpley, A. Jelenak, and M. J. Pavolonis, 2005: A new AVHRR cloud climatology. *Proc. SPIE*, **5658,** doi:10.1117/12.579047

Heymsfield, A. J., 2003: Properties of Tropical and Midlatitude Ice Cloud Particle Ensembles. Part I: Median Mass Diameters and Terminal Velocities. *J. Atm. Sci.*, **60,** 2573-2591.

Heymsfield, A. J. and C. M. R. Platt, 1984: A parameterization of the particle spectrum of ice clouds in terms of the ambient temperature and the ice water content. *J. Atm. Sci.*, **41**.

Heymsfield, A. J. and R. M. Sabin, 1989: cirrus crystal nucleation by homogeneous freezing of solution droplets. *J. Atmos. Sci.*, **46,** 2252-2264.

Heymsfield, A. J. and J. Iaquinta, 2000: Cirrus crystal terminal velocities. *J. Atmos. Sci*, **5,** 916-938

Heymsfield, A. J., L. M. Miloshevich, C. Schmitt, A. Bansemer, C. Twohy, M. R. Poellot, A. Fridlind, and H. Gerber, 2005: Homogeneous Ice Nucleation in Subtropical and Tropical Convection and Its Influence on Cirrus Anvil Microphysics. *J. Atmos. Sci.*, **62,** 41-64.

Hobbs, P. V. and A. Deepak, 1981: Clouds : Their Formation, Optical Properties and Effects. *Academic Press: New York* 497.

Houze, R. A., 1994: Cloud Dynamics. *Academic press*.

Hu, Y.-X., P. Yang, B. Lina, G. Gibsona, and C. Hostetler, 2002: Discriminating between spherical and non-spherical scatterers with lidar using circular polarization: a theoretical study. *Journal of Quantitative Spectroscopy and Radiative Transfer*, **79-80,** 757-764.

Hu, Y., Z. Liu, D. Winker, M. Vaughan, V. Noel, L. Bissonnette, G. Roy, and M. McGill, 2006: Simple relation between lidar multiple scattering and depolarization for water clouds. *Opt. Lett.*, **31,** 1809-1811.

Hu, Y., D. Winker, M. Vaughan, B. Lin, A. Omar, C. Trepte, D. Flittner, P. Yang, S. L. Nasiri, B. Baum, W. Sun, Z. Liu, Z. Wang, S. Young, K. Stamnes, J. Huang, R. Kuehn, and R. Holz, 2009: CALIPSO/CALIOP Cloud Phase Discrimination Algorithm. *J. Atmos. Oceanic Technol.*, **26,** 2293-2309.

Hubanks, P., M. King, S. Platnick, and R. Pincus, 2008: MODIS Atmosphere L3 Gridded Product Algorithm Theoretical Basis Document. *ATBD Reference Number: ATBD-MOD-30.*

Hunt, G. E., 1982: On the sensitivity of a general circula- tion model climatology to changes in cloud structure and radiative properties. *Tellus* **34,** 29-38.

Inoue, T., 1987: A cloud type classification with NOAA 7 split-window measurements. . *J. Geophys. Res.*, **92,** 3991-4000.

IPCC, 2001: IPCC Third Assessment Report "Climate Change 2001" and the Synthesis Report.

IPCC, r., 2007: Climat change 2007: The physical science basis.

Iwabuchi, H. and T. Hayasaka, 2002: Effects of Cloud Horizontal Inhomogeneity on the Optical Thickness Retrieved from Moderate-Resolution Satellite Data. *J. Atmos. Sci.*, **59,** 2227-2242

Jensen, E. J., S. Kinne, and O. B. Toon, 1994: Tropical cirrus cloud radiative forcing: Sensitivity studies. *Geophys. Res. Lett.*, **21,** 2023-2026.

Kärcher, B. and U. Lohmann, 2003: A parameterization of cirrus cloud formation: Heterogeneous freezing. *J. Geophys. Res.*, **108,** 4402-4416.

Kaufman, Y. J., C. Ichoku, L. Giglio, S. Korontzi, D. A. Chu, W. M. Hao, R.-R. Li, and C. O. Justice, 2003: Fire and smoke observed from the earth observing system MODIS instrument - products, validation, and operational use. *Int. J. Rem. Sens.*, **24,** 1765-1781.

Key, J. R. and J. M. Intrieri, 2000: Cloud particle phase determination with the AVHRR. *J. Appl. Meteor.*, **39,** 1797-1804.

Kiehl, J. T. and K. E. Trenberth, 1997: Earth's Annual Global Mean Energy Budget. *Bull. Amer. Meteor. Soc.*, **78,** 197-208.

King, M., Y. Kaufman, W. Menzel, D. Tanre, N. Center, and M. Greenbelt, 1992: Remote sensing of cloud, aerosol, and water vapor properties fromthe moderate resolution imaging spectrometer (MODIS). *Geoscience and Remote Sensing, IEEE Transactions on*, **30,** 2-27.

King, M. D., 1987: Determination of the Scaled Optical Thickness of Clouds from Reflected Solar Radiation Measurements. *Journal of the Atmospheric Sciences*, **44,** 1734-1751.

King, M. D., S. C. Tsay, S. E. Platnick, M. Wang, and K. Liou, 1997: Cloud Retrieval Algorithms for MODIS: Optical Thickness, Effective Particle Radius, and Thermodynamic Phase, MODIS Algorithm Theoretical Basis Document No. *ATBDMOD-05 MOD06–Cloud product*.

King, M. D., S. Platnick, P. Yang, G. T. Arnold, M. A. Gray, J. C. Riédi, S. A. Ackerman, and K. N. Liou, 2004: Remote Sensing of Liquid Water and Ice

Cloud Optical Thickness and Effective Radius in the Arctic: Application of Airborne Multispectral MAS Data. *J. Atmos. Oceanic Technol.*, **21,** 857–875.

Kokhanovsky, A. A., O. Jourdan, and J. P. Burrows, 2006: The Cloud Phase Discrimination From a Satellite. *IEEE Trans Geosc. Rem. Sens.*, **3,** 103-106.

Kristiansen, J. and J. E. Kristjansson, 1999: Shortwave cloud forcing of marine stratocumulus clouds. *Phys. Chem. Earth (B)*, **24,** 225-230.

Lamquin, N., C. J. Stubenrauch, and J. Pelon, 2009: Upper tropospheric humidity and cirrus geometrical and optical thickness: Relationships inferred from 1 year of collocated AIRS and CALIPSO data. *J. Geophys. Res.*, **113,** 114(D8), doi:10.1029/2008JD010012.

Lawson, R. P., A. J. Heymsfield, S. Aulenchach, and T. L. Jensen, 1998: Shapes, sizes and light scattering properties of ice crystals cirrus and a persistent contrail during SUCESS. *Geophys. Res. Lett.*, **25,** 1331-1334.

Le Treut, H. and Z.-X. Li, 1991: Sensitivity of an atmospheric general circulation model to prescribed SST changes: feedback effects associated with the simulation of cloud optical properties. *Climate Dynamics*, **5,** 175-187.

Leroy, M., J. L. Deuze, F. M. Bréon, O. Hautecoeur, M. Herman, J. C. Buriez, D. Tanre, S. Bouffies, P. Chazette, and J. L. Roujean, 1997: Retrieval of atmospheric properties and surface bidirectional reflectances over the land from POLDER. *J. Geophys. Res.*, **102,** 17,023-17,037.

Liou, K. N., 2002: An Introduction to Atmospheric Radiation. *Academic Press*, 583.

Liu, Z., A. H. Omar, Y. Hu, M. A. Vaughan, and D. M. Winker, 2005: CALIOP ATBD, Part 3: Scene Classification Algorithms. No. PC-SCI-202 Part 3 Release 1.0.

Loeb, N. G. and R. Davies, 1996: Observational evident of plane paralle model biases apparent dependence of cloud optical depth on solar zenith angle. *J. Geophys. Res.*, **101,** 1621-1634.

——, 1997: Angular dependence of observed reflectances: A comparison with plane parallel theory. *J. Geophys. Res.*, **102(D6),** 6865-6881.

Loeb, N. G. and J. A. Coakley, 1998: Inference of Marine Stratus Cloud Optical Depth from Satellite Measurements: Does 1D Theory Apply? *J. Climate*, **11,** 215-233.

Loeb, N. G., T. Várnai, and R. Davies, 1997: Effect of cloud inhomogeneities on the solar zenith angle dependence of nadir reflectance. *J. Geophys. Res.*, **102,** 9387-9395.

Loeb, N. J., T. Várnai, and D. M. Winker, 1998: Influence of Subpixel-Scale Cloud-Top Structure on Reflectances from Overcast Stratiform Cloud Layers. *J. Atm. Sci.*, **55,** 2960-2973.

Loyola R., D. G., W. Thomas, R. Spurr, and B. Mayer, 2010: Global patterns in daytime cloud properties derived from GOME backscatter UV-VIS measurements. *Int. J. Rem. Sens.*, **31,** 4295-4318.

Maddux, B. C., S. A. Ackerman, and S. Platnick, 2010: Viewing Geometry Dependencies in MODIS Cloud Products. *J. Atmos. Oceanic Technol.*, **27,** 1519-1528.

Malkova, V. S., 1973: Use of G.V.Rozenberg's asymptotic expressions for interpretation of cloud brightness measurement. *Izv. Acad. Sci. USSR. Atmos. Ocean. Phys.*, **9,** 548-552.

Marshak, A., S. Platnick, T. Várnai, G. Wen, and R. F. Cahalan, 2006: Impact of three-dimensional radiative effects on satellite retrievals of cloud droplet sizes. *J. Geophy. Res.*, **111,** D09207, 12pp, doi:10.1029/2005JD006686.

Martin, G. M., D. W. Johnson, and A. Spice, 1994: The measurement and parameterization of effective radius of droplets in warm stratocumulus clouds. *J. Atm. Sci.*, **51,** 1823 – 1842.

Menzel, W. P., R. A. Frey, B. A. Baum, and H. Zhang, 2006: Cloud Top Properties and Cloud Phase - Algorithm Theoretical Basis Document. *Products: 06_L2, 08_D3, 08_E3, 08_M3.   ATBD Reference Number: ATBD-MOD-04.*

Miles, N. L., J. Verlinde, and E. E. Clothiaux, 2000: Cloud droplet size distributions in low-level stratiform clouds. *J. Atmos. Sci.*, **57,** 295-311.

Miloshevich, L. M. and A. J. Heymsfield, 1997: A balloon-borne continuous cloud particle replicator for measuring vertical profiles of cloud microphysical properties: Instrument Design, Performance and collection efficiency analysis. *J. Atmos. Oceanic Technol.*, **14,** 753-768.

Minnis, P., 1989: Viewing zenith angle dependence of cloudiness determined from coincident GOES East and GOES West data. *Journal of Geophysical Research*, **94**.

Minnis, P., D. F. Young, S. Sun-Mack, P. W. Heck, D. R. Doelling, and Q. Z. Trepte, 2004: CERES cloud property retrievals from imagers on TRMM, Terra, and Aqua. *SPIE Proceedings*, **5235,** 37-48.

Minnis, P., D. F. Young, B. A. Weilicki, D. P. Kratz, P. W. Heck, S. Sun-Mack, Q. Z. Trepte, Y. Chen, S. L. Gibson, and R. R. Brown, 2002: Seasonal and Diurnal Variations of Cloud Properties Derived for CERES from VIRS and MODIS Data. *11th Conference on Atmospheric Radiation*, 3-6 June, Ogden, UT, USA.

Mishchenko, M. I., W. B. Rossow, A. Macke, and A. A. Lacis, 1996: Sensitivity of cirrus cloud albedo, bidirectional reflectance and optical thickness retrieval accuracy to ice particle shape. *J. Geophys. Res.*, **101,** 16 973-16 985.

Mitchell, J. F. B., C. A. Senior, and W. J. Ingram, 1989: CO2 and climate: A missing feedback? . *Nature*, **341,** 132-134.

Moody, E. G., M. D. King, S. Platnick, C. B. Schaaf, and F. Gao, 2005: Spatially Complete Global Spectral Surface Albedos: Value-Added Datasets Derived From Terra MODIS Land Products. *IEEE Trans Geosc. Rem. Sens.*, **43,** 144-158.

Nakajima, T. and M. Tanaka, 1986: Matrix formulations for the transfer of solar radiation in a plane-parallel scattering atmosphere. *J. Quant. Spectrosc. Radiat. Transfer*, **35,** 13-21.

Nakajima, T. and M. D. King, 1990: Determination of the optical thickness and effective radius of clouds from reflected solar radiation measurements. Part I: Theory. *J. Atmos. Sci.*, **47,** 1878-1893.

Nakajima, T. Y. and T. Nakajima, 1994: Wide-area determination of cloud microphysical properties from NOAA AVHRR measurements for FIRE and ASTEX regions. *J. Atmos. Sci.*, **52,** 4043-4059.

Nasiri, S. L. and B. H. Kahn, 2008: Limitations of Bispectral Infrared Cloud Phase Determination and Potential for Improvement. *J. Appl. Meteor. Climatol.*, **47,** 2895-2910.

Nasiri, S. L., W. Madison, and G. R. McGarragh, 2004: The effects of multilayer clouds on MODIS cloud effective radius and optical thickness retrievals. *13th Conference on Satellite Meteorology and Oceanography*, 20-23,September, Norfolk, VA, USA.

Oreopoulos, L., 2005: The Impact of Subsampling on MODIS Level-3 Statistics of Cloud Optical Thickness and Effective Radius. *IEEE trans. geosci. remote sens*, **43,** 366 - 373.

Oreopoulos, L. and R. Davies, 1998: Plane parallel albedo biases from satellite observations. Part I: Dependence on resolution and other factors. *J Climate*, **11,** 919-932.

Oreopoulos, L. and R. F. Cahalan, 2005: Cloud Inhomogeneity from MODIS. *J. Climate*, **18,** 5110-5124, doi: 10.1175/JCLI3591.1

Paltridge, G. W., 1974: Infrared emissivity, short-wave albedo, and the microphysics of stratiform water clouds. *J. Geophys. Res.*, **20,** 4053-4058.

Parol, F., J. Descloitres, and Y. Fouquart, 2000: Cloud optical thickness and albedo retrievals from bidirectional reflectance measurements of POLDER instruments during ACE-2. *Tellus*, **52B,** 888-908.

Parol, F., J. Buriez, C. Vanbauce, J. Riedi, and M. LC-Labonnote, 2004: Review of capabilities of multi-angle and polarization cloud measurements from POLDER. *Adv. Space Res*, **33,** 1080-1088.

Parol, F., C. Vanbauce, J. Riedi, F. Thieuleux, Z. Poussi, and A. Lifermann, 2007: Comparison and statistical analysis of cloud properties derived from POLDER and MODIS. *Proc. of the joint 2007 EUMETSAT and 15th AMS Conference*, Amsterdam, the Netherlands, 24-28.

Parol, F., J. Buriez, C. Vanbauce, P. Couvert, G. Seze, P. Goloub, and S. Cheinet, 1999: First results of the POLDER "Earth Radiation Budget andClouds" operational algorithm. *Geoscience and Remote Sensing, IEEE Transactions on*, **37,** 1597-1612.

Pilewskie, P. and S. Twomey, 1987: Cloud phase discrimination by reflectance measurements near 1.6 and 2.2 μm. *J. Atmos. Sci.*, **44,** 3410-3420.

Pincus, R. and M. B. Baker, 1994: Effect of precipitation on the albedo susceptibility of clouds in themarine boundary layer. *Nature*, **372,** 250- 252.

Pincus, R., S. McFarlane, and S. Klein, 1999: Albedo bias and the horizontal variability of clouds in subtropical marine boundary layers: Observations from ships and satellites. *J. Geophys. Res.*, **104(D6)** 6183-6191.

Platnick, S. and F. P. J. Valero, 1995: A Validation of a Satellite Cloud Retrieval during ASTEX. *J. Atmos. Sci.*, **52** 2985-3001.

Platnick, S., M. King, P. Hubanks, and G. Wind, 2007: Cloud Optical Thickness over Land Retrieval Problem in Collection 005. *Internal report available at* http://modis-atmos.gsfc.nasa.gov/_docs/Cloud_Optical_Property_Retrieval_Problem_v1.pdf.

Platnick, S., J. Y. Li, M. D. King, H. Gerber, and P. V. Hobb, 2001: A solar reflectance method for retrieving the optical thickness and droplet size of liquid water clouds over snow and ice surfaces. *J. Geophy. Res.*, **106,** 15,185-15,199.

Platnick, S., M. King, S. A. Ackerman, W. P. Menzel, B. A. Baum, J. C. Riedi, and R. A. Frey, 2003: The MODIS cloud products: algorithms and examples from Terra. *IEEE Transactions on Geoscience and Remote Sensing*, **41,** 459-473.

Poetzsch-Heffter, C., Q. Liu, E. Ruperecht, and C. Simmer, 1995: ffect of Cloud Types on the Earth Radiation Budget Calculated with the ISCCP Cl Dataset: Methodology and Initial Results. *J. Climate*, **8,** 829-843.

Pruppacher, H. R., 1995: A new look at homogeneous ice nucleation in supercooled water drops. *J. Atmos. Sci.*, **52,** 1924-1933.

Pruppacher, H. R. and J. D. Klett, 1997: Microphysics of Clouds and Precipitation, Second Revised and Enlarged Edition with an Introduction to Cloud Chemistry and Cloud Electricity. *Kluwer Academic Pulishers, Dordrecht*.

Ramanathan, V., 1987: The Role of Earth Radiation Budget Studies in Climate and General Circulation Research. *Journal of Geophysical Research*, **92,** 4075 - 4095.

Ramanathan, V., E. J. Pitcher, R. C. Malone, and M. L. Blackmon, 1983: The response of a spectral General Circulation Model to Refinements in Radiative Processes. *J. Atmos. Sci*, **40,** 605-630.

Ramanathan, V., P. J. Crutzen, J. T. Kiehl, and D. Rosenfeld, 2001: Aerosols, Climate, and the Hydrological Cycle. *Science*, **294,** 2119-2124.

Ramanathan, V., R. D. Cess, E. F. Harrison, P. Minnis, B. R. Barkstrom, E. Ahmad, and D. Hartmann, 1989: Cloud-Radiative Forcing and Climate: Results from the Earth Radiation Budget Experiment. *Science*, **243,** 57-63.

—, 1989: Cloud-Radiative Forcing and Climate: Results from the Earth Radiation Budget Experiment. *Science*, **243,** 57 - 63.

Remer, L. A., Y. J. Kaufman, D. Tanré, S. Mattoo, D. A. Chu, J. V. Martins, R.-R. Li, C. Ichoku, R. C. Levy, R. G. Kleidman, T. F. Eck, E. Vermote, and B. N.

Holben, 2005: The MODIS aerosol algorithm, products and validation. *J. Atmos. Sci.*, **62,** 947-973.

Riedi, J., 2001: Analyse de la phase thermodynamique des nuages à l'échelle globale: unilisation des measures de polarisation du radiomètre spatial POLDER1/ADEOS1. *Ph.D. Thesis, Université Lille 1*.

Riedi, J., P. Goloub, and R. Marchand, 2001: Comparison of POLDER cloud phase retrievals to active remote sensors measurements at ARM SGP site. *Geophys. Res. Lett.*, **28,** 2185-2188.

Riedi, J., M. Doutriaux-Boucher, P. Goloub, and P. Couvert, 2000: Global distribution of cloud top phase from POLDER/ADEOS I. *Geophys. Res. Lett.*, **27,** 1707-1710.

Riedi, J., B. Marchant, S. Platnick, B. Baum, F. Thieuleux, C. Oudard, F. Parol, J. Nicolas, and P. Dubuisson, 2007: Cloud thermodynamic phase inferred from merged POLDER and MODIS data. *Atmos. Chem. Phys. Discuss*, **7,** 14103-14137.

Riedi, J., B. Marchant, S. Platnick, B. A. Baum, F. Thieuleux, C. Oudard, F. Parol, J.-M. Nicolas, and P. Dubuisson, 2010: Cloud thermodynamic phase inferred from merged POLDER and MODIS data. *Atmos. Chem. Phys.*, **10,** 11851-11865.

Robert A. Houze, J., 1994: Cloud Dynamics. *Academic Press*.

Roebeling, R. A., A. J. Feijt, and P. Stammes, 2006: Cloud property retrievals for climate monitoring: Implications of differences between Spinning Enhanced Visible and Infrared Imager (SEVIRI) on METEOSAT-8 and Advanced Very High Resolution Radiometer (AVHRR) on NOAA-17. *J. Geophys. Res.*, **111,** doi:10.1029/2005JD006990.

Roeckner, E., U. Schlese, J. Biercamp, and P. Loewe, 1987: Cloud optical depth feedbacks and climate modelling. *Nature*, **329,** 138-140.

Rogers, R. R. and M. K. Yau, 1989: *A short course in cloud physics (3rd edition)*.

Rossow, W. B. and A. A. Lacis, 1990: Global, Seasonal Cloud Variations from Satellite Radiance Measurements. Part II: Cloud Properties and Radiative Effects. *J Climate*, **3,** 1204-1253.

Rossow, W. B. and R. A. Schiffer, 1991: ISCCP cloud data products. *Bull. Amer. Meteorol. Soc.*, **71,** 2-20.

—, 1999: Advances in Understanding Clouds from ISCCP. *Bulletin of the American Meteorological Society*, **80,** 2261-2287.

Rossow, W. B., L. C. Garder, and A. A. Lacis, 1989: Global, Seasonal Cloud Variations from Satellite Radiance Measurements. Part I: Sensitivity of Analysi. *J. Climate,*, **2,** 419-458.

Rossow, W. B., C. Delo, and B. Cairns, 2002: Implications of the observed mesoscale variations of clouds for the Earth's radiation budget. *J Climate*, **15,** 557-585.

Roy, D. P., J. S. Borak, S. Devadiga, R. E. Wolfe, M. Zheng, and J. Descloitres, 2002: The MODIS Land product quality assessment approach. *Remote Sensing of Environment*, **83,** 62-76.

Sassen, K., Z. Wang, and D. Liu, 2008: Global distribution of cirrus clouds from CloudSat/Cloud-Aerosol Lidar and Infrared Pathfinder Satellite Observations (CALIPSO) measurements *J. Geophys. Res.*, **113,** 10.1029/2008JD009972.

Smith, R. N. B., 1990: A scheme for predicting layer clouds and their water content in a general circulation model. *Q. J. R. Meteorol. Soc*, **116,** 435–460.

Spangenberg, D., P. Minnis, M. Shupe, T. Uttal, and M. Poellot, 2005: Retrieval of Cloud Phase Using the Moderate Resolution. Imaging Spectroradiometer Data during the Mixed-Phase. Arctic Cloud Experiment. *Fifteenth Atmospheric Radiation Measurement (ARM) Science Team Meeting, Daytona Beach, FL (US), 03/14/2005--03/18/2005*.

Stamnes, K., S. C. Tsay, W. J. Wiscombe, and K. Jayaweera, 1988: Numerically stable algorithm for discrete-ordinate-method radiative transfer in multiple scattering and emitting layered media. *Applied Optics.*, **27,** 2502-2509.

Stephens, G. L., 2004: Cloud Feedbacks in the Climate System: A Critical Review. *J Climate*, **18,** 237-273.

Stephens, G. L., G. W. Paltridge, and C. M. R. Platt, 1978: Radiation Profiles in Extended Water Clouds. III: Observations. *J. Atmos. Sci.*, **35,** 2133-2141.

Strabala, K. I., S. A. Ackerman, and W. P. Menzel, 1994: Cloud Properties inferred from 8-12µm Data. *Journal of Applied Meteorology*, **33,** 212-229.

Strahler, A. H., J.-P. Muller, MODIS Science Team Members, 1999: MODIS BRDF/Albedo Product: Algorithm Theoretical Basis Document. Version 5.0, MODIS Product ID: MOD43.

Stubenrauch, C. J., F. Eddounia, and G. Rädel, 2004: Correlations between microphysical properties of large-scale semi-transparent cirrus and the state of the atmosphere. *Atmos. Res.*, **72,** 403-423.

Stubenrauch, C. J., S. Cros, A. Guignard, and N. Lamquin, 2010: A 6-year global cloud climatology from the Atmospheric InfraRed Sounder AIRS and a statistical analysis in synergy with CALIPSO and CloudSat. *Atmos. Chem. Phys. Discuss*, **10,** 8247-8296.

Stubenrauch, C. J., A. Chedin, G. Radel, N. A. Scott, and S. Serrar, 2006: Cloud Properties and Their Seasonal and Diurnal Variability from TOVS Path-B. *J Climate*, **19,** 5531-5553.

Szczap, F., H. Isaka, M. Saute, B. Guillemet, and A. Ioltukhovski, 2000: Effective radiative properties of bounded cascade nonabsorbing

clouds: definition of the equivalent homogeneous cloud approximation. *J. Geophys. Res*, **105,** 20,617-20,634.

Tselioudis, G. and W. B. Rossow, 1994: Global multiyear variations of optical thickness with temperature in low and cirrus clouds. *Geophys. Res. Lett.*, **21,** 2211-2214.

Tselioudis, G., W. B. Rossow, and D. Rind, 1992: Global Patterns of Cloud Optical Thickness Variation with Temperature. *J Climate*, **5,** 1484-1495.

Twomey, S., 1974: Pollution and the planetary albedo. *Atmos. Environ.*, **8,** 1251-1256.

Várnai, T. and R. Davies, 1999: Effects of cloud heterogeneities on shortwave radiation: Comparison of cloud top variability and internal heterogeneity. *J. Atmos. Sci.* , **56,** 4206-4223

Várnai, T. and A. Marshak, 2007: View angle dependence of cloud optical thickness retrieved by MODIS. *J. Geophys. Res.*, **112, ,** doi:10.1029/2005JD006912.

Vanbauce, C., J. C. Buriez, F. Parol, B. Bonnel, G. Seze, and P. Couvert, 1998: Apparent pressure derived from ADEOS-POLDER observations in the oxygen A-band over ocean. *Geophys. Res. Lett.*, **25,** 3159-3162.

Vaughan, M. A., S. A. Young, D. M. Winker, K. A. Powell, A. H. Omar, Z. Liu, Y. Hu, and C. A. Hostetler, 2005: Fully automated analysis of space-based lidar data: an overview of the CALIPSO retrieval algorithms and data products. *Proc. SPIE*, **5575,** 16-30.

Waquet, F., J. Riedi, L. C-Labonnote, P. Goloub, J. L. Deuzé, and F. Auriol, 2009: Aerosol remote sensing over clouds using the A-Train observations. *J. Atmos. Sci.*, **66,** 2468-2480.

Warren, S. G., C. J. Hahn, J. London, R. M. Chervin, and R. L. Jenne, 1986: Global distribution of total cloud cover and cloud type amounts over land**,** NCAR Technical Note, NCAR/TN-273+STR, National Center for Atmospheric Research, Boulder, Colorado.

—, 1988: Global distribution of total cloud cover and cloud type amounts over the ocean**,** NCAR Tech. Note, NCAR/TN-317+STR, National Center for Atmospheric Research, Boulder, Colorado.

Wielicki, B. A. and L. Parker, 1992: On the determination of cloud cover from satellite sensors: The effect of sensor spatial resolution. *Journal of Geophysical Research*, **97,** 12,799-12,823.

Wind, G., S. Platnick, M. D. King, P. A. Hubanks, M. J. Pavolonis, A. K. Heidinger, P. Yang, and B. A. Baum, 2010: Multilayer Cloud Detection with the MODIS Near-Infrared Water Vapor Absorption Band. *J. Appl. Meteor. & Climatol.*, **49,** 2315-2333.

Winker, D. M., J. R. Pelon, and M. P. McCormick, 2003: The CALIPSO mission: spaceborne lidar for observation of aerosols and clouds. *Proc. SPIE*, **4893,** 1-11.

Wolters, E. L. A., H. M. Deneke, J. F. Meirink, and R. A. Roebeling, 2008: Impact of broken and inhomogeneous clouds in satellite cloud-phase retrieval. *EUMETSAT Meteorological Satellite Conference, 8-12 September 2008, Darmstadt, Germany.*

Wolters, E. L. A., H. M. Deneke, B. J. J. M. v. d. Hurk, J. F. Meirink, and R. A. Roebeling, 2010: Impact of broken and inhomogeneous clouds on satellite cloud-phase retrieval. *J. Geophy. Res.,* **115,** D10214, doi:10.1029/2009JD012205.

Wylie, D. P. and W. P. Menzel, 1989: Two years of cloud cover statistics using VAS. *J. Clim. Appl. Meteor.*, **2,** 380-392.

Wylie, D. P., W. P. Menzel, H. M. Woolf, and K. I. Strabala, 1994: Four Years of Global Cirrus Cloud Statistics Using HIRS. *Journal of Climate*, **7,** 1972-1986.

Yang, P. and K. N. Liou, 2000: Light Scattering by Nonspherical Particles: Theory, Measurements, and Applications. Chapter 7. Finite-Difference Time Domain

Method for Light Scattering by Nonspherical and Inhomogeneous Particles. *Academic Press, San Diego*, 173-211.

Yao, M.-S. and A. D. Del Genio, 2002: Effects of cloud parameterization on the simulation of climate changes in the GISS GCM. Part II: Sea surface temperature and cloud feedbacks. *J. Climate*, **15,** 2491-2504.

Young, A., D. Winker, M. Vaughan, Y. Hu, and R. Kuehn, 2008: CALIOP ATBD, Part 4: Extinction Retrieval Algorithms. No. PC-SCI-202 Part 3 Release 1.0-Draft.

Zhang, Z., P. Yang, G. Kattawar, J. Riedi, L. C. Labonnote , B. Baum, S. Platnick, and H.-L. Huang, 2009: Influence of ice particle model on retrieving cloud optical thickness from satellite measurements: model comparison and implication for climate study. *Atmos. Chem. Phys. Discuss.*, **9,** 1757-1796.

Zhao, G. and L. Di Girolamo, 2004: A Cloud Fraction versus View Angle Technique for Automatic In-Scene Evaluation of the MISR Cloud Mask. *Journal of Applied Meteorology*, **43,** 860-869.

Zinner, T. and B. Mayer, 2006: Remote sensing of stratocumulus clouds: Uncertainties and biases due to inhomogeneity. *J. Geophys. Res.*, **111,** D14209, doi:10.1029/2005JD006955.

Annex

Gas		Center ν (cm^{-1}) (λ (μ m))	Band interval (cm^{-1})
H_2O	(Visible & NIR)	3703 (2.7) 5348 (1.87) 7246 (1.38) 9090 (1.1) 10638 (0.94) 12195 (0.82) 13888 (0.72) visible	2500-4500 4800-6200 6400-7600 8200-9400 10100-11300 11700-12700 13400-14600 15000-22600
	(UV)	< 0.21 0.6-0.72	
	(IR)	1594.8 (6.3) continuum	0-1000 640-2800 200-1200
CO_2	(Visible & NIR)	2526 (4.3) 3703 (2.7) 5000 (2.0) 6250 (1.6) 7143 (1.4)	2000-2400 3400-3850 4700-5200 6100-6450 6850-7000
	(UV)	-	-
	(IR)	667 (15) 961 (10.4) 1063.8 (9.4) 2349 (4.3)	540-800 850-1250 2100-2400
O_3	(Visible & NIR)	2110 (4.74) 3030 (3.3) visible	2000-2300 3000-3100 10600-22600
	(UV)	0.17-0.35 0.45-0.75	
	(IR)	1110 (9.01) 1043 (9.59) 705 (14.2)	950-1200 600-800 600-800
O_2	(Visible & NIR)	6329 (1.58) 7874 (1.27) 9433 (1.06) 13158 (0.76) 14493 (0.69) 15873 (0.63)	6300-6350 7700-8050 9350-9400 12850-13200 14300-14600 14750-15900
	(UV)	< 0.245	
	(IR)	-	

Annex 1 – *Main absorption bands of atmospheric gases in UV, visible, NIR and IR.*

RESUMÉ

Les observations des différents A-Train satellites fournissent une occasion sans précédent d'étudier les composants atmosphériques y compris les nuages. Dans cette étude, nous avons développé une analyse statistique afin de comparer le taux de couverture nuageuse, la phase thermodynamique et l'épaisseur optique des nuages restituées par deux capteurs passifs de l'A-Train: POLDER (Polarization and Directionality of the Earth Reflectance) et MODIS (MODerate Resolution Imaging Spectroradiometer).

Tout d'abord les variations régionales et saisonnières du taux de couverture nuageuse des deux captures et les biais entre eux sont étudiés. Ces biais sont retrouvés principalement liée avec la résolution spatiale, les aérosols, les cirrus et des types de surface.

Ensuite la phase thermodynamique des nuages sont analysées. Ces produits dérivés par deux capteurs passifs sont comparées et étudiées en s'appuyant sur les structures verticales et les propriétés optiques des nuages restituées simultanément par un autre A-Train membre, CALIOP (Cloud-Aerosol Lidar with Orthogonal Polarization). Cela permet d'identifier et de qualifier les biais présents dans l'ensemble des 3 données considérées. Parmi ces biais, l'impact des géométries d'observation, des cirrus fins, des aérosols, des surfaces enneigées, des nuages multicouches et fractionnés sont discutées. Les valeurs de haute confiance sont selectionées par la suite pour étudier à l'échelle mondiale ou régionale la transition verticale de l'eau liquide à la glace et les variations de cette transition avec les régimes de formation et de développement des nuages, tout particulièrement la dynamique à grande échelle et la microphysique des nuages.

Enfin l'épaisseur optique des nuages sont étudiées. Les effets de la résolution spatiale, de la microphysique et de l'hétérogénéité des nuages sont principalement étudiés pour mieux comprendre des écarts importants entre deux capteurs passifs.

ABSTRACT

The A-Train observations provide an unprecedented opportunity for synchronous monitoring of the entire atmosphere including clouds at the global scale. In this study we illustrate a statistical analysis and comparison of cloud cover, thermodynamic phase and cloud optical thickness mainly derived from the coincident POLDER (Polarization and Directionality of the Earth Reflectance), and MODIS (MODerate Resolution Imaging Spectroradiometer) sensors in the A-Train constellation.

We presented first the results of extensive study of the regional and seasonal variations of cloud cover from POLDER and MODIS and discuss the possible factors linked to the potential biases between them, among which the spatial resolution, aerosols, cirrus and particular surfaces are particularly concerned.

Cloud top phase products were then compared between the two passive sensors and discussed in view of cloud vertical structure and optical properties derived simultaneously from collocated CALIOP (Cloud-Aerosol Lidar with Orthogonal Polarization, another A-Train member) observations, which allow to identify and qualify potential biases present in the 3 considered dataset. Among those, we discussed the impact of observed geometries, thin cirrus, aerosols, snow/ice surfaces, multilayer and fractional cloud cover on global statistics of cloud phase derived from POLDER and MODIS passive measurements. Based on these analyses we selected cloud retrievals of high confidence to study the global and regional vertical ice-water transition and the variations of this transition with cloud formation and development regimes, particularly the impact of large-scale dynamics and cloud microphysics.

Cloud optical thicknesses were finally studied. The impacts of spatial resolution, cloud microphysics and heterogeneity are mainly discussed for the understanding of the significant biases on optical thickness from the two sensors.